

WESTERN SYDNEY
UNIVERSITY



An Investigation of
the Diffuse Radio Emission
in the Galaxy Cluster Abell S1136

Peter James Macgregor

A thesis submitted for the degree of
Master of Research
at
Western Sydney University

April 2020

Supervisors:

Prof. Ray Norris (Western Sydney University / CSIRO)

Dr Luke Barnes (Western Sydney University)

Dr Matthew Whiting (CSIRO Astronomy and Space Science)

Dr David Parkinson (Korea Astronomy and Space Science Institute)

© Peter James Macgregor – 2020

Acknowledgements

Personal Acknowledgements

This thesis was made possible by the support and guidance of the staff at Western Sydney University, the staff at the CSIRO Astronomy and Space Science (CASS) division, the staff at the Australia Telescope National Facility (ATNF), and the traditional owners of the land on which the Murchison Radio Observatory and the Australian Square Kilometre Array Pathfinder telescope is located.

This thesis is also the result of the support and guidance of many other people who have helped me on this journey. I give a special thanks to you.

To my friends and family, you know who you are, you have had to tolerate my many moods, thank you; to Professor Miroslav Filipović for encouraging me to enter into a research degree with Western Sydney University Astrophysical eSciences Laboratory, thank you; to my Western Sydney University primary and secondary supervisors, Professor Ray Norris and Doctor Luke Barnes, thank you; to my secondary supervisor Doctor David Parkinson from the Korea Astronomy and Space Science Institute (KASI), thank you; to the amazing people who were once my lecturers and who have also welcomed me into the team, Doctor Evan Crawford, Doctor Ain De Horta, and Doctor Nick Tothill, thank you; to my fellow research students Devika, Kieran, Maddie, Miranda, Nic, Pero, Rami, and Velibor, thank you; and to Doctor Jordan Collier, Doctor Andrew O'Brien, and Doctor Tim Galvin, the recent alumni from our small but amazing group, who have helped me in many ways, thank you. Without doubt, your advice and direction have been immeasurable. You have all taught me so much.

Scientific Acknowledgements

The main body of this thesis has used data obtained from the Australian Square Kilometre Array Pathfinder (ASKAP) and the Murchison Wide Field Array (MWA), which are a part of the Murchison Radio-astronomy Observatory in Western Australia. The Australian SKA Pathfinder is part of the Australia Telescope National Facility which is managed by CSIRO. Operation of ASKAP is funded by the Australian Government with

support from the National Collaborative Research Infrastructure Strategy. ASKAP uses the resources of the Pawsey Supercomputing Centre. Establishment of the ASKAP, the Murchison Radio-astronomy Observatory and the Pawsey Supercomputing Centre are initiatives of the Australian Government, with support from the Government of Western Australia and the Science and Industry Endowment Fund. I acknowledge the Wajarri Yamatji people as the traditional owners of the Observatory site.

The Pawsey Supercomputing Centre is supported by \$90 million funding as part of the Australian Government's measures to support national research infrastructure under the National Collaborative Research Infrastructure Strategy and related programs through the Department of Education.

This thesis has used data based on observations obtained with XMM-Newton, an ESA science mission with instruments and contributions directly funded by the ESA Member States and NASA.

This thesis has made use of the VizieR catalogue access tool, CDS, Strasbourg, France (DOI: 10.26093/cds/vizier). The original description of the VizieR service was published in 2000, A&AS 143, 23.

This thesis has made use of the Karma virtualisation toolkit (Gooch, 1995) for image production.

This thesis made use of ds9, a tool for data visualization supported by the Chandra X-ray Science centre (CXC) and the High Energy Astrophysics Science Archive centre (HEASARC) with support from the JWST Mission office at the Space Telescope Science Institute for 3D visualization.

This thesis made use of the software package MIRIAD. Miriad is a radio interferometry data reduction package, which can be used for the reduction of radio continuum and spectral line data.

This thesis has used the Ned Wright Cosmology Calculator (Wright, 2006).

This thesis has used images from the Digitized Sky Survey (DSS) and the Second Palomar Observatory Sky Survey (POSS-II). The Digitized Sky Surveys were produced at the Space Telescope Science Institute under U.S. Government grant NAG W-2166. The images of these surveys are based on photographic data obtained using the Oschin Schmidt Telescope on Palomar Mountain and the UK Schmidt Telescope. The plates were processed into the present compressed digital form with the permission of these institutions. The National Geographic Society - Palomar Observatory Sky Atlas (POSS-I) was made by the California Institute of Technology with grants from the National Geographic Society. The Second Palomar Observatory Sky Survey (POSS-II) was made by the California Institute of Technology with funds from the National Science Foundation, the National Geographic Society, the Sloan Foundation, the Samuel Oschin Foundation, and the Eastman Kodak Corporation. The Oschin Schmidt Telescope is operated by the California Institute of Technology and Palomar Observatory. The UK

Schmidt Telescope was operated by the Royal Observatory Edinburgh, with funding from the UK Science and Engineering Research Council (later the UK Particle Physics and Astronomy Research Council), until 1988 June, and thereafter by the Anglo-Australian Observatory. The blue plates of the southern Sky Atlas and its Equatorial Extension (together known as the SERC-J), as well as the Equatorial Red (ER), and the Second Epoch [red] Survey (SES) were all taken with the UK Schmidt. All data are subject to the copyright given in the copyright summary. Copyright information specific to individual plates is provided in the downloaded FITS headers. Supplemental funding for sky-survey work at the ST ScI is provided by the European Southern Observatory.

This thesis makes use of data products from the Wide-field Infrared Survey Explorer, which is a joint project of the University of California, Los Angeles, and the Jet Propulsion Laboratory/California Institute of Technology, and NEOWISE, which is a project of the Jet Propulsion Laboratory/California Institute of Technology. WISE and NEOWISE are funded by the National Aeronautics and Space Administration.

This thesis has made use of NASA's Astrophysics Data System (NASA ADS), and the NASA/IPAC Extragalactic Database (NED) which is operated by the Jet Propulsion Laboratory, California Institute of Technology, under contract with the National Aeronautics and Space Administration.

This thesis made use of TOPCAT, an interactive graphical viewer and editor for tabular data (Taylor, 2005)

The work presented in this thesis is, to the best of my knowledge and belief, original except as acknowledged in the text.

I hereby declare that I have not submitted this material, either in full or in part, for a degree at this or any other institution.

.....
Peter James Macgregor April 30, 2020

Foreword

The Master of Research at Western Sydney University is a two-year program, consisting of one year of masters level course work, and one year of research. At all stages, this work has been performed under the excellent supervision of my primary and secondary supervisors.

Contents

List of Tables	v
List of Figures	vi
Abstract	x
List of Abbreviations	xii
1 Introduction	1
1.1 From the Big Bang to Galaxy Formation	1
1.2 Galaxy Grouping and Clustering	8
1.2.1 The Virial Theorem	9
1.2.2 Critical Density	10
1.2.3 The Geometrical Models for Universe Expansion	10
1.3 The Morphology and Classification of Galaxies and Galaxy Clusters .	12
1.3.1 Galaxies	12
1.3.1.1 The Hubble Tuning Fork	12
1.3.1.2 The De Vaucouleurs System	14
1.3.2 Galaxy Clusters	16
1.3.2.1 The Abell Classification Scheme	16
1.3.2.2 The Bautz–Morgan Classification Scheme	17
1.4 Galaxy Clusters at Different Wavelengths	18
1.4.1 Radio	19
1.4.2 Infrared	23
1.4.3 Optical	24
1.4.4 X-ray	26
1.4.5 Gamma Ray	27
1.5 Radio Emission in Galaxies and Galaxy Clusters	28
1.5.0.1 Spectral Index	28
1.5.1 A Taxonomy to Characterise Diffuse Radio Emission	29
1.5.1.1 VLBI Core	29

1.5.1.2	Confined Cluster Core (CCC) Source	29
1.5.1.3	Radio Galaxy: FRI, WAT, NAT	31
1.5.1.4	Classic Double: FRII	31
1.5.1.5	AGN Relic	32
1.5.1.6	Radio Phoenix	35
1.5.1.7	Radio “Gischt”	35
1.5.2	Radio Mini-Halo	35
1.5.2.1	Radio Halo	36
1.6	Evidence of Filamentary Structure in Recent Literature	37
1.6.1	The Galaxy Cluster Abell 2593	38
1.6.2	The Galaxy Cluster Abell 2626	40
1.6.3	The Galaxy Cluster MACS J0717.5+3745	40
1.6.4	The Galaxy Cluster Abell 1033	41
1.6.5	A Radio Relic in the Shapley Concentration Core, Between the Abell Galaxy Clusters A3558 and A3562	43
1.7	The Galaxy Cluster Abell S1136	45
1.8	Other Data used for Comparison	48
1.8.1	ATCA Radio	48
1.8.2	WISE Infrared	49
1.8.3	DSS Optical	51
1.8.4	MWA Phase I and Phase II Radio	51
1.8.4.1	MWA Phase I Radio	51
1.8.4.2	MWA Phase II Radio	56
1.8.5	XMM-Newton X-ray	58
1.9	Research Question	60
2	Data and Observations	62
2.1	The Australian Square Kilometre Array Pathfinder (ASKAP)	62
2.1.1	Observations with 16 Antennas	65
2.1.2	Observations with 33 Antennas	66
2.2	ASKAP Data Reduction and Imaging	67
3	Results	70
3.1	Images	70
3.1.1	ASKAP 16 Antenna Observations	70
3.1.1.1	ASKAP 16 Antenna Array, Taylor Term 0, Briggs Robustness - 0.5	72
3.1.1.2	ASKAP 16 Antenna Array, Taylor Term 0, Briggs Robustness + 2.0	76
3.1.2	ASKAP 33 Antenna Observations	79

3.1.2.1	ASKAP 33 Antenna Array, Taylor Term 0, Briggs Robustness -0.5	81
3.1.2.2	ASKAP 33 Antenna Array, Taylor Term 0, Briggs Robustness 0	83
3.1.2.3	ASKAP 33 Antenna Array, Taylor Term 0, Briggs Robustness +2.0	85
3.1.2.4	ASKAP 33 Antenna Array, Taylor Term 0, Briggs Robustness 0, 30", Gaussian Taper	87
3.1.3	ASKAP 16 and 33 Antenna Array: Contour Overlay	89
3.1.4	33 Antenna Array: Areas of Interest	92
3.2	Polarisation	95
3.3	Spectral Index	98
3.4	PKS 2333-318	101
3.5	The Abell S1136 Virial Radius	103
3.6	ASKAP Comparison with XMM-Newton X-ray	104
3.6.1	Initial Analysis	104
3.6.2	Analysis of a Potential Radio Channel in the X-ray Emission .	105
3.6.3	X-ray Temperature and Spectral Profile Analysis	106
3.7	ASKAP Comparison with DSS Optical	109
3.8	ASKAP Comparison with WISE Infrared	111
3.9	ASKAP Comparison with MWA Phase I	113
3.9.1	Images with MWA Phase I Radio Background	113
3.9.2	Images with ASKAP Radio Background	113
3.10	ASKAP Comparison with MWA Phase II	118
3.10.1	Images with MWA Phase II Radio Background	118
3.10.2	Images with ASKAP Radio Background	122
3.11	Image combining DSS Optical, MWA Phase I Radio, NVSS Radio, and the TFIR GMRT Sky Survey	126
4	Discussion	128
4.1	The Galaxy Cluster Abell S1136	128
4.1.1	Filamentary Structure and Spectral Index	129
4.1.2	Polarisation	131
4.1.3	The “Radio Channel”	132
4.1.4	Interaction Between Abell S1136 and PKS 2333-318	133
4.1.5	Classification of the Abell S1136 Radio Emission Using the Taxonomy in Section 1.5.1: Kempner et al. (2004)	133
4.1.6	Classification of the Abell S1136 Radio Emission Using Feretti et al. (2012)	137

4.1.6.1	Radio Relics (aka. “Gischt”)	137
4.1.6.2	Radio Halos	139
4.1.6.3	Radio Mini-Halos	141
4.1.6.4	Discussion on Abell S1136 Diffuse Emission Using Feretti et al. (2012a)	143
4.1.7	Classification of the Abell S1136 Radio Emission when Com- pared with the Recent Literature	145
5	Conclusions and Future Work	147
5.1	Conclusions	147
5.2	Future Work	149
References		151
A	Data Processing Parameters	171
A.1	Data Processing Parameters	171
B	Paper in Preparation	174
B.1	EMU Observations of Filamentary Structures in the Abell S1136 Galaxy Cluster	174
C	Abell S1136 Poster Presentation	175
D	Catalogue of Abell Clusters	176

List of Tables

1.1	The Yerkes System for Galaxy Classification	15
1.2	Celestial Objects at Different Wavelengths	20
1.3	Properties of the Infrared Spectrum	25
1.4	A Summary of Diffuse Emission Characteristics from Kempner et al. (2004)	30
2.1	Summary Details of the 2017 and 2019 Observations of Abell S1136 with the ASKAP	64
3.2	MWA Phase I Contour Levels used in the Comparison with ASKAP Radio Images	113
3.3	MWA Phase II Contour Levels used in the Comparison with ASKAP Radio Images	118
A.1	Processing parameters for ASKAP 16 antenna observation	172
A.2	Processing parameters for ASKAP 33 antenna observation	173
D.1	Abell Southern Clusters	176

List of Figures

1.1	Timeline of the Universe	2
1.2	Dark Matter Distribution in the Cosmic Web	3
1.3	Hubble’s Velocity to Distance Relationship	5
1.4	Cosmological Redshift	7
1.5	The Local Group of Galaxies	8
1.6	The Critical Density of the Universe	11
1.7	Hubble’s Tuning Fork Galaxy Classification	13
1.8	The Hubble - de Vaucouleurs Galaxy Morphology Diagram	15
1.9	A Comparison of the Wavelengths in the Electromagnetic Spectrum .	18
1.10	The Milky Way Viewed at Different Wavelengths	21
1.11	Some of the ASKAP Antennas at the Murchison Radio Observatory .	22
1.12	Wiens Law: Temperature Versus Wavelength	24
1.13	An Example of a Fanaroff-Riley Type I Radio Galaxy	32
1.14	An Example of a Fanaroff-Riley Type II Radio Galaxy	33
1.15	The “Smoking Gun” Galaxy from the Emu Pilot Survey (Norris+, in prep)	34
1.16	The Galaxy Cluster Abell 2593 (Mandal et al., 2020)	39
1.17	The Galaxy Cluster Abell 2626 (Ignesti et al., 2018)	40
1.18	The Galaxy Cluster MACS J0717.5+3745 (Bonafede et al., 2018) .	41
1.19	The Galaxy Cluster Abell 1033 (de Gasperin et al., 2017)	42
1.20	A Radio Relic in the Shapley Concentration Core, Between the Abell Galaxy Clusters A3558 and A3562 (Venturi et al., 2017a)	43
1.21	A Candidate Relic in Abell 3558 (Venturi et al., 2017a)	44
1.22	The Location of the Abell S1136 Galaxy Cluster in the Pisces-Cetus Supercluster	46
1.23	An Image of Abell S1136 from the Original Optical Plates	47
1.24	An Image of Abell S1136 from the Australia Telescope Compact Array Radio Telescope	49
1.25	An Image of Abell S1136 from the Wide-field Infrared Survey Explorer Telescope	50

1.26	An Image of Abell S1136 from the 2nd Digitised Sky Survey	52
1.27	MWA Phase I Array Configuration	53
1.28	MWA Phase IIA Compact Array Configuration	54
1.29	MWA Phase IIB Extended Array Configuration	55
1.30	An Image of Abell S1136 from the MWA Phase I Observations at 139- 170 MHz, Overlaid with Contours from the 2019 ASKAP Observations	56
1.31	An Image of Abell S1136 from the MWA Phase II Observations at 215 MHz, Overlaid with Contours from the 2019 ASKAP Observations	57
1.32	An Image of Abell S1136 from the XMM-Newton X-ray Telescope, Overlaid with Contours from the 2019 ASKAP Observations	59
2.1	The ASKAP Antenna Locations for the 2017 and 2019 Observations of Abell S1136	63
2.2	The ASKAP Beam Footprints used in the 2017 and 2019 Observations of Abell S1136	65
2.3	The ASKAP Early Science Data Reduction Pipeline	68
3.1	The Abell S1136 “Hot Spots”	71
3.2	Abell S1136 with ASKAP 16 Antenna, robust = -0.5, Taylor Term 0, No Contours	73
3.3	Abell S1136 with ASKAP 16 Antenna, robust = -0.5, Taylor Term 0, with ASKAP 16 Contours	74
3.4	Abell S1136 Diffuse Structure with ASKAP 16 Antenna, robust = -0.5, Taylor Term 0	75
3.5	ASKAP 16, robust = +2.0, Taylor Term 0, No Contours	76
3.6	ASKAP 16, robust = +2.0, Taylor Term 0, with ASKAP 16 Contours	77
3.7	Abell S1136 Diffuse Structure with ASKAP 16 antenna, robust = +2.0, Taylor Term 0	78
3.8	ASKAP 33 Antenna, robust = -0.5, Taylor Term 0, No Contours	81
3.9	ASKAP 33 Antenna, robust = +2.0, Taylor Term 0, with ASKAP 33 Contours	82
3.10	ASKAP 33 Antenna, robust = 0, Taylor Term 0, No Contours	83
3.11	ASKAP 33 Antenna, robust = 0, Taylor Term 0, with ASKAP 33 Contours	84
3.12	ASKAP 33 Antenna, robust = +2.0, Taylor Term 0, No Contours	85
3.13	ASKAP 33 Antenna, robust = +2.0, Taylor Term 0, with ASKAP 33 Contours	86
3.14	ASKAP 33 Antenna, “alt” Image at robust = 0 with a 30” Gaussian Taper, Taylor Term 0, No Contours	87

3.15	ASKAP 33 Antenna, “alt” Image at $\text{robust} = 0$ with a 30” Gaussian Taper, Taylor Term 0, with ASKAP 33 Contours	88
3.16	ASKAP 16, $\text{robust} = -0.5$, Taylor Term 0, with ASKAP 16 and 33 contours	90
3.17	ASKAP 16, $\text{robust} = +2.0$, Taylor Term 0, with ASKAP 16 and 33 contours	91
3.18	Areas of Interest in the ASKAP 33 Antenna $\text{robust} = 0$ Image	93
3.19	Areas of Interest in the ASKAP 33 Antenna $\text{robust} = 0$ “alt” Image	94
3.20	Peak-P Polarisation Emission in the Central 4 Beams of the ASKAP 33 Antenna Observation	96
3.21	Peak-P Polarisation Emission in the Central 4 Beams of the ASKAP 33 Antenna Observation, Overlaid with ASKAP 33 Contours	97
3.22	Abell S1136 Spectral Index Map at $\text{robust} = 0$	99
3.23	Abell S1136 Spectral Index Map at $\text{robust} = +1.0$	100
3.24	The PKS 2333-318 Fat Radio Lobe	102
3.25	Abell S1136 r_{200} Virial Radius	103
3.26	Abell S1136 ASKAP Image with XMM-Newton Contours	105
3.27	Abell S1136 X-ray Image Overlaid with ASKAP 33 Antenna Contours)	106
3.29	ASKAP Comparison with DSS Optical, Overlaid with Contours from ASKAP and DSS	110
3.30	ASKAP Comparison with WISE Infrared, Overlaid with Contours from ASKAP and WISE	112
3.31	ASKAP Comparison with MWA Phase I at 139-170 MHz, MWA Background	114
3.32	ASKAP Comparison with MWA Phase I at 170-231 MHz, MWA Background	115
3.33	ASKAP Comparison with MWA Phase I at 139-170 MHz, ASKAP Background	116
3.34	ASKAP Comparison with MWA Phase I at 170-231 MHz, ASKAP Background	117
3.35	ASKAP Comparison with MWA Phase II at the C121 Frequency Band, MWA Background	119
3.36	ASKAP Comparison with MWA Phase II at the C145 Frequency Band, MWA Background	120
3.37	ASKAP Comparison with MWA Phase II at the C169 Frequency Band, MWA Background	121
3.38	ASKAP Comparison with MWA Phase II at the C121 Frequency Band, ASKAP Background	123

3.39	ASKAP Comparison with MWA Phase II at the C145 Frequency Band, ASKAP Background	124
3.40	ASKAP Comparison with MWA Phase II at the C169 Frequency Band, ASKAP Background	125
3.41	The radio emission from Abell S1136 (Duchesne et al., 2017)	127
4.1	Combined ASKAP, MWA Phase I, and MWA Phase II Radio Image with Contours, Showing the Filamentary Structure in Abell S1136 . .	131
4.2	An Elongated Relic in the Galaxy Cluster CIZA J2242.8+5301 (van Weeren et al., 2010)	138
4.3	Polarisation and Spectral Index in the Galaxy Cluster CIZA J2242.8+5301 (Feretti et al., 2012)	139
4.4	A Roundish Relic in the Galaxy Cluster Abell 1664 (Giovannini and Feretti, 2004a)	140
4.5	A Radio Mini-Halo in the Galaxy Cluster RXJ1347.5-1145 (Feretti et al., 2012)	142

Abstract

In this thesis, I present observations of radio emission from the cluster of galaxies in Abell S1136. These observations were made with the Australian Square Kilometre Array Pathfinder (**ASKAP**) telescope, as part of the Early Science program of the Evolutionary Map of the Universe (**EMU**) (Norris, 2017).

I have compared these observations with data from the Murchison Wide Field Array (**MWA**) Phase I and Phase II radio telescopes, the XMM-Newton (**XMM**) X-ray Multi-Mirror Mission telescope, the Wide-field Infrared Survey Explorer (**WISE**) infrared telescope, the Australia Telescope Compact Array (**ATCA**) radio telescope, and the Digitised Sky Survey (**DSS**) optical plates. I have produced polarisation maps and spectral index maps to help determine the nature of the emission.

The diffuse radio emission in the centre of the cluster has been previously identified as a radio halo in surveys with **MWA**. When observed with the higher sensitivity and resolution of the **ASKAP**, I found that the diffuse emission breaks up into a number of filamentary structures, extending from the core of the Abell S1136 galaxy cluster in what appears to be a reverse “S” shape. This emission is similar to a Fanaroff-Riley Type I (**FRI**) Wide Angle Tail (**WAT**) radio galaxy and is interpreted as synchrotron emission from shock-excited electrons. There is evidence that the bright radio lobe in the southern tail of the **WAT** might be a high redshift background source.

Using data from the **MWA** and the **ASKAP**, I found the filamentary structure on both arms of the reverse “S” has a very steep spectral index at $\lesssim -2.0$ as it moves outward from the middle along the arms of emission. Using data from the **ATCA** and the **ASKAP**, I found little polarisation coming from the central sources of the galaxy cluster. Using data from **WISE**, **DSS**, and the **ASKAP**, I found the southern most central source of Abell S1136 has either very faint or no optical or infrared counterpart.

Using data from **XMM** and the **ASKAP**, I found the X-ray emission and radio emission to be coincident with the centre of the galaxy cluster, located on ESO 470-20 (Lauberts and Valentijn, 1989). I also found evidence of a possible channel in the X-ray emission extending to the north of the cluster, aligned with the radio emission.

In addition, I show serendipitous radio observations of the radio-loud Active Galactic Nuclei (**AGN**) PKS 2333-318, which lies to the north-west of the Abell S1136 galaxy cluster, and found PKS 2333-318 to be within the extent of both the cluster’s

Intra-Cluster Medium (**ICM**) and the cluster’s virial radius. When observed with the **ASKAP**, PKS 233-318 appears as a single-tailed “fat lobe” of radio emission, with subtle sub-structure, significant polarisation, and spectral index of ~ -0.8 . There is an indication in the results presented in this thesis that there may be an interaction between PKS 2333-318 and Abell S1136, although more observations are required to determine the nature.

The work in this thesis, and the draft paper in Appendix **B.1**, shows resolved filamentary structure in the radio emission from the galaxy cluster Abell S1136. This is the first time this structure has been observed in Abell S1136.

List of Abbreviations

AGN	Active Galactic Nuclei
APEC	Astrophysical Plasma Emission Code
ASKAP	Australian Square Kilometre Array Pathfinder
ATCA	Australia Telescope Compact Array
ATOA	Australia Telescope Online Archive
BCG	Brightest Cluster Galaxy
CCC	Confined Cluster Core
CXO	Chandra X-ray Observatory
DSS	Digitised Sky Survey
eeHIFLUGCS	extremely expanded HIghest X-ray FLUx Galaxy Cluster Sample
EMU	Evolutionary Map of the Universe
FOV	Field of View
FRG	First Ranked Galaxy
FRI	Fanaroff-Riley Type I
FRII	Fanaroff-Riley Type II
GLEAM	GaLactic and Extragalactic All-sky MWA survey
GLEAM-X	GaLactic and Extragalactic All-sky MWA eXtended survey
GMRT	Giant Metrewave Radio Telescope
ICM	Intra-Cluster Medium
IRSA	NASA/IPAC Infrared Science Archive
kpc	kiloparsec
LOFAR	Low-Frequency Array
Mpc	megaparsec
MRO	Murchison Radio-astronomy Observatory
MWA	Murchison Wide Field Array

NAT	Narrow Angle Tail
NRAO	National Radio Astronomy Observatory
NVSS	National Radio Astronomy Observatory (NRAO) Very Large Array (VLA) Sky Survey
PAF	Phased Array Feed
PAWSEY	Pawsey Supercomputing Centre
SCM	Standard Cosmological Model
TGSS	Tata Institute of Fundamental Research (TIFR) Giant Metrewave Radio Telescope (GMRT) Sky Survey
TIFR	Tata Institute of Fundamental Research
VLA	Very Large Array
VLBI	Very Long Baseline Interferometry
WAT	Wide Angle Tail
WENSS	Westerbork Northern Sky Survey
WISE	Wide-field Infrared Survey Explorer
WSRT	Westerbork Synthesis Radio Telescope
XMM	XMM-Newton

Chapter 1

Introduction

In this chapter, I introduce the formation of galaxies and galaxy clusters in the context of an expanding universe. I proceed to discuss observations of galaxies and clusters of galaxies at multiple wavelengths, before introducing the specific galaxy cluster that forms the focus of this project: Abell S1136.

1.1 From the Big Bang to Galaxy Formation

The Big Bang Model ([Luminet, 2015](#); [Planck Collaboration et al., 2016](#)) (also called the Standard Cosmological Model ([SCM](#))) is the currently accepted theory of how the Universe began ([Peebles et al., 1994](#)). This theory states that approximately 13.8 billion years ago, all the current matter and energy of the observable Universe was contained in a hot and dense primordial state. From this dense early state, the Universe expanded and cooled. The baryonic matter in the Universe first formed nuclei, and then atoms. Over the next approximately 400 million years, the atoms joined to form the first stars. A pictorial representation of this is in Figure 1.1.

As the first stars grew, they created bigger groups, and more stars were born. Over billions of years, structures such as galaxies and clusters formed when regions of high density collapsed under gravity, while regions of low density formed cosmic voids - better known as the cosmic web. Figure 1.2^{[\[1,2\]](#)} shows the cosmic web as seen in the Millenium Simulation ([Springel et al., 2005](#)).

On sufficiently large scales, the Universe is both homogeneous (the same in all locations) and isotropic (the same in all directions). However, on smaller scales, we start to see perturbations and changes, and it becomes non-homogeneous and anisotropic. One way to think of this is through satellite imagery of Earth. From a distance, the Earth

¹<https://www.mpa-garching.mpg.de/>

²<https://wwwmpa.mpa-garching.mpg.de/galform/virgo/>

³<https://map.gsfc.nasa.gov/media/060915/index.html>

⁴<https://wwwmpa.mpa-garching.mpg.de/galform/virgo/millennium/>

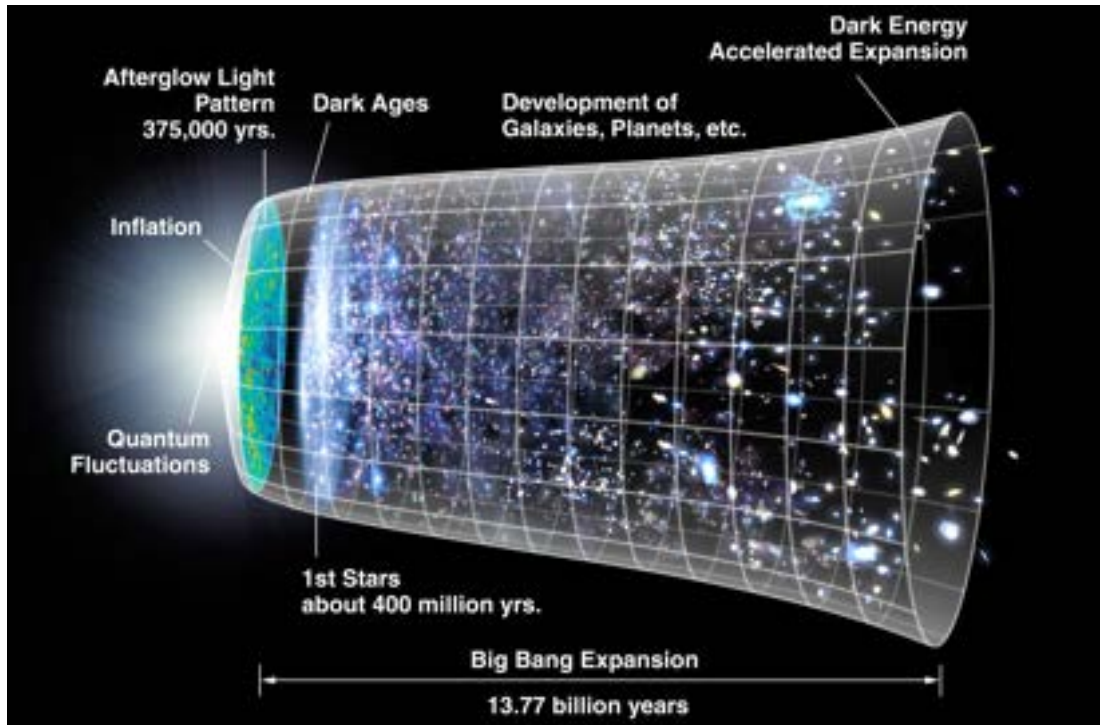


Figure 1.1: The image above is a pictorial representation of the Big Bang, showing from left to right the evolution of the Universe over 13.8 billion years. (Credit: NASA / WMAP Science Team.³)

looks perfectly smooth and spherical, “homogeneous and isotropic”. As we zoom in to a smaller and smaller area, features such as lakes, rivers, mountains become apparent, “non-homogeneous and anisotropic”.

In discussing the size of the Universe after the Big Bang, we are referring to the size of the observable Universe, not the Universe in its entirety (Davis and Lineweaver, 2004). The observable Universe is approximately 93 billion light-years across⁵ and is defined as the maximum distance that light could have travelled since the Big Bang. The remaining light emission is still on its way to our telescopes and detecting instruments; however, due to the rate of expansion of the Universe, this light may never reach us.

The idea that the Universe is expanding was a theoretical prediction by Alexander Friedmann in 1922, with his work on general relativity. From this work, Friedmann pioneered the theory that the Universe was expanding, governed by a set of equations now known as the Friedmann equations (Friedmann, 1922; Friedman, 1999).

Five years later, in 1927, Georges Lemaître derived independently from Friedmann that the Universe might be expanding (Lemaître, 1927), suggesting the existence of a constant, and estimating a value, explaining the linear relationship between the distance to a stellar object and its recessional velocity; the redshift to distance relationship.

⁵<http://www.astro.ucla.edu/~wright/cosmoall.htm>

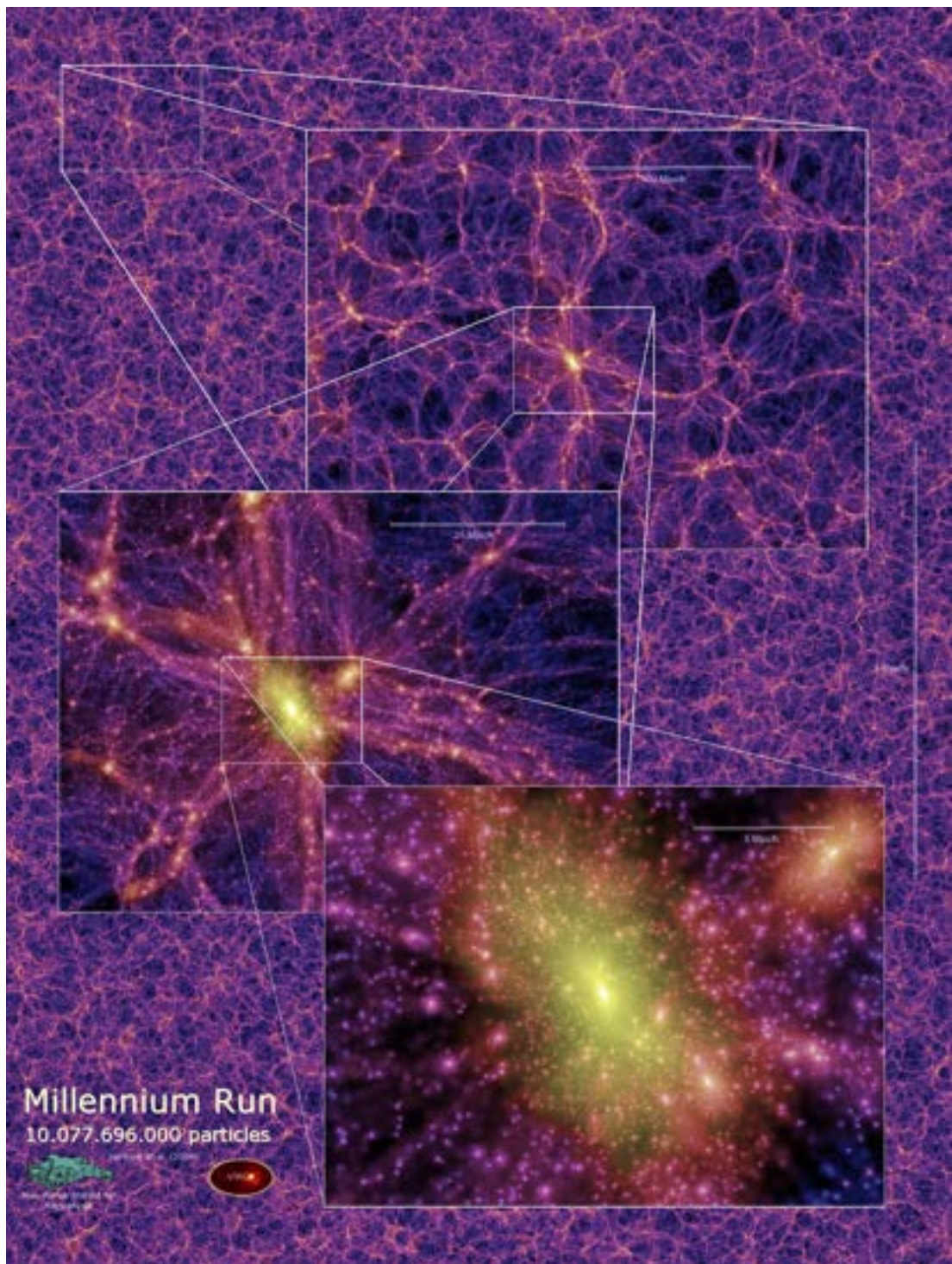


Figure 1.2: A poster from the Millenium Simulation Project, showing the simulation of galaxy clustering in the cosmic web, via the “evolution of the matter distribution” in the Universe. The poster shown here is the projected density field for a 15 megaparsec (Mpc)/h thick slice of the Universe at redshift $z = 0$. (Credit: Millennium Simulation Project.⁴)

In 1919, Edwin Hubble, helped by Milton Humason, began work at the Mount Wilson Observatory in California⁶. Over the next nearly five years, Hubble used the 100-inch (2.5 m) Hooker Telescope⁷ to make observations of Cepheid variables, a class of object in the category known as a “standard candle” (Fernie, 1969); discovered in 1908 by Henrietta Swan Leavitt (Leavitt, 1908). A standard candle is an astrophysical object which has a known luminosity, due to a characteristic of the entire class of object. Standard candles are one way to measure distance; the further away an object is, the more spread out the light of that source will be. Because of this quality, a Cepheid variable can be used to determine the distance to a star. By comparing its known luminosity to its observed brightness, the distance is computed using the inverse-square law:

$$F = \frac{L}{4\pi d^2} \quad (1.1)$$

where:

F = flux density in W/m^2

L = Luminosity in W

d = distance in meters

Hubble applied this theory of faint objects being further away, to his observations of faint galaxies. By observing the galaxy spectra and measuring the shift in the spectral lines, Hubble found that in general, their spectral lines were “redshifted” - meaning the galaxies were moving away from the Milky Way galaxy (redshift is explained further on page 6). By using distances based on cepheid variable standard candles, and using the property mentioned above that a less luminous object is further away, Hubble determined the galaxies that appeared smaller in size were, therefore, further away.

It was through these observations that Hubble determined the “velocity to distance” relationship $v \propto d$, shown in Figure 1.3, and discovered the Universe was expanding.

We know from laboratory experiments that all elements in the periodic table emit photons, and they are emitted at specific wavelengths. Caused entirely by an expanding Universe, redshift is observed when the photons emitted from an element experience an increase in wavelength. This increase in wavelength occurs because, as the Universe is moving away from us, the light from an observed galaxy is still moving towards us. As a result, the space between cosmological bodies in the Universe is expanding, and so the length of the wave, which is embedded in space, also expands.

⁶<https://www.mtwilson.edu/>

⁷<https://www.mtwilson.edu/building-the-100-inch-telescope/>

Velocity-Distance Relation among Extra-Galactic Nebulae.

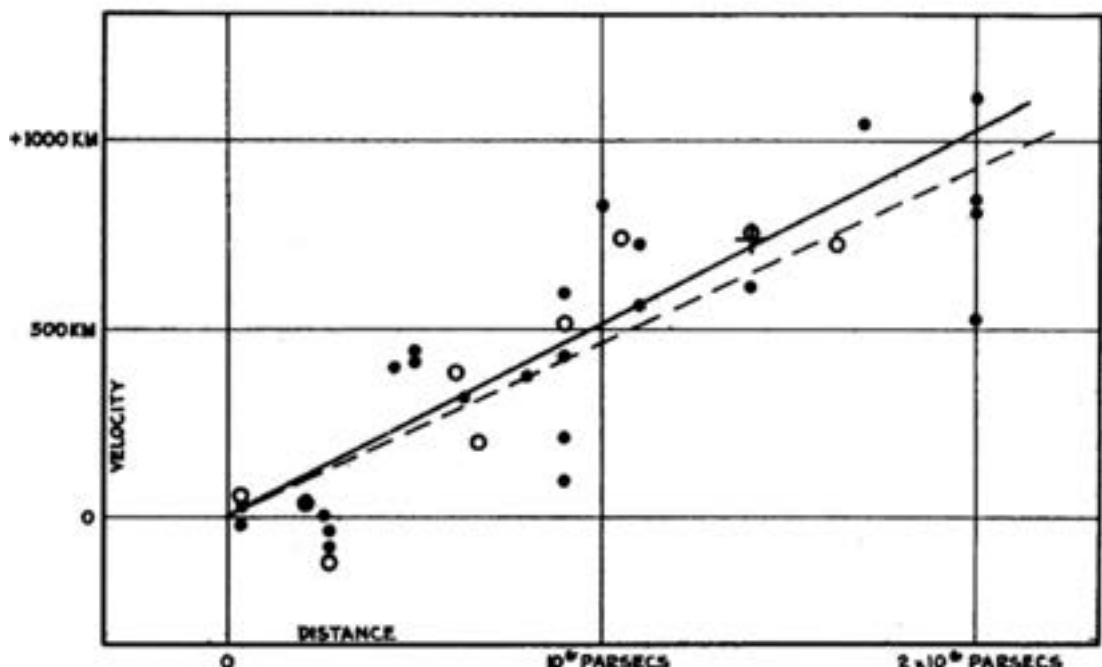


Figure 1.3: From the [Hubble \(1929\)](#) paper: “A Relation Between Distance and Radial Velocity Among Extra-Galactic Nebulae,” this image shows the velocity to distance relation among extra-galactic nebulae. “Radial velocities, corrected for solar motion, are plotted against distances estimated from involved stars and mean luminosities of nebulae in a cluster. The black discs and full line represent the solution for solar motion using the nebulae individually; the circles and broken line represent the solution combining the nebulae into groups; the cross represents the mean velocity corresponding to the mean distance of 22 nebulae whose distances could not be estimated individually”. Velocity units are in kilometres per second.

There are two types of redshift I will discuss here, as they have an important distinction in the cause of the spectral shift of the light which is emitted from the host galaxy ([Bedran, 2002](#)): (1) Doppler redshift, based on the Doppler effect, ([Doppler and Studnica, 1903](#)) and (2) cosmological redshift. Redshift is generally assumed to be cosmological redshift and is distinct from the Doppler effect. Doppler effect is a potential cause of redshift; however, throughout this thesis, “redshift” refers to cosmological redshift. Figure 1.4 shows how light is “redshifted” and stretched as a result of cosmological redshift.

Doppler redshift and cosmological redshift both measure the change in frequency of a sound wave relative to the observer; however, with Doppler redshift, the motion of the object emitting the radiation is taken into account. For objects moving away from us, the light will be redshifted, and for objects moving towards us, the light will be blueshifted. In cosmological redshift, we measure the distance to the object and observe the radiation of the object at that point in time. From then on, unless our Universe stops expanding ([Wang et al., 2004](#)), the object is *always* moving away from us.

The formula for redshift is given by:

$$z = \frac{\lambda_{obs} - \lambda_{rest}}{\lambda_{rest}} \quad (1.2)$$

where:

z = redshift

λ_{obs} = the wavelength observed

λ_{rest} = the wavelength at rest

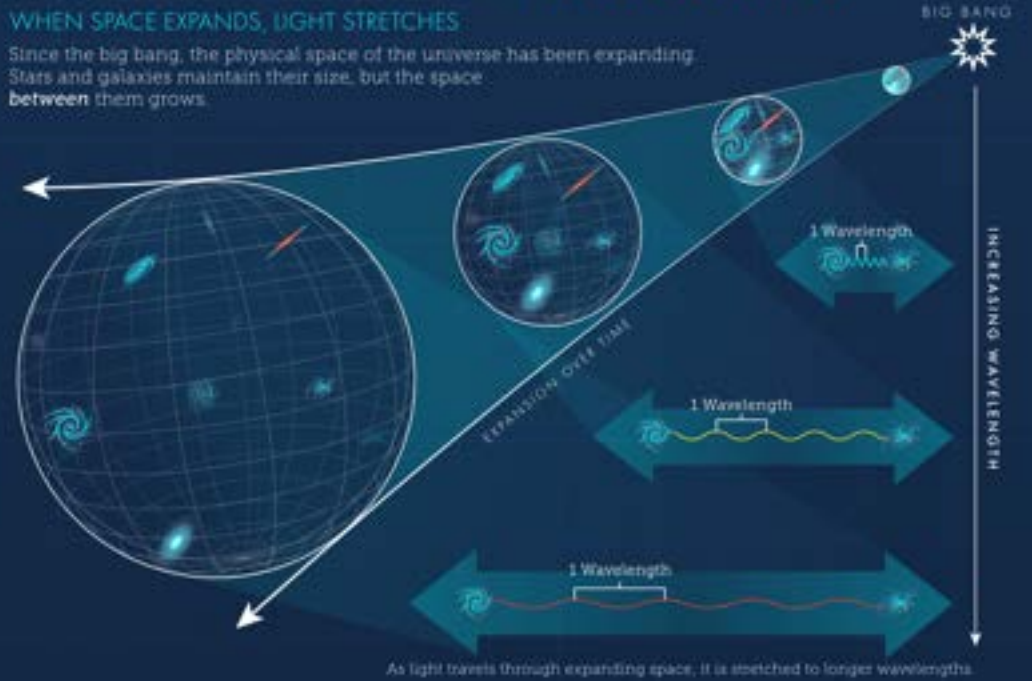
The observable Universe has at least 2 trillion galaxies ([Conselice et al., 2016](#)). It is through homogeneity, isotropy, cosmological redshift, and the expansion of the Universe that we can investigate the distribution and number density of galaxies, which makes them an excellent indicator of the underlying distribution of matter in the Universe. Further, by analysing the clustering of galaxies, it is possible to measure the underlying cosmological properties of our Universe. Also, if we know the rate of expansion of the Universe, we can better understand the movements of galaxies over time, which helps determine the physics of galaxy mergers into clusters.

⁸<https://hubblesite.org/image/4509>

WHAT IS COSMOLOGICAL REDSHIFT?

WHEN SPACE EXPANDS, LIGHT STRETCHES

Since the big bang, the physical space of the universe has been expanding. Stars and galaxies maintain their size, but the space between them grows.



REDDER THAN RED

The longest visible wavelength is red. Beyond red are longer wavelengths that we can't see, starting with infrared. When light is stretched by the expansion of space, we say that it is **redshifted**—from its original wavelength to a longer, redder one.



Figure 1.4: As the Universe expands, light travelling through space is “stretched”. This stretching is known as cosmological redshift. A higher redshift means the light has travelled further. Adapted from images on the Hubble Space Telescope website. (Credit: NASA HUBBLE SITE.⁸)

1.2 Galaxy Grouping and Clustering

Galaxy groups are some of the most massive structures in the Universe. Bound by gravity, galaxy groups contain an average of fifty member galaxies, with member galaxies having a luminosity at least as bright as the Milky Way galaxy. The group is typically 1 to 2 Mpc in diameter, with a mass of approximately $10^{13} M_{\odot}$. One example is the Local Group, as seen in Figure 1.5, the galaxy group which contains the Milky Way. The local group is roughly 10 million light-years (~ 3 Mpc) in diameter, with a total mass in the order of $2 \times 10^{12} M_{\odot}$.

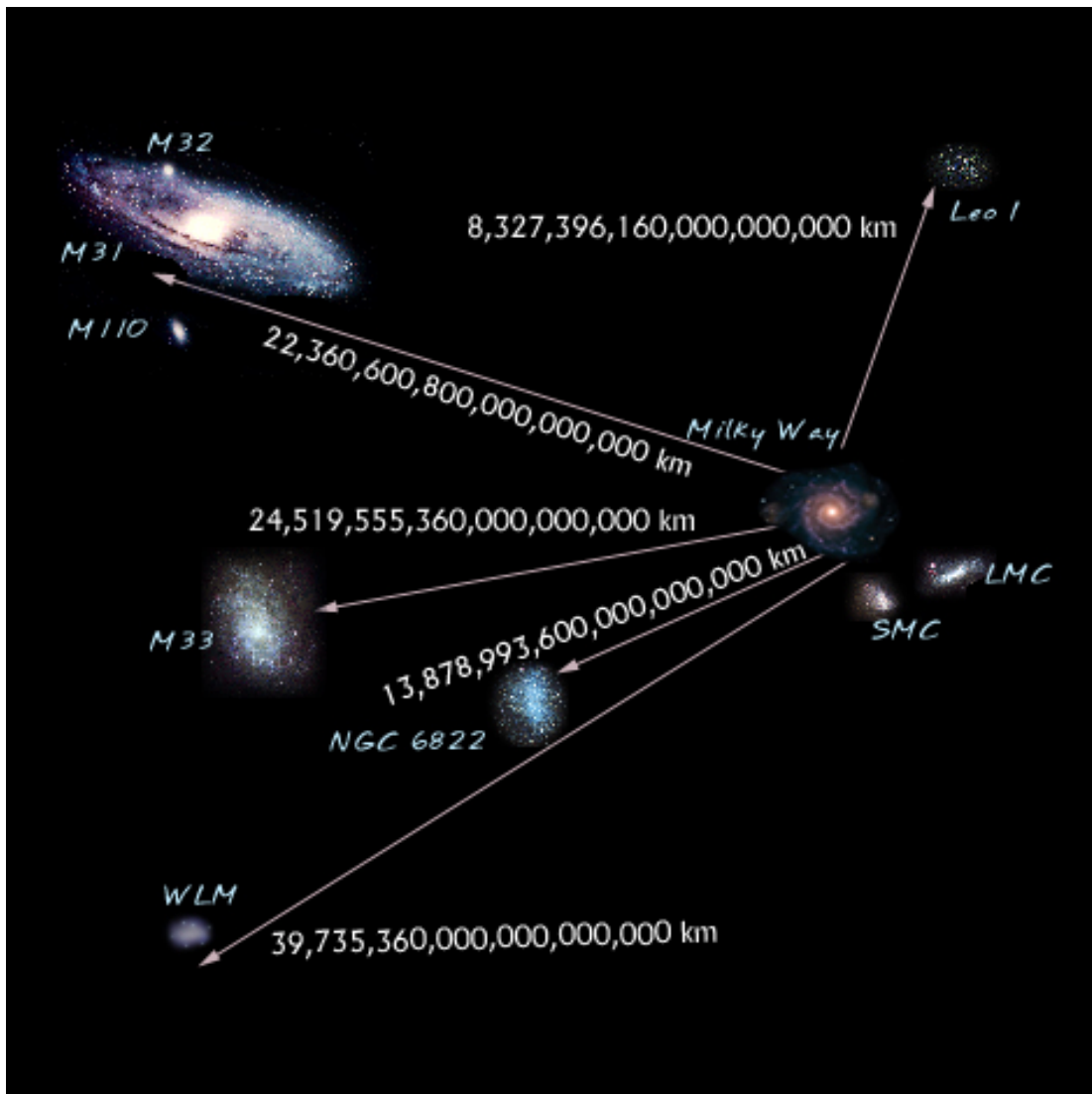


Figure 1.5: A term introduced by Edwin Hubble, “The Local Group” is a group of galaxies “local” to the Milky Way. Member galaxies include Messier 31 (the Andromeda Galaxy), the Milky Way, and the Large and Small Magellanic Clouds. (Credit: NASA.⁹)

Galaxy clusters are larger structures, also gravitationally-bound, containing hun-

⁹https://imagine.gsfc.nasa.gov/features/cosmic/local_group.html

dreds to thousands of galaxies, and typical masses of 10^{14} to $10^{15} M_{\odot}$. 90% of this mass is Dark Matter, 9% is the **ICM**, and only 1% is the galaxies that make up the cluster. Galaxy clusters were first classified by George Abell in 1958 ([Abell, 1958a](#)) as having a shape of *regular* or *irregular*, and a “richness class” of *rich* or *poor*, as defined in Section [1.3.2](#).

The **ICM** consists of heated gas between the galaxies, typically hot X-ray gas, with the mass of the X-ray gas being potentially greater than the mass of the stars in the component cluster galaxies. It has also been observed that galaxy clusters can have magnetic fields in the order of 0.1 to 1 μG ([Johnston-Hollitt, 2003](#); [Clarke et al., 2001](#); [Bonafede et al., 2010](#)). Although they are bound by gravity, they may not yet be fully stabilised, and may still be in the process of reaching a state of dynamic equilibrium ([Collins, 1978](#)).

1.2.1 The Virial Theorem

Galaxy clusters in equilibrium are described by the virial theorem ([Clausius, 1870](#), [2003](#)). The virial theorem relates the total kinetic energy of a self-gravitating body due to the motions of its constituent parts, T , to the gravitational potential energy, U , of the body. Further, virial equilibrium exists when “the total kinetic energy of the objects in a stable, self-gravitating body with a spherical distribution, T , is equal to minus half the total gravitational potential energy, U ”¹⁰:

$$T = -\frac{1}{2}U \quad (1.3)$$

To apply this to galaxy clusters, we consider the case of N objects each of mass m and moving at velocity v :

1. the kinetic energy of each object is equal to $\frac{1}{2}mv^2$
2. the kinetic energy of the total system T is equal to $\frac{1}{2}mNv^2 = \frac{1}{2}M_{\text{tot}}v^2$

The gravitational potential energy of the system, is calculated as:

$$P.E.(\text{system}) \simeq -\frac{1}{2}G\frac{N^2m^2}{R_{\text{tot}}} = -\frac{1}{2}G\frac{M_{\text{tot}}^2}{R_{\text{tot}}} \quad (1.4)$$

Assuming that $T = -\frac{1}{2}U$, we get:

$$\frac{1}{2}M_{\text{tot}}v^2 = +\frac{1}{4}G\frac{M_{\text{tot}}^2}{R_{\text{tot}}} \quad (1.5)$$

¹⁰<http://hosting.astro.cornell.edu/academics/courses/astro201/vt.htm>

which results in:

$$M_{tot} \simeq 2 \frac{R_{tot} v^2}{G} \quad (1.6)$$

Swiss astronomer Fritz Zwicky was the first person to apply the virial theorem in observational and theoretical astronomy, with observations in 1933 of the Coma galaxy cluster. Zwicky observed a gravitational anomaly in the Coma cluster; he calculated the mass that would be expected based on the luminosity of the member galaxies (I will call this the cluster mass) and compared that with the gravitational mass calculated from the rotational velocity of luminous matter. Zwicky discovered that the cluster mass was approximately 400 times less than the gravitational mass. He used this to infer the existence of a mass we cannot see - which, when added to the cluster mass, would make it equal to the gravitational mass. Zwicky named this “Dunkle Materie”, or “dark matter” (Zwicky, 1937; de Swart et al., 2017).

1.2.2 Critical Density

An important aspect of the viral theorem is the “critical density” of a system. The term “critical density” refers to “the average density of matter required for the system to *just* halt its expansion, and “close” the system, but only after an infinite time.¹¹”. Critical density refers to the geometric shape of the Universe and is discussed in Section 1.2.3.

One way in which critical density is used, is in calculating the R_{200} virial radius of a galaxy cluster. This is the radius within which the mean interior density of the cluster is 200 times the critical density. The equation for calculating the R_{200} virial radius is provided by Carlberg et al. (1997):

$$R_{200} = \frac{\sqrt{3}\sigma_r}{10H(z)} \quad (1.7)$$

where $H(z)$ is the Hubble constant at redshift z .

1.2.3 The Geometrical Models for Universe Expansion

In terms of the expansion of the Universe, there are three geometrical models: open, closed, and flat. It is noted, the cosmological constant¹², denoted as Λ , changes the relationship between critical density and when a universe will eventually recollapse; however, that discussion is not part of this thesis. Shown in Figure 1.6, the three geometric models are detailed as follows:

1. “open”: in an open Universe, the density of matter is low, and self-gravity is too

¹¹<https://ned.ipac.caltech.edu/level5/Glossary/frames.html>

¹²<https://web.archive.org/web/20011201205845/http://pancake.uchicago.edu/~carroll/encyc/>

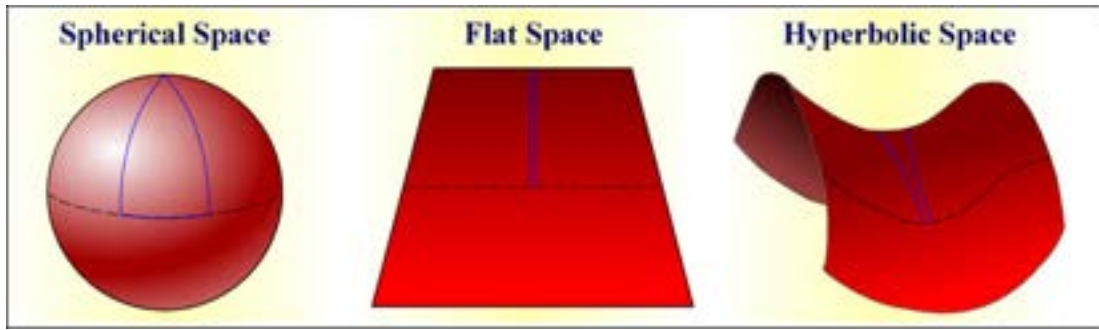


Figure 1.6: The critical density of the Universe depicted by the three possible geometries. In a closed or “spherical space” Universe, where the matter density is high, locally parallel beams of light (blue lines) will eventually converge. In an open or “hyperbolic space” Universe, where the matter density is low, locally parallel beams of light will eventually diverge. In a flat Universe or “flat space”, where the density of matter is the ‘critical density’, locally parallel lines remain parallel. (Credit: Swinburne Astronomy Online.¹³)

low to stop expansion. The Universe will expand forever; however, the rate of expansion will gradually slow over time. Parallel beams of light will *diverge* at some extremely distant point. An open Universe has a hyperbolic geometry.

2. “closed”: in a closed Universe, the density of matter is high, and self-gravity will slow the expansion of the Universe to such an extent that expansion stops, and ultimately falls back in on itself. Parallel beams of light will *converge* at some extremely distant point.
3. “flat”: Balanced between the models of open and closed, is the flat Universe. The density of a flat Universe is called the “critical density” - in this system, expansion is halted only after an *infinite* time. Parallel beams of light will remain parallel and do not diverge or converge as in the open and closed geometric models.

¹³<http://astronomy.swin.edu.au/cosmos/C/Critical+Density>

1.3 The Morphology and Classification of Galaxies and Galaxy Clusters

1.3.1 Galaxies

The earliest and most common system used for classifying galaxy morphology is the “Hubble Sequence”, shown in Figure 1.7. More commonly known as the “tuning fork diagram”, the Hubble Sequence was invented in 1926 by American astronomer Edwin Hubble (Hubble, 1926a; J., 1936) as a way to group galaxies based on their visual appearance. This has been expanded in later years by the de Vaucouleurs system (de Vaucouleurs, 1959) and the Yerkes (or Morgan) scheme (Morgan, 1958a, 1959a).

1.3.1.1 The Hubble Tuning Fork

The classification divides the galaxies into three main visual classes, and a fourth class (irregulars) for galaxies that do not fit the visual methodology:

1. Elliptical Galaxies: Denoted by the letter “E”, elliptical galaxies are generally found near the centre of galaxy clusters (Dressler, 1980). Elliptical galaxies range in size from tens of millions to over one hundred trillion stars. Their shape is approximately ellipsoidal, with a smooth, nearly featureless image.
2. Spiral Galaxies: Denoted by the letter “S”, spiral galaxies usually have two arms formed by stars spreading out in a spiral structure from the central bulge (a concentration of stars), with a flattened disk. Another type of spiral galaxy is the “barred spiral”, which has a bar-like structure in the central bulge. Barred spirals are designated with the letters “SB”.
3. Lenticular Galaxies: denoted by “S0”, lenticular galaxies are similar in structure to a spiral galaxy however they do not have the visible spiral structure; instead they have an extended disk-like structure with no active star formation.
4. Irregulars: Irregular galaxies are galaxies that do not have a regular structure, and have two classes:
 - Irregular “class I” galaxies are asymmetric and have no central bulge or obvious spiral structure; instead, the structure is comprised of individual clusters of young stars.
 - Irregular “class II” galaxies are also asymmetric; however, they have not yet formed into individual stars or stellar clusters

¹⁴<https://www.spacetelescope.org/images/heic9902o/>

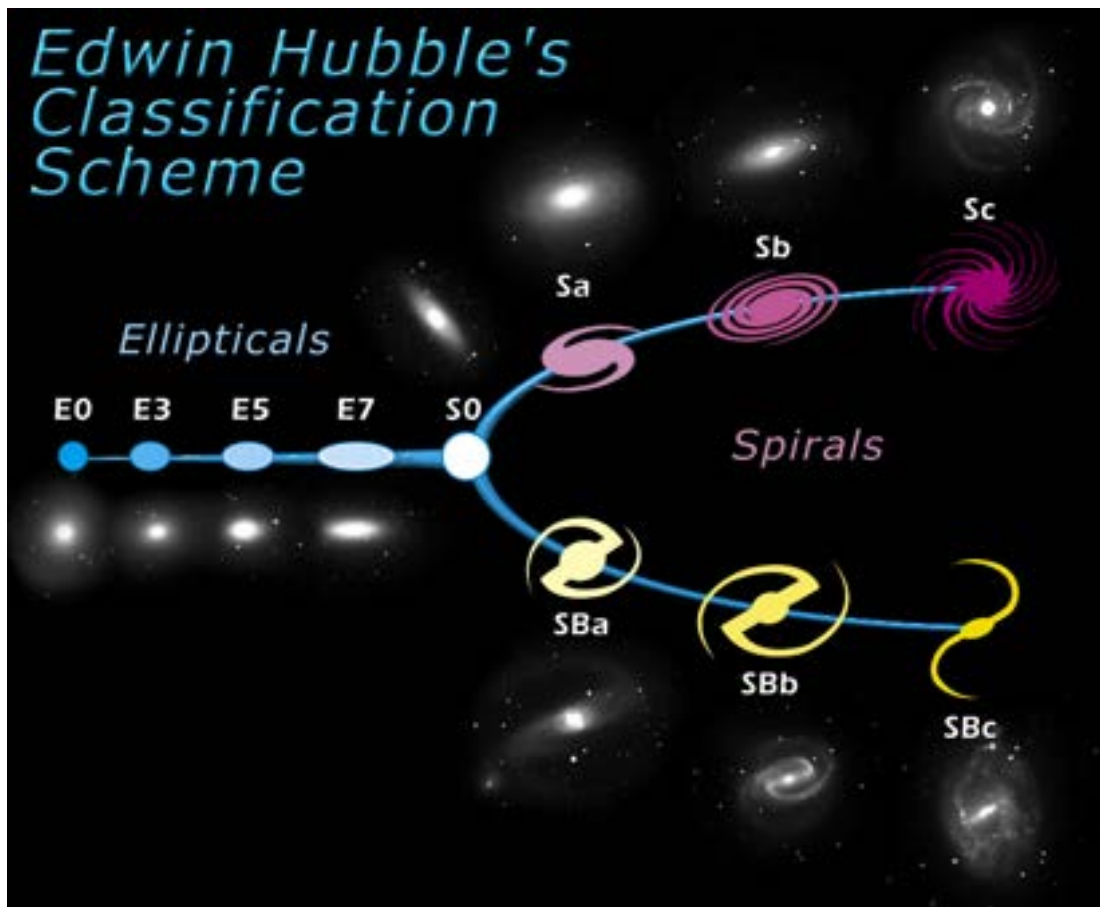


Figure 1.7: A reproduction of Edwin Hubble’s tuning fork galaxy classification scheme. Hubble classified all galaxies into 4 distinct groups ([Hubble, 1926a,b, 1927](#)). The first, along the main branch, is the Elliptical galaxies, with the E number relating to how elliptical it was as a ratio between its semi-major and semi-minor axis, omitting the decimal places. Along the top branch are the standard spiral galaxies, with the lower case character denoting how tightly wound the spiral is. The bottom branch is similar to the top; however, they have a bar in the centre of the spiral. Irregular galaxies do not fit on this ‘tuning fork’. Credit: NASA and ESA¹⁴

1.3.1.2 The De Vaucouleurs System

The Hubble sequence was extended by Gerard de Vaucouleurs (De Vaucouleurs, 1959), and this extended version is now widely used. De Vaucouleurs believed the two-dimensional classification used by Hubble did not adequately describe galaxy morphology and was limited in its classification of spiral galaxies by only observing the presence of a bar or the tightness of the spiral arms.

Adding to the Hubble sequence, de Vaucouleurs introduced a further classification for spiral galaxies, subsequently re-classifying 1500 bright galaxies (de Vaucouleurs, 1963). The modifications de Vaucouleurs applied to the Hubble sequence included changes to bars, arms, and rings:

1. Bars: de Vaucouleurs added two notations, the first notation “SA” to include spiral galaxies without bars, to complement the original classification SB for spiral galaxies with bars, and the second notation “SAB” to denote an intermediate class - or a “weakly barred spiral”. Further classification included lenticular galaxies, and included unbarred lenticular “SA0” and barred lenticular “SB0”.
2. Spiral arms: The most extensive changes de Vaucouleurs made were to galaxies with spiral arms. He added the following additional classes, extending the definitions from observations based only on the tightness of the spiral arms:
 - (a) Sd (SBd): Denotes spiral galaxies with diffuse arms spreading from a very faint central bulge, composed of individual nebulae and stellar clusters.
 - (b) Sm (SBm): Denotes a Spiral Barred Magellanic galaxy, they have no discernable bulge and an irregular appearance. The Large Magellanic Cloud is an example of this¹⁵
 - (c) Im: Denotes an Irregular Magellanic galaxy, they are extremely irregular galaxies. The Small Magellanic Cloud is an example of this¹⁶
3. Rings: For galaxies that have a ring-like structure, de Vaucouleurs added the notations “r” for a galaxy with a ring-like structure, “s” for a ring-less galaxy, and “rs” for a galaxy in a transition state.

Another system for classifying galaxies is the “Yerkes” scheme. This system, as shown in Table 1.1 (Morgan, 1958b, 1959b, 1971; Morgan and Mayall, 1957), uses the galaxies light concentration and morphology to assign a population group. The groups are determined by the spectra of stars, the shape, and the central concentration.

¹⁵<http://ned.ipac.caltech.edu/byname?objname=LMC>

¹⁶<http://ned.ipac.caltech.edu/byname?objname=SMC>

¹⁷https://commons.wikimedia.org/wiki/File:Hubble_-_de_Vaucouleurs_Galaxy_Morphology_Diagram.png

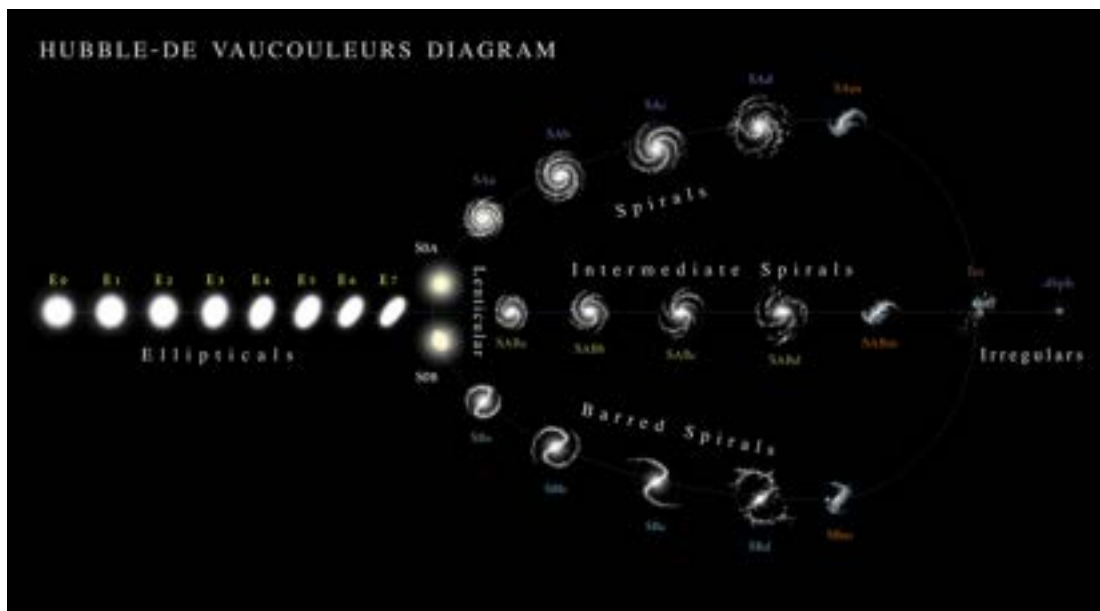


Figure 1.8: The Hubble - de Vaucouleurs Galaxy Morphology Diagram, reproduced here under the Creative Commons license CC BY 3.0 (Credit: Antonio Ciccolella / M. De Leo¹⁷)

Table 1.1: The Yerkes System for galaxy classification, reproduced from <https://ned.ipac.caltech.edu/level5/CLASSIFICATION/yc.html>

Form family	Description
B	Barred spirals
D	Galaxies with rotational symmetry but showing neither spiral structure nor ellipticity
cD	Supergiant D galaxies, predominantly found in clusters [120] and embedded in an extensive halo
db	Dumb-bell systems
E	Ellipticals
Ep	Peculiar ellipticals containing conspicuous absorption patches
I	Irregulars
L	Low-surface-brightness systems
N	High-luminosity nucleus superimposed on a considerably fainter outer envelope, see also [129]
Q	Quasi-stellar objects
S	Ordinary spirals

1.3.2 Galaxy Clusters

In addition to the classifications for single galaxies described above, galaxy clusters have similar systems, and there are a few methods by which we can classify them. The morphology and classification of single galaxies and galaxy clusters have various systems that have developed over the years, including those from Abell, Zwicky Bautz-Morgan, Rood-Sastry, López-Cruz, and Panko. As this thesis is dealing with the Abell S1136 galaxy cluster, for brevity, I will only outline here the Abell Classification Scheme and the Bautz–Morgan Classification Scheme. For information on the other systems the reader is invited to read [Panko \(2015\)](#).

1.3.2.1 The Abell Classification Scheme

The first system for classifying galaxy clusters was developed by [Abell \(1958a\)](#), who provided a catalogue of clusters that was sufficiently large enough to enable comparison between their characteristics and observe the distribution of clusters. The criteria used by Abell are historical, we now have more precise methods for detecting distance (redshift measurements), and more accurate constraints on the Hubble constant. Abell used the following four “criteria” to identify the clusters for inclusion in the survey:

1. The “Richness criterion”: A cluster must have at a minimum $N = 50$ members, whose brightness is no more than two magnitudes fainter than the third brightest cluster member; m_3 to $m_3 + 2$. Abell then divided the richness class into six richness groups, based on the number of member galaxies in the cluster:
 - (a) Group 0: $N = 30 - 49$ member galaxies
 - (b) Group 1: $N = 50 - 79$ member galaxies
 - (c) Group 2: $N = 80 - 129$ member galaxies
 - (d) Group 3: $N = 130 - 199$ member galaxies
 - (e) Group 4: $N = 200 - 299$ member galaxies
 - (f) Group 5: $N = \text{greater than } 299$ member galaxies

It is worth noting that although Abell specified a cluster should have a minimum 50 members, this was not a strict cutoff and the final catalogue *does* include clusters with fewer than 50 members, designated Group 0.

2. The “Compactness criterion”: A galaxy must be “sufficiently compact” so that the $N \geq 50$ cluster members are within an “Abell radius” r defined as $\frac{1.72}{z}$ arcminutes, assuming a Hubble constant of $H_0 = 180\text{km/sec} \times 10^6 \text{ pc}$ ([Humason et al., 1956](#)), equal to a space distance of $8.3 \times 10^5 \text{ pc}$. [Abell \(1958a\)](#) noted that the (galaxy member) counts “are not particularly sensitive to the estimate

of the red shift or to the linearity of the red-shift law”, and in practice the main concentration of member galaxies was always within the radius.

3. The “Distance criterion”: The distance of the galaxy cluster from Earth must be such that the counts of the cluster members fit onto one photographic plate; primarily because cataloguing a galaxy cluster over multiple plates would make it difficult to compare with other clusters.
4. The “Galactic-latitude criterion”: In order to completely identify galaxy clusters, photographic plates at extremely low galactic latitude were carefully examined, and plates in the Milky Way were generally excluded; in these regions, the density of the star fields may have precluded complete identification of a galaxy cluster.

1.3.2.2 The Bautz–Morgan Classification Scheme

In 1970 Laura P. Bautz and William Wilson Morgan developed the “Bautz–Morgan classification” ([Bautz and Morgan, 1970a,b](#)), which defined galaxy clusters based on their morphology (similar to Hubble) into three main types and uses the family classifications from the Yerkes (Morgan) system described in Section [1.3.1](#).

1. Type I: Dominated by a very bright, super-massive cD type galaxy (see Table [1.1](#)). Examples include Abell 2029 and Abell 2199.
2. Type II: Relative to types I and III, the brightness of galaxies in type II is intermediate. An example of a type II galaxy cluster is the Coma Cluster.
3. Type III: The galaxy members are not remarkable in any way, with low brightness. It also has two sub-types:
 - (a) Type IIIE: Type IIIE contains a majority of elliptical galaxies and very few giant spirals.
 - (b) Type IIIS: Type IIIS contains a majority of giant spirals and very few elliptical galaxies.

1.4 Galaxy Clusters at Different Wavelengths

The goal of any astronomical survey of galaxy clusters is to obtain data on a group of objects, analyse the data, and further our current knowledge of the type of objects being observed. When studying galaxy clusters, this increase in knowledge helps us to define more precisely our understanding of the physics of galaxy clusters, and subsequently, our understanding of the origin and development of the Universe.

Galaxy clusters can be observed across multiple wavelengths. Figure 1.9 shows the ranges through which astronomers observe the sky, and only some of this can be performed from the Earth's surface - those observations where the Earth's atmosphere is not blocking the ingress of the electromagnetic waves - in this case, radio and optical. The remaining observations are best achieved from space, where the telescope will receive an adequate noise signal from which to re-create an image.

Moving from left to right on the picture, we can see the low energy radio wavelengths, through infra-red, optical, ultra-violet, and x-ray, up to the very high energy gamma-ray wavelengths. When viewed from left to right, the different ranges are characterised by increasing energy, increasing frequency, and decreasing wavelength.

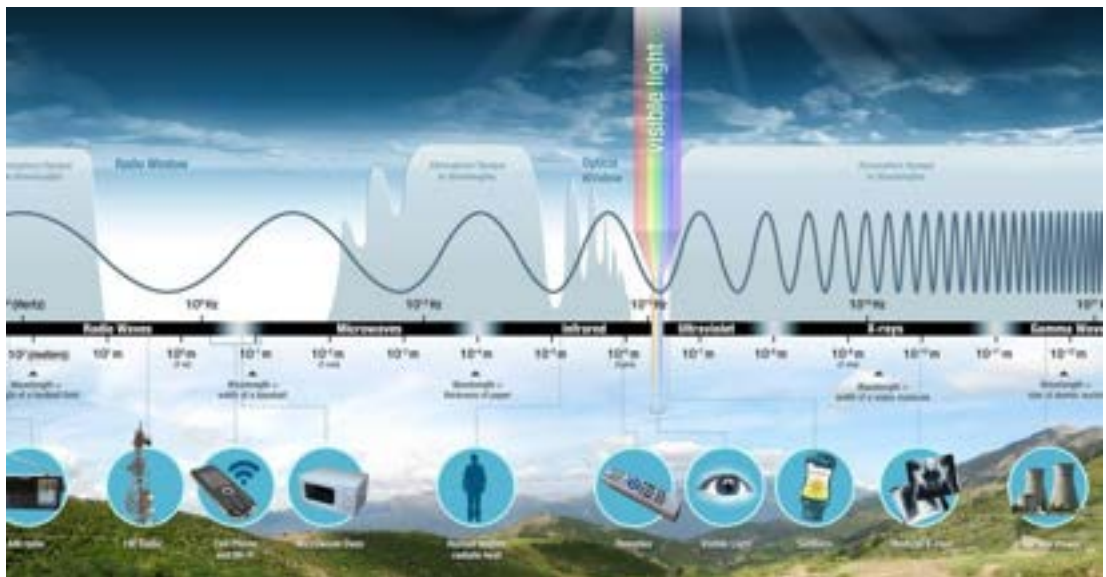


Figure 1.9: A visualisation of the wavelength of different astronomical regimes. (NASA, 2019)

Historically, an astronomer would specialise in a particular wavelength, and build knowledge of an object that way. This would be a limiting factor in the expansion of our knowledge because the separate communities only had data on their particular slice of the frequency range. Modern astronomy allows us to expand radically on this, with state of the art ground and space-based telescopes, computational access to super-computer networks, and global network access that allows for the sharing of vast amounts of data relatively quickly. With this ability to better collaborate nationally and

internationally, observing at multiple frequencies across the electromagnetic spectrum allows us to build more coherent pictures of the processes involved in galaxy formation and clustering. For example, an ordinary-looking optical galaxy might look very different under an infrared telescope like Spitzer, with high energy X-rays informing us that there might be a black hole feeding at the core of the galaxy.

By observing at different wavelengths, astronomers get different information about celestial objects. Table 1.2 shows information about each wavelength, including the type of objects that can be viewed in a particular band, examples of sources, and some of the telescopes used at a particular wavelength.

The critical point is that different physical processes produce emissions at different wavelengths. By observing at those wavelengths, we can gain an understanding of the physical conditions that exist on or near that object. Ideally, information obtained from each wavelength is combined to give a fuller understanding of an object. One of the most studied objects at multiple wavelengths is the Milky Way. Listed in order from low energy at the top to high energy at the bottom, Figure 1.10 shows maps of the Milky Way at ten different wavelengths, with each image extending up and down to 5° either side of the galactic plane.

1.4.1 Radio

Telescopes that operate in the radio frequency spectrum can detect galaxies billions of light-years away, so observing the radio emission from galaxies helps us understand galaxy formation and evolution, which will lead to a better understanding of the Universe. Radio surveys are an important astrophysical tool to measure the clustering of galaxies, as they provide large samples of galaxies for studying cosmology or galaxy evolution (Norris, 2017). Unfortunately, before the construction of the latest generation radio survey telescopes, the study of galaxy clustering has been hampered by the low number density of galaxies visible in the radio frequency regime (Rees, 2017).

One of these radio survey telescopes is the one seen in Figure 1.11, the ASKAP (Johnston et al., 2007, 2008; McConnell et al., 2016), a precursor to the Square Kilometre Array (SKA) project (Dewdney et al., 2009; Schilizzi et al., 2010). With the latest generation radio telescopes estimated to detect tens of millions of new sources (Norris, 2017), we can now observe the clustering of galaxies in the radio regime - an important tool for measuring the cosmological properties of the Universe.

The radio emission from clusters consists of three components: (a) the radio emission from the constituent galaxies, including bent-tail galaxies, (b) a diffuse halo of emission broadly centred on the centre of the cluster, and (c) diffuse elongated radio

¹⁷<http://www.spitzer.caltech.edu/>

¹⁸https://asd.gsfc.nasa.gov/archive/mwmw/mmw_images.html

¹⁹<https://www.csiro.au/en/Research/Facilities/ATNF/ASKAP>

Table 1.2: This table shows the wavelength (Type of Radiation), the frequency in Hertz, and the wavelength range in nanometers, with example sources typical of that part of the spectrum, as well as temperature and example telescopes.

Radiation Type	Wavelength range (nm)	Frequency range (Hz)	Typical Sources	Temperature of radiating object	Examples of telescopes
Radio	$>1 \times 10^6$	$<3 \times 10^{11}$	Interstellar medium, cool gas, electrons	<10 K	ATCA ^a , Parkes ^b ,
Infrared	$10^3 - 10^6$	$3 \times 10^{11} - 4 \times 10^{14}$	cool clouds of dust and gas; planets, exterior of stars	$10 - 10^3$ K	Spitzer Space Telescope ^c
Visible	400 - 700	$4 \times 10^{14} - 7.5 \times 10^{14}$	supernova remnants, very hot stars	103 - 105 K	AAT ^d , Gemini ^e , HST ^f
Ultraviolet	20 - 400	$7.5 \times 10^{14} - 3 \times 10^{16}$	supernova remnants, gas in clusters of galaxies, stellar corona	105 - 106 K	FUSE ^g
X-ray	0.01 - 20	$3 \times 10^{16} - 3 \times 10^{19}$	hypernova, accretion disks around black holes	106 - 108 K	Chandra ^h , XMM-Newton ⁱ
Gamma-ray ^j	<0.01 nm	$>3 \times 10^{19}$		>108 K	INTEGRAL ^k , GLAST ^l

^a<http://www.narrabri.atnf.csiro.au/>

^b<https://www.parkes.atnf.csiro.au/>

^c<http://www.spitzer.caltech.edu/mission>

^d<http://www.ao.no.au/>

^e<https://www.gemini.edu/pio/>

^f<https://asd.gsfc.nasa.gov/archive/hubble/>

^g<http://fuse.pha.jhu.edu/>

^h<https://chandra.harvard.edu/>

ⁱ<https://sci.esa.int/web/xmm-newton>

^j<https://heasarc.gsfc.nasa.gov/docs/cgro/egret/>

^k<https://sci.esa.int/web/integral>

^l<https://glast.sites.stanford.edu/>

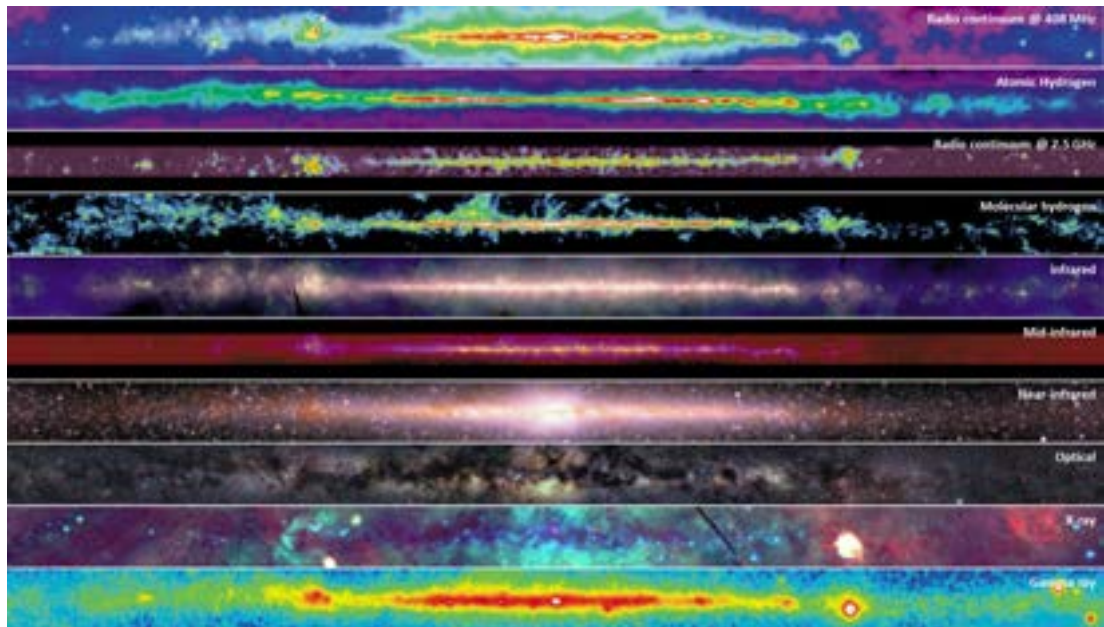


Figure 1.10: Observations of the Milky Way at different wavelengths - Radio Continuum @ 408 MHz: Jodrell Bank Mark I and Mark IA, Bonn 100-meter, and Parkes 64-meter; Atomic Hydrogen: Dwingeloo 25-m radio telescope; Radio Continuum @ 2.5 GHz: Bonn 100-meter, and Parkes 64-meter radio telescopes; Infrared: Infrared Astronomical Satellite (IRAS); Mid Infrared @ 6.8 to 10.8 microns: 2MASS; Optical @ 0.4 to 0.6 micron: assembled from sixteen wide-angle photographs taken by Dr. Axel Mellinger using a standard 35-mm camera and color negative film; X-ray: Röntgen Satellite (ROSAT); Gamma ray: Energetic Gamma-Ray Experiment Telescope (EGRET) instrument on the Compton Gamma-Ray Observatory (CGRO). (Credit: NASA Goddard Space Flight Centre.¹⁸)



Figure 1.11: Shown here are some of the 36 [ASKAP](#) radio antenna at the Murchison Radio-astronomy Observatory ([MRO](#)) in Western Australia. (Credit: CSIRO¹⁹.)

“relics” typically found on the periphery of the cluster.

Radio halos are sources of diffuse radio emission associated with the cluster centre. With a general size of ~ 1 [Mpc](#), they can be identified by the absence of an optical counterpart, low surface brightness, a steep radio spectrum. It is noted by [Giovannini et al. \(1999a\)](#) that “the occurrence of cluster halos and relics is higher in clusters with high X-ray luminosity and high temperature”.

Radio relics are similar to radio halos in that they are extended, diffuse sources that do not have an optical counterpart and their radio emission is steep spectrum. However, unlike radio halos, they are mostly located at the cluster periphery. Relics tend to appear as an elongated radio structure, with emission that is linearly polarised at ~ 10 to 30 percent ([Giovannini and Feretti, 2004a](#); [Feretti et al., 2012](#); [Govoni et al., 2001b](#)). However, relics in merging galaxy clusters have been reported to have polarisation at the 50 to 60% level ([van Weeren et al., 2010](#)).

All these classes of radio emission are assumed to be generated by synchrotron emission, caused by the interaction of electrons with magnetic fields. The spectral energy distribution (SED) of the emission is a function of the ages of electron populations and the possible shock-driven re-acceleration from merger events ([Feretti et al., 2012](#); [Bonafede et al., 2014](#)).

The main body of work in this thesis used data from the **ASKAP**. Further details are in section 2.

1.4.2 Infrared

Whereas radio astronomy detects radio wave emission, and X-ray and gamma-ray astronomy detect X-ray and gamma-ray emission, infrared astronomy detects heat energy. Infrared emission can be detected from any object that emits heat; therefore, every astronomical object emits infrared energy. As a result, what may generally be invisible in another part of the electromagnetic spectrum becomes visible in infrared. Infrared observations can probe through clouds of dust to see things not visible in optical.

The infrared part of the spectrum has three spectral regions: near-infrared, mid-infrared, and far-infrared. The deciding factor for whether an observation is near, mid, or far is based mainly on the type of detector in the instrument, and the wavelength/s included. The wavelength to temperature is an inverse relationship, described by Wien's displacement law²⁰:

$$\lambda_{\text{peak}} = \frac{b}{T} \quad (1.8)$$

²⁰https://ned.ipac.caltech.edu/level5/Glossary/Glossary_W.html

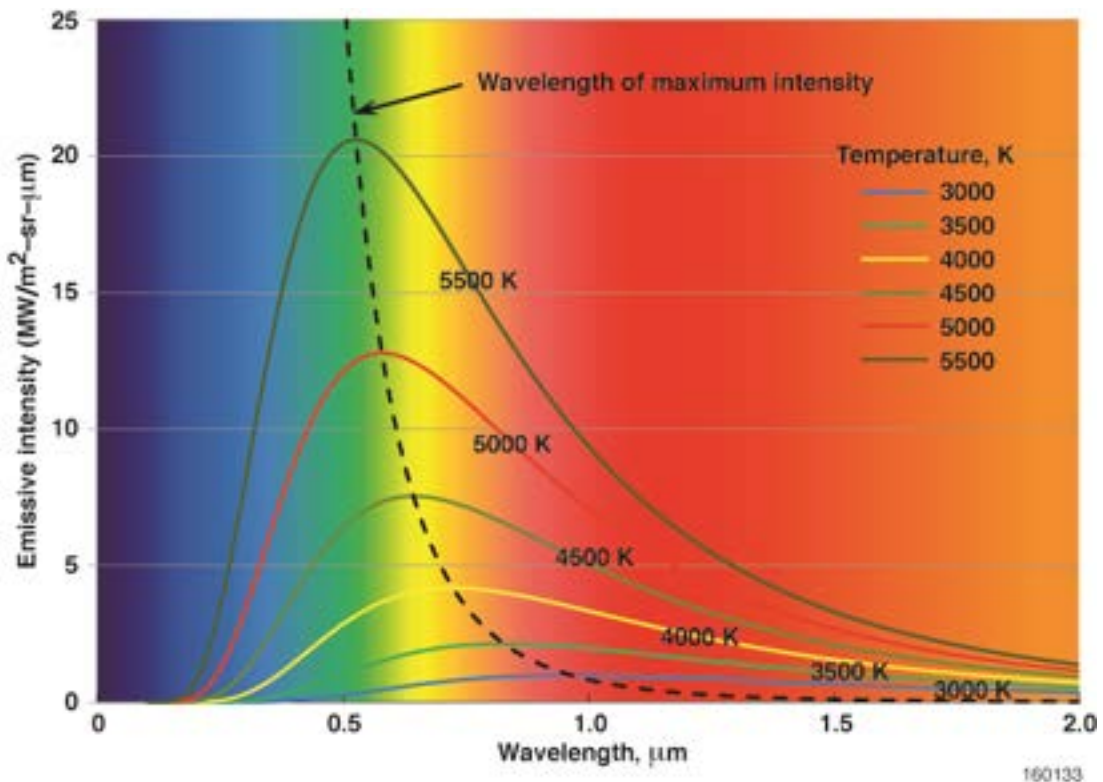


Figure 1.12: “Emissive intensity versus wavelength calculated from the Planck distribution equation. The wavelength at the maximum spectral intensity calculated from Wien’s displacement law is also shown.” (Credit: NASA Technical Reports Server²².)

where:

λ_{peak} = The wavelength where the maximum light is emitted

T = The absolute temperature in kelvins

b = Constant of Proportionality equal to $2.897771955\dots \times 10^{-3}$

Wien’s law states that the temperature of an object will peak at different wavelengths in an inverse relationship, which follows a black-body²¹ radiation curve; the higher the wavelength, the lower the infrared temperature.

Figure 1.12 shows the black-body radiation curves for flux density emission at different temperatures. Table 1.3 shows more defined properties for the infrared bands.

1.4.3 Optical

Because light can pass through the atmosphere, and is the primary mechanism through which humans view the world, optical astronomy is the oldest form of astronomy. From

²¹https://ned.ipac.caltech.edu/level5/Glossary/Glossary_B.html

²²<https://ntrs.nasa.gov/archive/nasa/casi.ntrs.nasa.gov/20160009112.pdf>

²³http://coolcosmos.ipac.caltech.edu/cosmic_classroom/ir Tutorial/irregions.html

Table 1.3: Infrared spectrum properties: spectral region, wavelength, temperature range, common astronomical object or occurrence²³.

SPECTRAL REGION	WAVELENGTH RANGE(microns)	TEMPERATURE RANGE(degrees Kelvin)	WHAT WE SEE
Near-Infrared	(0.7-1) to 5	740 to (3,000-5,200)	Cooler red stars Red giants Dust is transparent
Mid-Infrared	5 to (25-40)	(92.5-140) to 740	Planets, comets and asteroids Dust warmed by starlight Protoplanetary disks Emission from cold dust
Far-Infrared	(25-40) to (200-350)	(10.6-18.5) to (92.5-140)	Central regions of galaxies Very cold molecular clouds

its beginnings in ancient cultures, who used the stars for navigation and reference to season change, optical astronomy as we know it today was founded in the early 17th century by craftsmen who were developing lenses to refract and reflect light.

Galaxy observations at optical wavelengths allow us to scan for an over density of galaxies, indicating the existence of clustering. Because optical observations contain the colours of the visible light spectrum, we can use colour information to determine galaxy types, which again allows for identification of possible clustering activity as many clusters contain red elliptical galaxies.

An important aspect of galaxy observations at optical wavelengths is the ability to obtain the redshift, described in Section 1.1. The two main methods to determine the optical redshift of an astronomical body are 'spectroscopic redshift' and 'photometric redshift'. Spectroscopic redshift observations of astronomical objects were first conducted in 1868 by English astronomer Sir William Huggins ([Huggins, 1868](#)). Spectroscopic redshift is by direct measurement of the emission lines from an object. Photometric redshift measurements came much later. First developed in the 1960s, [Baum \(1966\)](#) described a method to determine redshift by observing differences in stellar populations across the arms of spiral galaxies.

The Abell catalogue was originally observed in optical and gave rise to the 'richness' classifications for galaxy clusters described in Section 1.3.2.

1.4.4 X-ray

Unlike radio and optical astronomy, X-ray astronomy is space-based as emission in that part of the spectrum does not penetrate the Earth's atmosphere. X-ray emission emanates from objects with a temperature of approximately 1 million kelvin (K) and higher([Bhardwaj et al., 2007](#)). However, the emission is not uniform, and we see areas of 'hot spots' in the photon counts, which are not associated with galaxies.

X-ray telescopes use a technique called "grazing incidence" ([Giacconi et al., 1969](#)) or "glancing angle reflection" to detect X-rays in the collector. This technique uses a smooth, high-density metal surface, positioned at an extremely shallow angle to reflect X-rays through to a collector. The detectors are designed for energy detection, as opposed to wavelength detection. This also requires long focal lengths, typically in the order of several metres. Because X-ray telescopes are all space-based, until recent years this has been an issue as the capability to launch heavy payloads requires large rockets.

This ability to detect regions of hot dense gas means X-ray observations are set to discover many new galaxy clusters. [Merloni et al. \(2012\)](#) predict that telescopes such as eRosita ²⁴ will detect many new galaxy clusters ($\sim 10^5$) out to redshifts $z > 1$.

²⁴<https://www.mpe.mpg.de/eROSITA>

Galaxy clusters are the brightest, and most common, extra-galactic X-ray source ([Cavaliere et al., 1971](#)), and are extremely luminous. With the exception of quasars, X-ray sources have the most luminous X-ray emission in the Universe²⁵. As a result, our understanding of the hot X-ray emitting gas in the **ICM** of a galaxy cluster has increased tremendously.

Observations of galaxies and galaxy clusters at X-ray wavelengths have many advantages, as we have many known effects which tell us a lot about the cluster: X-ray luminosity correlates with cluster classification, with irregular galaxy clusters having low luminosity, and regular clusters having high luminosity; X-ray luminosity in clusters correlates with mass, and also with temperature; and hydrogen gas deficiencies, particularly HI, also correlate with luminosity and cluster richness.

1.4.5 Gamma Ray

Gamma-ray astronomy observes the highest frequency waves in the electromagnetic spectrum, at a wavelength smaller than ten picometres, and frequencies higher than 10^{19} Hz. They are similar to X-rays, with the difference being the source of emission. As with X-ray emission, gamma rays are invisible to the human eye and are mostly blocked by the atmosphere of the Earth, with direct observations of gamma-rays requiring the use of space-based telescopes.

However, if the photon is highly excited and the energies are higher ~ 30 GeV, the gamma rays are detectable on Earth. Telescopes capable of doing this include the Cherenkov Telescope Array²⁶ (CTA), and the High Energy Spectroscopic System²⁷ (HESS).

Gamma rays are generally emitted as a product of radioactive decay (gamma decay), with energies ranging from 100 keV up to MeV and GeV ranges. Some astronomical bodies that produce gamma rays include solar flares from stars, pulsars, quasars, supernovae, and hypernovae. When one of these objects produces high-energy electrons, the electrons produce secondary radiation in the form of gamma rays, through processes such as bremsstrahlung, synchrotron radiation, and inverse Compton scattering.

In 1961 the first gamma-ray telescope, Explorer-11²⁸, was launched into orbit. The telescope was housed in a satellite that had no active pointing, and so was set on a tumbling trajectory to scan the celestial sphere. In 23 days and 9 hours of observations, the onboard instruments detected 22 gamma-ray events ([Kraushaar and Clark, 1962](#); [Kraushaar et al., 1965](#)).

²⁵<https://ned.ipac.caltech.edu/level5/March02/Sarazin/frames.html>

²⁶<https://www.cta-observatory.org/>

²⁷<https://www.mpi-hd.mpg.de/hfm/HESS/>

²⁸<https://heasarc.gsfc.nasa.gov/docs/heasarc/missions/explorer11.html>

1.5 Radio Emission in Galaxies and Galaxy Clusters

Diffuse emission refers to the non-thermal, non-localised, widespread radiation that surrounds an astronomical object. In this work, I am looking specifically at diffuse radiation in the radio part of the electromagnetic spectrum, and using X-ray, optical, and infrared radiation for comparison and analysis.

As stated by Feretti et al. (2012), the detection of diffuse emission in radio can be quite tricky, as the telescope must have a balance between high angular resolution and high sensitivity to low surface brightness. This is a critical factor for low-surface brightness objects such as Abell S1136.

Diffuse emission sources in galaxy clusters all have a very steep spectral index (Feretti et al., 2012; van Weeren et al., 2019), typically $\alpha \lesssim -1$ (van Weeren et al., 2019). For these reasons, diffuse emission from radio sources is best observed at low frequencies; $< 2\text{GHz}$ (van Weeren et al., 2019), and $\lesssim 1.4\text{GHz}$ (Feretti et al., 2012). Also, as noted in Section 1.4.1, a radio relic and a radio halo will differ clearly in their polarisation, with the central sources being less polarised than the peripheral sources (Feretti et al., 2012).

The study of diffuse emission has evolved significantly in the last decade; however, there is still uncertainty surrounding the physical origins.

1.5.0.1 Spectral Index

The spectral index of an astronomical source, denoted as α , measures the dependence of a source's radiative flux density S_ν (the “radiative flux per unit of frequency”) on its frequency ν . The formula for spectral index is $S_\nu \propto \nu^\alpha$.

The integrated spectral index of the diffuse emission in radio sources is still lacking in data, and due to various reasons is difficult to obtain (Lisenfeld and Völk, 2000; Feretti et al., 2012; van Weeren et al., 2019). A specific problem is that the diffuse emission from extra-galactic radio sources is very faint, and requires a telescope with high sensitivity and resolution to obtain good measurements. To measure the spectral index accurately, you need two radio telescopes at different frequencies, with the same resolution, to produce a good result. Convoluting one observation to match the other is a good approximation, but that in itself introduces calibration uncertainties.

Compounding this, the radio emission from galaxies and galaxy clusters is composed of thermal bremsstrahlung radiation, synchrotron emission, and diffuse synchrotron emission, all of which have a different spectral index (Lisenfeld and Völk, 2000). The total spectral index of the radio emission is, therefore, dependant on the relative contribution of each emission type, and the processes which shape them.

1.5.1 A Taxonomy to Characterise Diffuse Radio Emission

Kempner et al. (2004) describe a method to characterise diffuse radio emission, using the distinct physical properties of the sources instead of the subjective approach of the researcher; described by Kempner et al. (2004) as a “phenomenological approach”. As shown in Table 1.4, the large-scale radio sources in galaxy clusters have sizes ranging from tens of parsecs up to a megaparsec or more and have different radio morphology properties.

According to (Kempner et al., 2004) and (Feretti et al., 2012), diffuse radio emission in galaxy clusters can be classified into two basic classes: emission associated with an AGN, and emission associated with the ICM. Emission from AGN can then be classified further into emission from an active AGN, and emission from a dead or dying AGN. The classification of emission associated with AGN comprises the majority of the radio source characteristics shown in Table 1.4.

I have adopted this taxonomy in this thesis, as well as in the draft paper shown in Appendix B.1. I have included in Section 4.1.6 an alternative discussion from Feretti et al. (2012). These taxonomies are being used to distinguish more clearly between emission sources, and enabling discussion of the possible emission mechanism associated with Abell S1136. I have summarised this taxonomy below.

Radio Sources Associated with Active AGN

1.5.1.1 VLBI Core

Typically on scales of 10 to 100pc, these sources are single-sided or double-sided small-scale jets that are only resolved with the millisecond resolution of Very Long Baseline Interferometry (VLBI) observations. They consist of a core associated with a central black hole, with multiple knots of emission, sometimes accompanied by diffuse emission.

There is very low circular polarisation in some sources, on the scale of $\lesssim 1\%$ (Rayner et al., 2000; Homan et al., 2001), and some sources have linear polarisation of a few percent (Homan, 2005).

The core spectrum is usually flat, with the jets having a typical spectral index of $\alpha \sim -0.5$, (where $S_\nu \propto \nu^\alpha$).

1.5.1.2 Confined Cluster Core (CCC) Source

Existing on scales of ~ 10 kiloparsec (kpc) and are generally associated with the centres of cooling flow clusters. Confined Cluster Core (CCC) sources do not often show two distinct radio lobes as we see with FRI radio galaxies (shown in Section 1.5.1.3), where the individual lobes are usually obscured in a diffuse radio halo which extends in all

Table 1.4: A Summary of Properties of Cluster Radio Sources

Type	Size	Radio Source Characteristics			Relationship to Hot Gas	Prototype
		Morphology	α	Polarisation		
Associated with active radio galaxies:						
VLBI Core	10 to 100 pc	multiple point sources core + halo that may or may not include distinct lobes	-0.5	few %	None	3C 345
Confined Cluster Core Source	10 kpc	core + jets + outer lobes, possibly misaligned	$\lesssim -1.5$	$\lesssim 60\%^{\ddagger,*}$	Anti-correlated	Perseus
Radio Galaxy	$\text{few} \times 10^2$ kpc	core + jets	$<-0.6^{\dagger}$	$\text{few} \times 10\%^{\ddagger}$	May be anti- correlated	Hydra A
Classical Double*	$\text{few} \times 10^2$ to 10^3 kpc	core + jets	$<-0.6^{\dagger}$	$\text{few} \times 10\%^{\ddagger}$	May be anti- correlated	Cygnus A
Associated with extinct/dying radio galaxies:						
AGN Relic [‡]	$\text{few} \times 10$ kpc	filamentary + some diffuse emission; more extended at low frequency	$\lesssim -1.5$	$\lesssim 20\%$	May be anti- correlated	A133
Phoenix [‡]	10^2 kpc	filamentary + some diffuse emission; more extended at low frequency	$\lesssim -1.5$	10 to 30%	Merger / accretion shocks	A85
Not associated with radio galaxies:						
Radio Gisch [‡]	$\text{few} \times 10^2$ to 10^3 kpc	possible filaments, mostly diffuse; often two symmetric sources	$\lesssim -1.2$	10 to 30% lin.	Merger shocks	A3667
Mini-Halo	$\text{few} \times 10^2$ kpc	diffuse, centrally peaked	<-1.5	$\lesssim \text{few } \%$	Correlated	Perseus
Halo	10^3 kpc	diffuse, centrally peaked, may be asymmetric, may have substructure	$\lesssim -1.1$	none	Correlated	1E0657-56

* Rare at low redshift.

[†] Frequency dependent.

^{*} Variable across source.

[‡] Often called “radio relic” in the literature.

horizontal angles from the centre of the core. Often the radio lobes are distorted, as Taylor et al. (2002a) shows, in observations of Centaurus A. It should be noted that an **FRI** radio source will clearly show distinct radio lobes and jets, whereas a **CCC** source *might* have jets that can be clearly identified. The size difference between an **FRI** and **CCC** will also enable more precise identification.

The radio plasma of a **CCC** source is confined by the high density of the **ICM**, creating a morphology lacking in a clear structure. It interacts strongly with the **ICM** and inflates large holes, or “bubbles”, in the hot gasses **ICM** (De Young, 2003; Gardini and Ricker, 2004; Blanton et al., 2010). As stated previously, **CCC** sources are generally associated with cooling flow clusters, and not in merging clusters which have a less dense ICM medium at the cluster centre.

1.5.1.3 Radio Galaxy: **FRI**, **WAT**, **NAT**

Classic **FRI** radio galaxies, as shown in Figure 1.13 (Perley et al., 1979) have typically symmetric jets which extend to $\sim 10 \text{ kpc}$, at which point the radio lobes form and can grow up to 100 kpc . The jets and radio envelopes are very well defined. **FRI** radio galaxies can also have faint diffuse emission extending far beyond the inner lobes (Lane et al., 2005; Owen et al., 2000a), with a morphology that is often misaligned with the inner portion. This misalignment gives rise to the terms “Wide Angle Tail” (**WAT**) for sources whose tails are at $\theta > 90^\circ$, and “Narrow Angle Tail” (**NAT**) for sources whose tails are at $\theta < 90^\circ$. If the host galaxy has a high velocity through the cluster, the tail can bend to such an extent that it can be termed a “Narrow Angle Tail (**NAT**)”. The bending of the galaxy tail, or “radio lobes”, is thought to be the result of the host galaxy’s motion through the **ICM**.

Symmetric jets extend $\sim 10 \text{ kpc}$ from the core of the **AGN**, before the formation of the outer envelope. At this point, a drop in **ICM** density may cause separation of the radio jets and the outer envelope.

Lane et al. (2003) and Taylor (2003), show that at large radii emission in the radio regime can extend nearly perpendicular to the inner lobes. As seen by McNamara et al. (2000), Safi-Harb and Kotani (2003), and Bogdanov et al. (2018), the radio and X-ray emission from the inner lobes is typically anti-correlated, however this is not the case in the extended diffuse bent tail, which do not always exhibit this anti-correlation.

1.5.1.4 Classic Double: **FRII**

As with an **FRI** type radio galaxy, a Fanaroff-Riley Type II (**FRII**) radio galaxy is relatively symmetric and linear about its **AGN** core. **FRII**’s have weak jets, or sometimes no jets, and often only one jet is visible although it has bright lobes. The appearance of an **FRII** radio galaxy is dependent on the environment of the host galaxy, appearing at

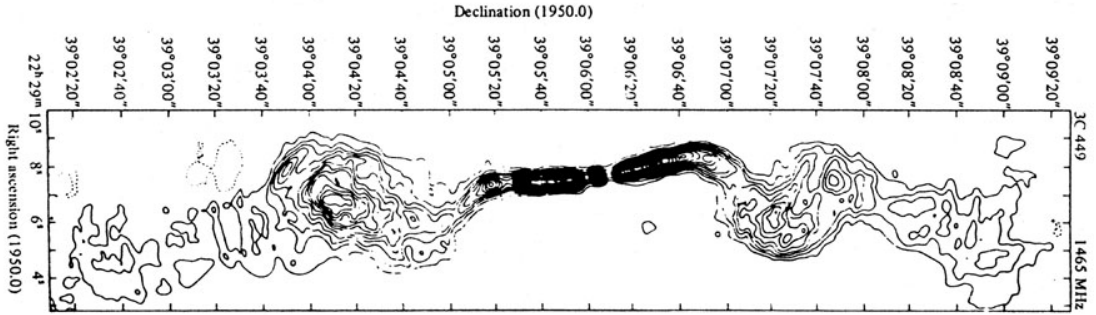


Figure 1.13: This image shows the Fanaroff-Riley Type I Radio Galaxy 3C98 from [Perley et al. \(1979\)](#), characterised by the central bright core with plume like lobes of synchrotron emitting electrons, which extend in double jets from the core. This is distinct from Fanaroff-Riley Type II Radio Galaxy 3C31 shown in Figure 1.14, which is characterised by its dim core with tightly collimated jets ending in bright hotspots.

higher luminosities in more massive galaxies ([Fanaroff and Riley, 1974](#)). Typical sizes for an **FRII** type radio galaxy are in the order of 100 **kpc** and are more luminous than the other sources discussed in this taxonomy ([Owen and Ledlow, 1994](#)).

As shown in Figure 1.14, the radio lobes are often connected to the core with radio emission bridges ([Kempner et al., 2004](#)). The radio lobes in an **FRII** are commonly understood to be the visible result of shocks that have been formed when the supersonic jets terminate ([Meisenheimer et al., 1989](#)).

Radio Sources Associated with Extinct or Dying AGN

1.5.1.5 AGN Relic

An AGN relic is characterised by an extinct or dying AGN, where the radio outburst has switched off, and the remaining plasma evolves passively. Because of this, the relic is found close to the source galaxy, in the inner tens of **kpc** of the galaxy cluster. When observed with sufficient angular resolution ([Slee et al., 2001](#)) the sources are often filamentary.

A recent example of a potential AGN relic has come from the **EMU** Pilot Survey (Norris et al., in prep), which has been performed to test the **ASKAP** telescope in preparation for the full **EMU** survey ([Norris, 2017](#)). The team have found a double-lobed radio galaxy which looks typically standard, with the exception there is no apparent activity; instead, it consists of two diffuse lobes either side of a faint spheroidal galaxy.

Shown in Figure 1.15, nicknamed “The Smoking Gun”, this galaxy presents with an extremely low surface brightness, where there is evidence of past AGN activity that has since shut off, and left behind two remnant clouds of cooling electrons.

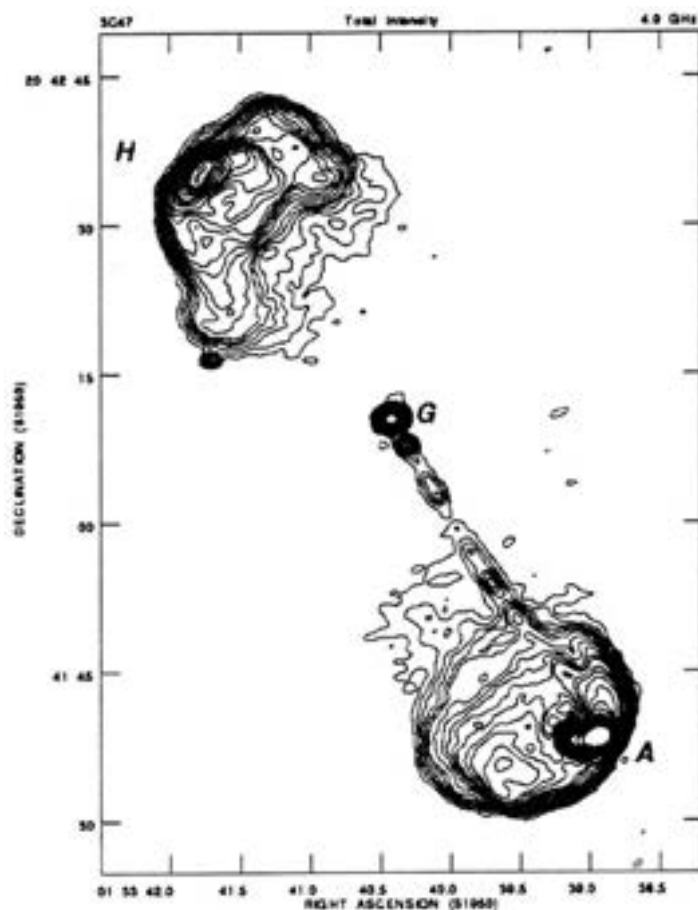


Figure 1.14: This image shows the Fanaroff-Riley Type II Radio Galaxy 3C31 shown in Figure 1.14 from Bridle et al. (1994), which is characterised by its dim core with tightly collimated jets ending in bright hotspots. This is distinct from the Fanaroff-Riley Type I Radio Galaxy 3C98 shown in Figure 1.13, characterised by the central bright core with plume like lobes of synchrotron emitting electrons extending in double jets from the core.

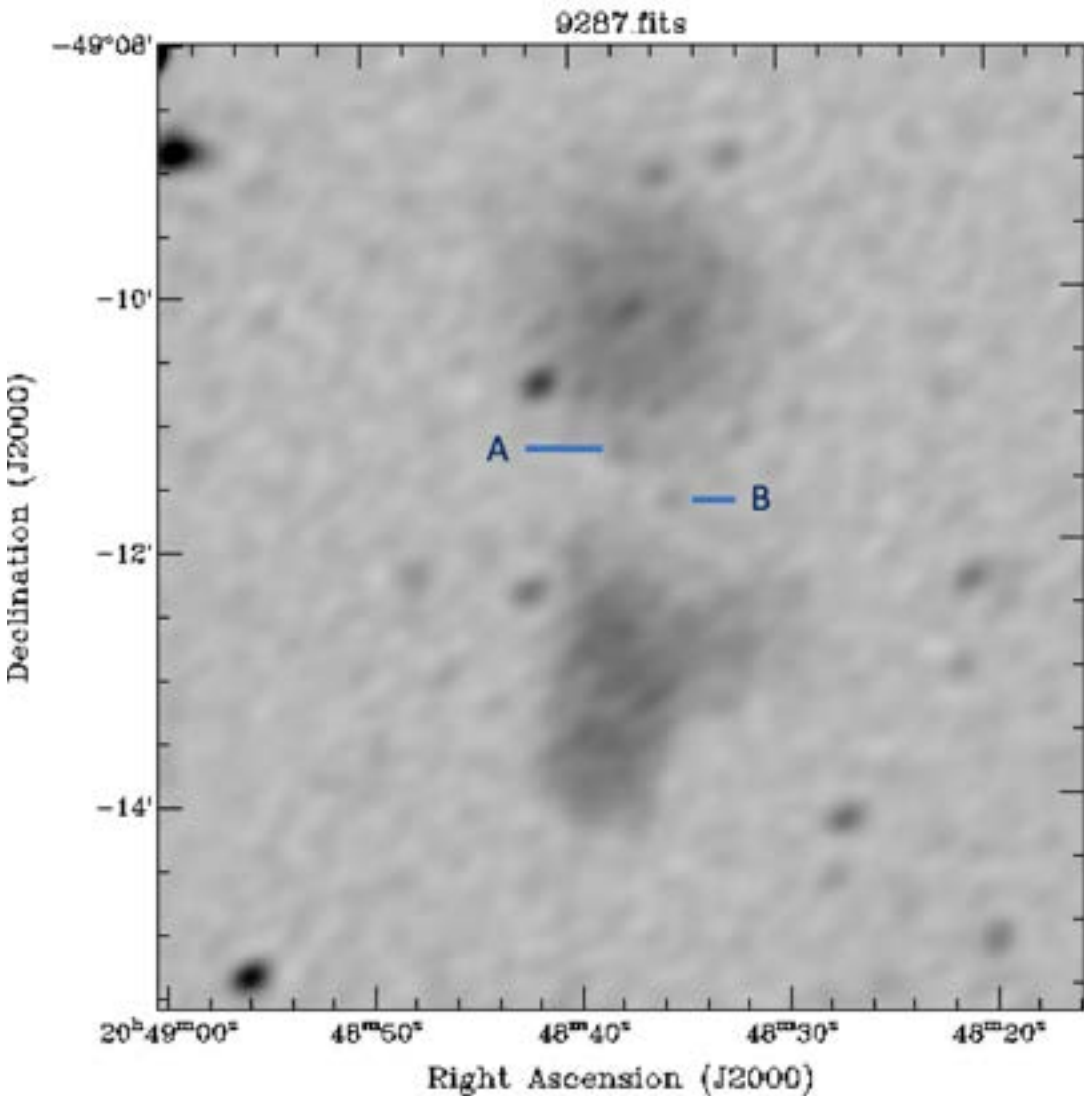


Figure 1.15: The extremely low surface brightness “Smoking Gun” galaxy, discovered in the [EMU](#) Pilot Survey 2019 (Norris et al., in prep), showing potential **AGN** sources labelled “A” and “B”, suspected to be the putative host galaxies. Source “A” is $\sim 260 \mu\text{Jy beam}^{-1}$, source “B” is $\sim 200 \mu\text{Jy beam}^{-1}$. The Smoking Gun appears to be a double-lobed radio galaxy, except for the absence of any activity; instead, there appear to be two diffuse radio lobes either side of a faint spheroidal galaxy; perhaps evidence of prior **AGN** activity which has switched off and left behind two remnant clouds of cooling electrons.

1.5.1.6 Radio Phoenix

A Radio Phoenix is related to [AGN](#), typically a few hundred kpc in size. Because their origin as a radio galaxy, their existence is only possible due to being acted on by the [ICM](#). The electrons in a radio phoenix have aged considerably and no longer emit synchrotron radiation ([Feretti et al., 2012](#)). A radio phoenix forms when fossil radio plasma is compressed by a merger or shock event, the electrons become re-energised and are once again visible in the radio regime. The fossil plasma is “re-born”. Lying close to its host [AGN](#), [Feretti et al. \(2012\)](#) interpret a radio phoenix to be old radio lobes from previous AGN activity, which because of substantial losses from synchrotron and inverse Compton effects the fossil plasma is no longer visible until it is re-energised by a shock wave. A radio phoenix is commonly located near the dominant radio [AGN](#), however, is not coincident with it.

Radio Sources Associated with the Intra-Cluster Medium

1.5.1.7 Radio “Gischt”

A “radio gischt” is often referred to as a “radio relic” in the literature. The term “radio gischt” is German for “sea-foam” or “sea-spray”, and refers to the physical nature of these sources being “synchrotron radiation from electrons being directly accelerated from the thermal plasma in merger shocks”. The radio emission from the ageing electrons should roughly trace the structure of the associated shock. The gischt should often come in pairs, at least in the intermediate stages of mergers between clusters with relatively equal masses. They are generally found at large distances from the cluster centre, where the surface brightness of the X-ray emission is very low. The morphology of the pairs displays on opposite sides of the cluster along the merger axis, appearing as elongated, perpendicular to the axis.

A radio gischt is generally found on the cluster periphery, and will exhibit a spectral index of $\alpha \sim -1.2$, with linear polarisation of $\sim 10\%$ to 30% (example: Abell 2256, [Clarke and Ensslin \(2001\)](#)). The morphology is such that the individual radio structures will trace the shock.

At the time this taxonomy was developed, only a few symmetric “gischt” have been seen; in Abell 3667 ([Rottgering et al., 1997](#); [Johnston-Hollitt et al., 2002](#)), Abell 3376 ([Bagchi, 2002](#)), and Abell 1240 ([Kempner and Sarazin, 2001a](#)), with the last of these has yet to be confirmed by deep pointed observations.

1.5.2 Radio Mini-Halo

A radio mini-halo is typically found at the centre of relaxed, cool core clusters, with the diffuse emission associated with the dominant radio galaxy ([Feretti et al., 2012](#)).

With sizes ranging from a few hundred kpc to ~ 500 Mpc, a mini-halo is characterised by the steep spectral index of the diffuse emission regions and low surface brightness. Examples of mini-halos can be seen in PKS 0745-191 ([O'Dea and Baum, 1991](#)), Perseus ([Burns et al., 1992](#)), Virgo ([Owen et al., 2000b](#)), Abell 2626 ([Rizza et al., 2000](#)), and Abell 1068, Abell 1413, Abell 1650, Abell 1835, Abell 2029, and Ophiuchus ([Govoni et al., 2009](#); [Murgia et al., 2010a](#)). [Taylor et al. \(2002b\)](#) suggest the high magnetic field cool core clusters will give the cluster sources very short radiative lifetimes, so re-energisation of the electrons must occur *in-situ*. Whereas a radio halo and radio phoenix draw their energy from major merger events, large mergers and cooling flows exhibit anti-correlation, so mini-halos probably draw their energy from something else. One suggestion, by [Gitti et al. \(2002a\)](#), is that the energy comes from the cooling flow itself. It is thought that mini-halos are tied to an ongoing cluster merger event.

1.5.2.1 Radio Halo

Radio halos are completely non-polarised and thought to be the result of a merger between approximately equal mass galaxy clusters, as opposed to mini-halos which are thought to be tied to an ongoing cluster merger event. As of 2004, radio halos had only been discovered in clusters with an ongoing or nearly complete merger. X-ray luminosity appears strongly correlated with the cluster radio power ([Liang et al., 2000](#); [Feretti, 2000](#)). It is noted, at the time this taxonomy was written, the effect of observational selection effects on the luminosity / power relationship was still being explored.

The favoured hypothesis regarding the origin of a radio halo is re-acceleration by turbulence from low energy electrons. Turbulence as an energiser is attractive, as it can be directly related to the local properties of the **ICM**, as demonstrated by [Govoni et al. \(2001a,b\)](#), who measured strong correlations between X-ray emission and surface brightness distribution in a host cluster.

1.6 Evidence of Filamentary Structure in Recent Literature

It is well known that shock and turbulence in the intra-cluster medium can produce cluster-wide synchrotron emission from shock-excited electrons; however, the physics behind these processes is not well understood. As outlined in Section 1.5.1, candidates for fossil plasma in galaxy clusters include the tails and lobes of radio galaxies, whose properties include steep spectral indices due to ageing of the synchrotron emission, as well as losses through inverse Compton scattering, where the part of the energy of the electrons is transferred to a photon as the electron scatters the photon to higher energy.

At gigahertz frequencies, fossil electrons in the ICM are only visible for a few mega-years. However, when a process such as a merger shock compresses an aged lobe or tail of a cluster member galaxy, the electrons become re-energised. This has the effect of increasing the visibility of the fossil electrons at sub-GHz frequencies (Enßlin and Gopal-Krishna, 2001; Enßlin and Brüggen, 2002), and creating radio phoenixes (Mandal et al., 2020).

Feretti et al. (2012) outlines the breakthroughs in recent discoveries ($\lesssim 20$ years) of radio halos and radio relics at 1.4 GHz and lower, most of which are at sub-GHz frequencies. Giovannini et al. (1999a), using all-sky survey data from the VLA and Westerbork Synthesis Radio Telescope (WSRT), combined with 205 X-ray bright Abell type clusters from Ebeling et al. (1996), detected and confirmed (using 1.4 GHz VLA data) 18 new radio halo and radio relic candidates - a significant addition to the already known 11 radio halo and radio relic candidates. Kempner and Sarazin (2001b) discovered seven new candidates at 327 MHz using data from the Westerbork Northern Sky Survey (WENSS) Westerbork Northern Sky Survey (Rengelink et al., 1997).

Also noted are the more recent observations by Rudnick and Lemmerman (2009), looking for Mpc radio emission in reprocessed WENSS images; Venturi et al. (2007, 2008), who surveyed massive galaxy clusters at $z = 0.2$ to 0.4 using the GMRT, and discovered ten galaxy clusters containing diffuse sources - within these 10 clusters, the team discovered “three new radio halos, two new core-halo sources and three new halo or relic candidates”; the follow up of the 610 MHz GMRT Radio Halo Survey Giacintucci (2011), looking at the spectral properties of cluster diffuse sources images at 325 MHz; and van Weeren et al. (2011), who discovered two new radio halos, six new radio relics, and a potential double system, using data from the GMRT, VLA, and the WSRT.

These observations at sub-GHz frequencies have probed more deeply, and with higher sensitivity, the diffuse emission from galaxy clusters, adding substantially to our understanding of emission in galaxy clusters. Now, observations with new generation low-frequency radio telescopes at high resolution are revealing definition in the cluster

emission and exposing the filamentary structure within the diffuse radio emission and the galaxy cluster ICM.

It is likely that radio halos with a steep spectral index, at $\alpha \sim -1.7$ and steeper, are missed with observations at GHz frequencies (Cassano, 2010). It is only at sub-GHz radio frequencies, using highly sensitive telescopes, that the radio halo population is revealed. It has not been until recent years, with the commissioning of these higher sensitivity radio telescopes, improvements and upgrades to existing telescopes, and enhanced data processing techniques, that such high sensitivity, low-frequency radio observations of galaxy clusters has been possible. Venturi (2011), provides an excellent example from recent literature, discussing the search for ultra-steep spectrum in galaxy cluster radio halos.

The work in this thesis has used observations from the ASKAP, and produced excellent results. In addition to the research involved in this thesis, recent work from Mandal et al. (2020), Ignesti et al. (2018), Bonafede et al. (2018), de Gasperin et al. (2017), and Venturi et al. (2017a) shows similar exciting discoveries.

1.6.1 The Galaxy Cluster Abell 2593

Mandal et al. (2020) identified three candidate radio phoenix sources from the 150 MHz TIFR GMRT Sky Survey and the 1.4 GHz NRAO VLA Sky Survey (NVSS) sky survey. Using radio data from Low-Frequency Array (LOFAR) and GMRT, X-ray data from Chandra or XMM, and archival optical observations, Mandal et al. (2020) have discovered filamentary structure in Abell 2048, Abell 2593, and SDSS-C4-DR3-3088. A section of Figure 1 from Mandal et al. (2020), showing filaments in Abell 2593, is reproduced here in Figure 1.16. They found the three sources had (a) an intricate radio morphology which contained filamentary sub-structure, (b) possible curved spectra, and (c) are most likely related to radio AGN fossil plasma. Mandal et al. (2020) used Kempner et al. (2004) to classify the sources, and concluded that the sources are “radio phoenixes”.

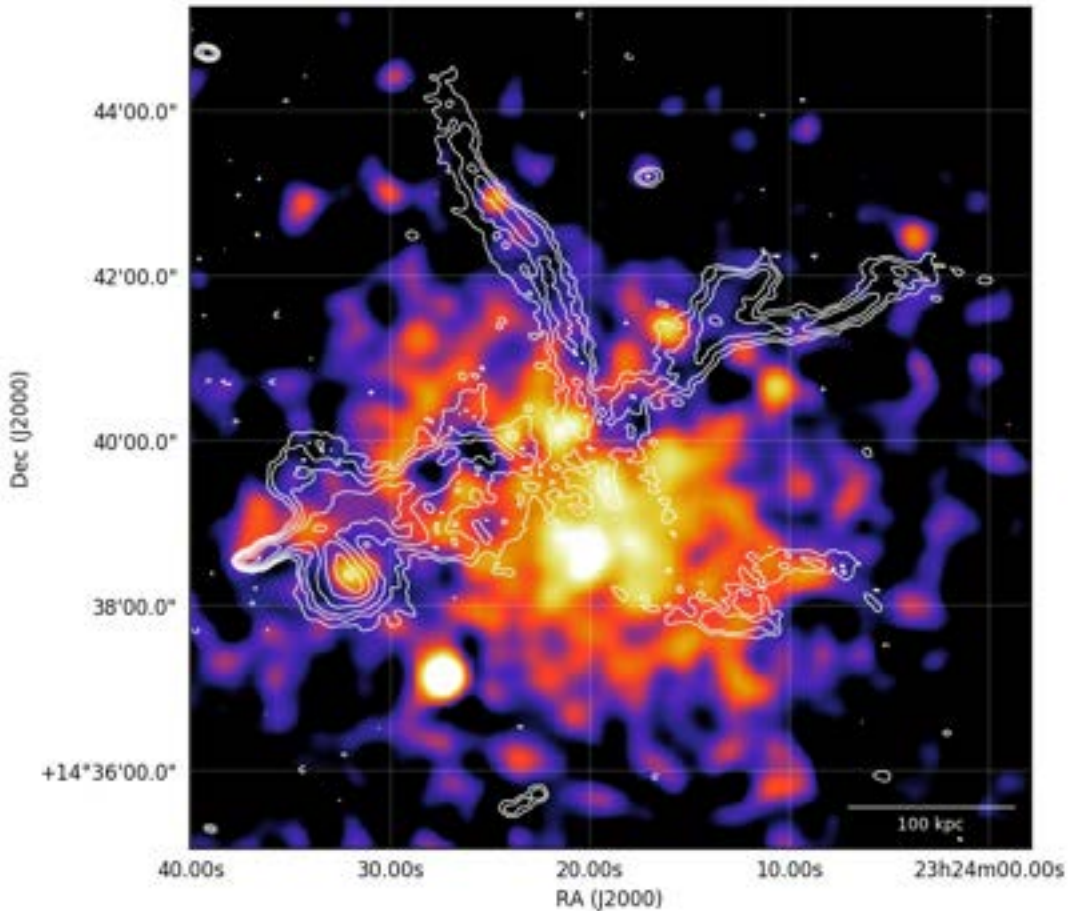


Figure 1.16: Abell 2593, reproduced from [Mandal et al. \(2020\)](#): “Full-resolution LOFAR image contours in white, contours are from the 150 MHz LOFAR image ($9'' \times 6''$), show the $(1, 2, 4, \dots) \times 5 \times \sigma_{\text{LOFAR}150}$, where $\sigma_{\text{LOFAR}150} = 219 \mu\text{Jy}/\text{beam}$, of Abell 2593, overlaid on an exposure-corrected Chandra image in the 0.5-2.0 keV energy band with a total integration time of 7ks.”

1.6.2 The Galaxy Cluster Abell 2626

The radio emission from Abell 2626 contains a system of symmetric arcs shaped like a diamond “kite”. Before the work by Ignesti et al. (2018), the radio arcs did not have any known correlation with the thermal emission in X-ray. Ignesti et al. (2018) made X-ray observations of Abell 2626 using Chandra X-ray Observatory (**CXO**), to try and understand the origin of the radio arcs. The results show “a cold front spatially coincident with the radio arcs”. Figure 1 from Ignesti et al. (2018), showing the radio arcs in Abell 2626, is reproduced here in Figure 1.17.

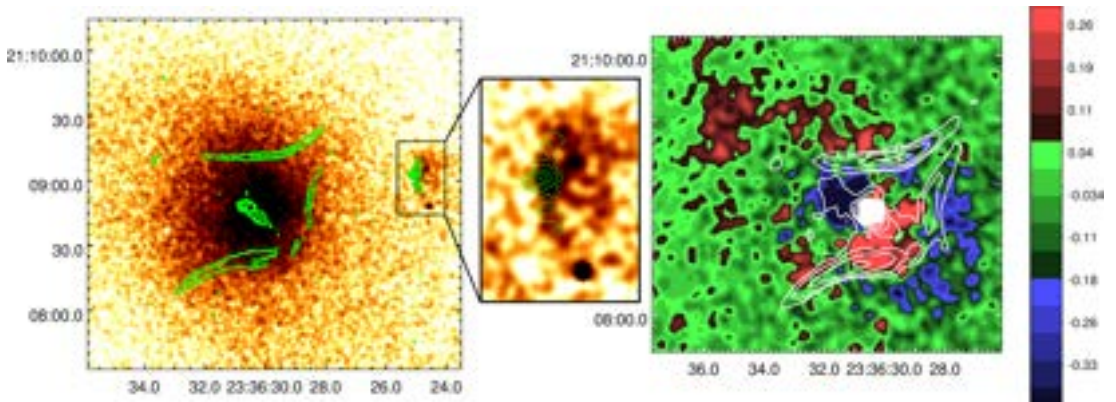


Figure 1.17: Abell 2626, reproduced from Ignesti et al. (2018): “Left: 0.5–2 keV Chandra image of A2626 smoothed with a 3-pixel Gaussian filter (1 ACIS pixel = 0.5”), with a zoom on IC5337 and with the 1.4 GHz radio emission overlaid in green contours (from Fig. 2 of Gitti (2013), resolution $\sim 1.2''$). Right: SB residual map obtained by subtracting the β -model, smoothed with an 8-pixel Gaussian filter (color map), and with the 1.4 GHz radio emission overlaid in white contours (from Fig. 3 of Gitti (2013), resolution $\sim 4.2''$). As indicated by the color-bar on the right, the over-densities in units of counts $\text{px}^{-2} \text{s}^{-1}$ are shown in red and the subdensities in blue.”

It is theorised that the X-ray gas and the location of the radio arcs in Abell 2626 is connected; either via “sloshing” of the hot X-ray gas interacting with the electrons in the radio arcs, possibly tracing where they have been re-accelerated by turbulence from the sloshing; or perhaps through gentle compression of the electrons by the X-ray gas, causing ghost relativistic bubbles; or, as postulated by Mazzotta and Giacintucci (2008), in a non-merging cluster the sloshing of gas could be the brightest parts of a mini-halo that is generated via interaction between the region of the core bounded by the sloshing cold fronts.

1.6.3 The Galaxy Cluster MACS J0717.5+3745

The MACS J0717.5+3745 galaxy cluster has at least four sub-clusters undergoing a violent merger (Bonafede et al., 2018). There is also a radio halo evident. Using **LOFAR** and **GMRT**, new observations of MACS J0717.5+3745 have shown the intra-

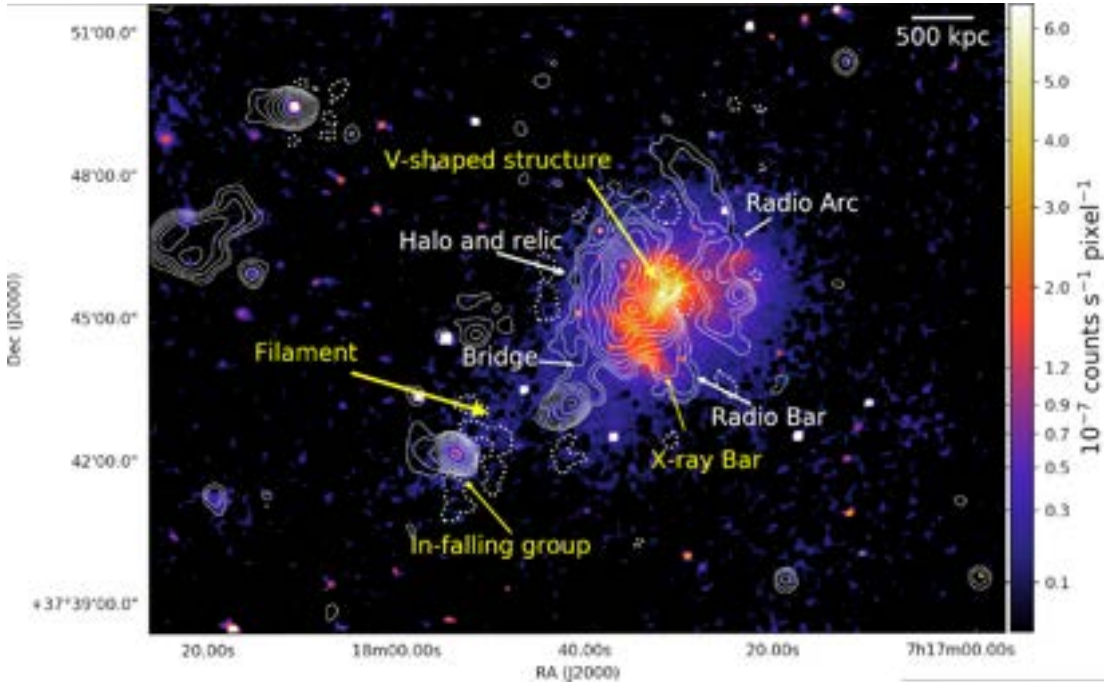


Figure 1.18: MACS J0717.5+3745, reproduced from Bonafede et al. (2018): “Colours: X-ray emission from Chandra in the band 0.2 - 5 keV. Contours: radio emission from LOFAR at 147 MHz. The beam is $19'' \times 18''$. The rms noise (σ) is $0.16 \text{ mJy beam}^{-1}$. Contours start at 4σ and are spaced by a factor 2. The contour at -4σ is dashed. The main components of the cluster emission in the X-rays and radio are labelled in yellow and white, respectively.”

cluster medium to be masking new filamentary radio structure. The new structure shows many new results, including a halo and relic in the eastern edge of the X-ray periphery. Spectral index maps from the observation show a steep spectral index of ~ -1.3 to -2.3 across the radio bar, the radio arc, and the radio bridge. Figure 1 from Bonafede et al. (2018), showing the radio filament structure in MACS J0717.5+3745, is reproduced here in Figure 1.18.

1.6.4 The Galaxy Cluster Abell 1033

Abell 1033 contains a wide-angle tailed radio galaxy on the eastern side, with unusual spectral properties and brightness (de Gasperin et al., 2017). As with the discoveries in Abell S1136 shown in this thesis, and the other discoveries mentioned immediately above, the newly identified structure is only visible at low frequencies. Using LOFAR and GMRT, (de Gasperin et al., 2017) observed what they have termed a “GReET”, or “Gently ReEnergized Tail”. A “GReET” occurs when the non-thermal fossil radio plasma is gently re-energised by perturbations in the ICM. They also observed in the south of the cluster a source they have classified as a radio phoenix and described as the most luminous source in the Abell 1033 cluster. Figure 1 from de Gasperin et al. (2017), showing the radio arcs in Abell 1033, is reproduced here in Figure 1.19.

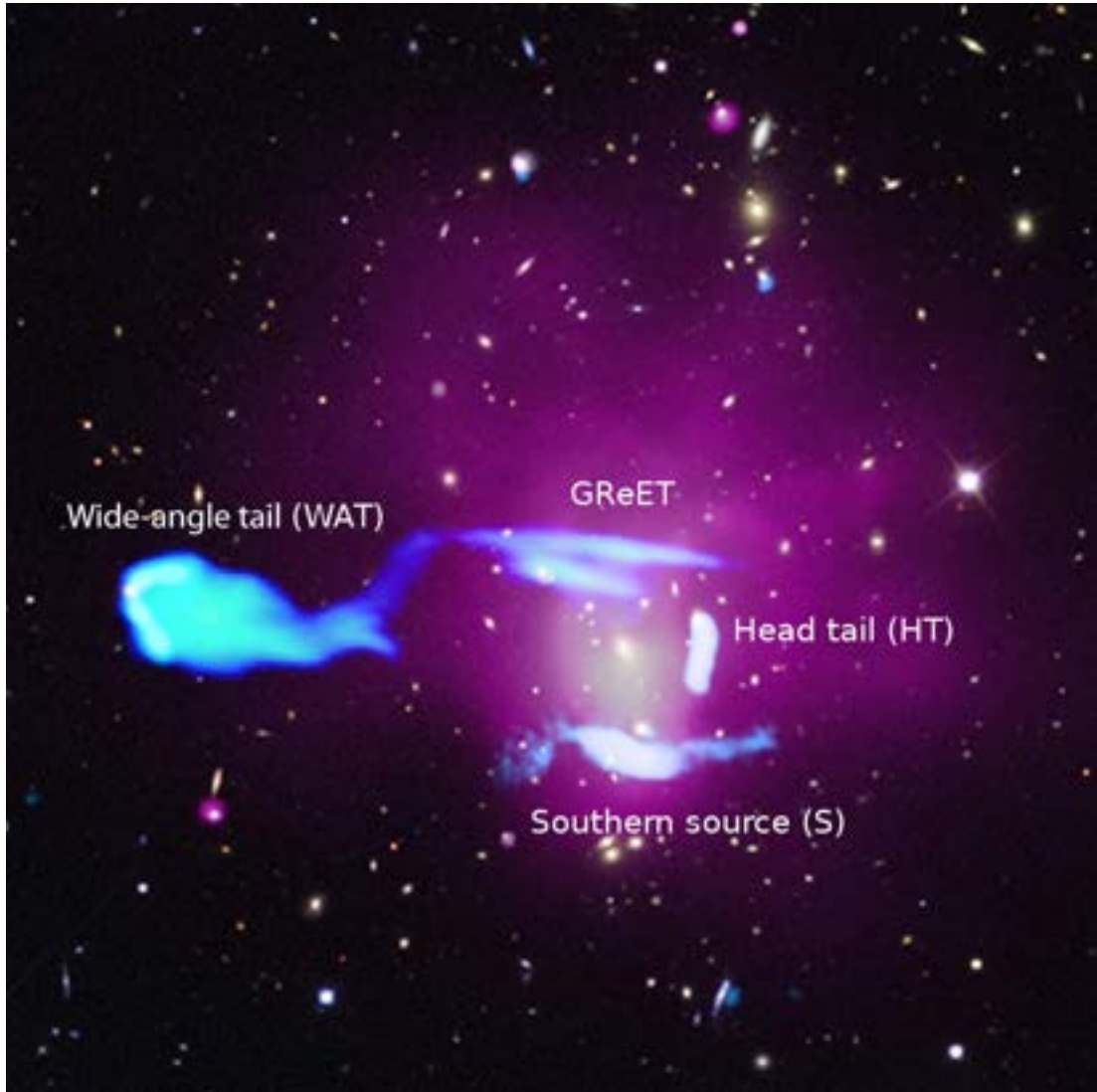


Figure 1.19: Abell 1033, reproduced from [de Gasperin et al. \(2017\)](#): “Composite image showing optical, radio, and x-ray emission of the galaxy cluster Abell 1033. The background image shows optical data from the Sloan Digital Sky Survey (i, r, and g filters). In purple, we show the x-ray surface brightness (0.5 to 4 keV, from the Chandra X-ray Observatory) tracing thermal gas, and in blue, we show the radio emission [from Low-Frequency Array (LOFAR)] tracing CR. The source labeled GReET is the main topic of this work. The source labeled Southern source is a probable radio phoenix (23). The image size is around $1 \text{ Mpc} \times 1 \text{ Mpc}$.”

1.6.5 A Radio Relic in the Shapley Concentration Core, Between the Abell Galaxy Clusters A3558 and A3562

The Shapley Concentration Group, or Shapley Supercluster ([Shapley, 1930](#)), is an over-density of galaxies located at $z \sim 0.03$ to 0.05 , situated in the Local Group (Section [1.2](#)); at the centre of the Shapley Concentration is a “chain” of galaxy clusters that includes Abell 3562, Abell 3558, and Abell 3556. Located within the Abell 3558 and Abell 3562 galaxy clusters, are the Shapley Concentration groups SC 1327–312 and SC 1329–313, shown in Figure [1.20](#).

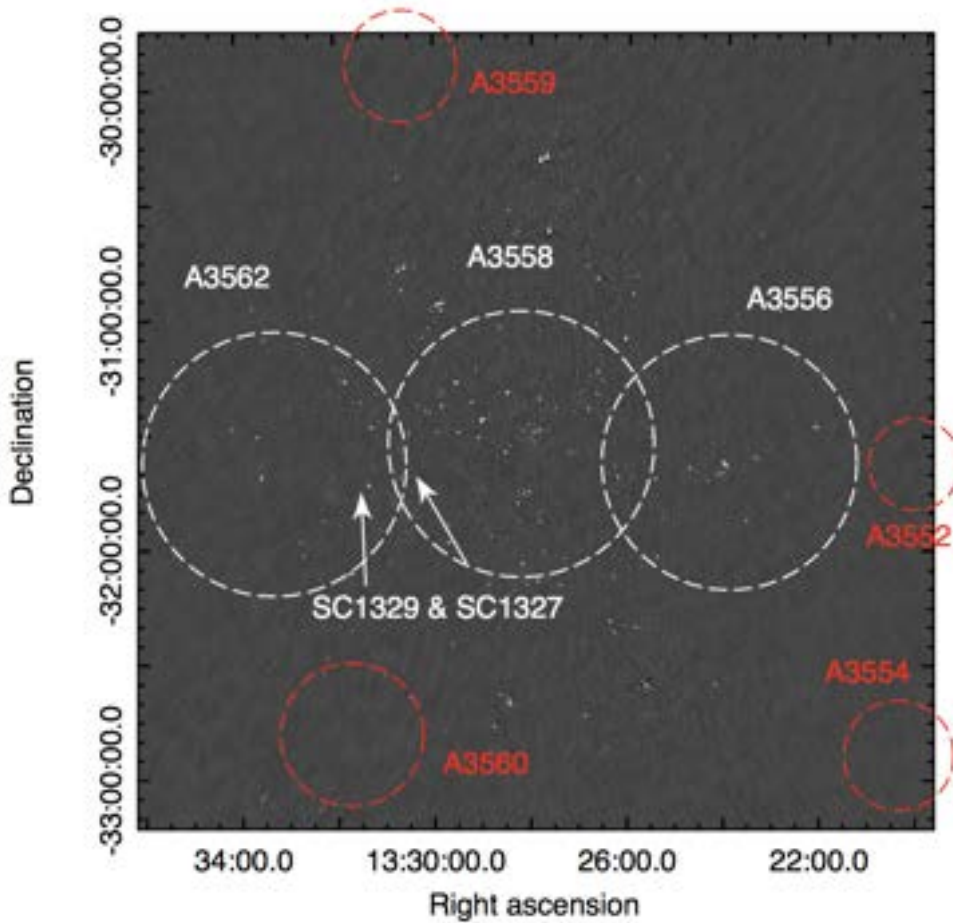


Figure 1.20: Reproduced from [Venturi et al. \(2017a\)](#), showing SC 1327–312 and SC 1329–313 in relation to Abell 3562 and Abell 3558: “Gray-scale version of the 325 MHz Giant Metrewave Radio Telescope (GMRT) image. The full field of view centered on A3558 is shown. The Abell clusters and groups are indicated. The restoring beam is $20'' \times 16''$. ”

Using observations and date from the [GMRT](#), [Venturi et al. \(2017a\)](#) discovered a radio relic situated between SC 1327–312 and SC 1329–313. The relic is ~ 350 Kpc in size, similar to the filaments in Abell S1136. Figure [1.21](#) shows the location of the candidate relic in the Abell 3558 diffuse emission. As noted by [Venturi et al. \(2017a\)](#),

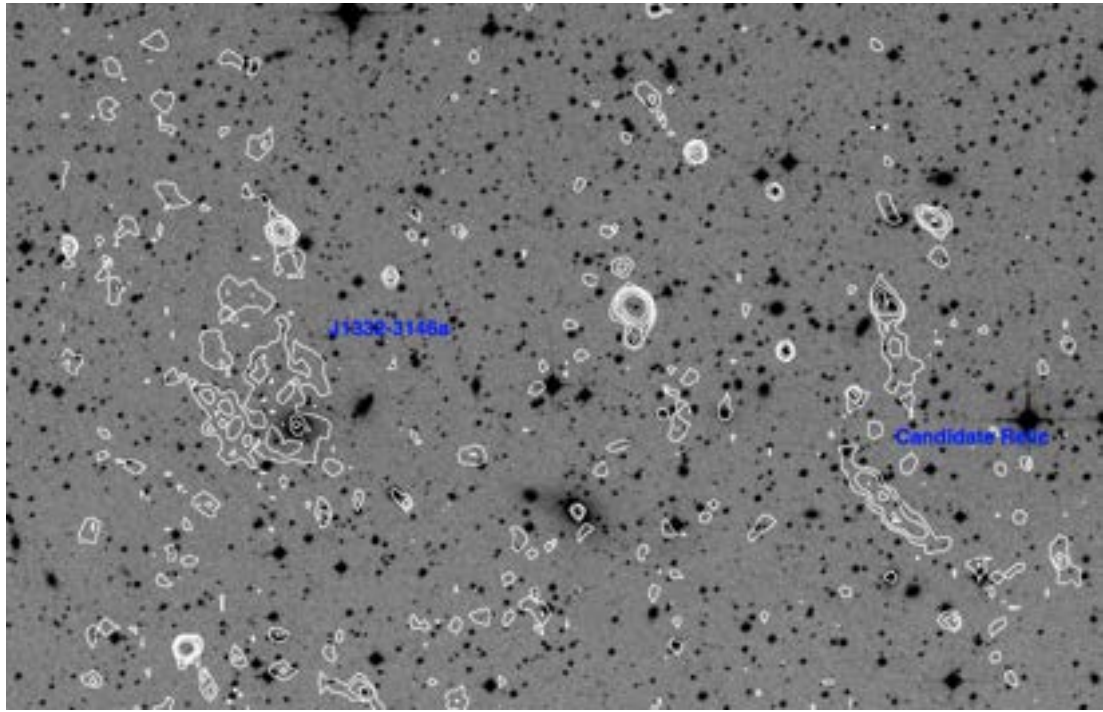


Figure 1.21: Abell 3558 and Abell 3562, reproduced from [Venturi et al. \(2017a\)](#): “Radio contours at 325 MHz overlaid on the Digitized Sky Survey (DSS2) - red optical frame of the region between A3558 and A3562, where the two Shapley Concentration (SC) groups are located. The radio image is primary beam corrected. The contours start at $0.4 \text{ mJy beam}^{-1}$ and are drawn as powers of two. The resolution of the image is $16.3'' \times 11.9''$.“

the emission labelled as the “candidate relic” does not show any optical counterpart to the radio emission.

1.7 The Galaxy Cluster Abell S1136

The Abell S1136 galaxy cluster is located in the Pisces-Cetus supercluster, shown in Figure 1.22 (Porter and Raychaudhury, 2005).

Abell S1136 is located at J2000 RA 23 36 14.3 and J2000 DEC -31 36 24, and is part of the Abell all-sky catalogue of 4073 rich clusters of galaxies (Abell et al., 1989), which includes the “Northern Survey” of 1958 (Abell, 1958b), and the “Southern Survey” of 1988 (Olowin, 1988); it was in this Southern Survey that Abell S1136 was first observed as part of the Abell catalogues. The catalogue of Abell southern clusters has been reproduced in Appendix D. The clusters in the catalogue obtained from the Vizier Online Catalogue (Ochsenbein, 2000) are referred to as “ACO”xxxx, which refers to the authors of the catalogue George Abell, Harold Corwin Jr, and Ronald Olowin, and the “Abell” number assigned to the galaxy cluster. For clarity, all reference in this thesis will refer to them as the “Abell” clusters.

Figure 1.23 shows an image of Abell S1136 at 535 nm (green). The original of this image was made using the UK Schmidt telescope (new optics), with this image being reproduced in 1994. The image is from the Space Telescope Science Institute (ST Sci) digitized Schmidt survey plates (Lasker et al., 1996), covering the entire sky to obtain the image data needed for construction of the Guide Star Catalog (GSC) (Lasker et al., 1990; Trove, 1994). In his original paper, (Olowin, 1988) the galaxy clusters were classified using the Abell (1958a) and Bautz-Morgan Bautz and Morgan (1970a,b) system.

The Abell S1136 cluster was classified in Olowin (1988) as a Bautz–Morgan type III cluster, which as discussed in Section 1.3.2 means the cluster members are not remarkable in any way and have low spectral brightness. Abell S1136 cluster was originally defined as having $N = 21$ members, with the Brightest Cluster Galaxy (**BCG**) designated as ESO 470-20 (Lauberts and Valentijn, 1989). **BCGs** are the Universe’s most luminous galaxies and the most luminous galaxy in a galaxy cluster. The **BCG** is generally located close to the kinematic and spatial centre of the cluster, and their formation is thought to be the result of the merging of several massive galaxies in the clusters early history.

Work by Hilton et al. (2005), which correlated data between the “2dF Galaxy Redshift Survey” (De Propris et al., 2002) and the “ROSAT-ESO flux-limited X-ray galaxy cluster survey (REFLEX) (Böhringer et al., 2004)”, resulting in corrections to the membership of Abell S1136, showing an increase from $N = 21$ to $N = 43$.

The member populations of $N = 21$ and $N = 43$ stated above both give a Richness Class of 0 (zero) (Abell et al., 1989); the lowest of 6 classes in the Abell All Sky catalogue - refer to Section 1.3.2.1. Based on galaxy population, Abell S1136 is therefore classified as a “poor” cluster.

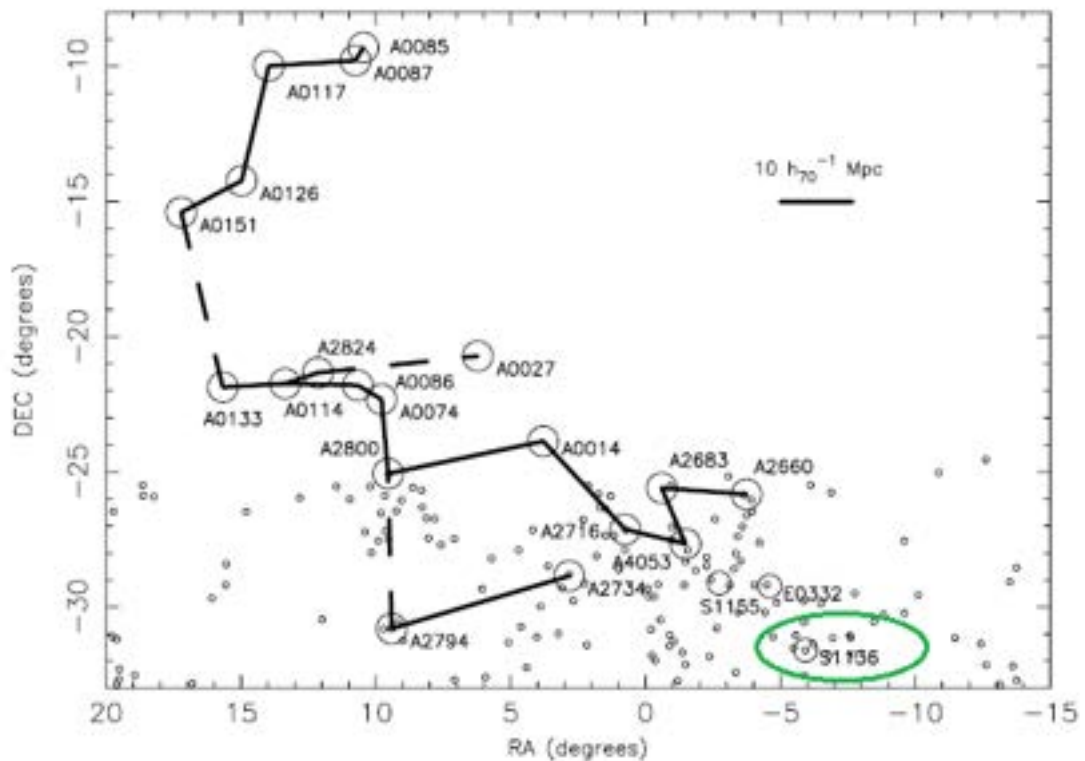


Figure 1.22: Adapted from Porter and Raychaudhury (2005), the location of the Abell S1136 galaxy cluster is shown here in the Pisces-Cetus supercluster. The Abell S1136 cluster of galaxies is circled in green in the lower lower right hand corner.

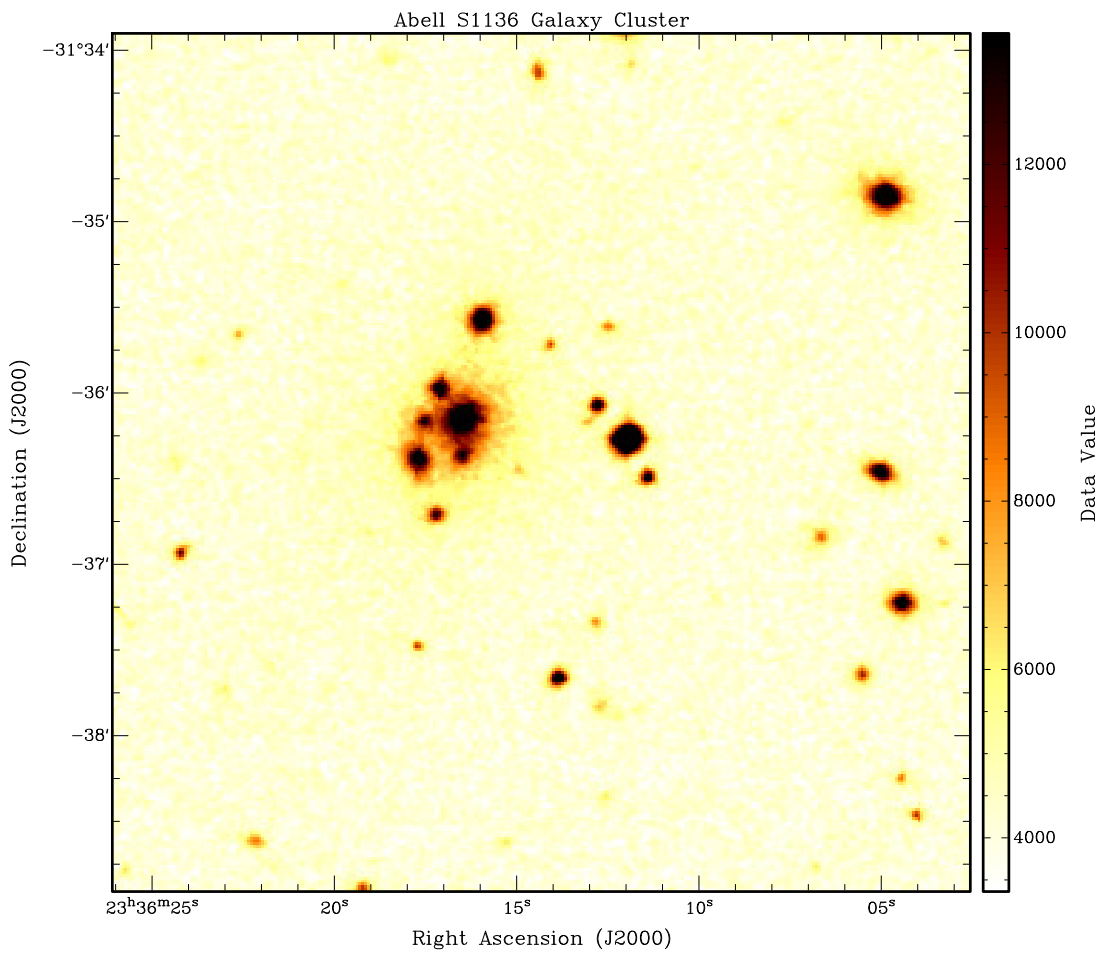


Figure 1.23: Abell S1136, located at Right Ascension (J2000) 23 36 17.000 and Declination (J2000) -31 36 37.00, as observed on 18 August 1977, by [Olowin \(1988\)](#) using the UK Schmidt telescope (new optics). The image is from the Space Telescope Science Institute (ST ScI) digitized Schmidt survey plates ([Lasker et al., 1996](#)), covering the entire sky to obtain the image data needed for construction of the Guide Star Catalog (GSC, [Lasker et al. \(1990\)](#); [Trove \(1994\)](#)).

The preferred redshift²⁹ for Abell S1136 is $z = 0.06250$. Spectroscopic redshift obtained from two other surveys shows measurements in close agreement with each other; A redshift of $z = 0.06234$ [uncertainty = 0.00031] in optical, obtained with the 2dF Galaxy Redshift Survey (De Propris et al., 2002), and a redshift of $z = 0.0620$ [no uncertainty given] from the work in Hilton et al. (2005).

The R_{200} virial radius (1.2.2) of the Abell S1136 galaxy cluster has been measured by Porter and Raychaudhury (2005), and Hilton et al. (2005).

Porter and Raychaudhury (2005) calculated the R_{200} virial radius of the Abell S1136 galaxy cluster to be 2.41 Mpc, with a velocity dispersion $\sigma_r = 602^{+68}_{-51} \text{ km s}^{-1}$, and a radial velocity $cz = 18,562 \text{ km s}^{-1}$. This was calculated using $N = 54$ cluster members. Hilton et al. (2005) calculated the R_{200} virial radius of the Abell S1136 galaxy cluster to be 1.6 Mpc, with a velocity dispersion $\sigma_r = 650 \pm 70 \text{ km s}^{-1}$, calculated using $N = 43$ cluster members. No radial velocity was provided.

Radio observations of Abell S1136 by Duchesne et al. (2017), shown in Figure 3.41, include the strong radio source PKS 2333-318 to the north-west, and a diffuse halo detected at 168 MHz using the MWA (Tingay et al., 2013). The observations described in this thesis were made to see how the structure of this halo changed at the higher frequency and resolution of the ASKAP telescope.

1.8 Other Data used for Comparison

Abell S1136 is a well-studied cluster, appearing in the NASA/IPAC Extragalactic Database³⁰, with 11 cross identifications, 12 external resource links, 22 references in scientific papers published between 1978 and 2019, and studies in many surveys including optical, radio, X-ray, and infrared.

In this section, I show images from other telescopes and surveys, which I have used in the analysis and discussion of the Abell S1136 diffuse radio emission.

1.8.1 ATCA Radio

Figure 1.24 shows an image of Abell S1136 from the ATCA radio telescope. Contours are from the robust = +2.0 image produced from the 2019 ASKAP 33 antenna observations; see Section 3.1.2.

The ATCA observation was made by Principle Investigators Stefan Duchesne and Melanie Johnston-Hollitt as a follow up to the MWA observations of Abell S1136 at 168 MHz (Duchesne et al., 2017). The observation was on 27 April 2016 with a 6A array configuration, at 2100 MHz (16cm),

²⁹<https://ned.ipac.caltech.edu/>

³⁰<https://ned.ipac.caltech.edu/>

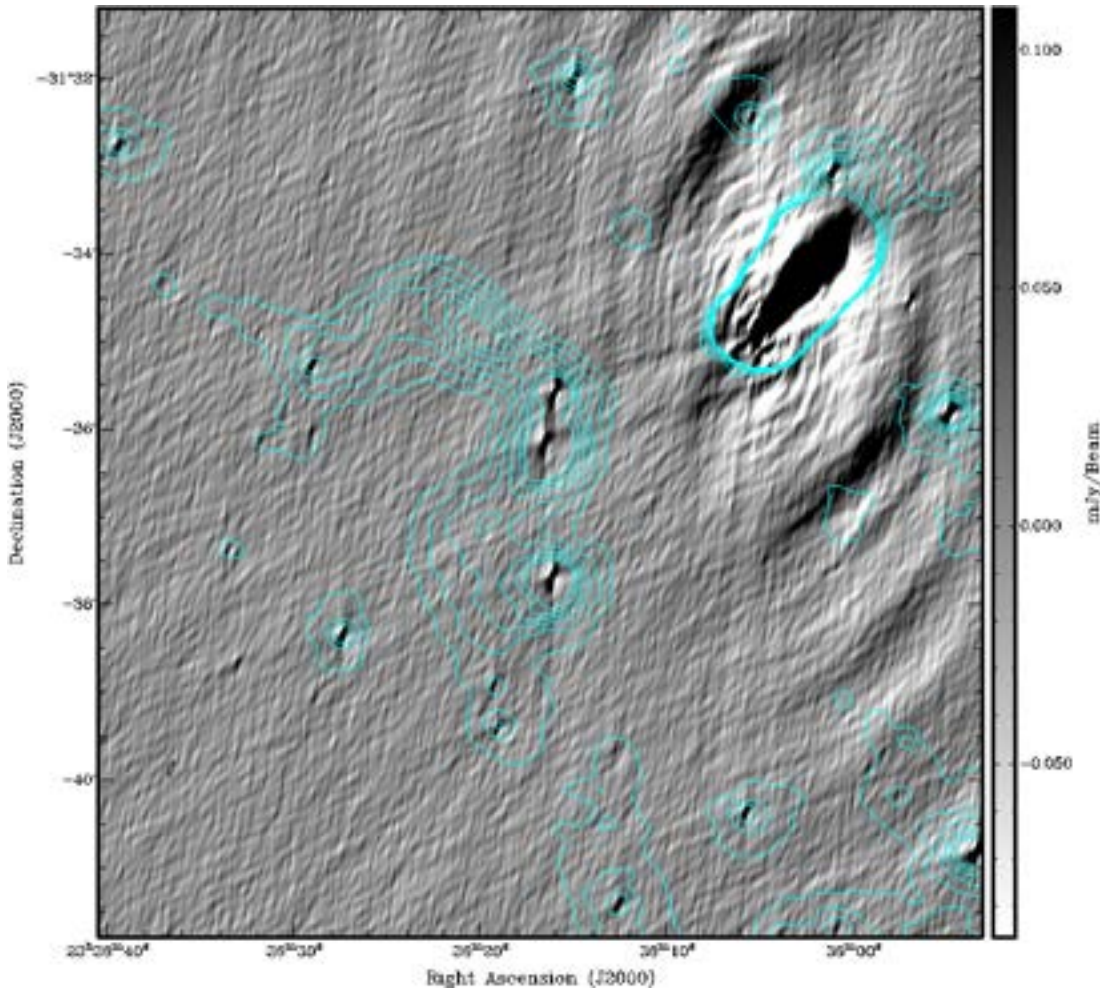


Figure 1.24: Greyscale image of Abell S1136 at 2100 MHz with the Australia Telescope Compact Array radio telescope. The ASKAP 33 radio contours in aqua start at 150 mJy beam $^{-1}$ and increase by $\sqrt{2}$ to 900 mJy beam $^{-1}$.

project code CX356. I re-processed this data, using data obtained from the Australia Telescope Online Archive ([ATOA](#))³¹.

1.8.2 WISE Infrared

Figure 1.25 shows an image of Abell S1136 from the [WISE](#) telescope. Contours are from the robust = +2.0 image produced from the 2019 ASKAP 33 antenna observations; see Section 3.1.2.

The observation was part of the [WISE](#) All-Sky Survey ([Wright et al., 2010](#)) which ran from January 2010 to February 2011. The RGB image was produced from data obtained at 14 THz (22 micrometres), 65 THz (4.6 micrometres), and 88 THz (3.4 micrometres). Data was obtained from the NASA/IPAC Infrared Science Archive ([IRSA](#)) Image Mosaic Service³².

³¹<https://atoa.atnf.csiro.au/>

³²<http://hachi.ipac.caltech.edu:8080/montage>

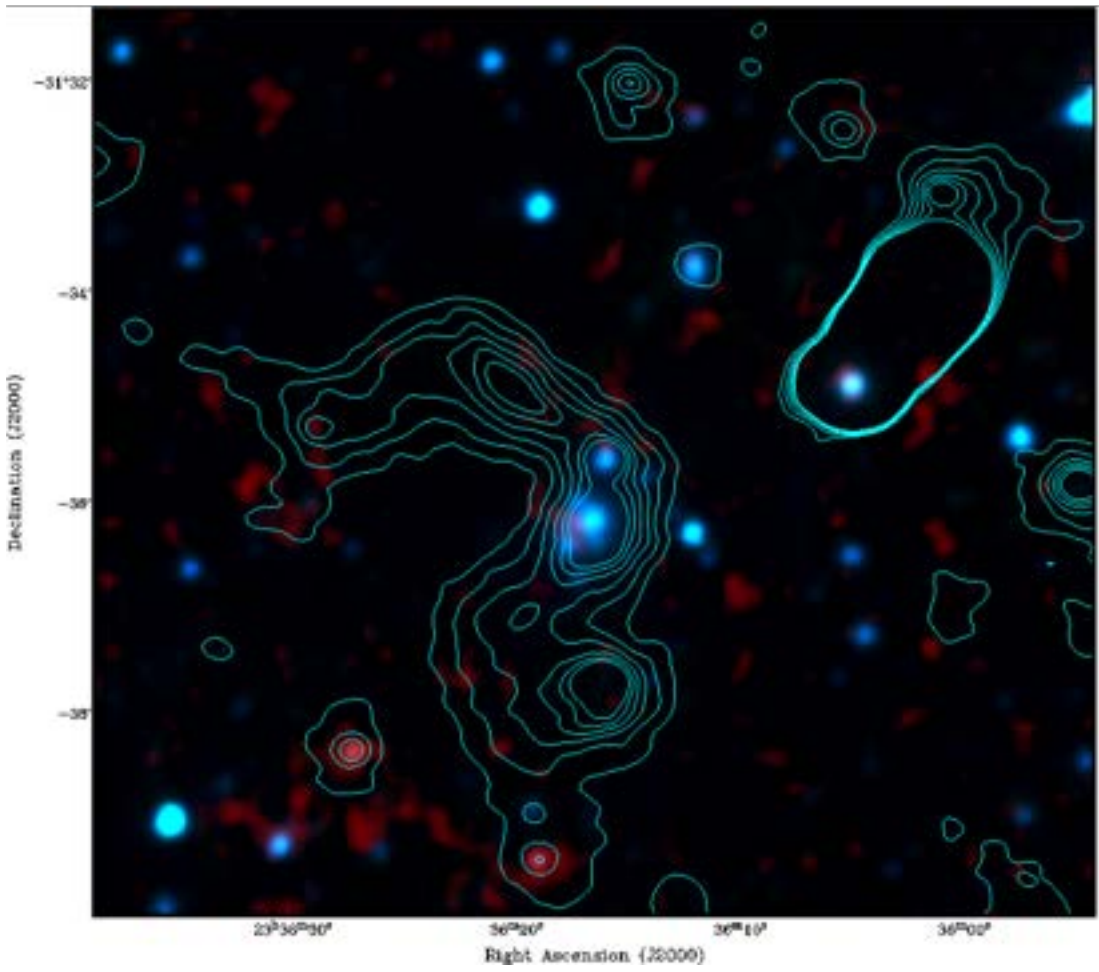


Figure 1.25: WISE Infrared RGB image overlaid with contours from the ASKAP 33 antenna observations. RGB colours are red = $22\text{ }\mu\text{m}$, green = $4.6\text{ }\mu\text{m}$, blue = $3.4\text{ }\mu\text{m}$. The ASKAP radio contours start at 150 mJy beam^{-1} and increase by $\sqrt{2}$ to 900 mJy beam^{-1} .

1.8.3 DSS Optical

Figure 1.26 shows an RGB image of Abell S1136 from the 2nd Digitised Sky Survey. Contours are from the robust = +2.0 image produced from the 2019 ASKAP 33 antenna observations; see Section 3.1.2.

The 2nd Digitised Sky Survey data is from the 48-inch (1.2-meter) Samuel Oschin Telescope³³ survey conducted in the 1980's, and digitised by the Space Telescope Science Institute³⁴. Named POSS-II, the "second" Palomar sky survey was a follow up to the original POSS I, the Palomar Digital Sky Survey (DPOSS) and is included in the Second-Generation Guide Star Catalog (Lasker et al., 2008). Data was obtained using the Skyview Query Form³⁵.

1.8.4 MWA Phase I and Phase II Radio

The MWA Phase I telescope is an interferometric radio telescope which operates at low frequencies (70 - 300 MHz). The telescope is comprised of an array of 128 'tiles'. Each tile contains fixed dipole antennas, has no moving parts, and a 610 deg² field of view at 150 MHz. The tiles are spread over ~ 3 km diameter area. Like the ASKAP, the MWA is a Square Kilometre Array precursor telescope also located at the MRO. Figure 1.27 shows the layout of the Phase I array.

MWA Phase II is an upgrade to the MWA Phase I telescope, adding 128 tiles split into two subset configurations. The upgrade provides enhancements to surface brightness sensitivity and longer baselines.

1. MWA Phase IIA Compact Array Configuration: 72 tiles in two compact hexagons, shown in Figure 1.28
2. MWA Phase IIB Extended Array Configuration: 56 tiles on baselines up to 5km in length, shown in Figure 1.29

1.8.4.1 MWA Phase I Radio

Figure 1.30 shows an image of Abell S1136 from the Galactic and Extragalactic All-sky MWA survey (GLEAM)³⁶ (Wayth et al., 2015; Hurley-Walker et al., 2017) survey. Contours are from the robust = +2.0 image produced from

³³<http://www.astro.caltech.edu/palomar/about/telescopes/oschin.html>

³⁴<http://www.stsci.edu/>

³⁵<https://skyview.gsfc.nasa.gov/current/cgi/query.pl>

³⁶<http://www.mwatelescope.org/gleam>

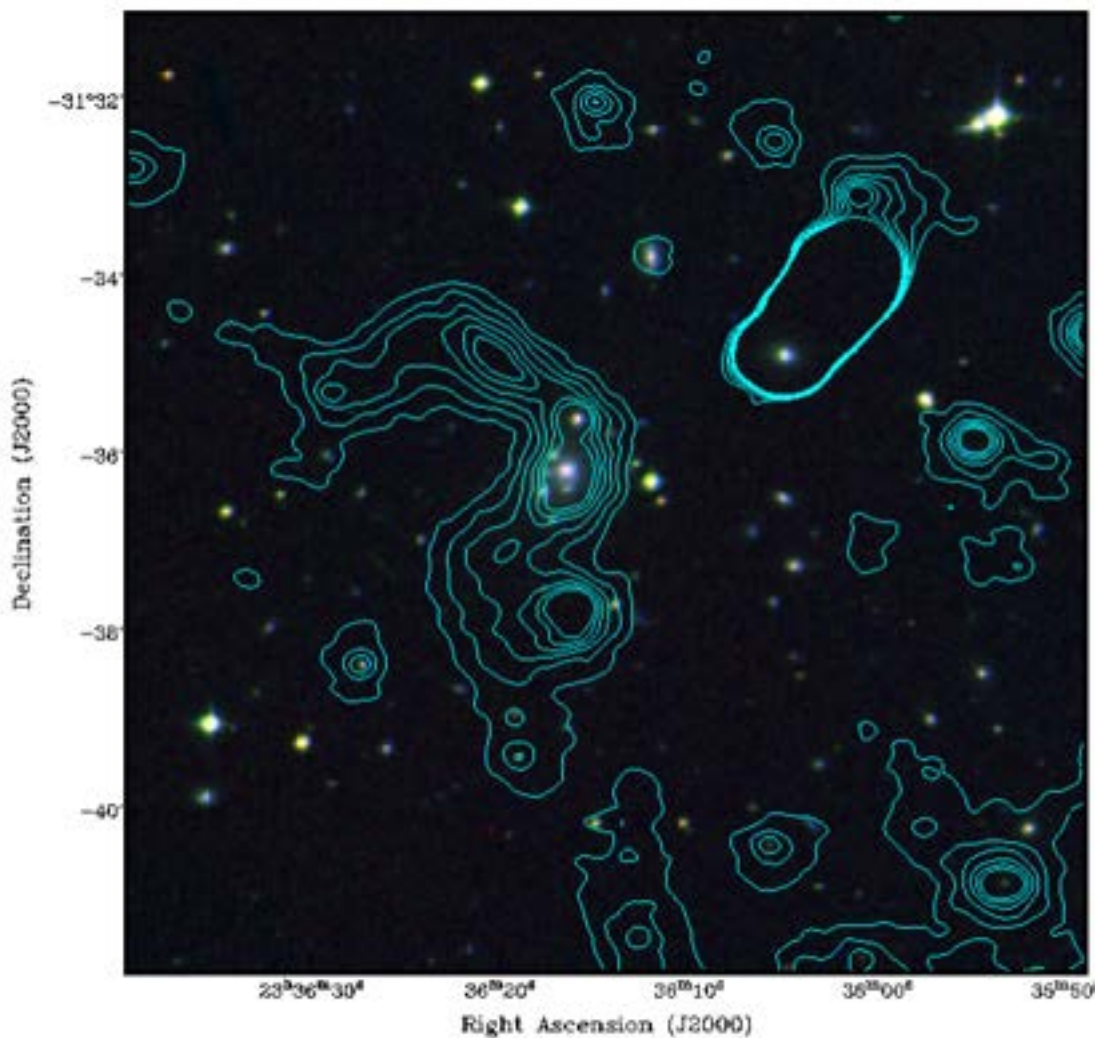


Figure 1.26: 2nd Digitised Sky Survey optical RGB image overlaid with contours from the ASKAP 33 antenna observations. RGB colours are red = DSS2 near infrared at 353 THz, green = DSS2 (red plate) IIIA-E band at 445 THz, blue = DSS2 (blue plate) IIIa-J band at 637 THz. The ASKAP radio contours start at $150 \text{ mJy beam}^{-1}$ and increase by $\sqrt{2}$ to $900 \text{ mJy beam}^{-1}$.

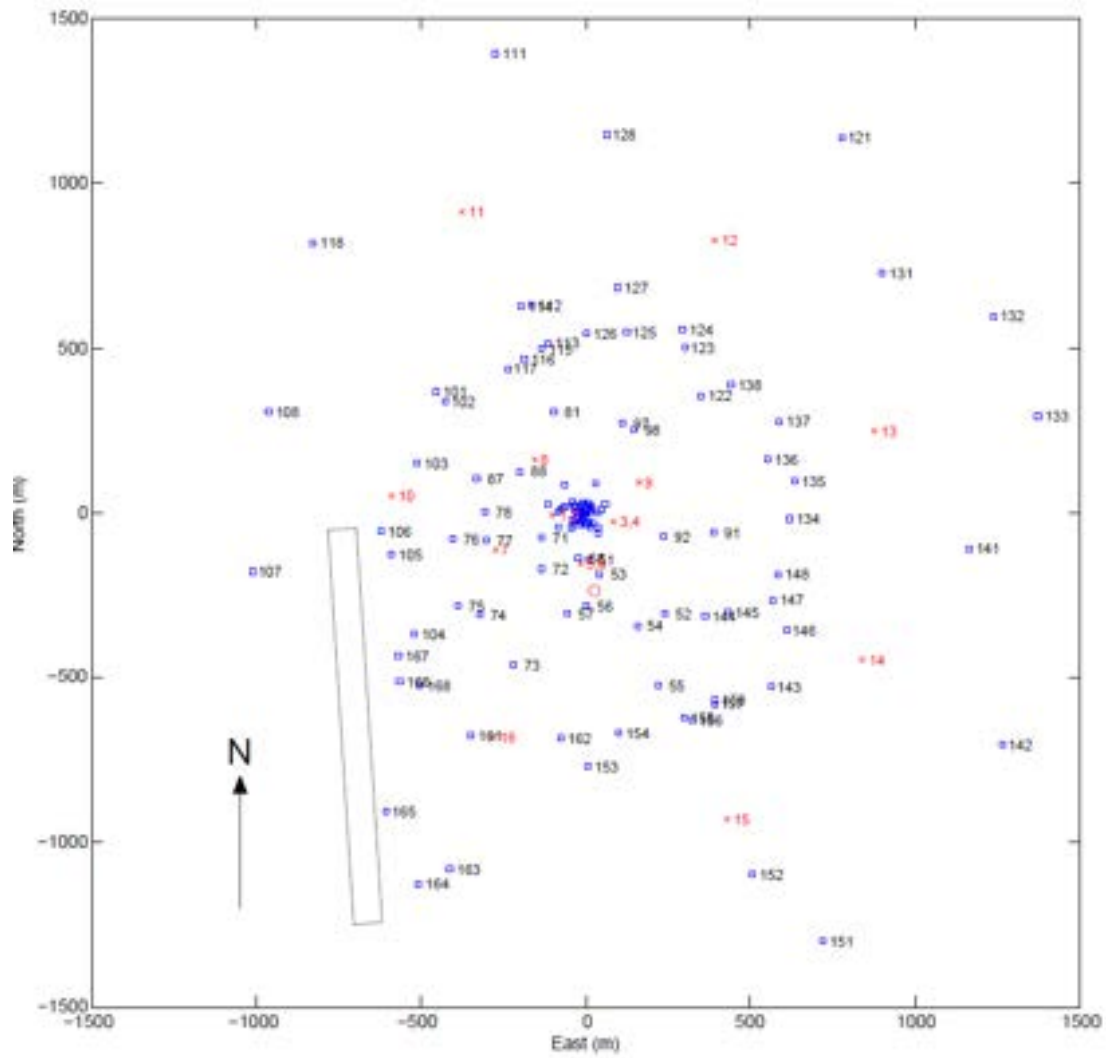


Figure 1.27: Reproduced from <http://www.mwatelescope.org/telescope/configurations/phase-i>, this image shows the placement of the 128 tiles in the **MWA** Phase I telescope.

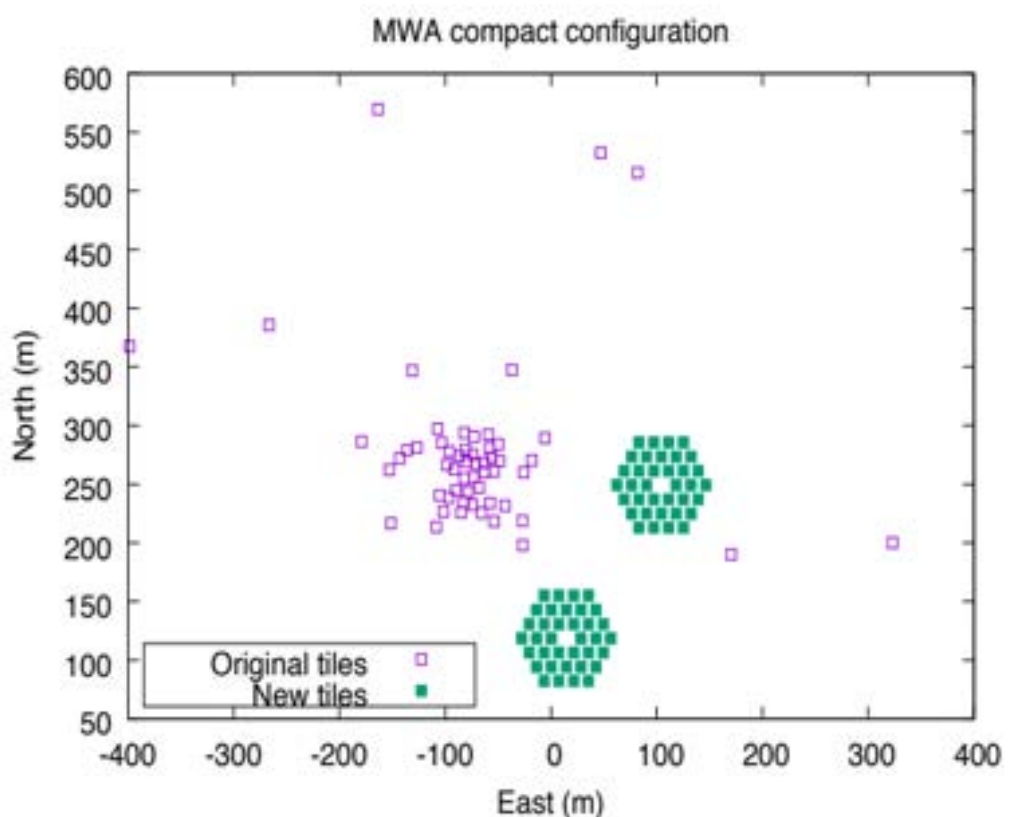


Figure 1.28: Reproduced from Wayth et al. (2018), this figure shows the **MWA** Phase II “compact configuration”. 72 of the new 128 tiles are arranged in “two regular hexagonal arrays (filled squares)”. Not to scale.

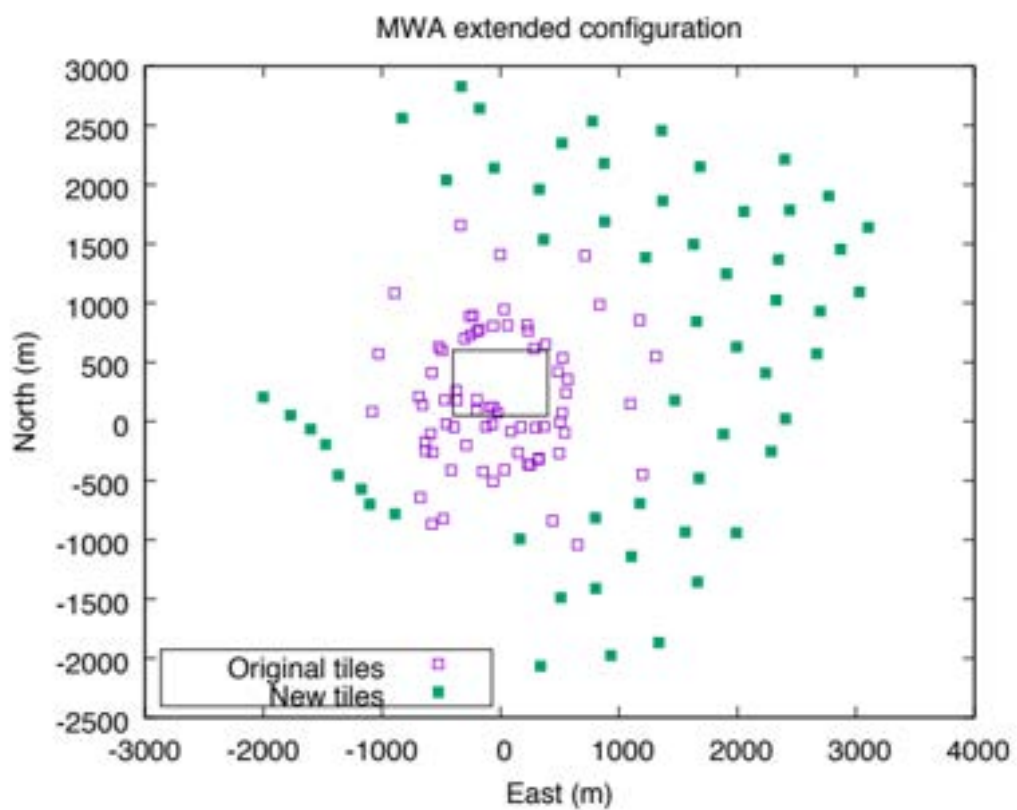


Figure 1.29: Reproduced from Wayth et al. (2018), this figure shows the **MWA** Phase II “extended configuration”. The 56 squares filled in with green show the new long baselines. Not to scale.

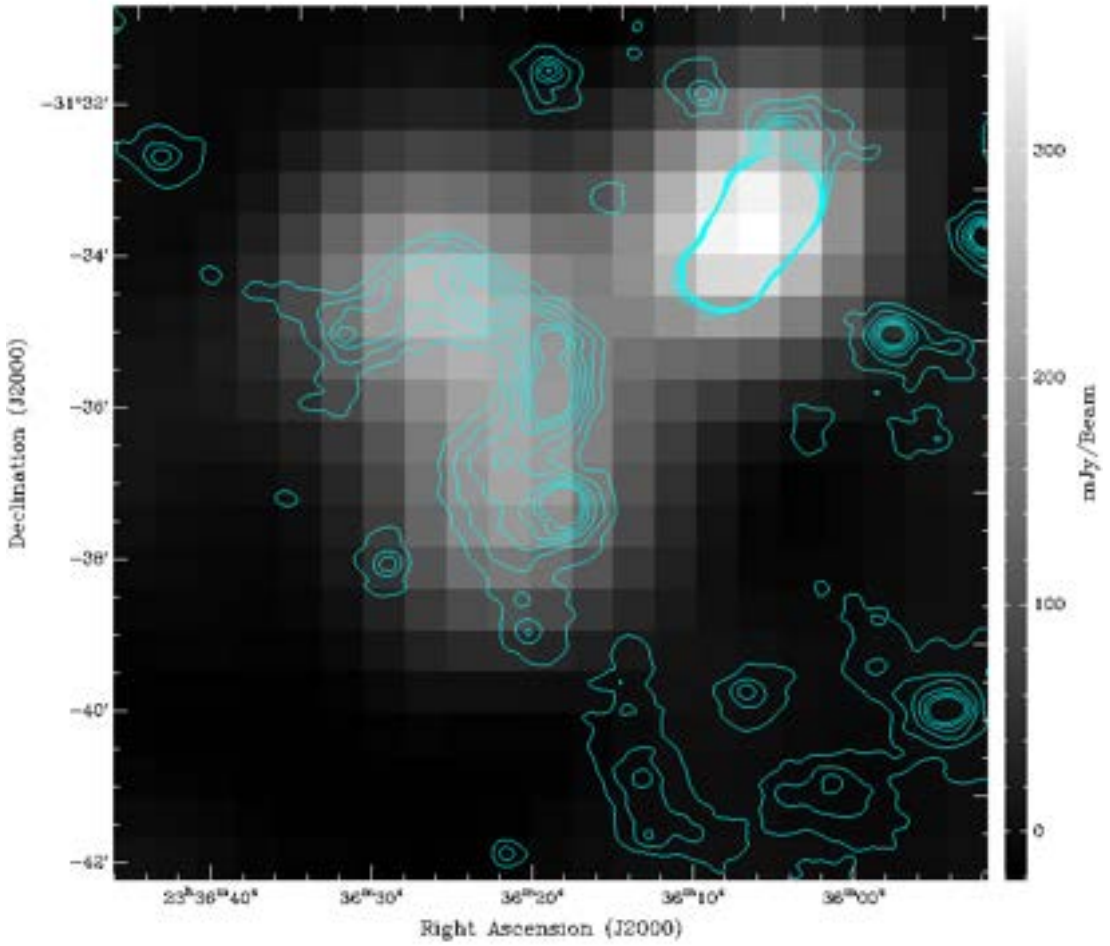


Figure 1.30: MWA Phase I radio image from the GLEAM survey, at 154.5 MHz centre frequency, overlaid with contours from the ASKAP 33 antenna observations. The ASKAP radio contours start at $150 \text{ mJy beam}^{-1}$ and increase by $\sqrt{2}$ to $900 \text{ mJy beam}^{-1}$.

the 2019 ASKAP 33 antenna observations; see Section 3.1.2. The **GLEAM** survey used the Murchison Wide Field Array radio telescope, which ran from August 2013 to June 2014.

Data used in this thesis was from the 139–170 MHz and 170–231 MHz frequency bands. The central frequency of each of these was 155 MHz and 200 MHz respectively. The images used here were downloaded from the **GLEAM Postage Stamp Service**³⁷. Only the image from the 170–231 MHz bandpass is shown here.

1.8.4.2 MWA Phase II Radio

Figure 1.31 shows an image of Abell S1136 from the GaLactic and Extragalactic All-sky MWA eXtended survey (**GLEAM-X**)³⁸ survey. Contours are from the

³⁷http://mwa-web.icrar.org/gleam_postage/q/form

³⁸<http://www.mwatelescope.org/gleam-x>

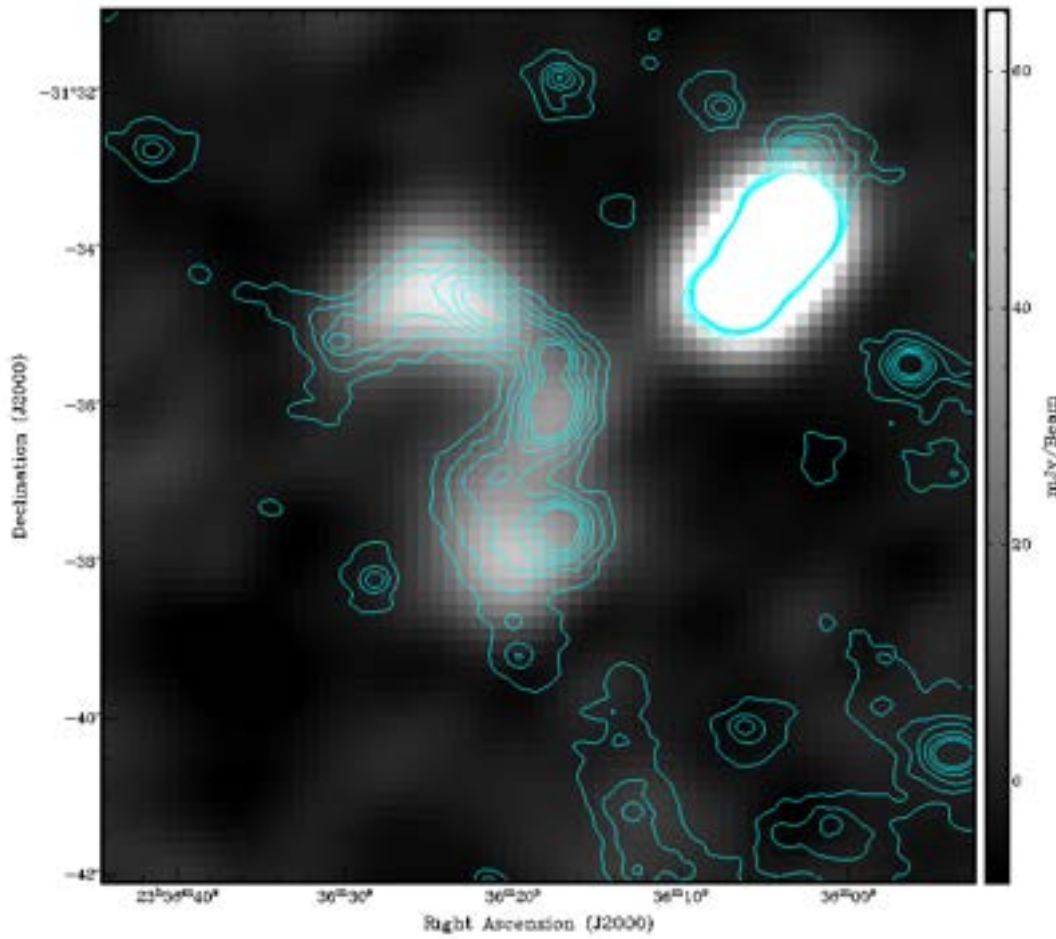


Figure 1.31: MWA Phase II radio image from the GLEAM-X survey, at 215 MHz centre frequency, overlaid with contours from the ASKAP 33 antenna observations. The ASKAP radio contours start at $150 \text{ mJy beam}^{-1}$ and increase by $\sqrt{2}$ to $900 \text{ mJy beam}^{-1}$.

`robust = +2.0` image produced from the 2019 ASKAP 33 antenna observations; see Section 3.1.2. . The **GLEAM-X** survey began in January 2018 and still being observed and processed. **GLEAM-X** uses the Phase II Murchison Wide Field Array radio telescope (Wayth et al., 2018).

This data was kindly shared by Stefan Duchesne, who is using this in his PhD research (in prep). Stefan is also a collaborator on the draft paper in Appendix B.1. Data used in this thesis was from the C169, C145, and C121 frequency bands. These bands have a central frequency of 215 MHz, 185 MHz, and 154 MHz respectively, and were chosen to match the frequency bands of the images in Section 1.8.4. Only the C169 image is shown here.

1.8.5 XMM-Newton X-ray

Figure 1.32 shows an RGB image of Abell S1136 from the extremely expanded HIghest X-ray FLUx Galaxy Cluster Sample (eeHIFLUGCS) survey (Reiprich, 2017), taken using the XMM-Newton X-ray telescope³⁹. Contours are from the robust = +2.0 image produced from the 2019 ASKAP 33 antenna observations; see Section 3.1.2. .

The images here are with the “medium” filter. The XMM-Newton X-ray telescope operates over the 0.1-15 keV range, with energy resolution at 6.5keV of $E / dE \sim 50$. The X-ray observations were on 27 November 2015. Images were downloaded from the XMM-Newton Science Archive ⁴⁰. More information on the XMM-Newton instrumentation can be found at https://heasarc.gsfc.nasa.gov/docs/xmm/xmmhp_inst.html.

³⁹<https://www.cosmos.esa.int/web/xmm-newton/home>

⁴⁰<http://nxsa.esac.esa.int/nxsa-web/#home>

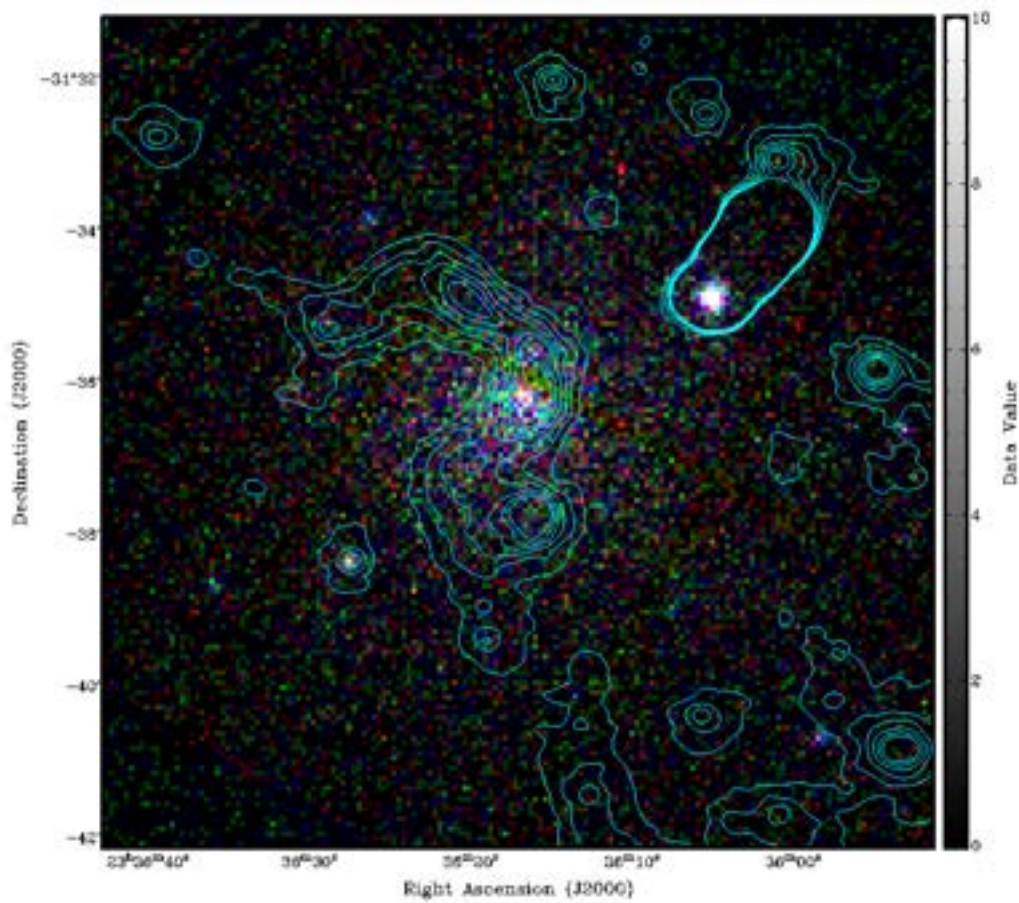


Figure 1.32: XMM-Newton X-ray telescope RGB image, overlaid with contours from the ASKAP 33 antenna observations. RGB colours are red = Epic MOS 1 CCD, green = Epic MOS 2 CCD, blue = Epic PN CCD. The ASKAP radio contours start at $150 \text{ mJy beam}^{-1}$ and increase by $\sqrt{2}$ to $900 \text{ mJy beam}^{-1}$. Abell S1136 BCG can be seen in the centre.

1.9 Research Question

Until recent years, radio observations of galaxy clusters have failed to show prominent sub-structure in the diffuse radio emission. With new generation telescopes being able to low surface brightness diffuse radio emission at sub-GHz frequencies, we are now seeing sub-structure in the diffuse radio emission from galaxy clusters. As discussed further in this thesis, observations of the galaxy clusters Abell 2593 (Mandal et al., 2020), Abell 2626 (Ignesti et al., 2018), MACS J0717.5+3745 (Bonafede et al., 2018), Abell 1033 (de Gasperin et al., 2017), and the chain of clusters Abell 3562 / Abell 3558 / and Abell 3556 (Venturi et al., 2017a) in the Shapley Supercluster (Shapley, 1930), show exciting discoveries of diffuse emission breaking into filamentary sub-structure when observed at low frequencies.

Previous radio observations of the Abell S1136 galaxy cluster, by Duchesne et al. (2017), detected a low frequency diffuse radio halo at 168 MHz, using the Murchison Wide Field Array (Tingay et al., 2013).

This thesis concentrates on observations of the Abell S1136 galaxy cluster conducted with the Australian Square Kilometre Array Pathfinder at \sim 865 MHz. These observations were part of the Early Science Program of the EMU survey (Norris et al., 2011); a wide-field, radio continuum survey, planned for the Australian Square Kilometre Array Pathfinder (ASKAP) (Norris et al., 2011).

The goals for this research are multi-part:

1. As mentioned above, the Abell S1136 galaxy cluster is known to have a radio halo in the diffuse emission, when observed at low frequencies (Duchesne et al., 2017). Similar to the other recent discoveries referenced above: Does the diffuse radio emission associated with Abell S1136 “break up” into “filamentary” sub-structure when observed at the lower frequency, and higher sensitivity, of the ASKAP.
2. If the diffuse emission does break up into “filaments”, is it possible to define the filamentary sub-structure within the current models? For this I have used a taxonomy from two sources: Kempner et al. (2004) and Feretti et al. (2012).

The findings in this thesis aim to provide a further understanding of galaxy cluster radio emission. This will help us better understand the physics of these newly discovered filamentary sub-structures, enhancing

the opportunity to gain knowledge of diffuse emission mechanisms of galaxy clusters in the radio regime.

Chapter 2

Data and Observations

This thesis presents observations of Abell S1136, which were made using the **ASKAP** telescope, as part of the Early Science Program of the **EMU** survey (Norris et al., 2011). The observations themselves were actioned by the **ASKAP** processing team. However, once the data had passed through the ingest pipeline and into the Pawsey Supercomputing Centre (**PAWSEY**), all further data reduction and analysis were performed by me. I would also like to acknowledge that with regards to the work in this chapter, I did receive assistance from Matthew Whiting and Andrew O'Brien on the functions and uses of specific parameters in the pipeline. Their assistance was invaluable in helping me understand the ASKAPsoft data reduction pipeline and its subtleties, enabling me to produce images worthy of publication.

2.1 The Australian Square Kilometre Array Pathfinder (ASKAP)

The **ASKAP** telescope is an array of 36×12 -metre radio antennas situated at the **MRO** in Western Australia. The antennas are arranged in such a way that 32 of the antennas are within a diameter of 2.3km, with the remaining four antennas located outside this, giving baselines up to 6km in length if required. The observations detailed below were while the telescope was in the commissioning phase, giving one observation with 16 antennas and one observation with 33 antennas, as described in Sections 2.1.1 and 2.1.2, with previously mentioned maximum baselines of 2.3km and 6km respectively. Figure 2.1 shows the locations of the antennas used in the observations of Abell S1136.

Each of the 36 antennas of the array is equipped with a Phased Array

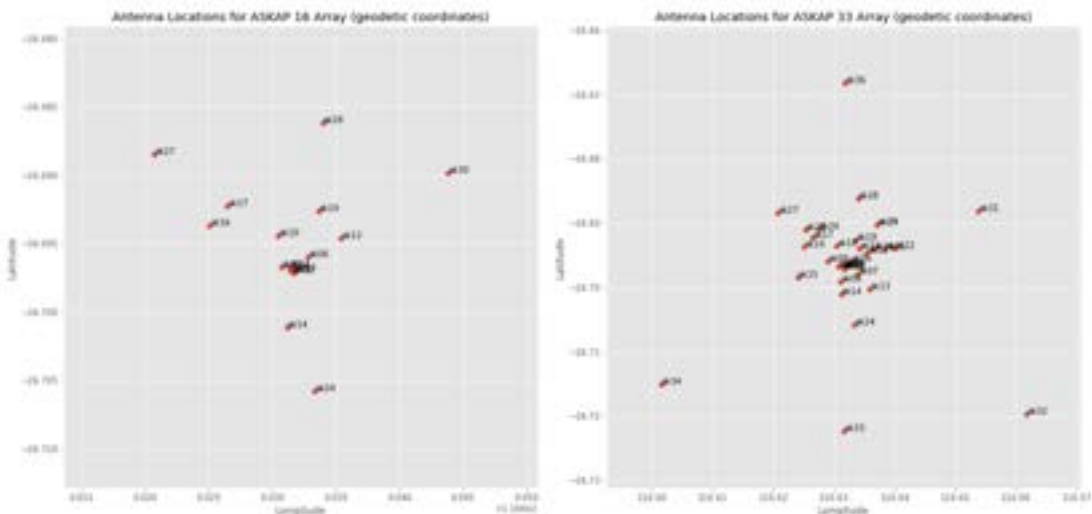


Figure 2.1: Locations of the antennas used in the 2017 and 2019 observations of Abell S1136 with the [ASKAP](#). The left hand side shows the locations of the 16 antennas used in 2017. The right hand side shows the locations of the 33 antennas used in the 2019 observations.

Feed ([PAF](#)) ([Heywood et al., 2016](#)), with each [PAF](#) having 94 dual-polarisation pixels (188 individual receivers), which allows for the forming of beams in a variety of configurations. The fully commissioned telescope is capable of observing over a frequency band of 700–1800 MHz, at an instantaneous bandwidth of 288 MHz. The telescope offers a wide Field of View ([FOV](#)) of 30 deg² of the sky in a single pointing.

The telescope is now in the final stages of commissioning, with the successful completion of the EMU Pilot Survey. The combination of Early Science observations and EMU Pilot observations with the [ASKAP](#) has shown the excellent low-surface brightness sensitivity of the telescope, with the EMU Pilot survey providing a catalogue of $\sim 200,000$ sources at a sensitivity between $\sim 25\text{--}35 \mu\text{Jy beam}^{-1}\text{rms}$ and a resolution of ~ 14 arcseconds; providing confidence we will have the ability to detect many more galaxies than current radio telescopes.

Two observations of Abell S1136 were made with the [ASKAP](#). The first observation was with an array of 16 antennas, and the second observation was with 33 antennas. Table 2.1 shows the observation details. The bandwidth of each observation was the full instantaneous bandwidth available at the time. The Ingest Mode determined the channels set at the [PAWSEY](#) Supercomputing Centre ¹; for the observations of Abell S1136 this was set to “continuum mode”, which averages 54 channels into one, and writes one measurement set per beam ([Mcconnell et al., 2019](#)). The

¹<https://pawsey.org.au/>

Table 2.1: Summary Details of the 2017 and 2019 Observations of Abell S1136 with the **ASKAP**

	ASKAP 16	ASKAP 33
Date	Dec-17	Jul-19
Interleave A		
RA (J2000)	23:36:17.0	23:36:17.0
DEC (J2000)	-31:36:37.00	-31:36:37.00
Interleave B		
RA (J2000)	23:38:24.4	no interleaving
DEC (J2000)	-32:03:33.08	no interleaving
Antennas	16	33
Antenna Numbers	1, 2, 3, 4, 5, 6 10, 12, 14, 16, 17 19, 24, 27, 28, 30	1, 2, 3, 4, 5, 6, 7, 8 9, 11, 12, 13, 14, 15, 16 17, 18, 19, 20, 21, 22 24, 25, 26, 27, 28, 29 31, 32, 33, 34, 35, 36
Centre Freq. (MHz)	864.5	864.5
Bandwidth (MHz)	240	240
Channels	240	240
RMS (μ Jy beam $^{-1}$)	\sim 596	\sim 40
Beams	36	36
Resolution (arcsec)	48.4×36.3	12.6×10.1
Position Angle (degrees)	85.5	82.4
Footprint	square 6x6	closepack 36
Duration (hr)	10.05	10.05

MIRIAD (Sault et al., 1995) task SIGEST (version 14-Apr-1999) was used for the rms calculations, with the region set to 66 percent.

Data and image processing used the ASKAPsoft software pipeline. For more information on the **ASKAP** design, the software pipeline, or other technical details including beam-forming parameters, the reader is directed to McConnell et al. (2019) and Australian Square Kilometre Array Pathfinder (ASKAP) Telescope.

As mentioned above, and detailed below in Sections 2.1.1 and 2.1.2, each antenna of the **ASKAP** uses a PAF which gives each antenna the ability to have the beams formed in a various patterns, or “footprints”, depending on the requirements of the observation. For the observations of Abell S1136, the beams were formed into footprints containing 36 beams, configured in a “square_6x6” and “closepack36” arrangement. Figure 2.2 shows each of these configurations, and should be used as a reference when reading the sections below. Each beam is formed from the weighted data from several pixels, and the weights are applied to the pixels,

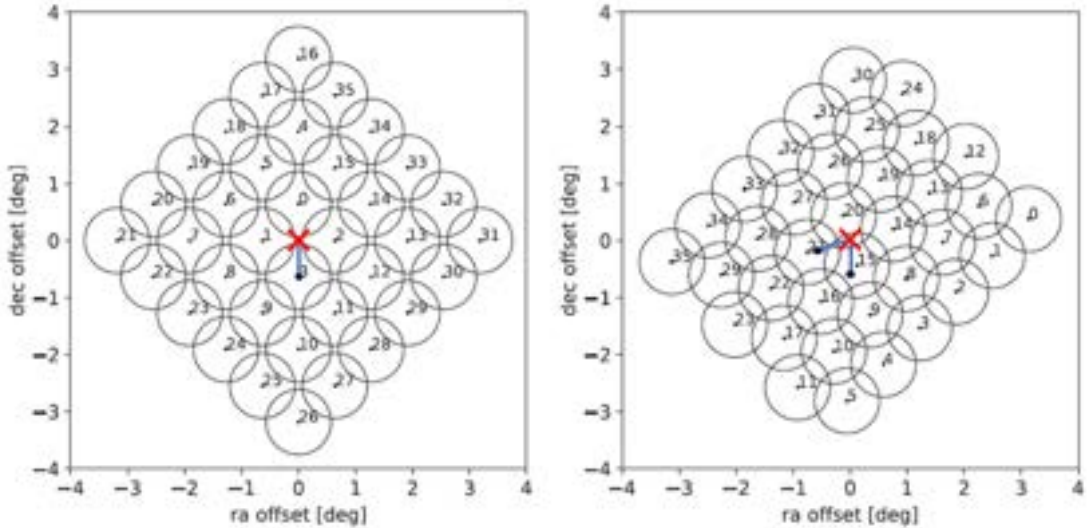


Figure 2.2: Diagram showing the **PAF** beam footprints of the **ASKAP** "square_6x6" **PAF** configuration (left side) and the "closepack36" **PAF** configuration (right side). Both configurations are at 0.90 degrees pitch (the distance between the beam centres), and a position angle of zero degrees. Table 2.1 shows the position angle for the observations discussed in this thesis. The footprint centre is marked by the red cross. The lines and circles extending from the centre of the footprint indicate the positions of the interleaving required for full tile coverage. The scales shown here are in degrees, celestial north is to the top of both diagrams.

not the beams. Initially, the weights for the individual pixels in the footprint are calculated by observing the sun, with each pixel "weighted" up or down to achieve the best signal-to-noise ratio.

2.1.1 Observations with 16 Antennas

The first observation of Abell S1136 with the **ASKAP** was in December 2017, using 16 antennas. The longest baseline was 2.30 km. The observation had a bandwidth of 240 MHz at a centre frequency of 864.5 MHz. The 36 beams in the **PAF** were formed into a "square_6x6" footprint, with a pitch of 0.90 degrees, and 45-degree rotation. The pitch defines the distance between the beam centres, while the rotation will turn the **PAF** so that the corners of the footprint are on a North / South / East / West orientation, and align the footprint with celestial coordinates. It was found by [McConnell \(2017\)](#) that 0.90 degrees gives optimal survey speed and beam-to-beam noise correlation. The resulting synthesised beam was 48.4 arcsec by 36.3 arcsec at 864.5 MHz. The observation was a single field with 10 hours on source. Figure 2.2 shows the layout of the square_6x6 beam pattern.

The spacing of beam positions across the imaged region should comply

with the Nyquist sampling criterion (Cornwell, 1988) in order to be as sensitive as possible to the diffuse emission. To achieve this, the 2017 observation with 16 antennas is then described by two pointings, an 'A' and a 'B'. The target is observed first on pointing 'A', with the interleaving offset used to observe pointing 'B'. The interleaved pointing is positioned such that the beams are centred on the mid-points between the beams of the A pointing, to smooth out the primary beam response.

1934-638 was used as the primary calibrator, to provide bandpass and gain calibration for imaging.

2.1.2 Observations with 33 Antennas

Because of the limitations inherent in the 16-antenna images, Abell S1136 was observed again in July 2019 with more antennas, higher sensitivity, improved software, and additional longer baselines, allowing us to see more clearly the extended emission from the cluster.

This second observation used 33 antennas (of a possible 36). The longest baseline was 6 km. The observation had the same bandwidth and centre frequency as the 2017 observation. For this observation, the beam configuration was different: the 36 PAF beams were formed into a “closepack36” footprint, and there was no interleaving. As in the 2017 observation, the beams were set at a pitch of 0.90 degrees, with a 45-degree rotation. The closepack36 configuration, as shown in Figure 2.2 puts the beams into a tighter lattice, and for this observation it was decided not to run any interleaving. Other survey teams had found that with this “closepack36” footprint the interleaving does not give a more significant reduction in rms across the field. The resulting synthesised beam was 12.6 arcsec by 10.1 arcsec at 864.5 MHz. The observation was a single field with 10 hours on source. As with the 2017 observations, PKS 1934-638 was used as the primary calibrator for bandpass and gain calibration.

Figures 2.1 and 2.2 show the antenna locations and beam footprints for the 2017 ASKAP 16 and 2019 ASKAP 33 observations.

2.2 ASKAP Data Reduction and Imaging

Data for both observations was processed in the ASKAPsoft pipeline using the parameters shown in Tables A.1 and A.2 in Appendix A. Both of these observations were at a bandwidth of 240MHz, with 12960 spectral-line channels. Once the data was on PAWSEY, the data reduction and imaging were achieved using “ASKAPsoft”, the ASKAP Early Science Pipeline, the flowchart of the pipeline is shown in Figure 2.3.

I would like to note that during the time I have been producing this work, the 16 antenna and 33 antenna data reduction used different versions of the ASKAPsoft pipeline, as the pipeline has undergone various upgrades in order to support the telescope commissioning. Although the functionality of the pipeline has changed during this time, with features been added or altered, for this thesis and the work herein, the functionality of the upgrades in the pipeline made no difference to the output here.

For each of the observations, images were produced with various robustness and restoring beam size, to try and coax out the diffuse emission. For both observations, the data was averaged down from 12960 spectral channels into 240×1 MHz channels to help minimise compute time. The data was gridded using multi-frequency synthesis, and then de-convolved using multi-scale clean. Source extraction and cataloguing was performed within the ASKAPsoft pipeline using the source extractor Selavy (Whiting and Humphreys, 2012).

As described in Section 2.1, the sensitivity of each observation was measured using the Miriad task SIGEST. Typical sensitivities for the 16 antenna observations are $\sim 600 \mu\text{Jy beam}^{-1}$, and the 33 antenna observations are $\sim 40 \mu\text{Jy beam}^{-1}$.

This substantial improvement between the two observations is due to (a) the larger number of antennas used in the 2019 observations, and (b) improvements in the ASKAP calibration and processing software.

Two images were produced for the 16 antenna observations of Abell S1136, using traditional robustness weighting: the main image at robust = -0.5, and a second image at robust = +2.0. These images are shown in Section 3.1, and discussed in Section 4.

Four images were produced for the 33 antenna observations of Abell S1136, using a combination of traditional robustness weighting, and gaussian tapering using Weiner filter preconditioning: the first two images

²<https://confluence.csiro.au/display/askapsst/Early+Science+Pipeline>

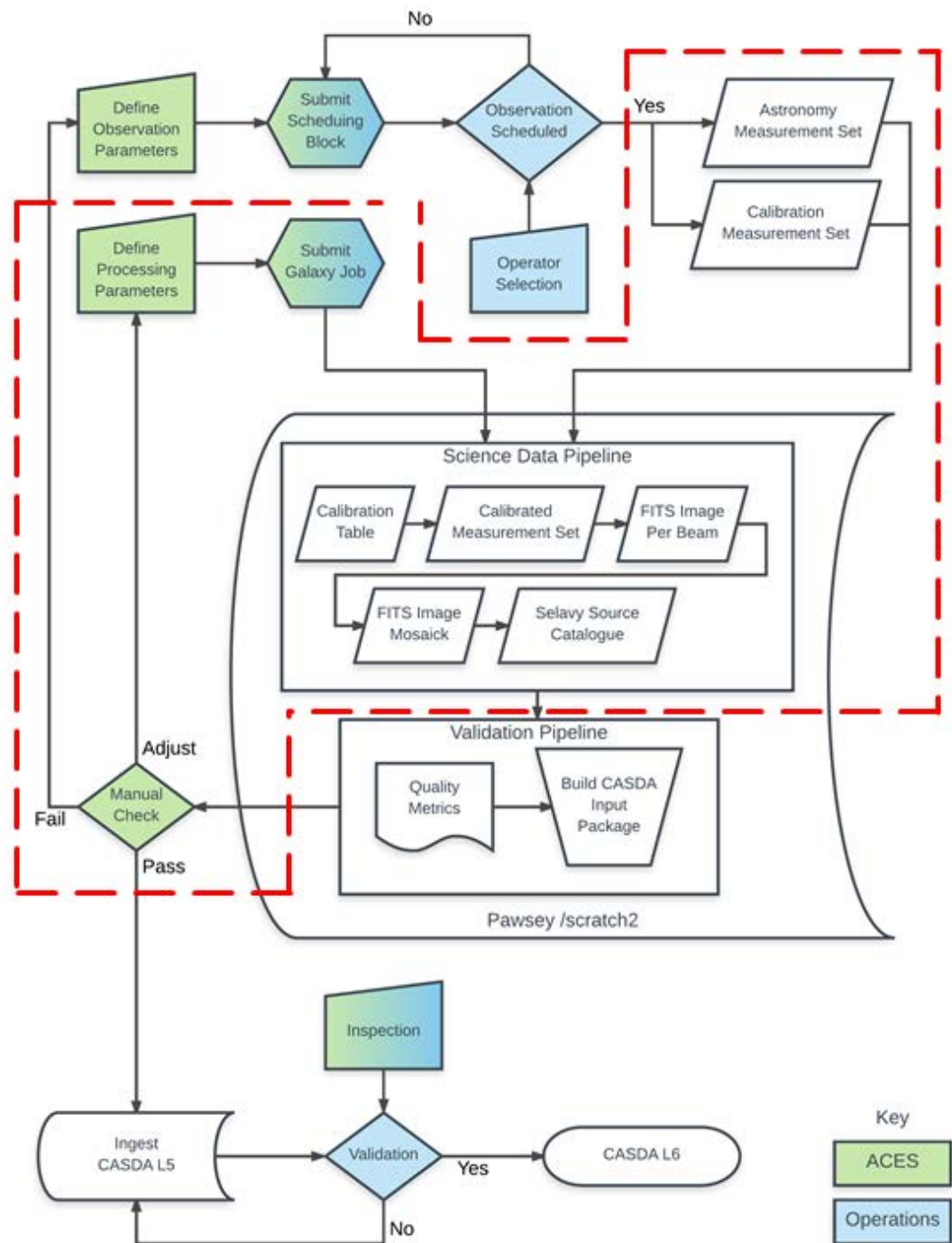


Figure 2.3: Diagram showing the ASKAP Early Science Pipeline. The processes inside the red dashed border were the ones used by myself in the data reduction and imaging process. (Credit: CSIRO²)

were produced separately at `robust` = -0.5 and `robust` = $+2.0$. In order to optimise for the very faint diffuse emission, a further two images were produced in the same pipeline run, one at `robust` = 0 , and the remaining image is the alternative (“alt”) image, tapered to a 30-arcsec resolution. These images are shown in Section 3.1, and discussed in Section 4.

Chapter 3

Results

Figure 3.8, from the 33 antenna array observations, has been reproduced here. This figure is marked with three red circles, aligned mostly vertically, to show the location of the three dominant AGN from which the emission seems to be emanating in Abell S1136. The middle red circle is the BCG of Abell S1136, identified as ESO 470-20 ([Lauberts and Valentijn, 1989](#)).

Figure 3.1 should be used as a reference to illustrate the results in this section.

3.1 Images

3.1.1 ASKAP 16 Antenna Observations

Visible in Figures 3.2 and 3.3, is the diffuse emission of Abell S1136 at robust = -0.5, presenting as possible filamentary structure. This filamentary structure extends from the three bright sources located in the central vertical line. These possible filaments extend to the north-east of the source located above the BCG, to the south-east of the central source (the BCG, and to the south-east of the source located below the BCG. Figure 3.4 shows the path I suspect these filaments take.

Visible in Figures 3.5 and 3.6, is the diffuse emission of Abell S1136 at robust = +2.0. The diffuse emission of Abell S1136 appears broader than the images at robust = -0.5, with the filaments still visible although somewhat obscured. Figure 3.7 shows the path I suspect these filaments take.

All the images show the strong radio source PKS 2333-318, appearing as a large blob to the north-west of Abell S1136 at 23h36m04.96s -31d34m51.3s

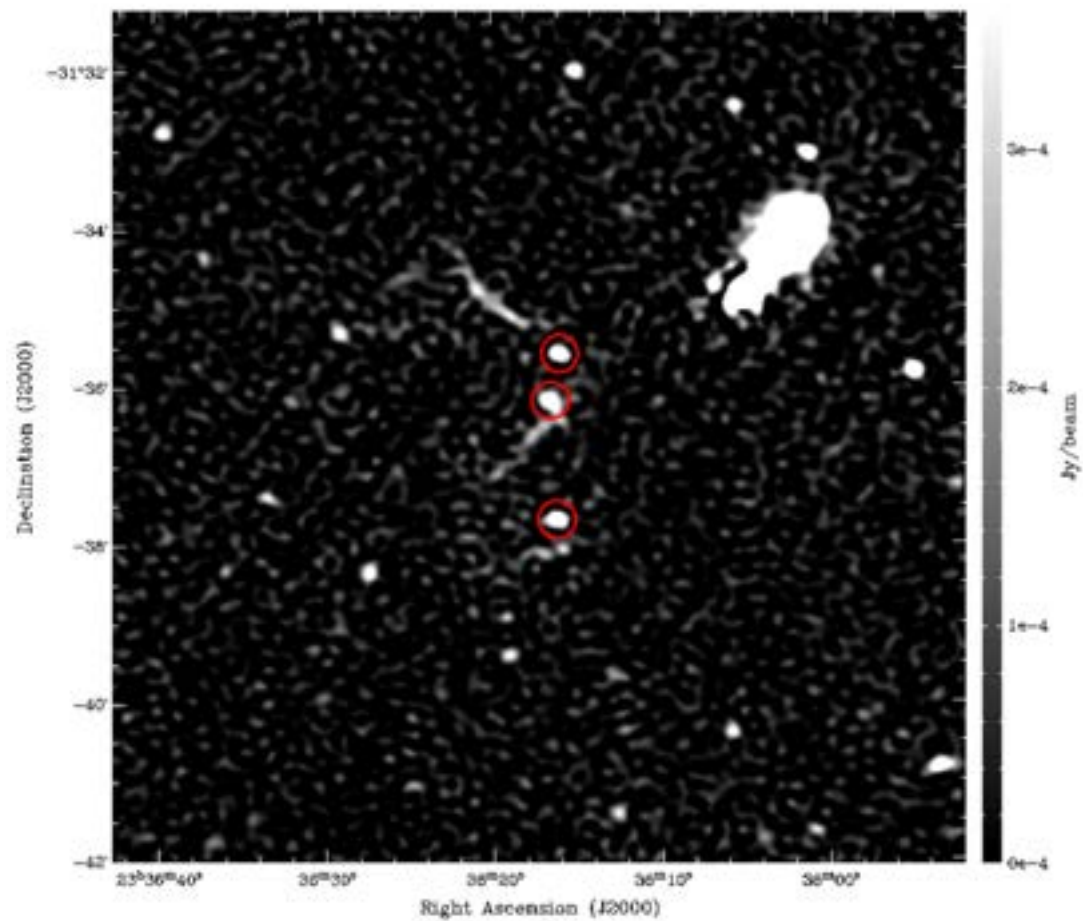


Figure 3.1: Figure 3.8 from the 33 antenna array observations, reproduced here to help with the analysis of the results in this section. The red circles indicate the sources of interest that are associated with the northern (top), BCG (middle), and southern (lower) filaments.

PKS 2333-318 is discussed further in the results in Section 3.4.

The data from the ASKAP 16 antenna observations suffered from limited uv coverage. The contour lines on Figure 3.3 define quite well the filament extending from the upper source; however, the filaments on middle and bottom sources do not give confidence that there is the existence of a filament. I was not positive if the possible filamentary structure on these lower two sources was just noise in the image or imaging artefact. The images did, however, confirm the possible presence of diffuse structure and possible filaments in Abell S1136. The images were considered valid; however, the ASKAP 16 antenna observations were deemed inadequate for addressing the full science goals.

The images from the 2017 observations of Abell S1136 using the ASKAP 16 antenna array, show evidence of filaments in the diffuse emission in the galaxy cluster that has been unseen in the previous radio surveys, shown in Section 1.8. This prompted further observations with the (then) recently operational 33 antenna ASKAP array.

3.1.1.1 ASKAP 16 Antenna Array, Taylor Term 0, Briggs Robustness - 0.5

Figures 3.2 and 3.3 show the diffuse structure in the radio emission from Abell S1136. Data is from the ASKAP 16 antenna array observations. These images are Taylor Term 0, at robust = -0.5. In sequence, the images show:

1. Figure 3.2 shows the radio emission of Abell S1136 with a 16 antenna array, imaged at robust = -0.5.
2. Figure 3.3 shows the same image, with contours in magenta around the radio emission of the 16 antenna observations. The contours start at $250 \mu\text{Jy beam}^{-1}$ increasing to 1 mJy beam^{-1} , in increments of $\sqrt{2}$
3. Figure 3.4 shows the possible morphology of the filamentary structure that is located within the diffuse emission.

In all three images we also see in the north-west the bright radio emission from the well-known radio galaxy PKS 2333-318¹

¹https://ned.ipac.caltech.edu/byname?objname=pk2333-318&hconst=67.8&omegam=0.308&omegav=0.692&wmap=4&corr_z=1

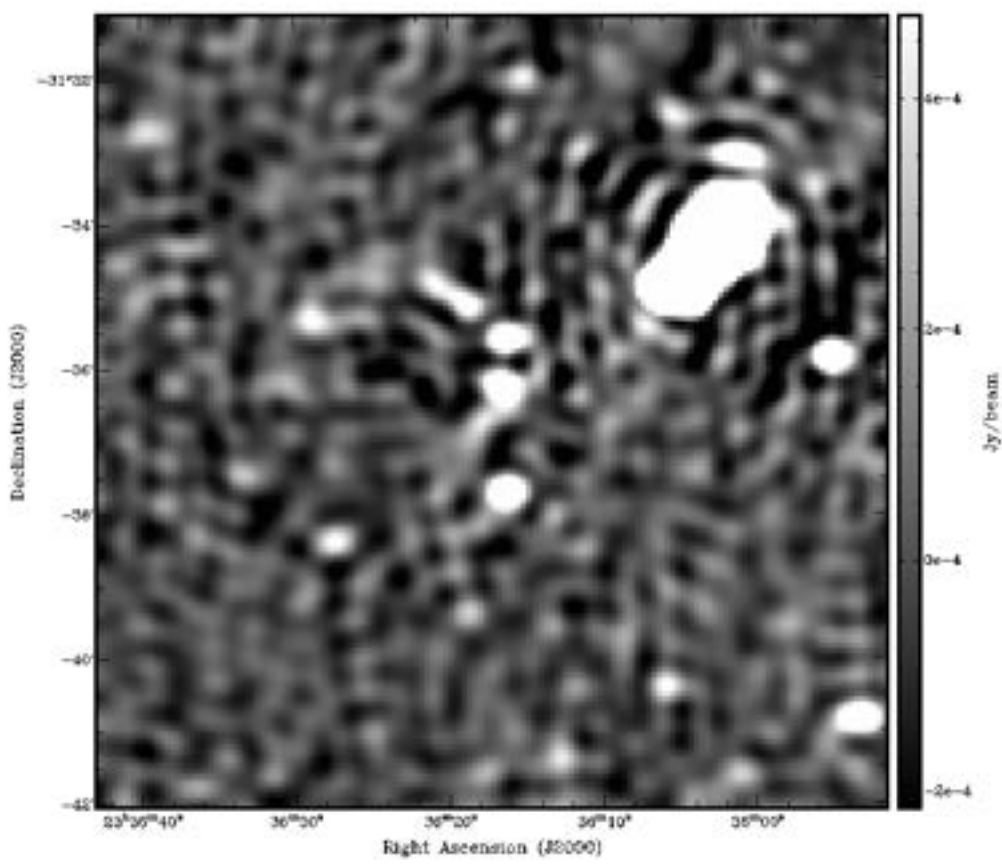


Figure 3.2: ASKAP 16, robust = -0.5 , Taylor Term 0, no contours

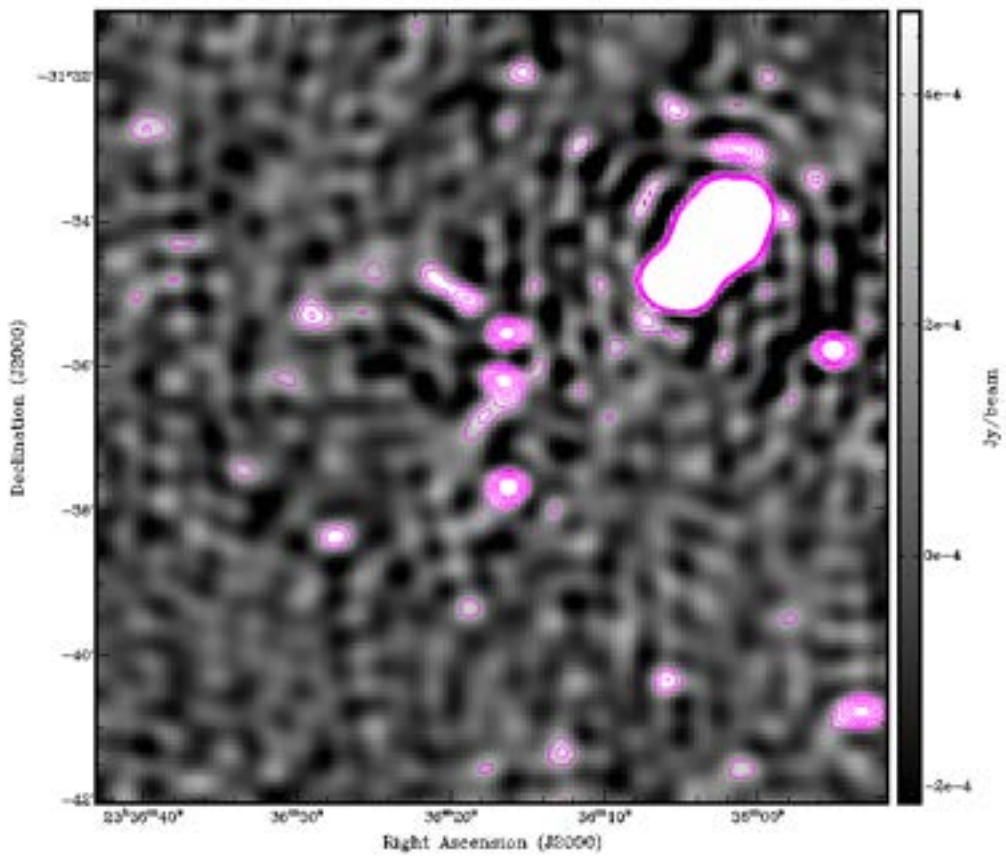


Figure 3.3: ASKAP 16, robust = -0.5 , Taylor Term 0, with ASKAP 16 contours in magenta starting at $250 \mu\text{Jy beam}^{-1}$ increasing to 1mJy beam^{-1} by $\sqrt{2}$

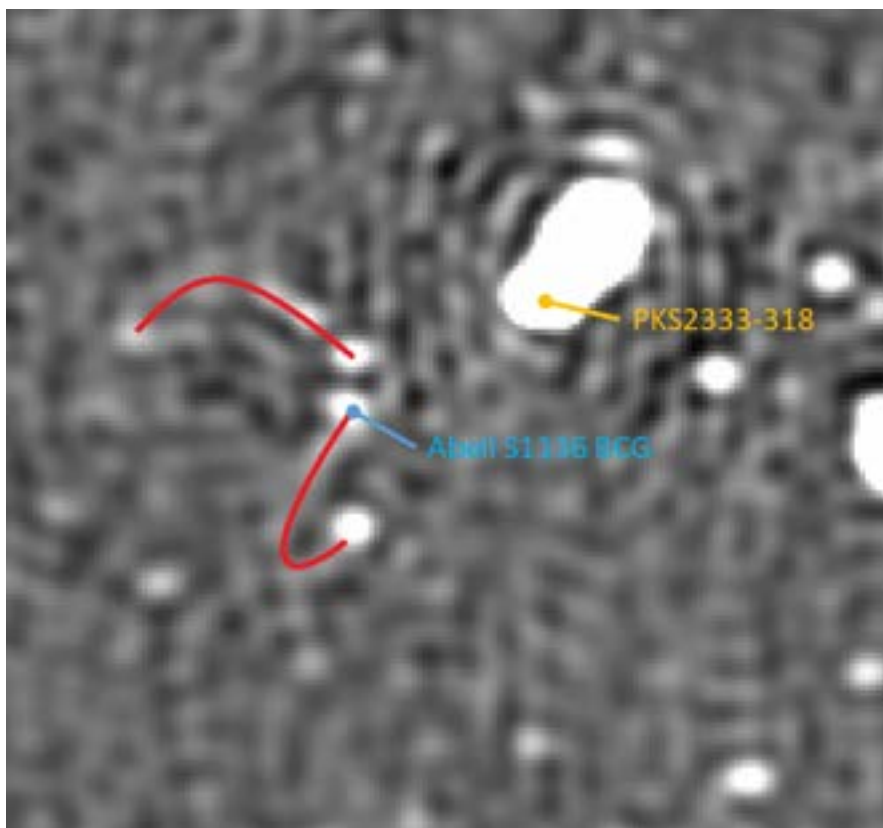


Figure 3.4: Abell S1136 diffuse structure with ASKAP 16 antenna, robust = -0.5, Taylor Term 0. The red lines show the possible connections of the filaments and the AGN in Abell S1136.

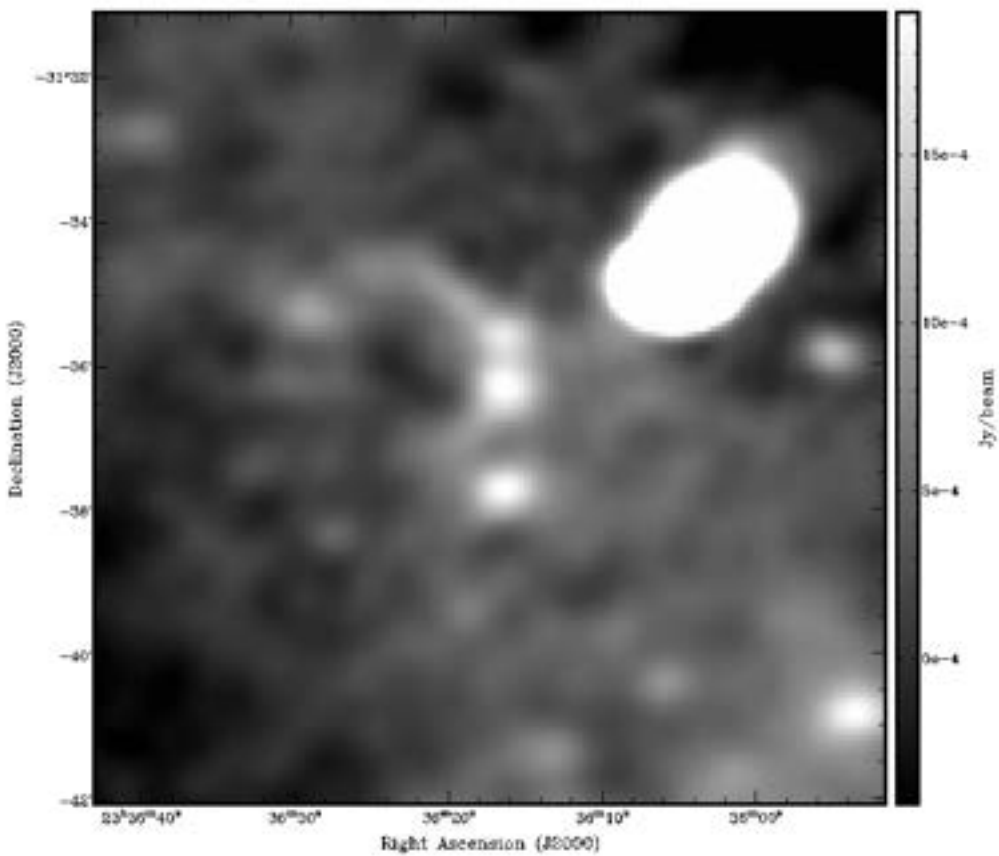


Figure 3.5: ASKAP 16, robust = +2.0, Taylor Term 0, no contours

3.1.1.2 ASKAP 16 Antenna Array, Taylor Term 0, Briggs Robustness + 2.0

Figures 3.5 and 3.6 show the diffuse structure in the radio emission from Abell S1136. Data is from the ASKAP 16 antenna array observations. These images are Taylor Term 0, at robust = +2.0. In sequence, the images show:

1. Figure 3.5 shows the radio emission of Abell S1136 with a 16 antenna array, imaged at robust = +2.0.
2. Figure 3.6 shows the same image, with contours in red around the radio emission of the 16 antenna observations. The contours start at $250 \mu\text{Jy beam}^{-1}$ increasing to 1 mJy beam^{-1} , in increments of $\sqrt{2}$.
3. Figure 3.7 shows the possible morphology of the filamentary structure that is located within the diffuse emission.

In all three images, we also see in the north-west the bright radio emission from catalogue source PKS 2333-318.

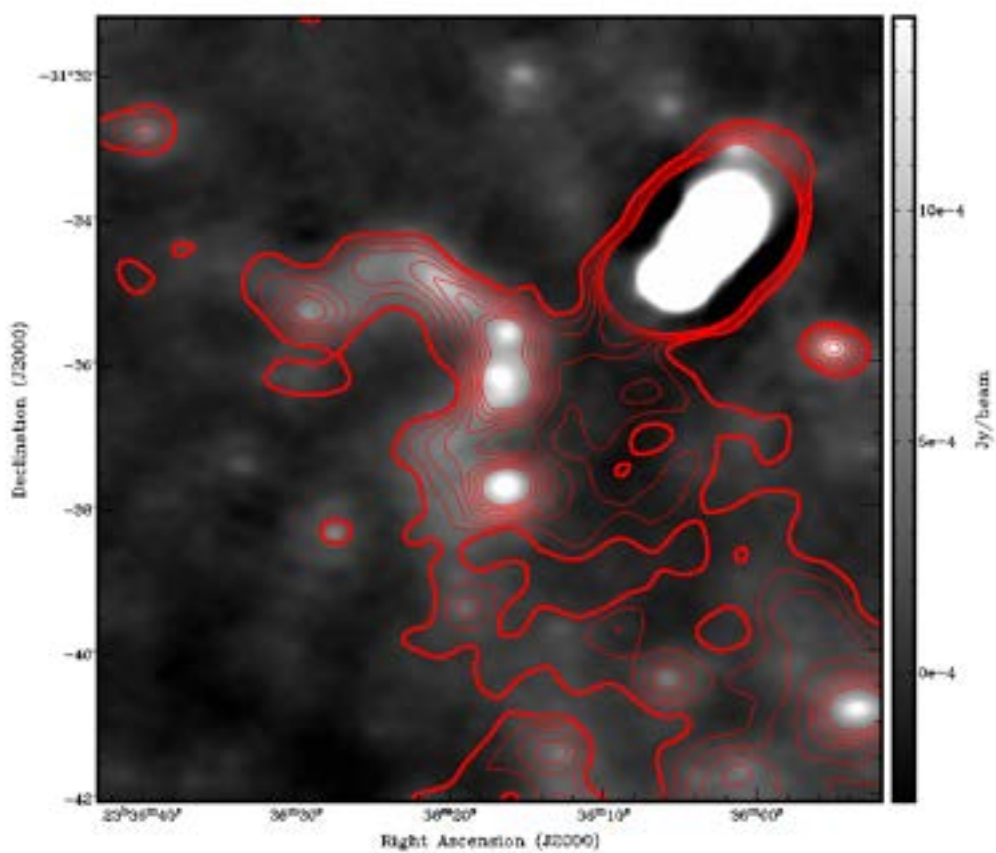


Figure 3.6: ASKAP 16, robust = +2.0, Taylor Term 0, with ASKAP 16 contours in red starting at $250 \mu\text{Jy beam}^{-1}$ increasing to 1mJy beam^{-1} by $\sqrt{2}$

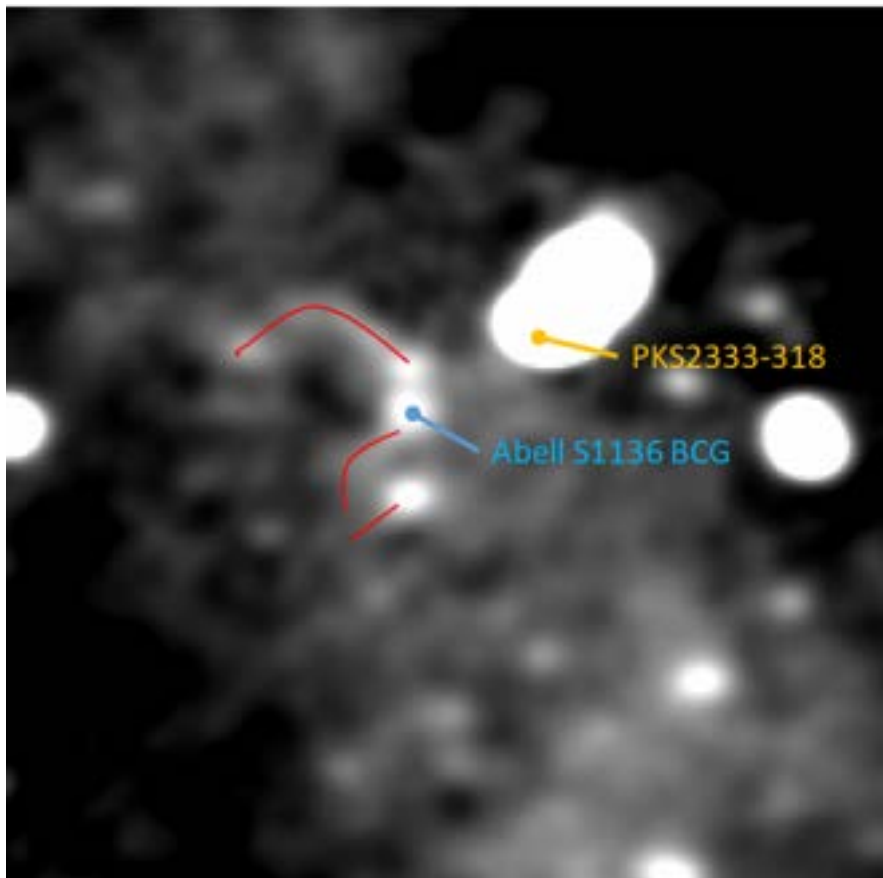


Figure 3.7: Abell S1136 diffuse structure with ASKAP 16, robust = +2.0, Taylor Term 0. The red lines show the possible connections of the filaments and the AGN in Abell S1136; note the southern filament in this is not joined to the southern source, as shown in Figure 3.4 - this is due to the lower resolution at robust = +2.0.

3.1.2 ASKAP 33 Antenna Observations

As with the results in the preceding section, this section refers to Figure 3.1. This figure is from the 33 antenna array observations. It has been marked with three red circles, aligned mostly vertically, to show the location of the three dominant AGN from which the emission seems to be emanating in Abell S1136. The middle red circle is the BCG of Abell S1136, identified as ESO 470-20 (Lauberts and Valentijn, 1989).

Data from the ASKAP 33 antenna observation showed excellent results, with the observations using 33 antenna having much better uv coverage. With the higher sensitivity and resolution of the ASKAP 33 antenna array, when observed at a centre frequency of 864.5 MHz, the filamentary structures in the diffuse emission of Abell S1136 appear strongly in the 2019 observations. Images with the 33 antenna array were produced at robust = -0.5, robust = 0, robust = +2.0, and robust = 0 with a 30'' Gaussian taper across the beams.

When comparing with the 16 antenna images, the 33 antenna images at robust = -0.5 shown in Figures 3.8 and 3.9, and using the three AGN aligned vertically in the cluster centre, we can clearly see the elongated emission from the top source extending to the north-east; however, the emission from the middle source (the BCG) is still visible but remains questionable as to whether this is noise or imaging artefact. The emission from the bottom circled source is more evident; however, there is still a question as to its viability as a filament.

As we increase robustness and move from natural weighting (minus 0.5) to uniform weighting (positive 2.0), the images start to show more diffuse emission surrounding the filaments.

The 33 antenna images at robust = 0, shown in Figures 3.10 and 3.11, show the same prominent filament extending from the upper source to the north-east of the cluster. The filament extending south-east from the BCG appears more strongly at robust = 0, as does the structure extending horizontally underneath the lowest AGN.

The contours on the filamentary structure of Abell S1136 at robust = 0, shown in Figure 3.11, all exhibit the same flux density level of $\sim 500 \mu\text{Jy}$ at the filament mid-line, indicating the electron population is the same age.

The remaining images from the 33 antenna observations are shown in Figures 3.12, 3.13, 3.14, and 3.15. Figures 3.12 and 3.13 show

the radio emission from Abell S1136 at robust = +2.0, while Figures 3.14, and 3.15 show the radio emission from Abell S1136 at robust = 0, with a 30 arcsec Gaussian taper. All four images show clearly the extent of the diffuse emission which contains the filaments. The three bright galaxies highlighted in red circles in Figure 3.1 appear very strongly. The diffuse emission visible in these four images now presents as a reverse “S” shape. From the galaxy in the upper red circle, the emission extends in an arc over to the north-west, and appears to link to the emission then extending from the BCG to the south-east, and then looping back around to the galaxy in the lowest circle.

Figures 3.12, 3.13, 3.14, and 3.15 also show clearly the filament in the emission extending from the source in the upper red circle in Figure 3.1. The filaments in the emission extending from the BCG and the lowest circled galaxy cannot be seen.

As with the 16 antenna images, all the images from the 33 antenna observation show the strong radio source PKS 2333-318, appearing as a large blob to the north-west of Abell S1136 at 23h36m04.96s -31d34m51.3s. PKS 2333-318 is discussed further in the results in Section 3.4.

The images below are from the 2019 observations with 33 antennas, at robust = -0.5, robust = 0, robust = +2.0.0, and robust = 0 with a 30'' Gaussian taper across the beams.

3.1.2.1 ASKAP 33 Antenna Array, Taylor Term 0, Briggs Robustness -0.5

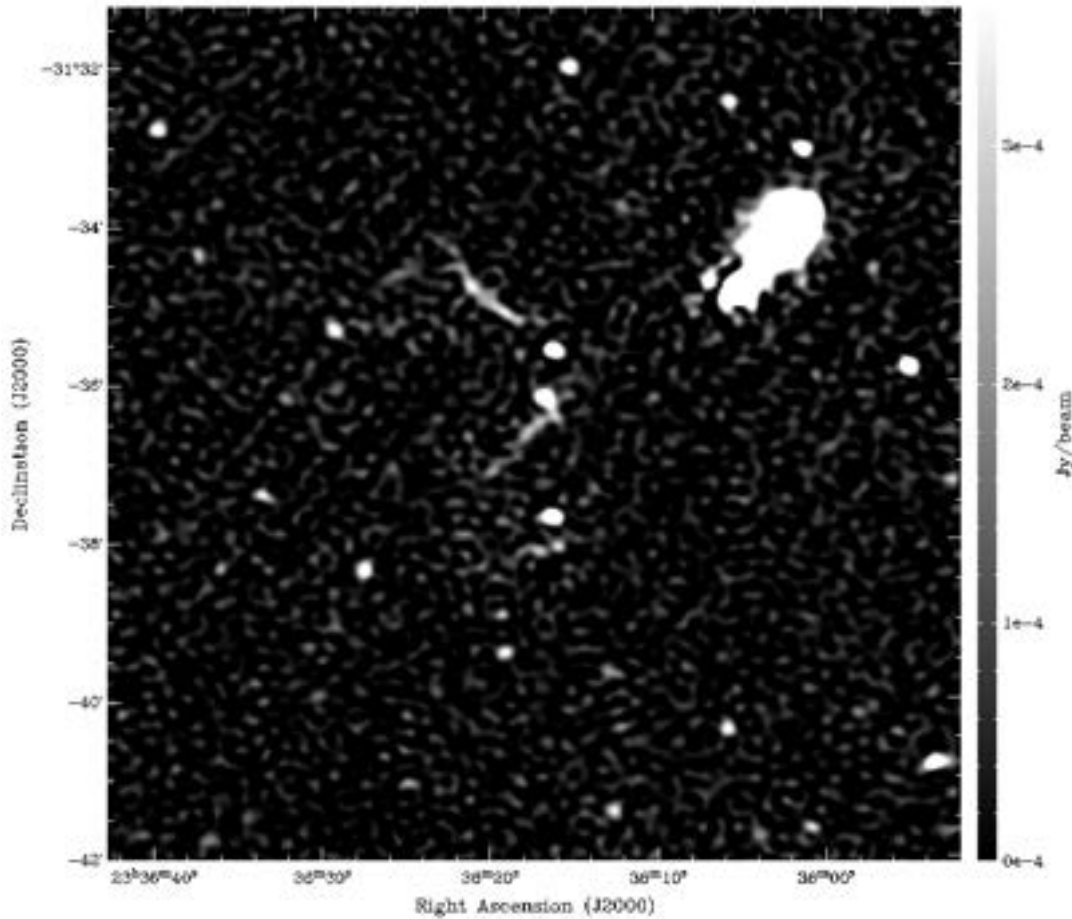


Figure 3.8: Abell S1136 diffuse structure with ASKAP 33, robust = -0.5 , Taylor Term 0, no contours.

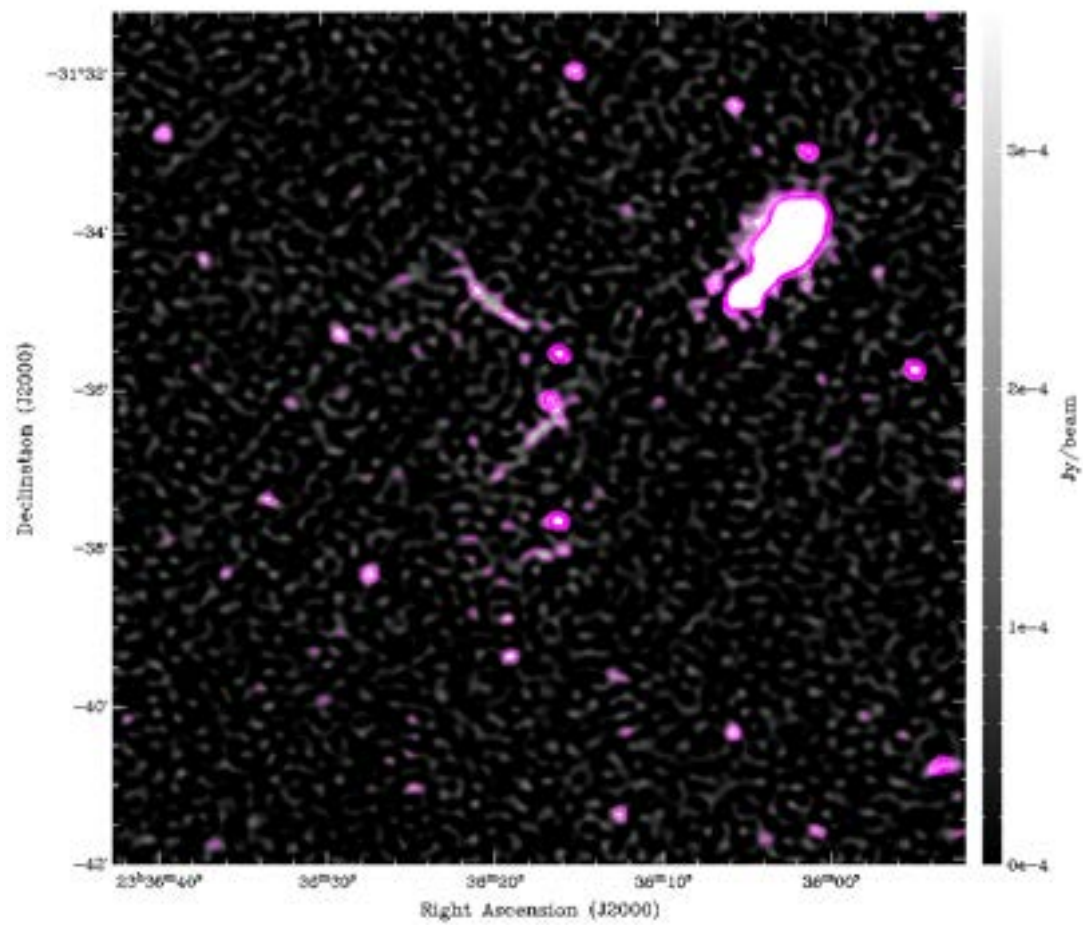


Figure 3.9: Abell S1136 diffuse structure with ASKAP 33, robust = -0.5, Taylor Term 0, contours in magenta starting at $150 \mu\text{Jy beam}^{-1}$ increasing to $900 \mu\text{Jy beam}^{-1}$, in increments of $\sqrt{2}$.

3.1.2.2 ASKAP 33 Antenna Array, Taylor Term 0, Briggs Robustness 0

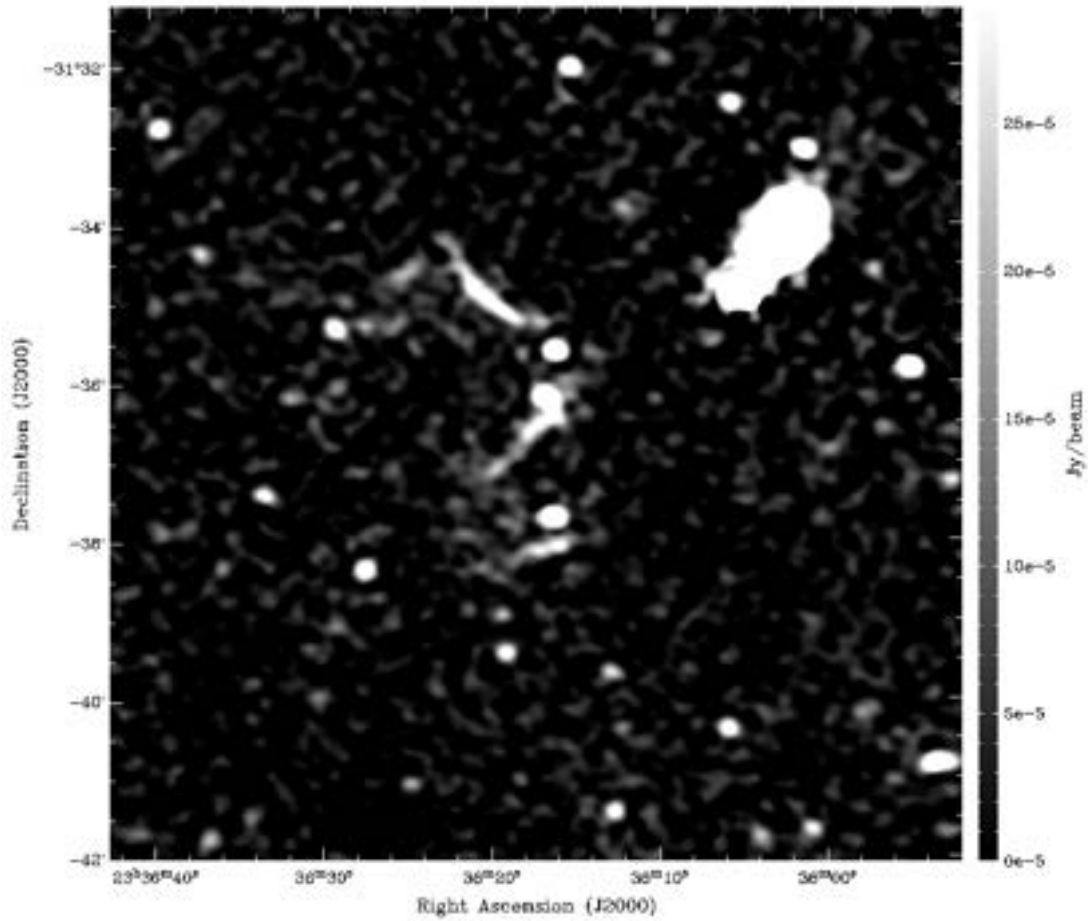


Figure 3.10: Abell S1136 diffuse structure with ASKAP 33, robust = 0, Taylor Term 0, no contours.

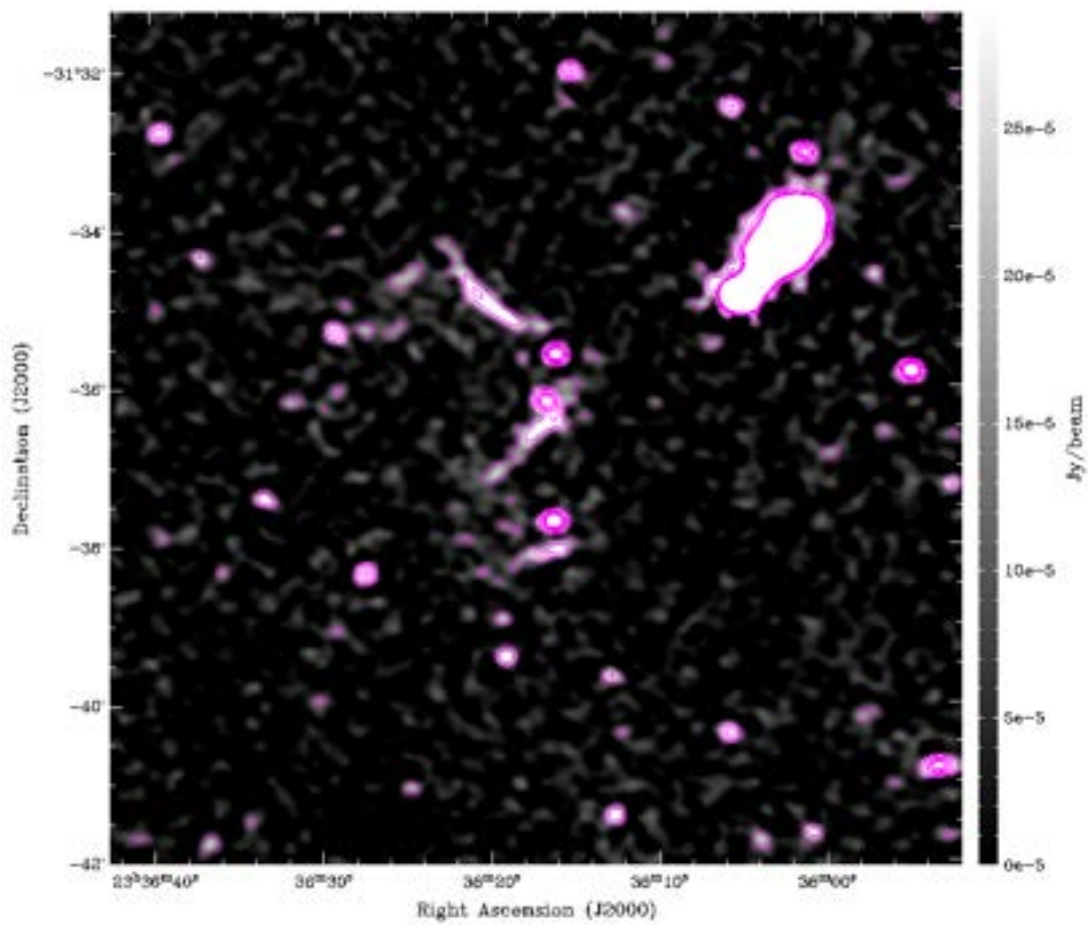


Figure 3.11: Abell S1136 diffuse structure with ASKAP 33, robust = 0, Taylor Term 0, contours in magenta starting at $150 \mu\text{Jy beam}^{-1}$ increasing to $900 \mu\text{Jy beam}^{-1}$, in increments of $\sqrt{2}$.

3.1.2.3 ASKAP 33 Antenna Array, Taylor Term 0, Briggs Robustness +2.0

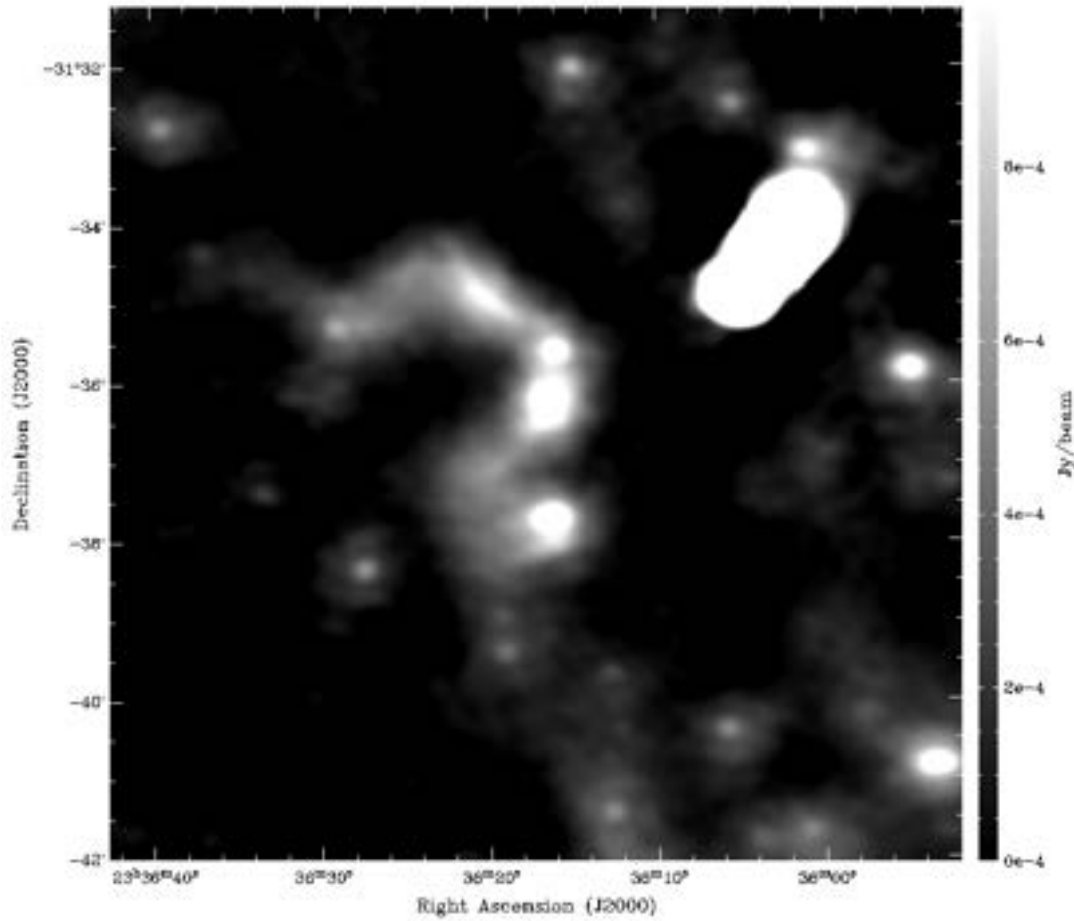


Figure 3.12: Abell S1136 diffuse structure with ASKAP 33, robust = +2.0, Taylor Term 0, no contours.

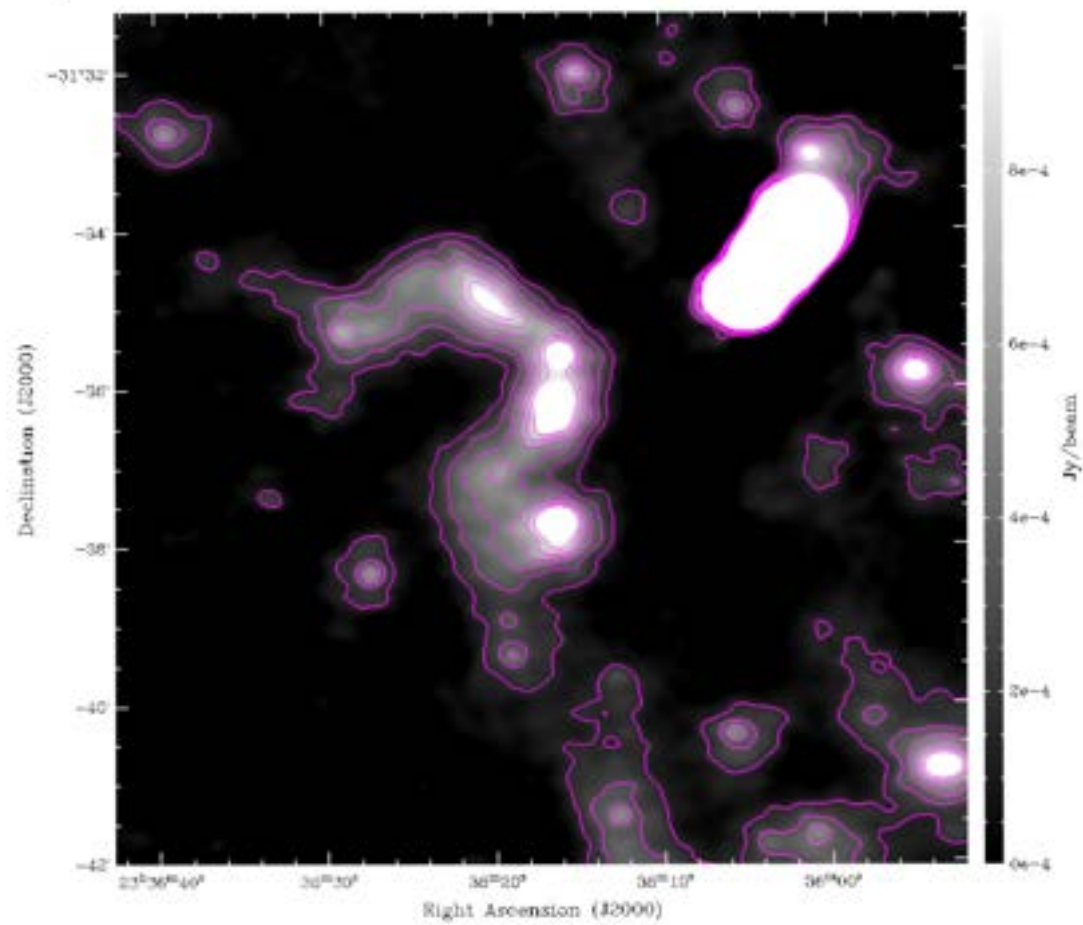


Figure 3.13: Abell S1136 diffuse structure with ASKAP 33, robust = +2.0, Taylor Term 0, contours in magenta starting at $150 \mu\text{Jy beam}^{-1}$ increasing to $900 \mu\text{Jy beam}^{-1}$, in increments of $\sqrt{2}$.

3.1.2.4 ASKAP 33 Antenna Array, Taylor Term 0, Briggs Robustness 0, 30'', Gaussian Taper

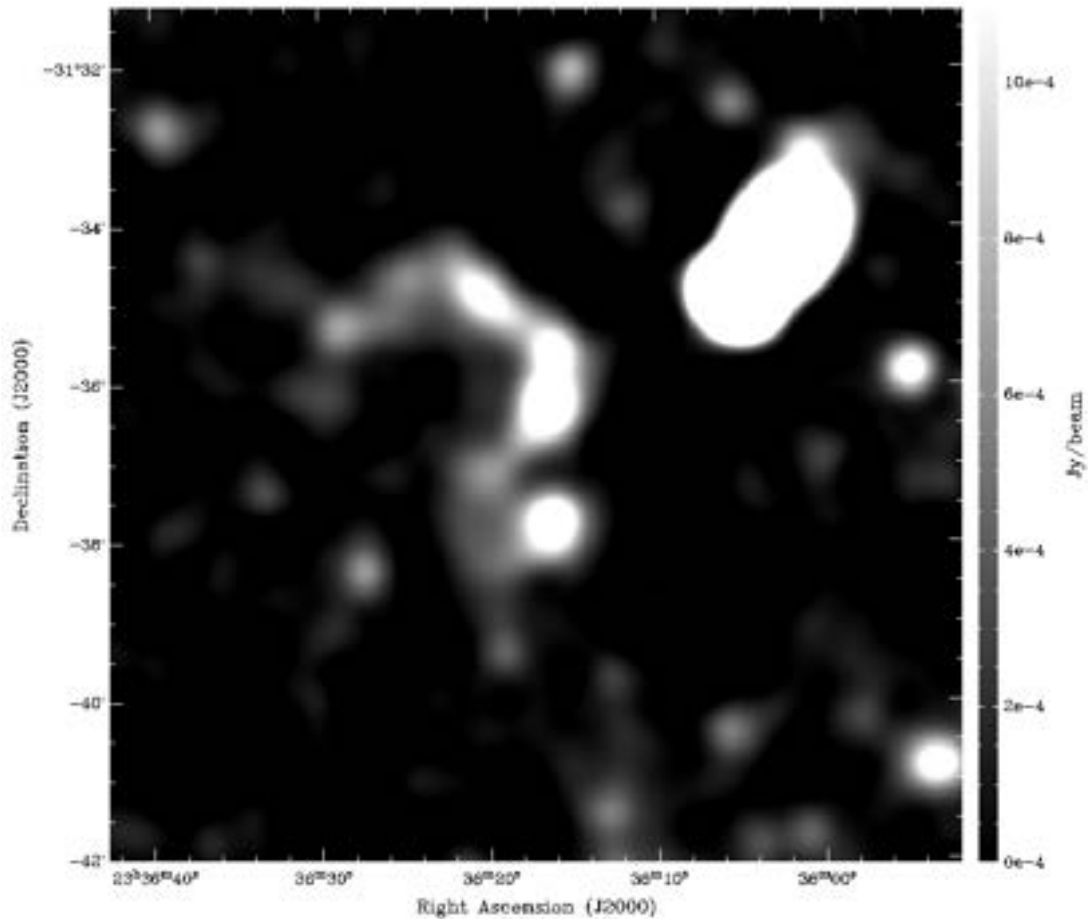


Figure 3.14: Abell S1136 diffuse structure with ASKAP 33, “alt” image at `robust = 0` with 30'' Gaussian taper, Taylor Term 0, no contours.

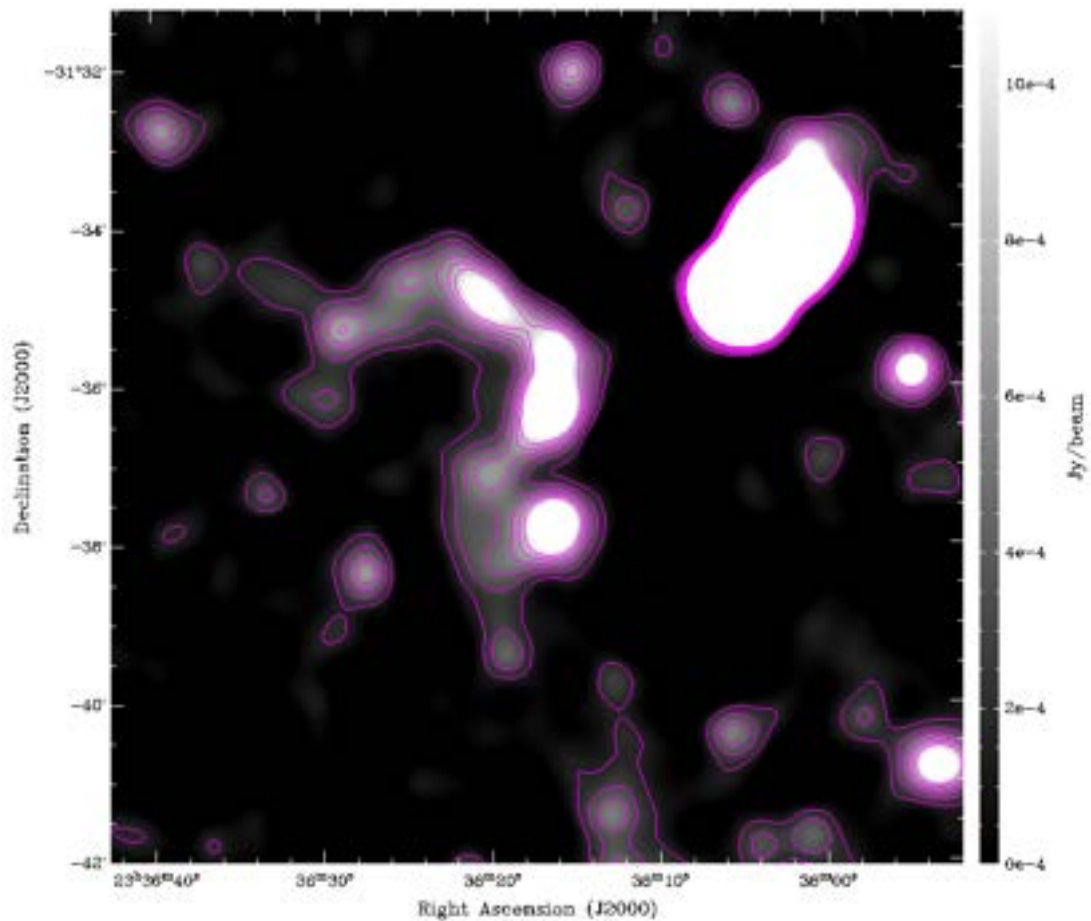


Figure 3.15: Abell S1136 diffuse structure with ASKAP 33, “alt” image at robust = 0 with 30'' Gaussian taper, Taylor Term 0, contours in magenta starting at $150 \mu\text{Jy beam}^{-1}$ increasing to $900 \mu\text{Jy beam}^{-1}$, in increments of $\sqrt{2}$.

3.1.3 ASKAP 16 and 33 Antenna Array: Contour Overlay

The following two images show Abell S1136 from the 16 antenna and 33 antenna array observations, overlaid with contours from both the 16 antenna and 33 antenna images. These images were made to show how the increased sensitivity and uv coverage between the 2017 and 2019 observations.

1. 16 antenna, robust = -0.5: Figure 3.16 shows Abell S1136 at robust = -0.5, overlaid with contours from the 16 antenna observation and the 33 antenna observation. The ASKAP 16 antenna contours are in magenta, starting at $250 \mu\text{Jy beam}^{-1}$ increasing to 1 mJy beam^{-1} , in increments of $\sqrt{2}$. ASKAP 33 contours in aqua starting at $150 \mu\text{Jy beam}^{-1}$ increasing to $700 \mu\text{Jy beam}^{-1}$, in increments of $\sqrt{2}$.
2. 16 antenna, robust = +2.0: Figure 3.17 again shows the same image, overlaid with contours from the 16 antenna observation and the 33 antenna observation. The ASKAP 16 antenna contours are in red, starting at $250 \mu\text{Jy beam}^{-1}$ increasing to 1 mJy beam^{-1} , in increments of $\sqrt{2}$. ASKAP 33 contours in aqua starting at $150 \mu\text{Jy beam}^{-1}$ increasing to $700 \mu\text{Jy beam}^{-1}$, in increments of $\sqrt{2}$.

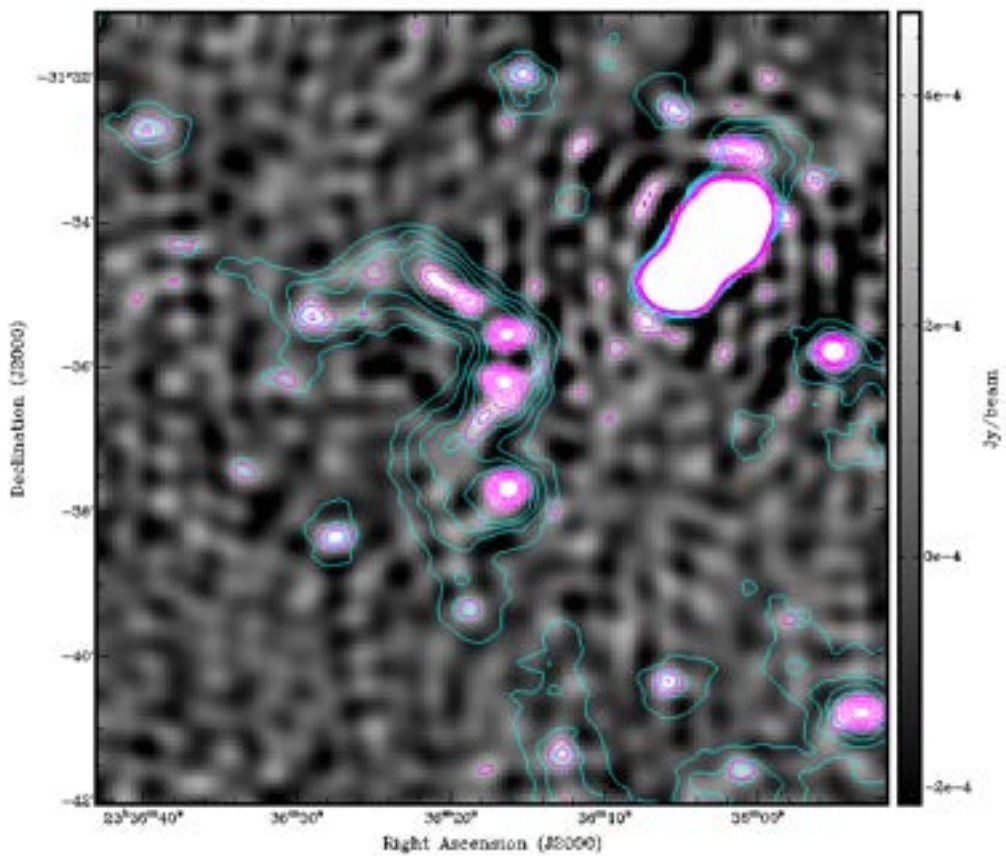


Figure 3.16: ASKAP 16, robust = -0.5 , Taylor Term 0, with ASKAP 16 and 33 contours. ASKAP 16 contours in magenta starting at $250 \mu\text{Jy beam}^{-1}$ increasing to 1 mJy beam^{-1} by $\sqrt{2}$. ASKAP 33 contours in aqua starting at $150 \mu\text{Jy beam}^{-1}$ increasing to $700 \mu\text{Jy beam}^{-1}$ by $\sqrt{2}$

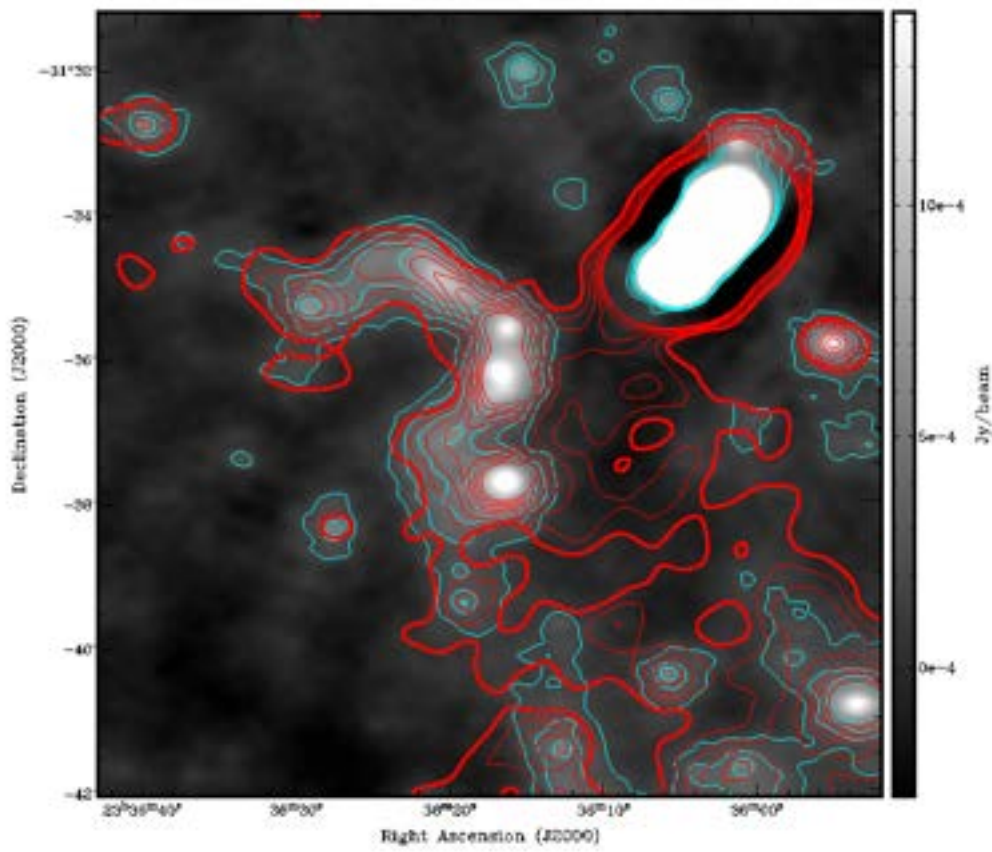


Figure 3.17: ASKAP 16, robust = +2.0, Taylor Term 0, with ASKAP 16 and 33 contours. ASKAP 16 contours in red starting at $250 \mu\text{Jy beam}^{-1}$ increasing to 1 mJy beam^{-1} by $\sqrt{2}$. ASKAP 33 contours in aqua starting at $150 \mu\text{Jy beam}^{-1}$ increasing to $700 \mu\text{Jy beam}^{-1}$ by $\sqrt{2}$.

3.1.4 33 Antenna Array: Areas of Interest

Figures 3.18 and 3.19 show regions of interest from the initial images produced from the 33 antenna array observations.

1. Figure 3.18:

- (a) In the red dashed circle, we can see the strong radio emission from PKS 2333-318.
- (b) In the black dashed circle, we can see the BCG. As with the 16 antenna observations, we can see the existence of two filaments extending within the structure - one of the filaments extends from the upper bright source in an arc up and over to the north-east, the other extends from the lower bright source down to the south-east.
- (c) In the white circle, we see another filament extending nearly horizontally.

1. Figure 3.19:

- (a) This image is marked up the same as the one above, however in the yellow dashed oval, we can see possible linking of the diffuse emission in the southern regions.

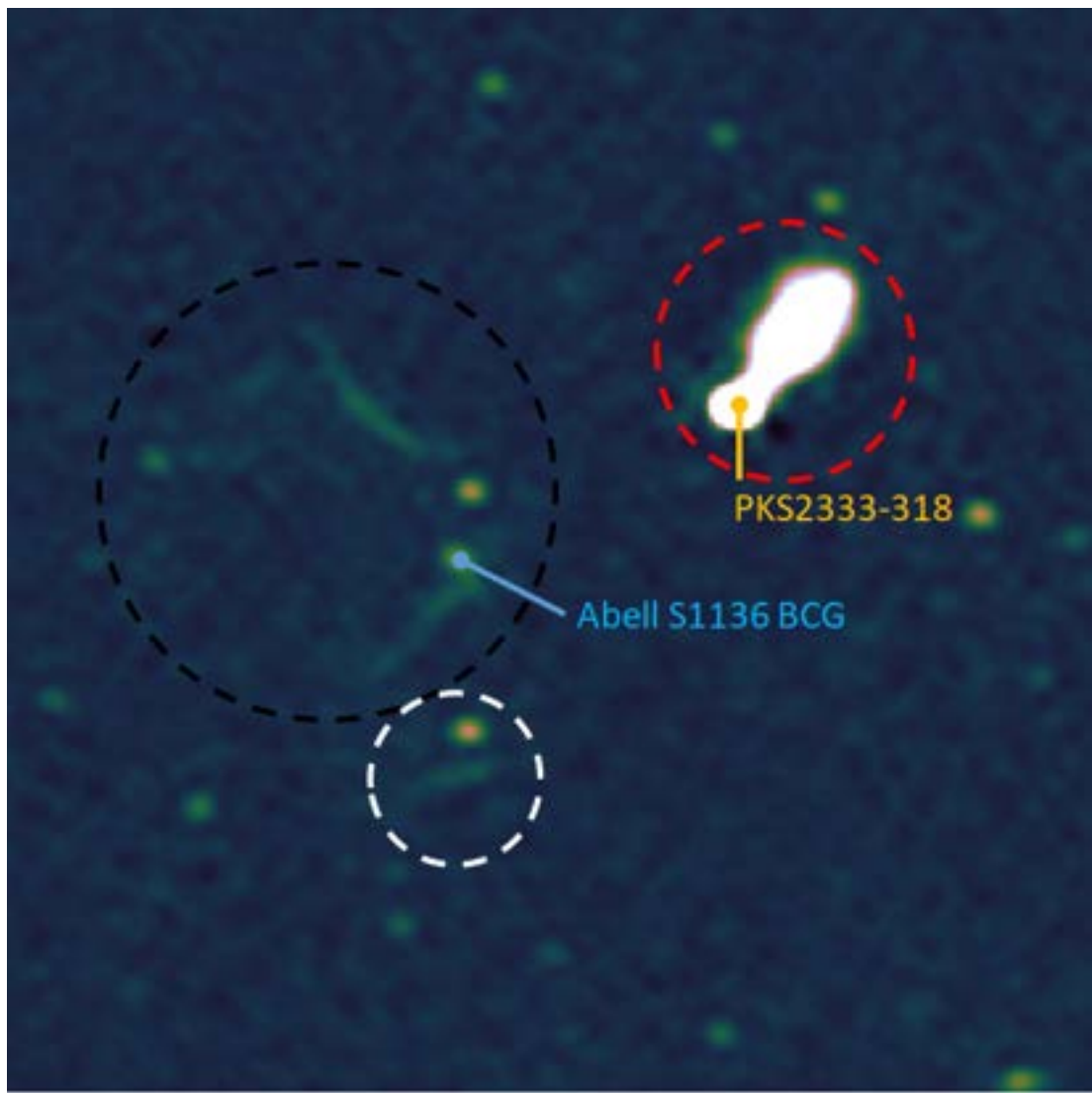


Figure 3.18: Abell S1136 diffuse structure with ASKAP 33, robust = 0, Taylor Term 0.

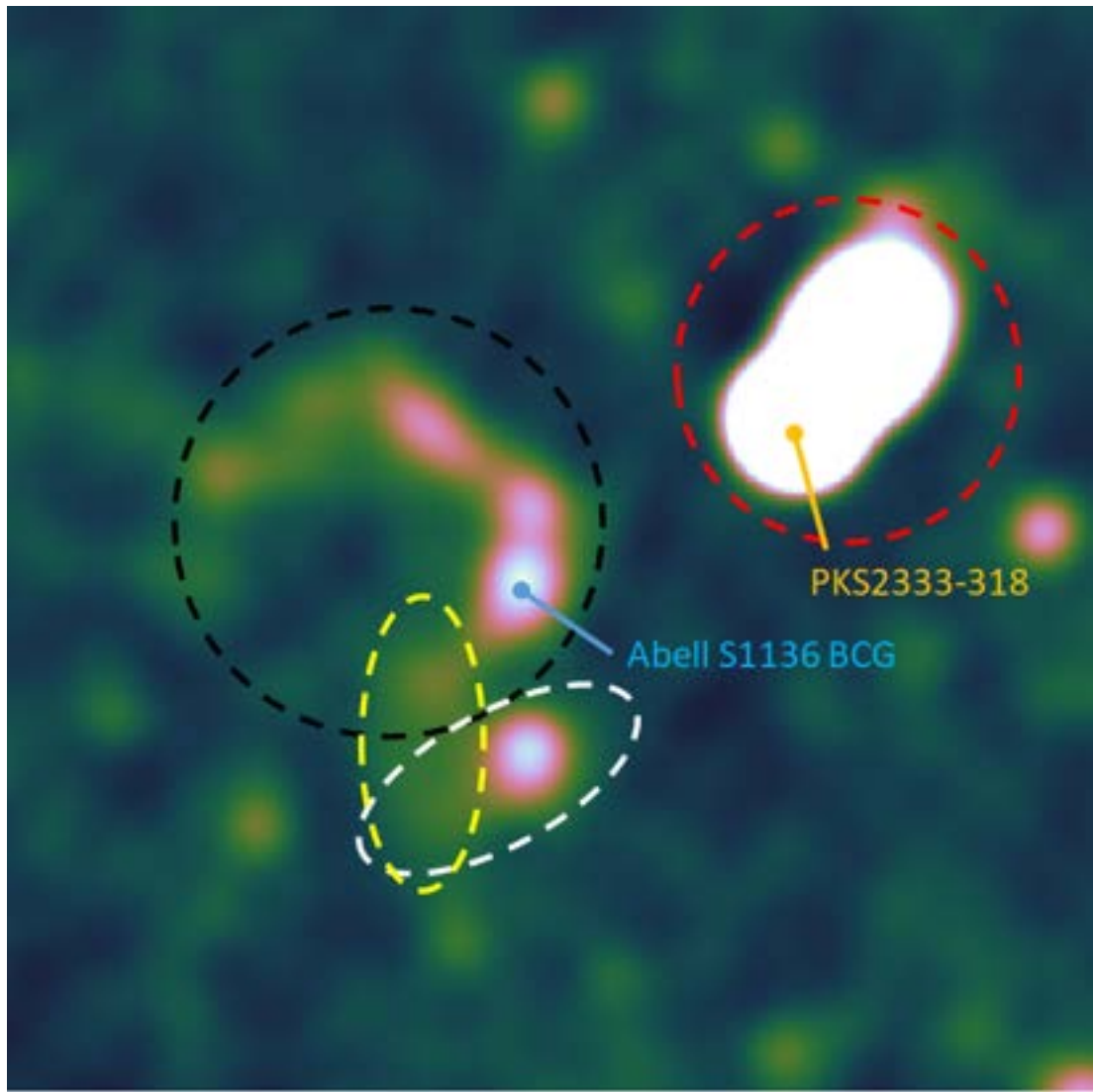


Figure 3.19: Abell S1136 diffuse structure with ASKAP 33 ALT image, robust = 0, Taylor Term 0.

3.2 Polarisation

The data obtained with 33 antennas in the July 2019 observations also contained measurements in Stokes Q , U , I , and V polarisation components. Polarisation was not measured for the 2017 observations with 16 antennas.

The images below show the Linearly Polarised Intensity P , obtained from the Stokes Q and Stokes U parameters, where $P = \sqrt{Q^2 + U^2}$. The **ASKAP** telescope observes across a 30 deg^2 field, and imaging the entire field consumes a lot of compute resource on the **PAWSEY** supercomputer. To reduce processing time, measurements for polarisation were run on only the centre four beams of the field, which contain Abell S1136 at the centre. The software tool “rmsynthesis” was used to obtain the peak-P emission from the Stokes Q and U cubes.

Figure 3.20 shows the peak-P polarisation for the centre four beams of the ASKAP 33 antenna observations. Leakage between Stokes V and Stokes I was measured as $(\frac{\text{Stokes}V}{\text{Stokes}I}) \sim 1\%$.

Figure 3.21 shows the peak-P polarisation zoomed in to Abell S1136. The dark elongated spot to the north-west corner of the red box is PKS 2333-318.

At low frequencies, the Abell S1136 galaxy cluster does not show any significant polarisation from any source in the Abell S1136 galaxy cluster, nor is there evidence of polarisation in the diffuse emission or filaments discussed above in Sections 3.1.1 and 3.1.2.

Figure 3.21 shows the peak-P emission (greyscale) centred on Abell S1136. The green contours in the image highlight the diffuse emission, while the red contours highlight the radio point sources in the centre of the cluster. The **BCG** is circled in blue. PKS 2333-318 shows obvious polarisation, while the Abell S1136 **BCG** shown in the blue circle appears non-polarised. There is also no emission apparent from any other radio source in the Abell S1136 galaxy cluster.

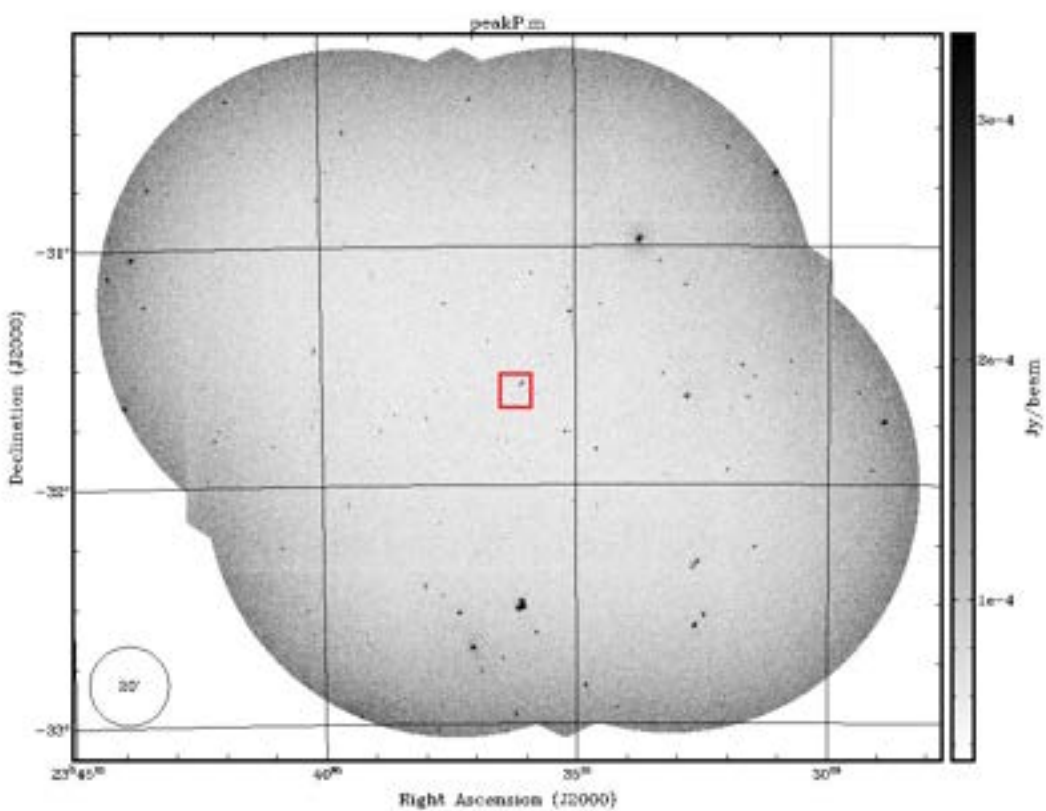


Figure 3.20: peak-P emission in the central 4 beams (15, 16, 20, 21) of the ASKAP 33 antenna observation

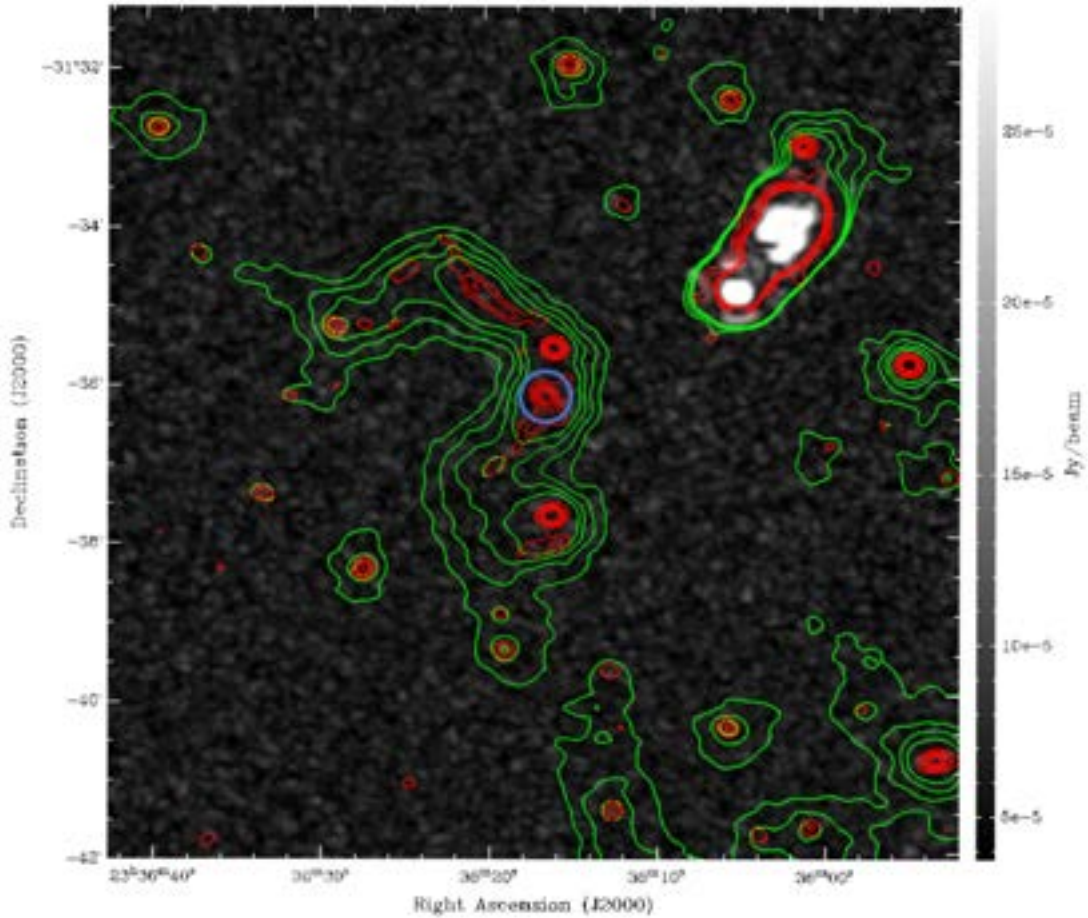


Figure 3.21: This image shows the peak-P emission (greyscale) centered on Abell S1136. ASKAP total intensity (Stokes I) are contoured as follows: the green contours are from the 33 antenna image at robust = +2.0, from $150 \mu\text{Jy beam}^{-1}$ to $700 \mu\text{Jy beam}^{-1}$ in increments of $\sqrt{2}$. The red contours are from the 33 antenna image at robust = 0, from $150 \mu\text{Jy beam}^{-1}$ to $900 \mu\text{Jy beam}^{-1}$ in increments of $\sqrt{2}$. The green contours highlight the diffuse emission, while the red contours highlight the radio point sources in the centre of the cluster. The BCG is circled in blue. PKS 2333-318 shows obvious polarisation, while the Abell S1136 BCG shown in the blue circle appears non-polarised. there is also no emission apparent from any other radio source in the Abell S1136 galaxy cluster.

3.3 Spectral Index

The data obtained with 33 antennas in the July 2019 observations of Abell S1136 provided images with flux density levels that enabled spectral index measurements.

In this section I show the spectral index maps, where the spectral index α is given by $S_\nu \propto \nu^\alpha$. The spectral index was calculated using a Python script provided by Dr Evan Crawford. The script was run using input images from MWA Phase II at 155 MHz, 185 MHz, and 215 MHz, and **ASKAP** at 864.5 MHz. The script automates the functions of convolving and regridding using the Miriad tasks “convol” and “regrid”, and saves in Miriad format images for further processing. After convolving, regridding to a common beam resolution, and saving to Miriad format, the images are “stacked”, and individual pixels in each image are then processed through a simple linear regression algorithm, with the slope of the best line of fit saved to a new image and output as a “fits”² file.

The images below were produced using the Karma software package³ ([Gooch, 1995](#)). I produced two output images, using input images at robust = 0 and robust = +1.0. The resulting images are shown at robust = 0 in Figure 3.22, and robust = +1.0 in Figure 3.23.

Figure 3.22 shows the spectral index map of Abell S1136 at robustness 0, overlaid with contours from MWA GLEAM (green), MWA Phase II (red), **ASKAP** (aqua).

Figure 3.23 shows the spectral index map of Abell S1136 at robustness 1, overlaid with contours from MWA GLEAM (green), MWA Phase II (red), **ASKAP** (aqua).

Both images show a steepening of the Abell S1136 cluster diffuse emission, as you move from the centre of the cluster out along the filaments to the north-east and south-east. The spectral index both the north-east and south-east regions steepens to ~ -2.1 to -2.3 .

Using the red circles in Figure 3.1 as a reference, we can see the emission centred around the central red circle (the **BCG**) has a spectral index of ~ -1.5 ; The spectral index of the filament extending to the north-east from the upper source A, steepens from -1.5 to ~ -2.5 or higher as we move outwards. The filament that extends from the middle source B (the **BCG**) steepens from -1.5 to ~ -2.5 . Furthermore, the

²<https://fits.gsfc.nasa.gov/>

³<https://www.atnf.csiro.au/computing/software/karma/>

spectral index in the lower filament, which extend horizontally underneath the lower source C, appears constant at ~ -2 to -2.3 .

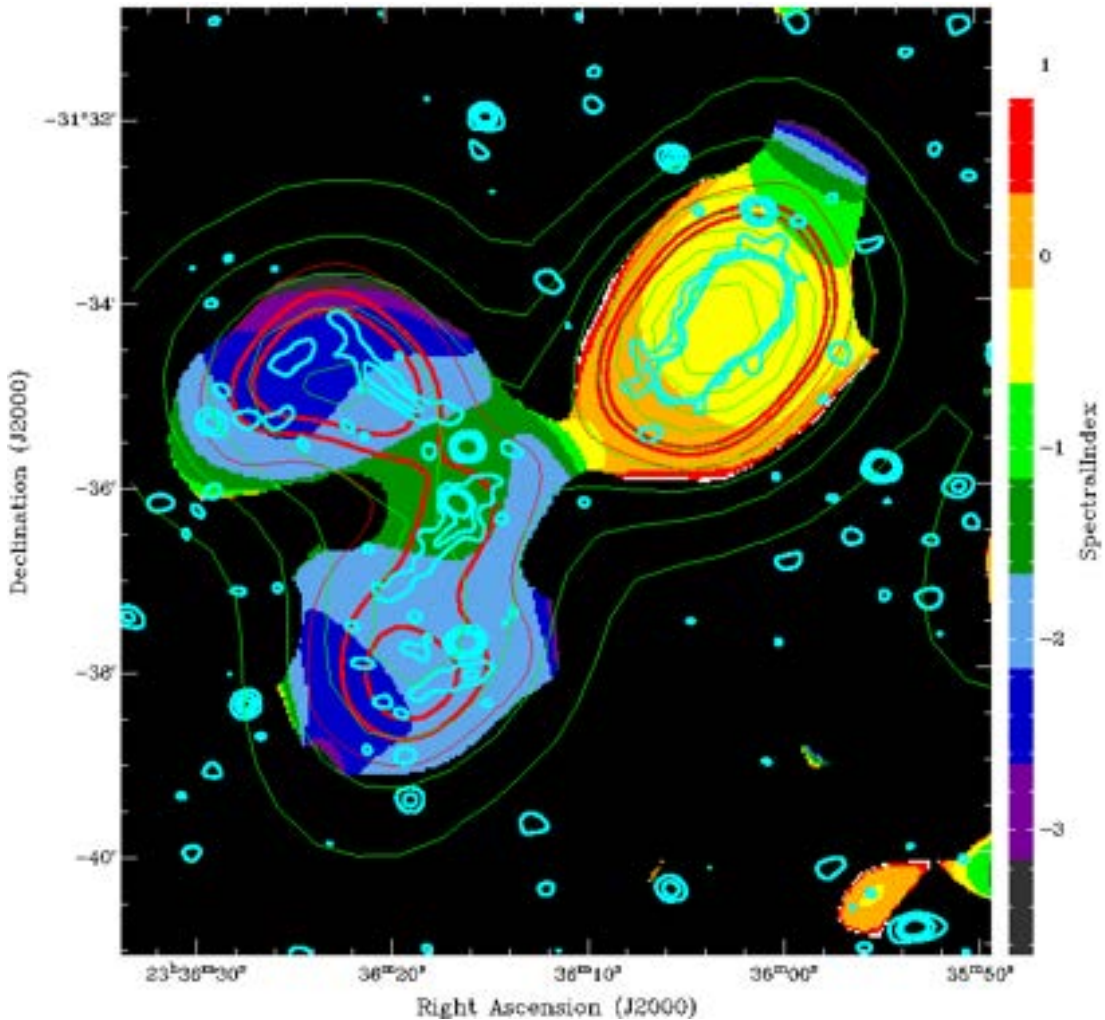


Figure 3.22: An image of Abell S1136 at robustness 0, showing the spectral index of the Abell S1136 galaxy cluster. Contours shown are from MWA (green), MWA Phase II (red) and ASKAP (aqua).

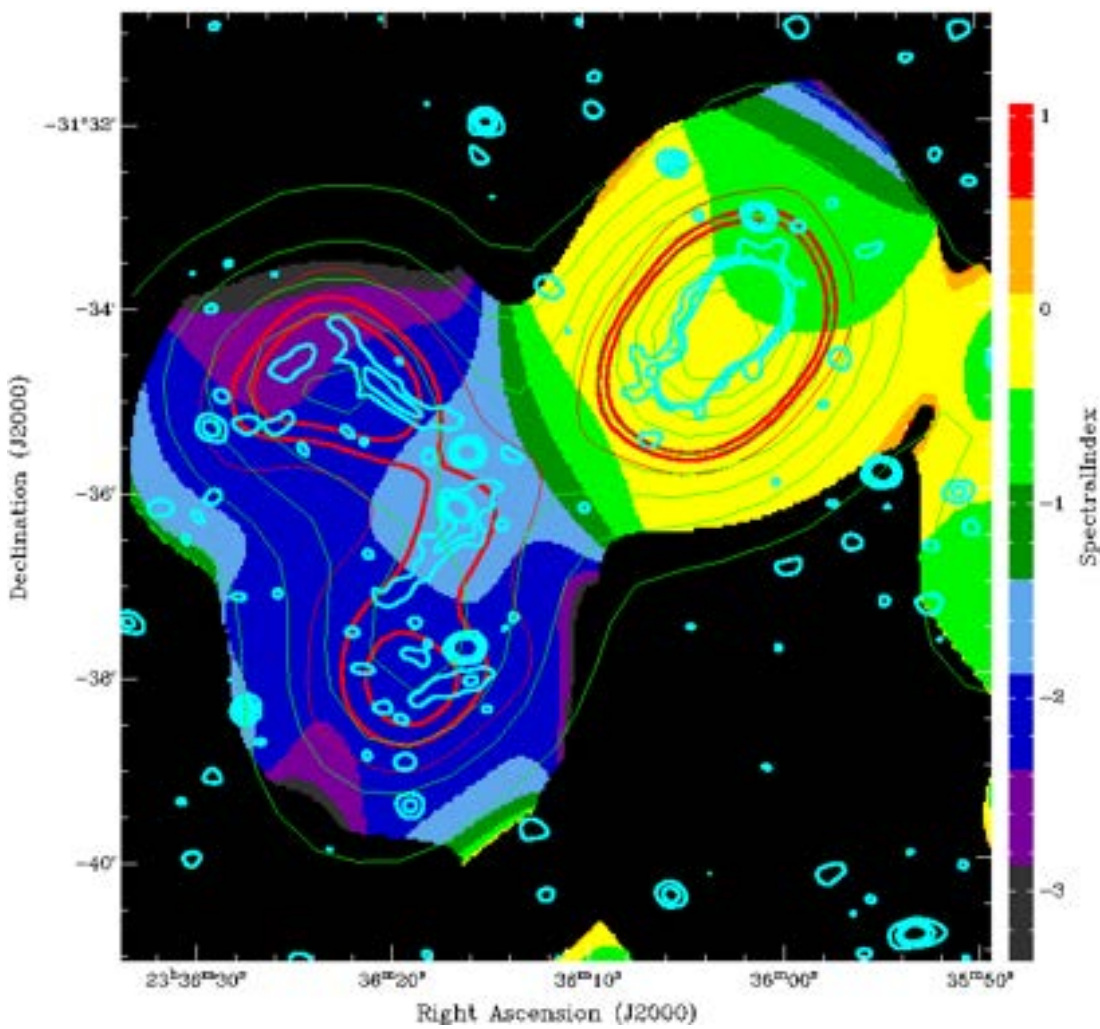


Figure 3.23: An image of Abell S1136 at robustness 1, showing the spectral index of the Abell S1136 galaxy cluster. Contours shown are from MWA (green), MWA Phase II (red) and ASKAP (aqua).

3.4 PKS 2333-318

Of interest in these results, because of its unique structure and proximity to the Abell S1136 galaxy cluster, is the radio-loud AGN PKS 2333-318. Located to the north-west of the Abell S1136 galaxy cluster at 23h36m04.96s -31d34m51.3s, the preferred redshift of PKS 2333-318 is $z = 0.06134$, relatively close to Abell S1136 at $z = 0.06250$. Here I discuss the radio, X-ray, and polarisation information for PKS 2333-318.

PKS 2333-318 has been mentioned in various papers, including [Dai et al. \(2015\)](#); [Lavaux and Hudson \(2011\)](#); [Puccetti et al. \(2011\)](#); [Jones et al. \(2009\)](#); [Mauch and Sadler \(2007\)](#); [Eke et al. \(2004\)](#) and [Grandi \(1983\)](#); [Shimmins and Bolton \(1974\)](#), however the information pertains mainly to redshift estimates, and inclusion in radio, infra-red, and X-ray survey catalogues. There does not appear to be a lot of science references or in-depth analysis of this radio source.

Shown in Figure 3.24, PKS 2333-318 appears as a tailed radio galaxy, with a unique single-sided *fat* tail. There is evidence of subtle sub-structure. The radio emission appears to extend from the bottom left to the top right, with the core of the AGN closest to the Abell S1136 cluster.

PKS 2333-318 appears highly polarised, as shown in Figure 3.21, with polarisation in the core and the emission.

The spectral index maps in Figures 3.22 and 3.23 show a spectral index steepening to ~ -0.8 .

As stated in Section 3.4, the preferred redshift of PKS 2333-318 is $z = 0.06134$, relatively close to Abell S1136 galaxy cluster with a preferred redshift of $z = 0.06250$. The redshift difference between Abell S1136 and PKS 2333-318 is close enough that there may be an interaction between the sources.

PKS 2333-318 also shows counterparts in optical (Figure 3.29), infrared (Figure 3.30), and X-ray (Figures 3.26 and 3.27).

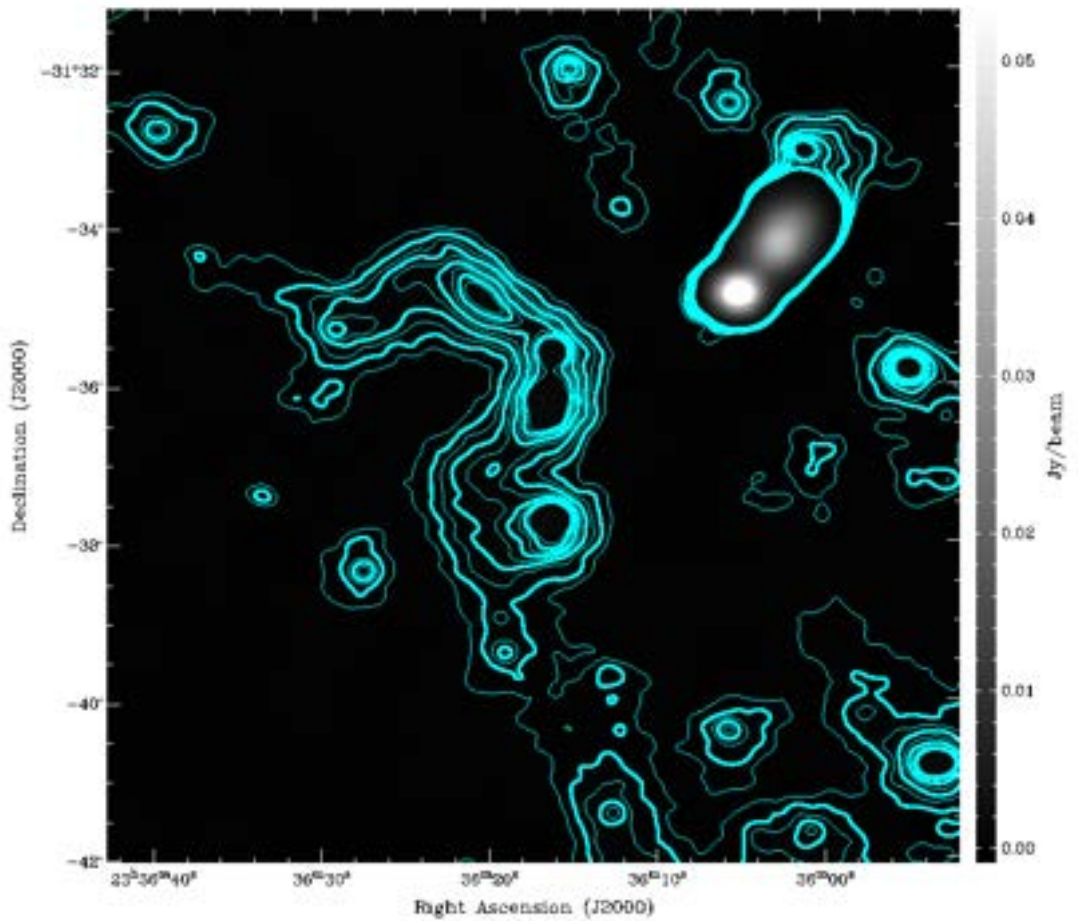


Figure 3.24: An image of Abell S1136, showing the fat single tailed radio lobe of PKS 2333-318 in the north-west. Contours are from the ASKAP 33 antenna observations, starting at $100 \mu\text{Jy beam}^{-1}$ increasing in $100 \mu\text{Jy beam}^{-1}$ steps to $900 \mu\text{Jy beam}^{-1}$.

3.5 The Abell S1136 Virial Radius

As mentioned in Section 1.7, the R_{200} virial radius of Abell S1136 has been measured by Porter and Raychaudhury (2005) and Hilton et al. (2005), at 1.6 Mpc and 2.41 Mpc respectively.

Figure 3.25 shows the 1.6 Mpc R_{200} virial radius of Abell S1136 on an optical background, with ASKAP contours. PKS 2333-318 can be seen to lie within the boundary of the Abell S1136 galaxy cluster virial radius.

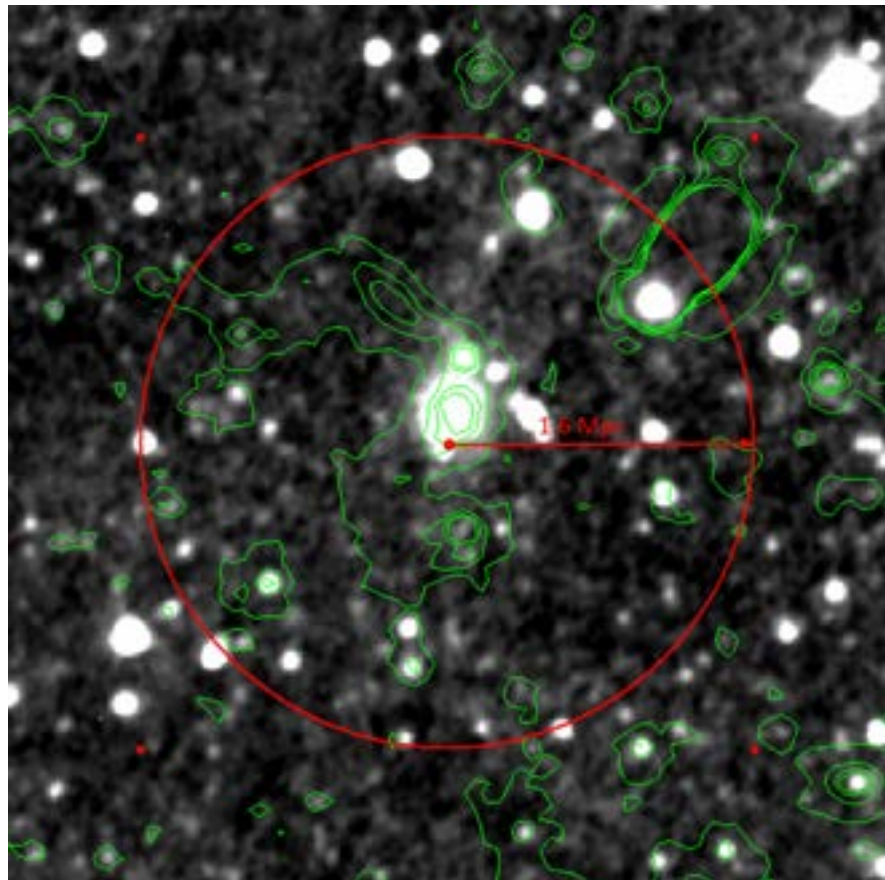


Figure 3.25: DSS optical background with ASKAP radio contours, red circle showing the Abell S1136 r_{200} virial radius = 1.6 Mpc, as detailed in Section 1.7. Angular size = 21.3 arcmin, calculated using <http://arcsec2parsec.joseonorbe.com/index.html>, and constants from the Planck 2016 Cosmological Model where $H_0 = 0.6731$, $\Omega_M = 0.315$, and $\Omega_L = 0.685$

3.6 ASKAP Comparison with XMM-Newton X-ray

3.6.1 Initial Analysis

Initial analysis of the X-ray emission in the Abell S1136 galaxy cluster was performed by me, using data from the ASKAP 33 antenna observations, combined with data from XMM-Newton.

Figure 3.26 shows the Abell S1136 radio emission from the ASKAP 33 antenna observation ($\text{robust} = -0.5$), overlaid with red contours from XMM X-ray survey. The Abell S1136 BCG is shown in the green circle.

In the image, we can see the well-formed circular X-ray emission from Abell S1136, and the BCG circled in green. The BCG is often associated with the geometric and kinematic galaxy centre, as well as the peak of the cluster X-ray emission (Lin and Mohr, 2004). We can see in figure 3.26 the BCG for Abell S1136 (identified as ESO 470-20 (Lauberts and Valentijn, 1989)), is in agreement with the BCG for Abell S1136 being located at the centre of the X-ray emission, and therefore being the geometric centre of the galaxy cluster.

The image shows what might be a bridge of X-ray emission extending to PKS 2333-318. Of particular interest is what may be a radio “channel” in the X-ray emission, shown in the yellow rectangle, with the radio and X-ray emission appearing anti-correlated. There are three thoughts regarding the “channel”: (1) the radio channel is being formed by the radio jets from the AGN forcefully displacing the hot X-ray gas, and forcing its way through the ICM. Examples of this have been seen in NGC 1275 (Boehringer et al., 1993), and postulated by Read et al. (2001) regarding observations of Abell S0102 in the galaxy pair ESO 295-IG022 (2) the radio filament is being confined by the X-ray medium, with the X-ray gas guiding the radio emission, rather than being the result of a channel being punched by the jet (Jones et al., 2017) (3) It is possible it is just a statistical fluctuation, This is discussed further in the next subsection.

The input images were convolved to the X-ray beam using Miriad, and the image was produced in kvis, however smoothing the data by convolving the beam breaks the Poisson statistics, which are useful to keep if some of the estimates have to be performed in the low counts’ regime. Also, it would be most useful to precisely locate the position of the radio features to optimise the X-ray measurements.

Figure 3.27 shows the XMM X-ray image of teh Abell!S1136 galaxy

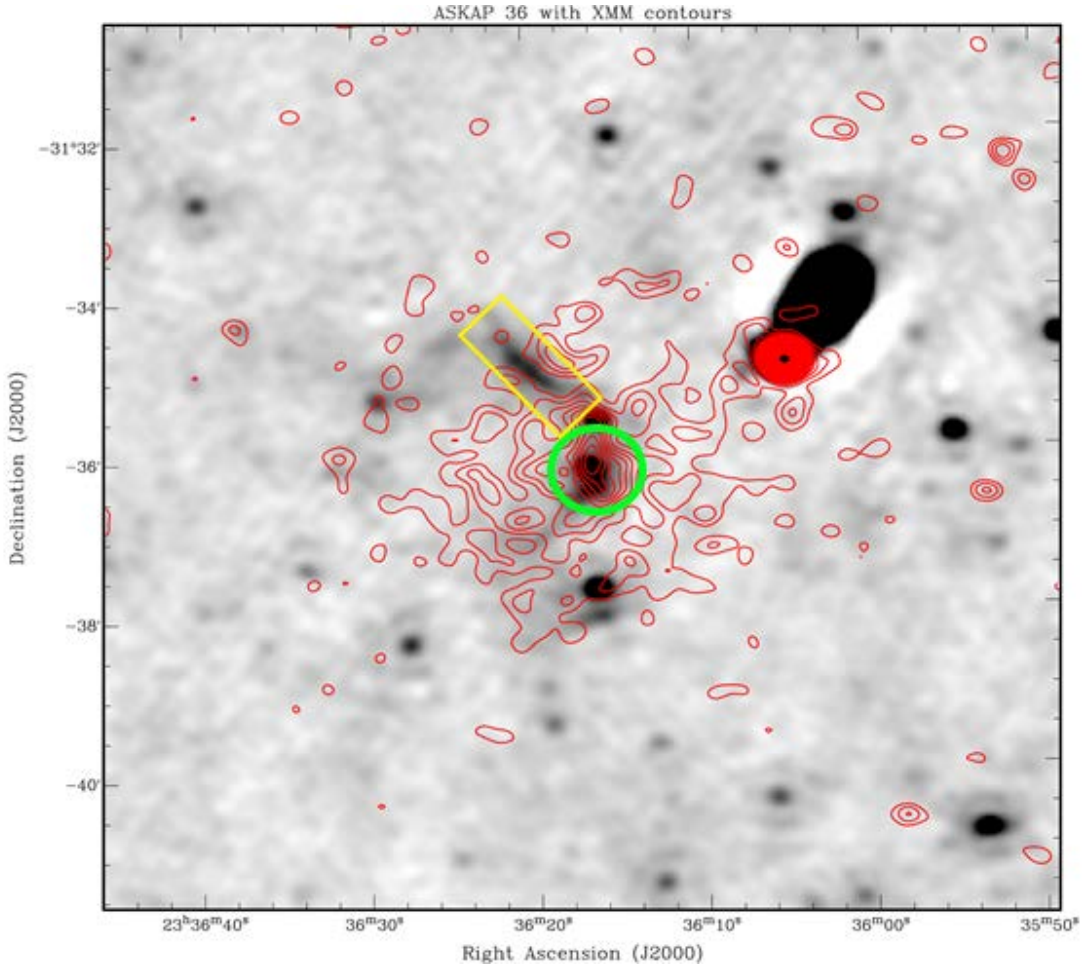


Figure 3.26: This image shows contours from XMM-Newton X-ray in red, overlaid on the background of ASKAP radio at 864 MHz. The Brightest Cluster Galaxy ESO 470-20 is circled in green. The XMM-Newton image was convolved with the ASKAP image before application of the contours. The yellow rectangle outlines a potential channel, where the radio is either punching through, or being confined by, the X-ray emission.

cluster. The instrumental background for each XMM / EPIC exposure was modelled, and an X-ray point source mask was produced to help with analysis. The X-ray map was then corrected for background and exposure. Analysis confirmed the X-ray peak to be coincident with the BCG defined at the coordinates in the ASKAP observations. The power ratios were found to be compatible with a relaxed cluster; however, there is a small centroid shift, which indicates the possibility of a slightly disturbed system.

3.6.2 Analysis of a Potential Radio Channel in the X-ray Emission

Further analysis of the radio “channel” in the X-ray emission was performed, and the significance was measured and estimated at $\sim 4.2 \sigma$. There is a centroid shift in the X-ray emission that could indicate a slightly

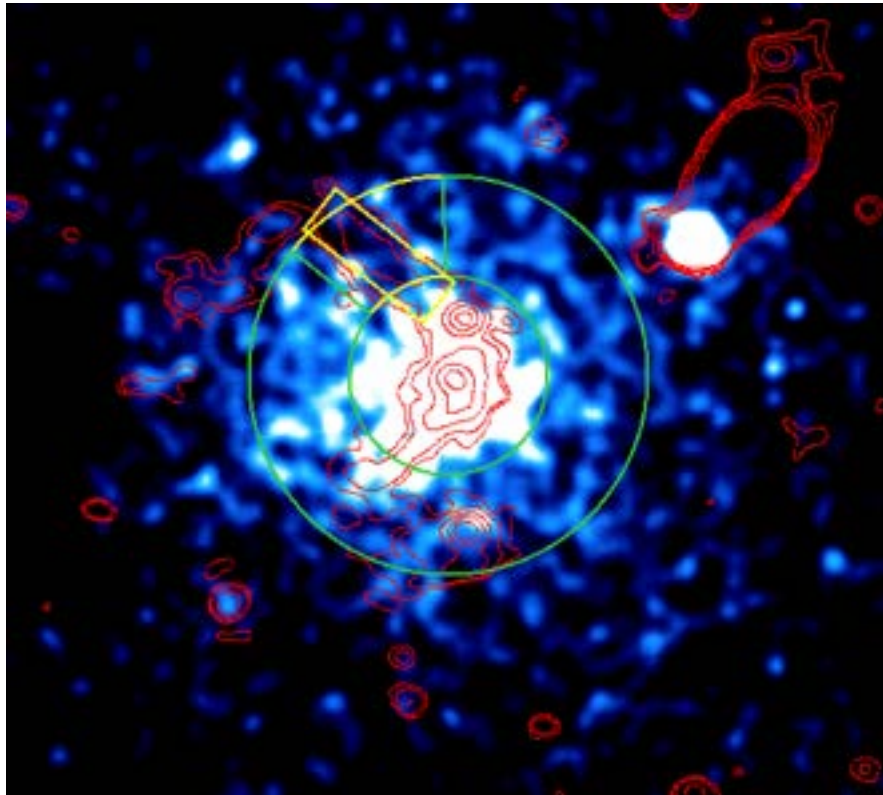


Figure 3.27: The **XMM** X-ray image showing an X-ray peak located at RA 354.06994 DEC -31.602406, coincident with the radio emitting **BCG** of Abell S1136. ASKAP contours are overlaid in red. Analysis indicates PKS 2333-318 is well within the projected extent of S1136's **ICM**.

disturbed system.

Figure 3.27 shows the peak of the thermal X-ray emission from Abell S1136 centred in the green circle at RA 354.06994 DEC -31.602406 (J2000), coincident with my findings of the radio emission centred on the **BCG**. The yellow rectangle outlines the suspected radio channel.

3.6.3 X-ray Temperature and Spectral Profile Analysis

To perform a more detailed spectroscopic analysis of the X-ray data, the X-ray point sources were removed from the analysis using a mask.

Firstly, the sky background in the outer regions of the observation was modelled by assuming that it consists of three components: a contribution from the unresolved active galactic nuclei (AGN) population, which has an absorbed power-law spectrum with a spectral index of 1.46; the emission from the Milky Way halo, which has an absorbed Astrophysical Plasma Emission Code (**APEC**) thermal model with solar metal abundance and a temperature of around 0.2 keV; and the emission from the local hot bubble, which is another absorbed thermal model with solar metalicity

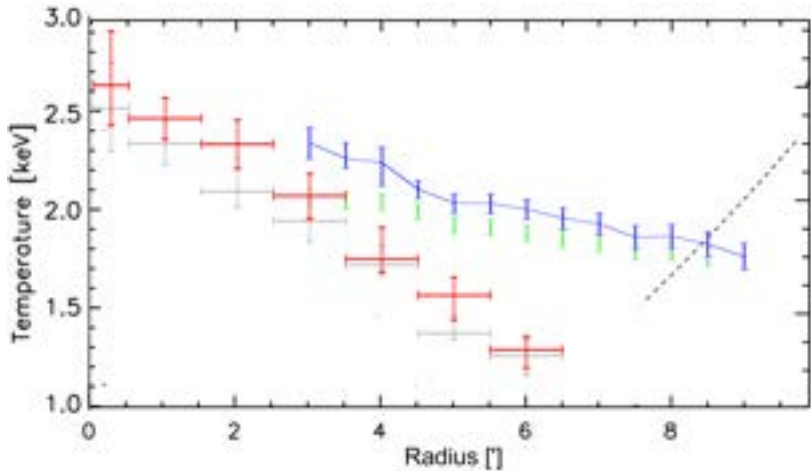


Figure 3.28: The X-ray temperature profile of the galaxy cluster Abell S1136. The blue line and error bars show the average cluster temperature (expressed as kT), estimated in apertures of increasing size (blue is the result leaving the metal abundance free, and green is for a fixed value of 0.3 solar). The dashed line shows the average $R_{500} - T$ relation for a cluster at $z = 0.062$, based on the galaxy cluster mass-temperature (M-T) relation of Arnaud et al. (2005). The red error bars shows the Abell S1136 X-ray temperature profile, showing the temperature plotted against radial distance in arcminutes (red is the result leaving the metal abundance free, and grey is for a fixed value of 0.3 solar). The temperature profile appears linear from the centre to the edge, with no drop in temperature towards the cluster centre.

and a temperature of around 0.1 keV. The spectral modelling used the **APEC** version 3.0.9 model and a fixed hydrogen column density of $1.23 \times 10^{20} \text{ cm}^{-2}$, obtained from the LAB survey (Górski et al., 2005; Kalberla et al., 2005; Land and Słosar, 2007). After modelling the sky background, spectra were extracted from regions of interest, and a further cluster **APEC** component was added to the sky background, which was re-scaled for the region of interest.

In Figure 3.28, the blue and green points represent the average temperature of the cluster, that has been estimated in apertures of increasing size.

The average relationship between R_{500} and T for a cluster located at $z = 0.0620$ is depicted by the dashed line in the figure. This relationship is calculated using the M-T relation provided by Arnaud et al. (2005). This allows us to estimate an approximate value for the cluster's R_{500}/M_{500} , where M_{500} is the halo mass and R_{500} is the radius within which the mass density is 500 times the critical density of the Universe. The average properties of the cluster are calculated by fitting the spectra extracted within R_{500} , and these results are presented in Table 3.1.

Table 3.1: The Abell S1136 average properties, as determined from the analysis of the **XMM** data. For the luminosities, the X-ray band (in keV) is indicated by the range in subscript.

	Size R_{500} (8.43')
Total mass	
M_{500}	6.664 (+0.401/-0.399) 10^{13} Msol
w. int. sc.	6.664 (+1.259/-1.543) 10^{13} Msol
ICM quantities within R_{500}	
T_{spec}	1.826 (+0.063/-0.065) keV
Z	0.362 (+0.049/-0.044) Z_{\odot}
$L_{0.5-2.0}$	1.913 (+0.036/-0.036) 10^{36} W
$L_{0.1-2.4}$	3.165 (+0.073/-0.074) 10^{36} W
L_{bol}	4.300 (+0.077/-0.077) 10^{36} W

The cluster appears to be in a relaxed state with a small centroid shift, but also shows a central surface brightness peak. Because of this, a projected temperature and abundance profile analysis was performed to determine if the cluster has a cool core ([Hudson et al., 2010](#)). The X-ray temperature profile, shown in red and grey in Figure 3.28, does not show cooler emission in the central parts, meaning it does not have the central temperature drop typical of a cool core. Instead, the central parts appear significantly hotter, which could indicate the cluster is not relaxed, or the central AGN within the BCG is also emitting X-rays.

3.7 ASKAP Comparison with DSS Optical

Figure 3.29 shows Abell S1136 radio background from the ASKAP 33 antenna observation, overlaid with contours from the DSS RGB optical image shown in Figure 1.26, and contours from the ASKAP 33 antenna observations ($\text{robust} = +2.0.0$). Contours for the DSS RGB image are in red, starting at 20% of the peak pixel value, rising to 90%, in 10% increments. Contours for the ASKAP radio emission are in aqua, starting at $150 \mu\text{Jy beam}^{-1}$, rising to $900 \mu\text{Jy beam}^{-1}$ in increments of $\sqrt{2}$.

Of interest is the lack of optical counterpart in the southern most lobe of the Abell S1136 emission, where there is prominent radio emission but no visible optical emission. It is not clear from these observations whether this bright lobe of radio emission is associated with the Abell S1136 cluster, or if it might be from a high-redshift background source. As outlined in my Conclusions and Future Work in Chapter 5, further high-resolution observations, and deeper optical data may be able to help with this classification.

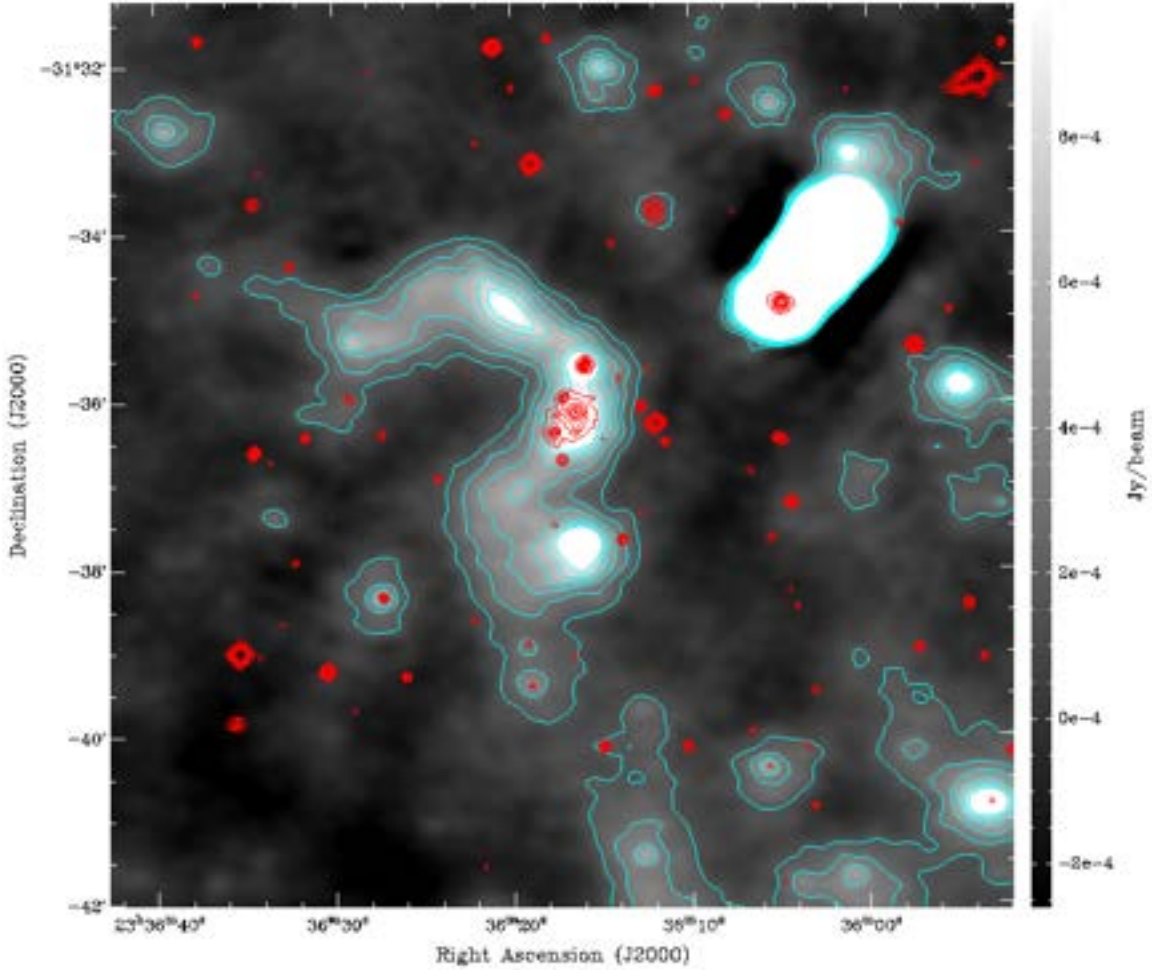


Figure 3.29: DSS Optical image overlaid with contours from the ASKAP 33 antenna observations at robust = +2.0.0. The DSS contours are in red, starting at 20% of the peak pixel value, rising to 90%, in 10% increments. The contours for the ASKAP radio emission are in aqua, starting at $150 \mu\text{Jy beam}^{-1}$, rising to $900 \mu\text{Jy beam}^{-1}$ in increments of $\sqrt{2}$.

3.8 ASKAP Comparison with WISE Infrared

Figure 3.30 shows Abell S1136 RGB infrared background from WISE, with contours from the ASKAP 33 antenna observation overlaid in aqua (robust = +2.0.0). The WISE infrared RGB colours are red = 22 μm , green = 4.6 μm , blue = 3.4 μm . Contours for the ASKAP radio emission are in aqua, starting at 150 $\mu\text{Jy beam}^{-1}$, rising to 900 $\mu\text{Jy beam}^{-1}$ in increments of $\sqrt{2}$.

Of interest is the lack of infrared counterpart in the southern most lobe of the S1136 emission, where there is prominent radio emission but no visible infrared emission. As with the [ASKAP Comparison with DSS Optical](#), it is not clear from these observations whether this bright lobe of radio emission is associated with the Abell S1136 cluster, or if it might be from a high-redshift background source. As outlined in my Conclusions and Future Work in Chapter 5, further infrared observations may be able to help with this classification.

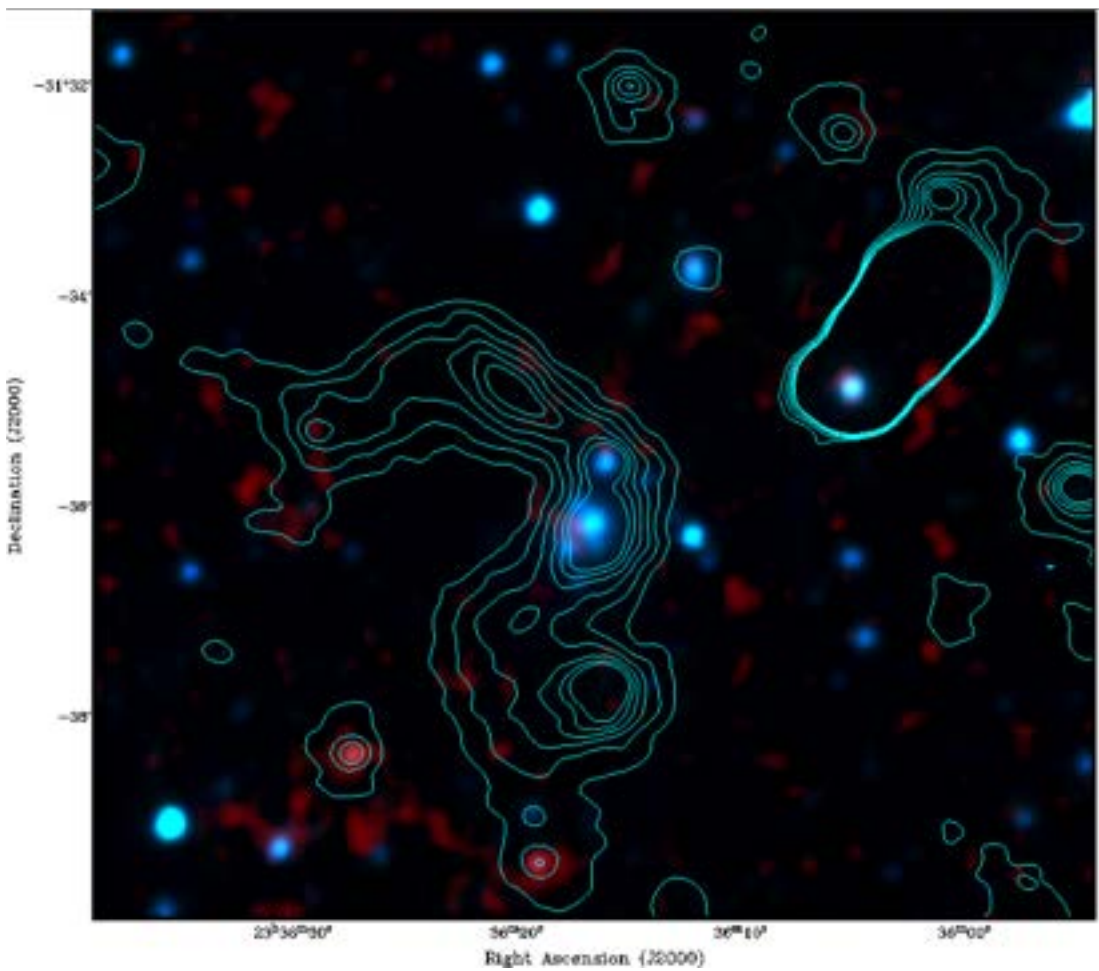


Figure 3.30: WISE Infrared RGB image overlaid with contours from the ASKAP 33 antenna observations at robust = +2.0.0. RGB colours are red = 22 μm , green = 4.6 μm , blue = 3.4 μm . The ASKAP radio contours start at 150 mJy beam⁻¹ and increase by $\sqrt{2}$ to 900 mJy beam⁻¹.

3.9 ASKAP Comparison with MWA Phase I

3.9.1 Images with MWA Phase I Radio Background

In this section I show images comparing the radio emission from the ASKAP 33 antenna observations ($\text{robust} = +2.0$) in aqua contours, with the radio emission from the [MWA](#) Phase I observations in green contours. The [MWA](#) contours in the images below were set at a level that would capture the boundary of the diffuse emission and were adjusted in each frequency band to maintain the edge distance and overall shape. The ASKAP contours were unchanged throughout the images. A summary of the contour levels is shown in Table 3.2. The sensitivity of the [MWA](#) Phase I is insufficient to resolve the diffuse emission into filamentary structure.

Figures 3.31 and 3.32 are [MWA](#) Phase 1 background with contours from [MWA](#) Phase I and ASKAP.

The [MWA](#) observations show in green contouring the radio halo that exists around the Abell S1136 galaxy cluster, bridging across to PKS 2333-318. The existence of filamentary structure shown with the ASKAP contours cannot be seen in the emission visible in the [MWA](#) Phase I observations.

Table 3.2: Contour Levels for MWA Phase I with ASKAP

Image and Frequency	Start (mJy beam $^{-1}$)	Stop (mJy beam $^{-1}$)	Contour Level (mJy beam $^{-1}$)
139-170 MHz background with MWA and ASKAP contours	15	300	30
170-231 MHz background with MWA and ASKAP contours	15	300	20
ASKAP background with ASKAP and MWA 139-170 MHz contours	15	300	30
ASKAP background with ASKAP and MWA 170-231 MHz contours	15	300	20

3.9.2 Images with ASKAP Radio Background

Figures 3.33 and 3.34 are similar to those in the previous section (Section 3.9.1 “Images with [MWA](#) Phase I Radio Background”), however these images have ASKAP 33 antenna observations as the background image.

In this section I show images comparing the radio emission from the ASKAP 33 antenna observations ($\text{robust} = +2.0$) in aqua contours, with the radio emission from the [MWA](#) Phase I observations in green contours. All contours in the images below are the same as those in the previous section. The [MWA](#) contours were set at a level that would capture the boundary of the diffuse emission and were adjusted in each

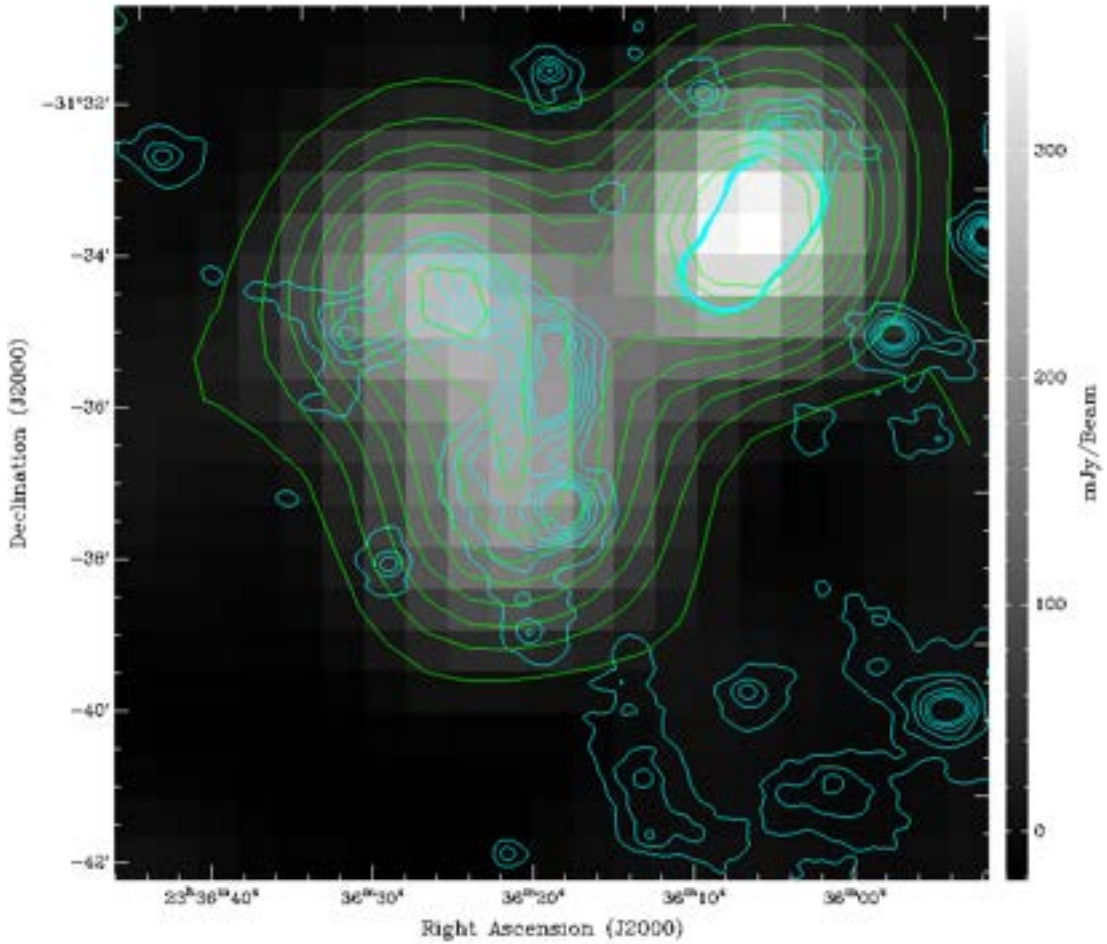


Figure 3.31: ASKAP Comparison with MWA Phase I at 139-170 MHz. The background image is from MWA Phase I at 139-170 MHz, overlaid with contours from MWA Phase I in green, and ASKAP 33 antenna observation (robust = +2.0) in aqua. MWA contours start at 15 mJy beam^{-1} , rising to $300 \text{ mJy beam}^{-1}$ in 30 mJy beam^{-1} increments. The ASKAP radio contours start at $150 \text{ mJy beam}^{-1}$ and increase by $\sqrt{2}$ to $900 \text{ mJy beam}^{-1}$.

frequency band to maintain the edge distance and overall shape. The ASKAP contours were unchanged throughout the images.

MWA observations show in green contouring the radio halo that exists around the Abell S1136 galaxy cluster, bridging across to PKS 2333-318. The filamentary structure detected with the ASKAP 33 antenna observations can be seen here to be located well within the boundary of the MWA radio halo.

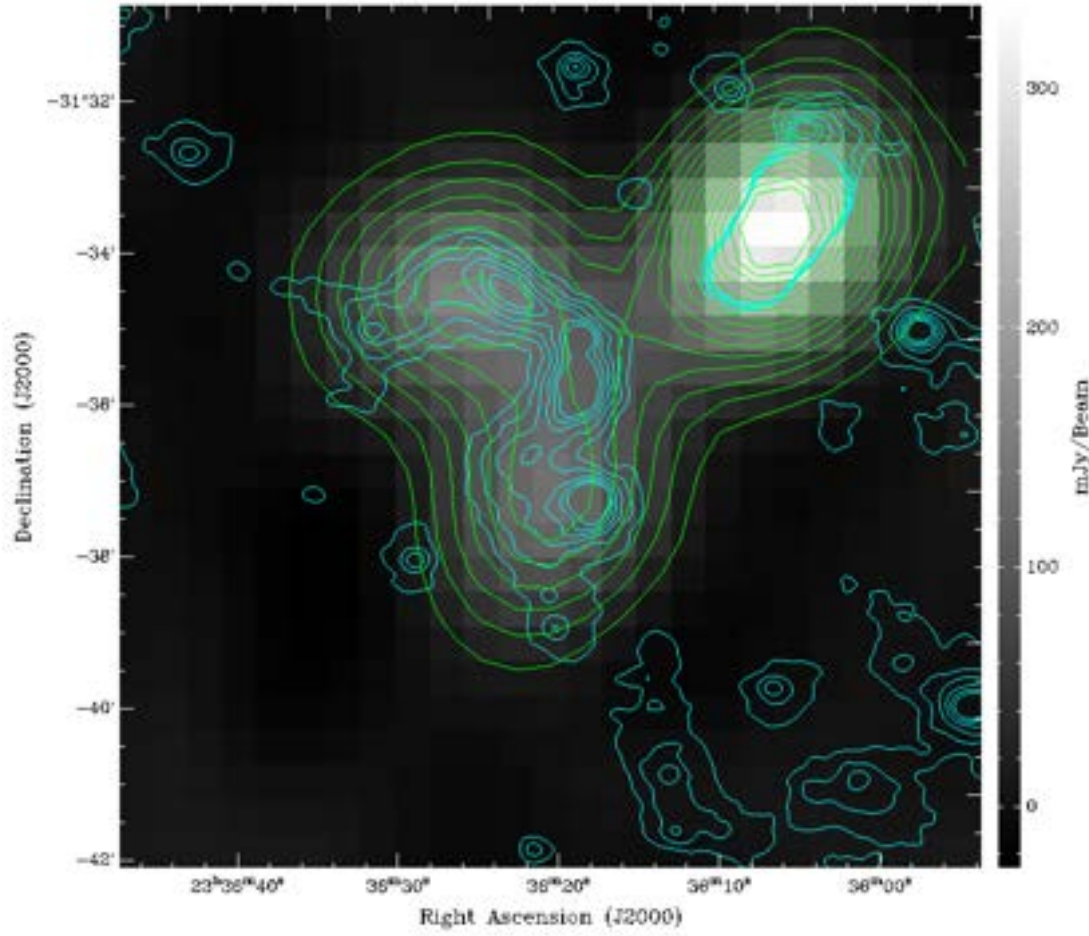


Figure 3.32: ASKAP Comparison with MWA Phase I at 170-231 MHz. The background image is from MWA Phase I at 170-231 MHz, overlaid with contours from MWA Phase I in green, and ASKAP 33 antenna observation ($\text{robust} = +2.0$) in aqua. MWA contours start at 15 mJy beam^{-1} , rising to $300 \text{ mJy beam}^{-1}$ in 20 mJy beam^{-1} increments. The ASKAP radio contours start at $150 \text{ mJy beam}^{-1}$ and increase by $\sqrt{2}$ to $900 \text{ mJy beam}^{-1}$

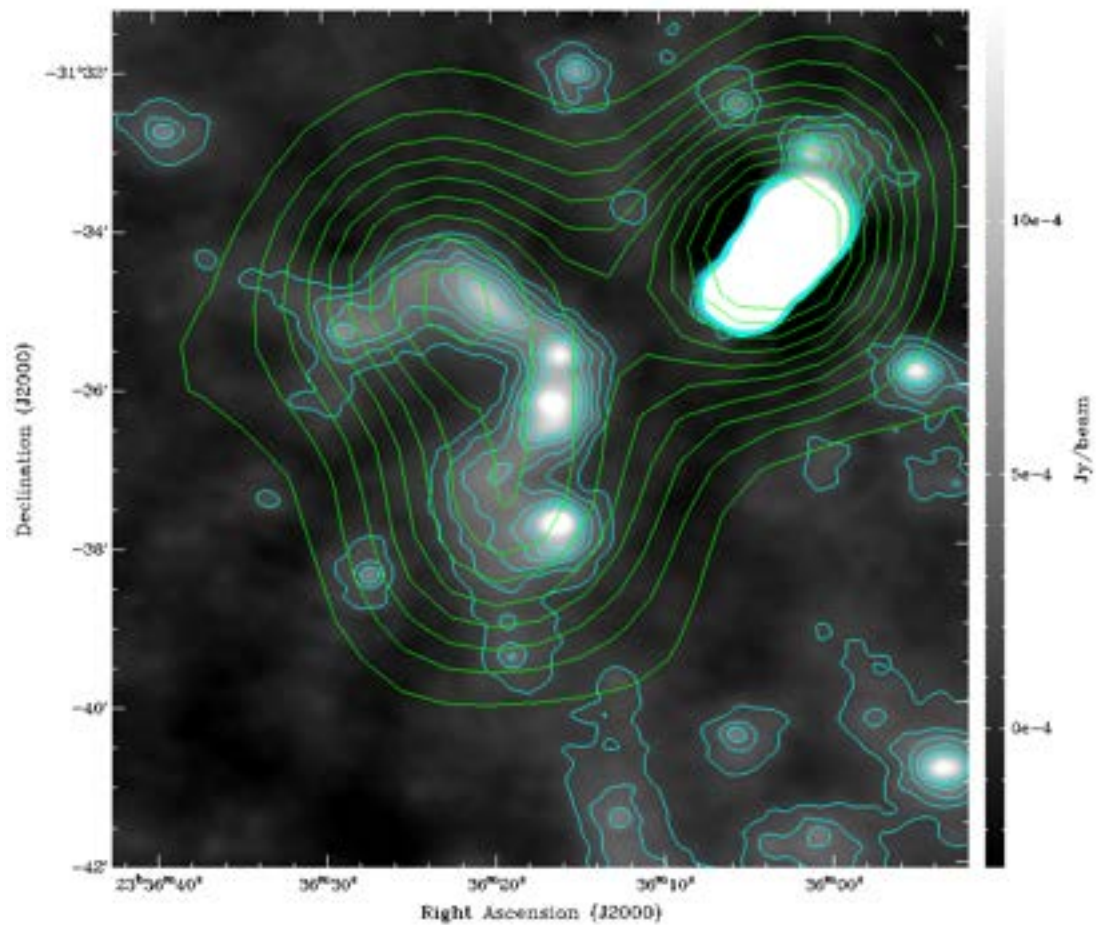


Figure 3.33: ASKAP Comparison with MWA Phase I at 139-170 MHz, overlaid with contours from MWA Phase I in green, and ASKAP 33 antenna observation (robust = +2.0) in aqua. MWA contours start at 15 mJy beam^{-1} , rising to $300 \text{ mJy beam}^{-1}$ in 30 mJy beam^{-1} increments. The ASKAP radio contours start at $150 \text{ mJy beam}^{-1}$ and increase by $\sqrt{2}$ to $900 \text{ mJy beam}^{-1}$

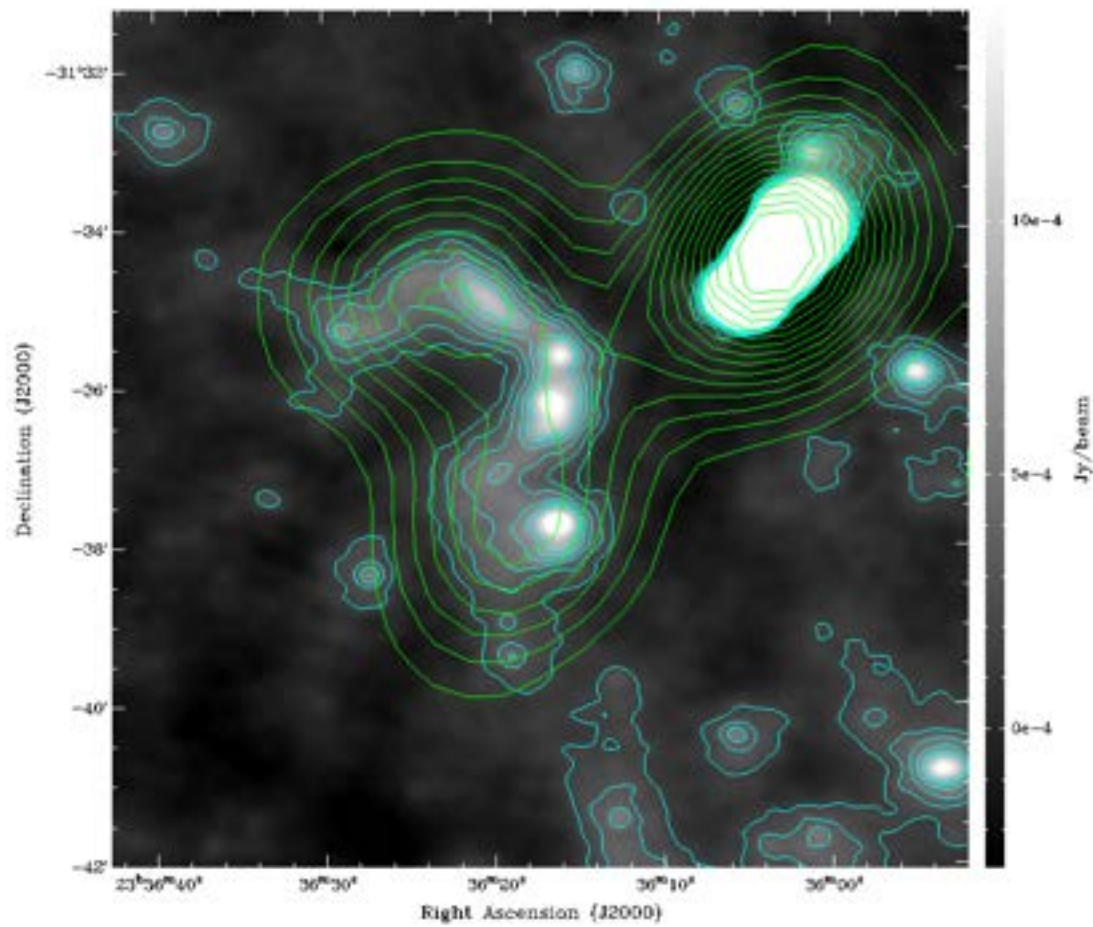


Figure 3.34: ASKAP Comparison with MWA Phase I at 170-231 MHz, overlaid with contours from MWA Phase I in green, and ASKAP 33 antenna observation (robust = +2.0) in aqua. MWA contours start at 15 mJy beam^{-1} , rising to $300 \text{ mJy beam}^{-1}$ in 20 mJy beam^{-1} increments. The ASKAP radio contours start at $150 \text{ mJy beam}^{-1}$ and increase by $\sqrt{2}$ to $900 \text{ mJy beam}^{-1}$

3.10 ASKAP Comparison with MWA Phase II

3.10.1 Images with MWA Phase II Radio Background

In this section I show images comparing the radio emission from the ASKAP 33 antenna observations ($\text{robust} = +2.0$) in aqua contours, with the radio emission from the [MWA](#) Phase II observations in green contours. The [MWA](#) contours in the images below were set at a level that would capture the boundary of the diffuse emission and were adjusted in each frequency band to maintain the edge distance and overall shape. The ASKAP contours were unchanged throughout the images. A summary of the contour levels is shown in Table 3.3. The sensitivity of the [MWA](#) Phase II is insufficient to resolve the diffuse emission into filamentary structure.

Figures 3.35, 3.36, and 3.37 are [MWA](#) Phase II background with contours from [MWA](#) Phase II and ASKAP. The increased sensitivity of [MWA](#) Phase II at higher frequencies can be seen in the starting contour levels changing from 15 mJy beam^{-1} at 154 MHz, to 6 mJy beam^{-1} at 185 MHz, and 3 mJy beam^{-1} at 215 MHz.

As with the [MWA](#) Phase I observations, the Phase II observations show in green contouring the radio halo that exists around the Abell S1136 galaxy cluster, bridging across to PKS 2333-318. The existence of filamentary structure shown with the ASKAP contours is still not visible in the emission of the [MWA](#) Phase II observations.

Table 3.3: Contour Levels for MWA Phase II with ASKAP

Image and Frequency	Start (mJy beam $^{-1}$)	Stop (mJy beam $^{-1}$)	Contour Level (mJy beam $^{-1}$)
MWA 154 MHz (C121) background with MWA and ASKAP contours	15	300	20
MWA 185 MHz (C145) background with MWA and ASKAP contours	6	300	19.6
MWA 215 MHz (C169) background with MWA and ASKAP contours	3	300	12
ASKAP background with ASKAP and MWA II 154 MHz (C121) contours	15	300	20
ASKAP background with ASKAP and MWA II 185 MHz (C145) contours	6	300	19.6
ASKAP background with ASKAP and MWA II 215 MHz (C215) contours	3	300	12

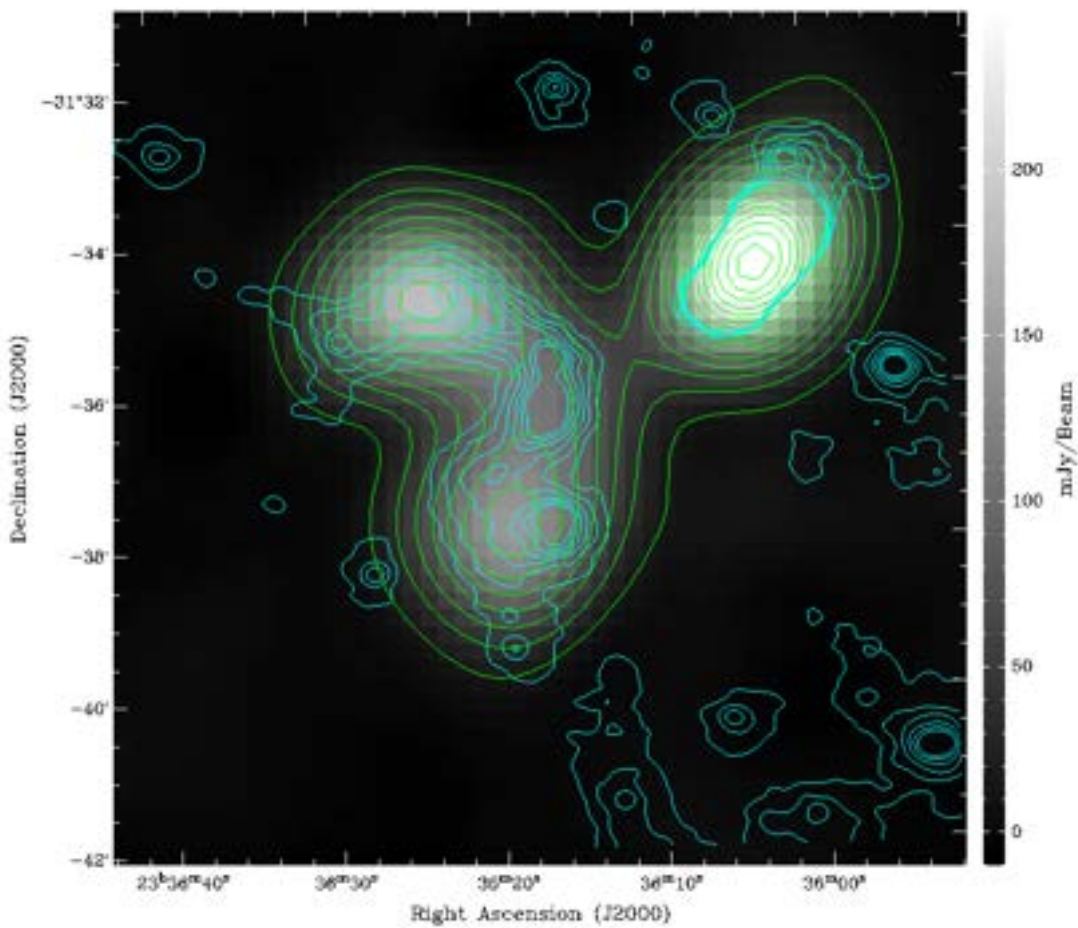


Figure 3.35: ASKAP Comparison with MWA Phase II at the C121 frequency band. The MWA contours are shown in Table 3.3. The ASKAP radio contours start at $150 \text{ mJy beam}^{-1}$ and increase by $\sqrt{2}$ to 900 mJy

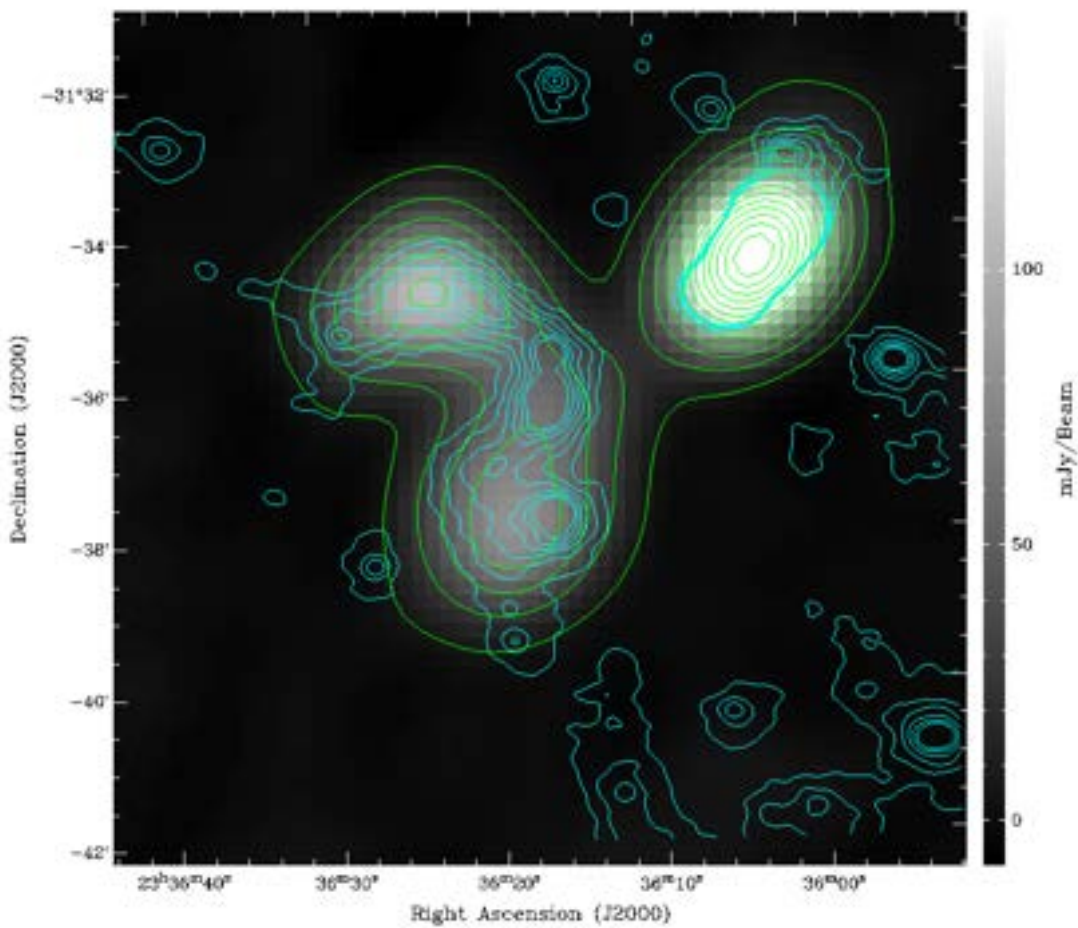


Figure 3.36: ASKAP Comparison with MWA Phase II at the C145 frequency band. The Montours are shown in Table 3.3. The ASKAP radio contours start at $150 \text{ mJy beam}^{-1}$ and increase by $\sqrt{2}$ to $900 \text{ mJy beam}^{-1}$

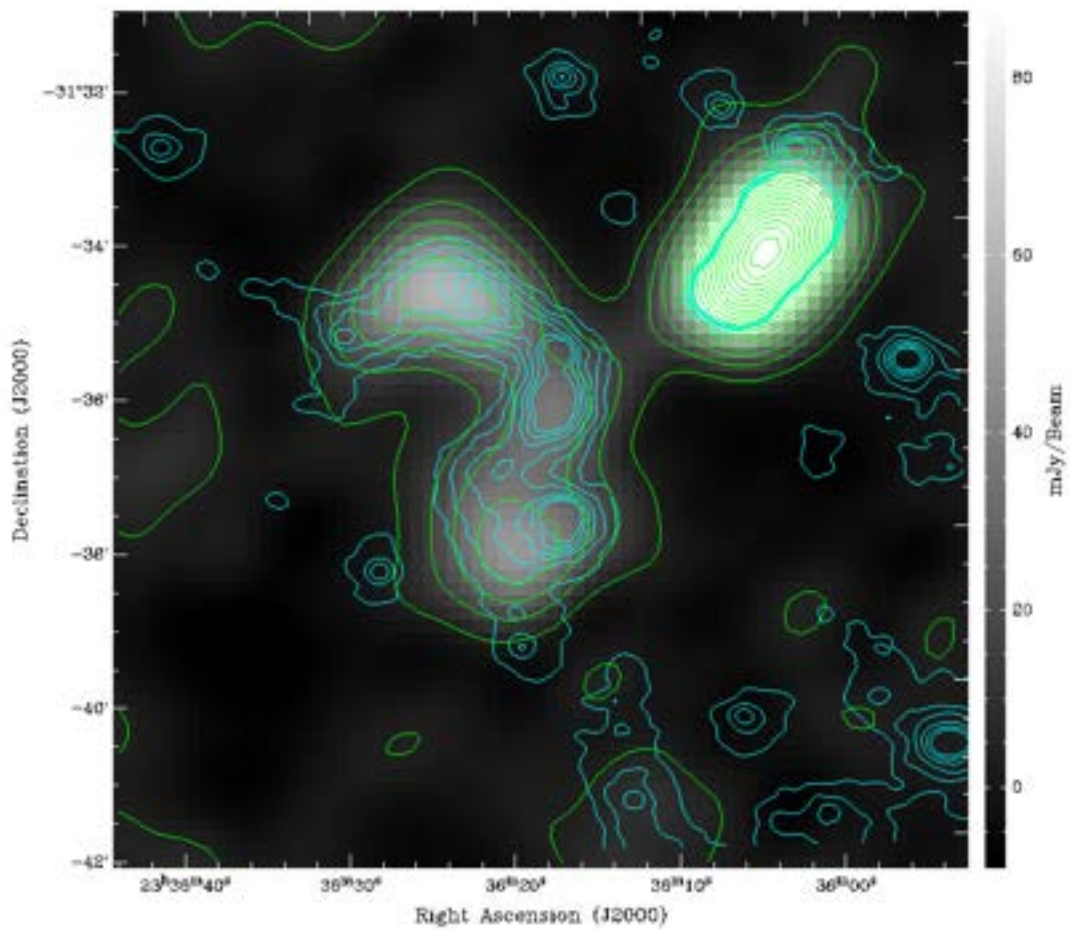


Figure 3.37: ASKAP Comparison with MWA Phase II at the C169 frequency band. MWA contours are shown in Table 3.3. The ASKAP radio contours start at 150 mJy beam $^{-1}$ and increase by $\sqrt{2}$ to 900 mJy beam $^{-1}$

3.10.2 Images with ASKAP Radio Background

Figures 3.38, 3.39 and 3.40 are similar to those in the previous section (Section 3.10.1 “Images with MWA Phase II Radio Background”), however these images have ASKAP 33 antenna observations as the background image.

In this section I show images comparing the radio emission from the ASKAP 33 antenna observations (robust = +2.0) in aqua contours, with the radio emission from the MWA Phase II observations in green contours. All contours in the images below are the same as those in the previous section. The MWA contours were set at a level that would capture the boundary of the diffuse emission and were adjusted in each frequency band to maintain the edge distance and overall shape. The ASKAP contours were unchanged throughout the images.

Observations with MWA Phase II show in green contouring show similar results as the MWA Phase I observations; however, the sensitivity is higher and shows the radio halo at a lower rms with higher frequency. The radio halo that exists around the Abell S1136 galaxy cluster, bridging across to PKS 2333-318, is seen. The filamentary structure detected with the ASKAP 33 antenna observations can be seen here to be located well within the boundary of the MWA radio halo.

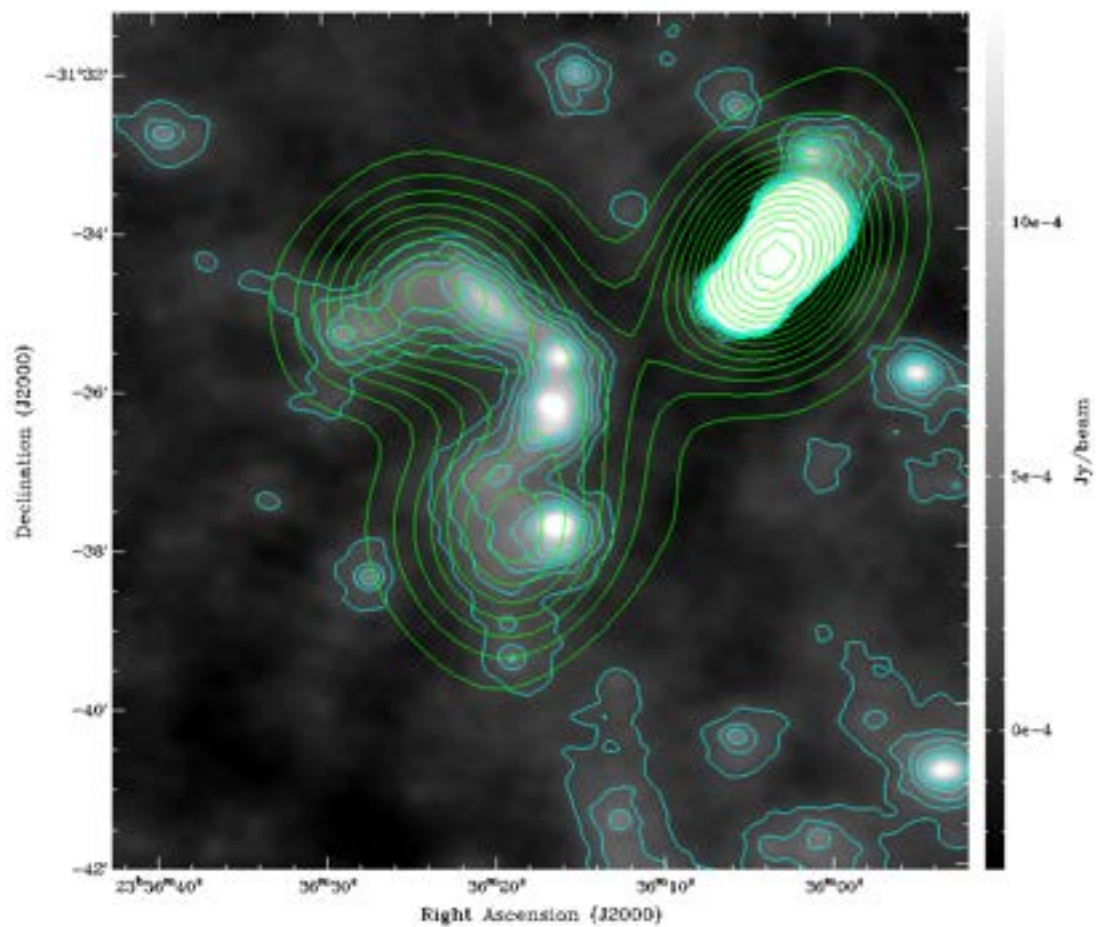


Figure 3.38: Comparison of ASKAP radio image background with MWA Phase II at the C121 frequency band. The MWA contours are shown in Table 3.3. The ASKAP radio contours start at $150 \text{ mJy beam}^{-1}$ and increase by $\sqrt{2}$ to $900 \text{ mJy beam}^{-1}$.

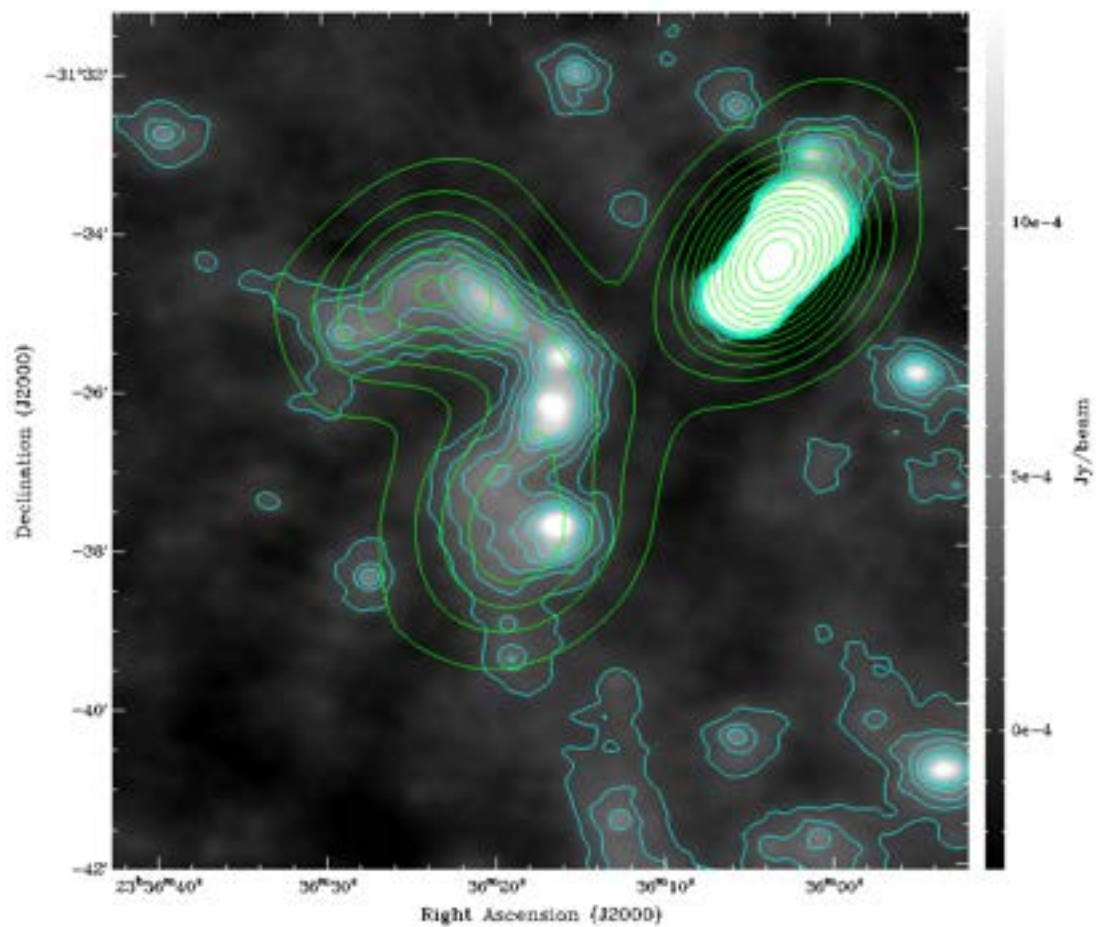


Figure 3.39: Comparison of ASKAP radio image background with MWA Phase II at the C145 frequency band. The MWA contours are shown in Table 3.3. The ASKAP radio contours start at 150 mJy beam $^{-1}$ and increase by $\sqrt{2}$ to 900 mJy beam $^{-1}$.

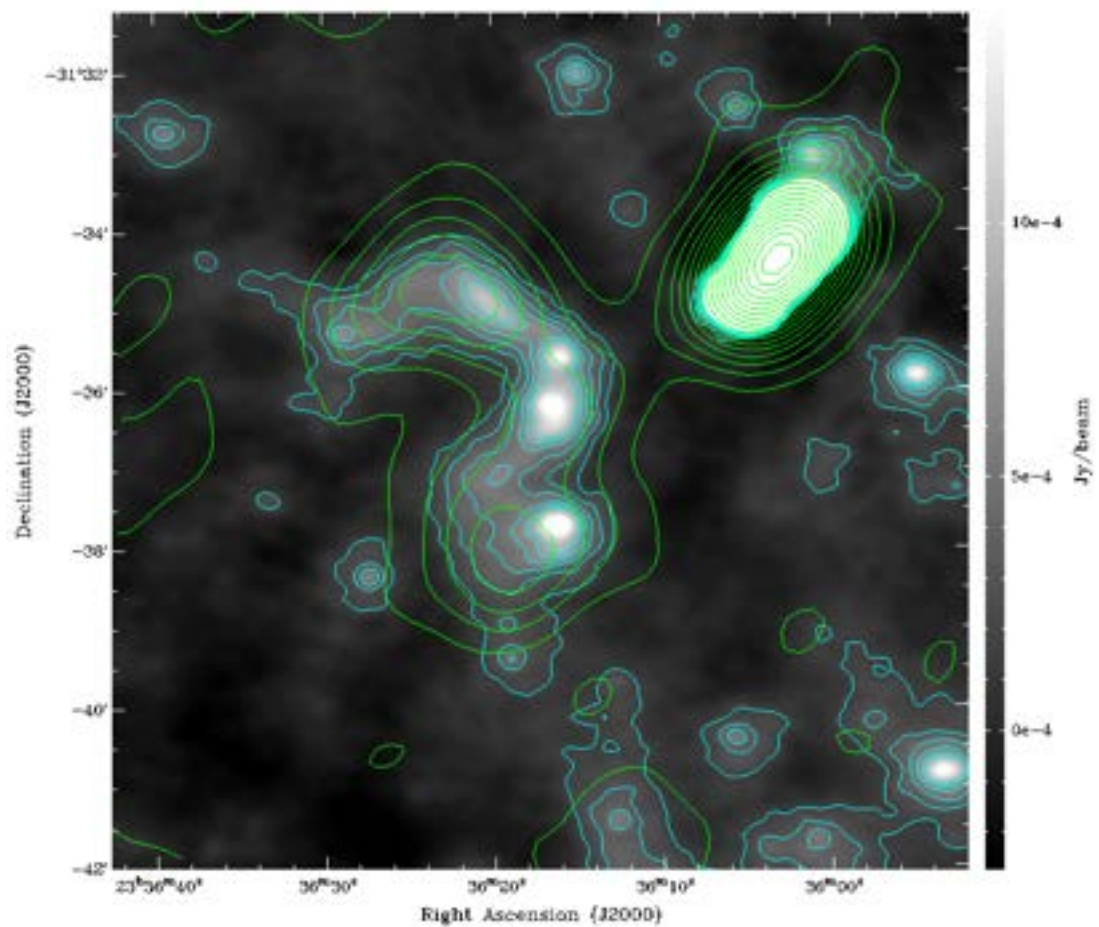


Figure 3.40: Comparison of ASKAP radio image background with MWA Phase II at the C169 frequency band. The MWA contours are shown in Table 3.3. The ASKAP radio contours start at 150 mJy beam $^{-1}$ and increase by $\sqrt{2}$ to 900 mJy beam $^{-1}$.

3.11 Image combining DSS Optical, MWA Phase I Radio, NVSS Radio, and the TFIR GMRT Sky Survey

For completeness, I have included here an image from [Duchesne et al. \(2017\)](#), shown in Figure 3.41. This image shows the Abell S1136 galaxy cluster, surveyed as part of the 168 MHz [MWA](#) Epoch of Reionization (EoR) project ([Bowman et al., 2013](#); [Offringa et al., 2016](#)). The image is an optical background from the Digitised Sky Survey, with contours overlaid from the [NRAO VLA](#) Sky Survey at 1400 MHz (red), the Murchison Wide Field Array Phase I EOR at 168 MHz (white), and the [TIFR GMRT](#) Sky Survey at 147.5 MHz (purple).

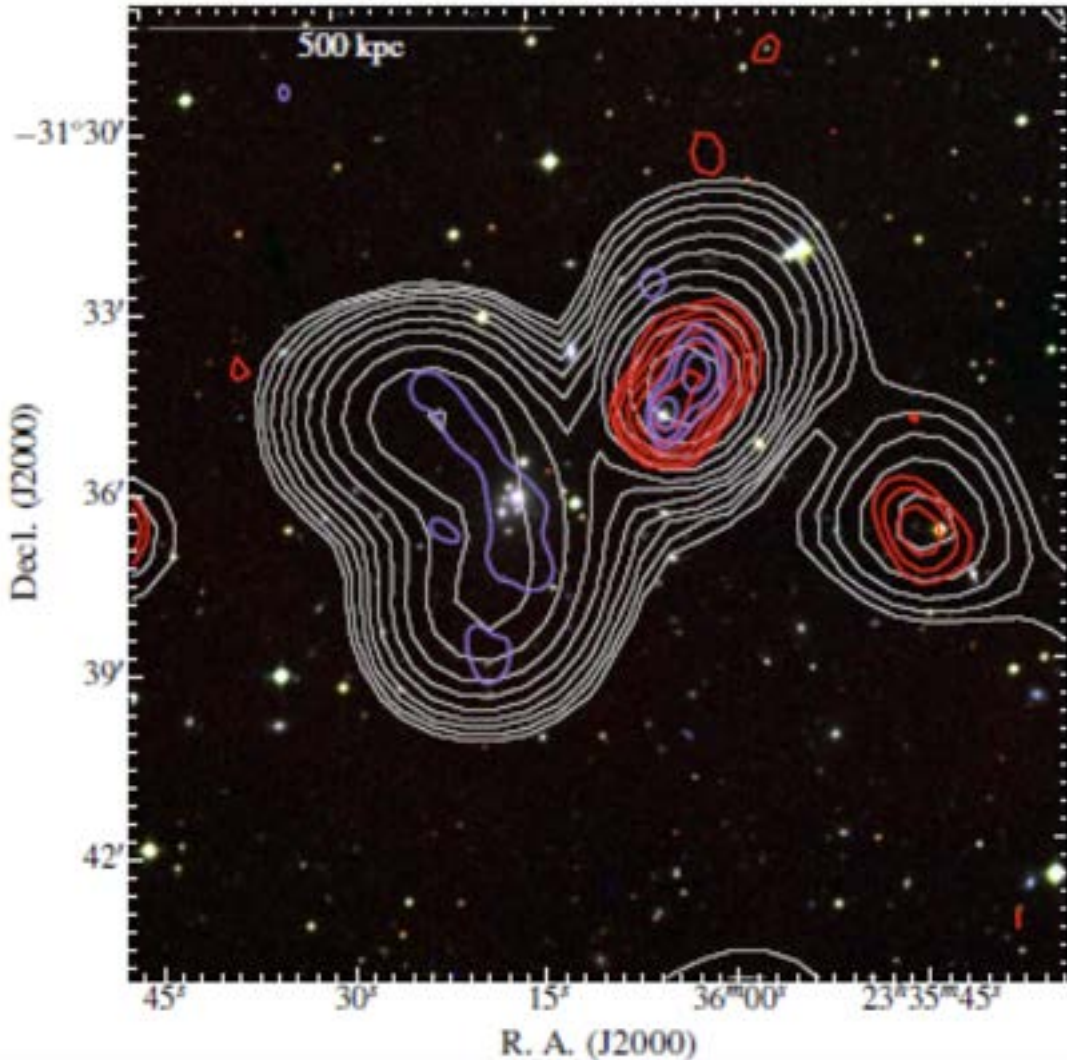


Figure 3.41: The radio emission from Abell S1136, reproduced from Duchesne et al. (2017). The background is an RGB image (DSS2: red and IR: blue). Contours are overlaid as follows: White contours show the 168 MHz EoR0 observations. The lowest contour is at 10 mJy beam^{-1} , and each higher contour increases by a factor of $\sqrt{2}$. The red contours show the 1400 MHz observations of NVSS (Condon et al., 1998), with the lowest contour at $1.5 \text{ mJy beam}^{-1}$, and each higher contour increasing by a factor of 2. The purple contours show the 147.5 MHz observations of the TFIR GMRT Sky Survey (alternate data release) (Intema et al., 2017), beginning at $14.4 \text{ mJy beam}^{-1}$ and increasing by a factor of 2.

Chapter 4

Discussion

The results described in Chapter 3 of this thesis show images of Abell S1136 produced by myself, using the Australian Square Kilometre Array Pathfinder ([ASKAP](#)) data reduction pipeline “ASKAPsoft”. Images were made at multiple levels of robustness, to try and “coax out” the diffuse emission. What I found was an amazing filamentary structure in the diffuse radio emission of Abell S1136. This has not been seen before in this galaxy cluster. In this chapter, I have also presented the results of my work looking at the spectral index and polarisation of Abell S1136, using data from [ASKAP](#) and other surveys. In this chapter, I also show serendipitous radio information for PKS 2333-318, which appears as a tailed radio galaxy with a unique single-sided *fat* tail.

4.1 The Galaxy Cluster Abell S1136

In Section 3, beginning on Page 70, I have presented results from my observations of the galaxy cluster Abell S1136, using data obtained using the [ASKAP](#) telescope. These observations were conducted with a 16 antenna array in 2017, and a 33 antenna array in 2019. These results include information on the low-frequency radio emission from Abell S1136, as well as work to obtain polarisation and spectral index measurements. In addition, I have made comparisons with data obtained from other surveys in the optical, X-ray, and radio regimes.

A recent survey of Abell S1136 with the Murchison Wide Field Array ([MWA](#)), shows a radio halo appearing strongly at 168 MHz ([Duchesne et al., 2017](#)). In my observations of the Abell S1136 galaxy cluster, using the 33 antenna array operating at the higher frequency and resolution of the [ASKAP](#) telescope, the previously-assumed diffuse emission seen

in the [MWA](#) observations appears as filamentary sub-structure in the diffuse emission of the galaxy cluster. This filamentary structure has not been seen before in Abell S1136.

4.1.1 Filamentary Structure and Spectral Index

The Abell S1136 diffuse emission, when imaged at robust = +2.0 as shown in the figures in Section [3.1.2.3](#), appears consistent with a Wide Angle Tail ([WAT](#)), but in a reverse “S” shape. However, as shown in Section [1.8 “Other Data used for Comparison”](#), the bright lobe of radio emission in the southern arm of the [WAT](#) does not have any DSS optical or [WISE](#) infrared counterpart and may be a high redshift background source.

Figure [4.1](#) shows an image from the ASKAP 33 antenna observations. The background is at robust = +2.0, overlaid with contours from MWA Phase I in green, MWA Phase II in red, and robust = -0.5 contours from the ASKAP 33 antenna observations in aqua. The [ASKAP](#) contours start at $150 \mu\text{Jy beam}^{-1}$ and increase to $900 \mu\text{Jy beam}^{-1}$ in increments of $\sqrt{2}$. Visible in the image contours are the extended radio halo MWA Phase I in green, which appears to bridge across to PKS 2333-318, the more sensitive observations with MWA Phase II in red, and the even more sensitive observations of ASKAP 33 antenna array in aqua. The reverse “S” shape is highlighted with the yellow line. On this yellow line, the filamentary structure in Abell S1136 is visible in three distinct areas:

1. The Northern Filament: The “Northern Filament” appears to extend north-east from the source labelled “A”, which is located immediately above the Brightest Cluster Galaxy ([BCG](#)), which is labelled “B”. This filament is ~ 700 to 800 kpc in length. The source labelled “A” has corresponding infrared and optical counterparts, as shown in sections [1.8.2](#) and [1.8.3](#). It would follow that the source marked as “A” is an Active Galactic Nuclei ([AGN](#)). The “Northern Filament” filament extends to the north-east and appears detached from the [AGN](#). The spectral index of this filament, as shown in Section [3.3](#) steepens as it moves away from the core. The core shows a spectral index of ~ -1.5 , with the filament showing an increase to ~ -2.5 or higher as we move along the filament.
2. The BCG Filament: The “BCG Filament” appears to extend south-east from the source marked “B”, the Abell S1136 [BCG](#) ([Lauberts and](#)

[Valentijn, 1989](#)). This filament is ~ 700 to 800 kpc in length. The **BCG** has corresponding infrared and optical counterparts, as shown in sections [1.8.2](#) and [1.8.3](#). It would follow that the source marked as “A” is an **AGN**. The “BCG Filament” extends to the south-east, and emission appears to be attached to the **AGN**. As with the “Northern Filament”, the spectral index of this filament, as shown in Section [3.3](#), steepens as it moves away from the core. The core, centred on the **BCG**, shows a spectral index of ~ -1.5 , with the filament showing a spectral index of ~ -1.5 increasing to ~ -2.5 as we move along the filament.

3. The Southern Filament: The “Southern Filament” appears to extend nearly horizontally under the source marked “C”, which located in the southern tail of the “reverse S”. The filament appears to sit tangentially to the cluster centre. This filament is the shortest at ~ 400 kpc in length. The spectral index of this filament, as shown in Section [3.3](#), remains mostly constant from east to west, at $\lesssim -2$ to ~ -2.3 .
4. The Southern “bright lobe” of Emission: As mentioned at the start of the section, and shown in sections [1.8.2](#) and [1.8.3](#), the source labelled “C” in Figure [4.1](#) has no corresponding infrared and optical counterparts. An extra-galactic source seen in radio but not optical is almost certainly an **AGN**. This bright lobe of radio emission in the southern tail might either be extended emission from another source in the cluster, possibly the **BCG** ESO 470-20 ([Lauberts and Valentijn, 1989](#)) or it might exist as a background source at high redshift.

The filaments in aqua contours shown in Figure [4.1](#), are located within the diffuse broader emission, and appear to follow the same directions as the diffuse emission; however, the northern filament has an apparent deviation away from the line of broad emission, and is mostly flat along the length; i.e., bending in the opposite direction from what you would expect.

The “northern filament” and the “**BCG** filament” appear to be associated with **AGN** activity in the centre of the Abell S1136 cluster. In contrast, the “southern filament” appears to be lying on its own and associated with the southern radio lobe.

As discussed above, the “northern filament” and the “**BCG** filament” both show a steep spectral index, which steepens as it moves away from

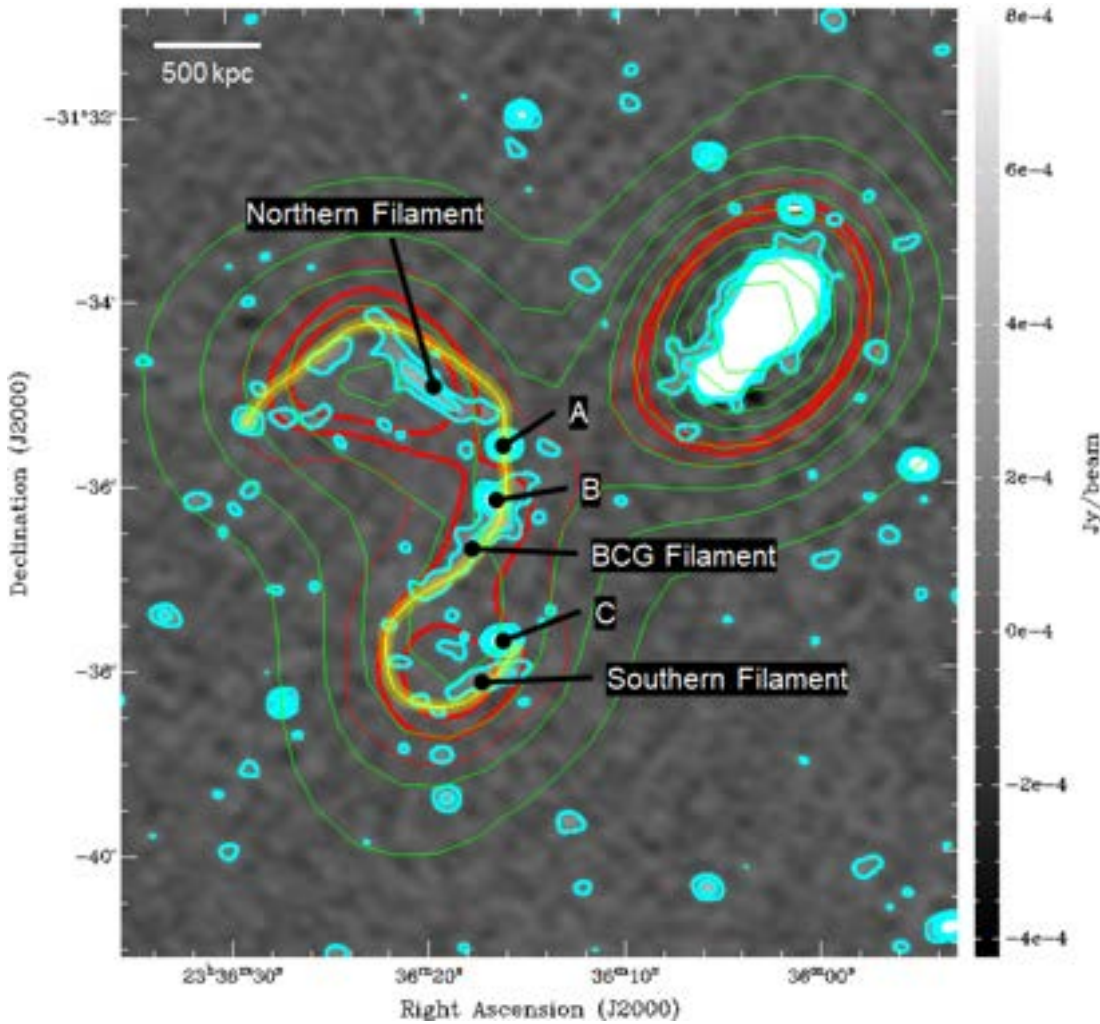


Figure 4.1: This image shows contours from MWA Phase I in green, MWA Phase II in red, and ASKAP in aqua, overlaid on an image from the ASKAP 33 antenna observations (robust = +2.0).

the core. The “southern filament” also shows a steep spectral index; however, the values remain mostly constant for the length of the filament. This is discussed in further detail below.

4.1.2 Polarisation

Synchrotron radiation emission accounts for the majority of radio continuum emission emitted from AGNs, and dominates the radio continuum emission from star-forming galaxies at frequencies below $\nu \sim 30$ GHz¹.

The polarisation of a radio-emitting source can be observed when you have an ordered magnetic field over a scale size comparable with the observing beam. The amount of polarisation of the radio emission increases with frequency (Westfold, 1959). A synchrotron source often

¹<https://www.cv.nrao.edu/~sransom/web/Ch5.html>

will not show a net polarisation, because it contains many different synchrotron radiators at different position angles. The vector sum of the individual emitters ends up with near-zero polarisation.

As shown in Section 3.2, the synchrotron emission from Abell S1336 is not seen to be polarised in the observations with the ASKAP. If the cluster is in a tangled magnetic field, there will be many different polarisation angles in the telescope beam, cancelling each other out, so the net result may be zero polarisation.

Alternatively, given the low surface brightness of the diffuse emission in the Abell S1136 galaxy cluster, the time on source may have been insufficient to yield polarisation measurements.

4.1.3 The “Radio Channel”

As shown in Section 3.6, “ASKAP Comparison with XMM-Newton X-ray”, Figure 3.26 shows my comparison between radio and X-ray observations revealing a potential radio “channel” in the X-ray emission. The significance of the radio channel was estimated to be $\sim 4.2 \sigma$. In Figure 3.27 we can see the X-ray emission centered on the Abell S1136 BCG ESO 470-20 (Lauberts and Valentijn, 1989), and although it exhibits a small centroid shift there is clear indication the hot X-ray gas is well formed and circular.

As outlined in Section 3.6, it is theorised the radio channel could be one of the following: (1) the radio channel is being formed by the radio jets from the AGN forcefully displacing the hot X-ray gas, and forcing its way through the Intra-Cluster Medium (ICM). Examples of this have been seen in NGC 1275 (Boehringer et al., 1993), and postulated by Read et al. (2001) regarding observations of Abell S0102 in the galaxy pair ESO 295-IG022 (2) the radio filament is being confined by the X-ray medium, with the X-ray gas guiding the radio emission, rather than being the result of a channel being punched by the jet (Jones et al., 2017) (3) It is possible it is just a statistical fluctuation, and the channel is simply a drop in the density of the ICM at that point, allowing the radio emission to appear as if it is creating a channel; or, the “channel” might be a dip in the photon count in that region.

Further work is required to analyse the significance of the radio channel.

4.1.4 Interaction Between Abell S1136 and PKS 2333-318

Analysis of the radio and X-ray emission in Sections 3 and 3.4 shows PKS 2333-318 and Abell S1136 in close proximity, with known redshifts of $z = 0.06134$, relatively close to Abell S1136 at $z = 0.06250$.

Coincident with my findings shown in Figure 3.25 in Section 3.5, PKS 2333-318 is within the 1.6 megaparsec ([Mpc](#)) R_{200} virial radius ([Porter and Raychaudhury, 2005](#)) of Abell S1136, (and consequently the 2.4 [Mpc](#) R_{200} virial radius ([Hilton et al., 2005](#))). PKS 2333-318 is well within the projected extent of Abell S1136's [ICM](#), as shown in Figure 3.27.

There is an indication in these results that there may be some kind of interaction between PKS 2333-318 and Abell S1136. PKS 2333-318 is within the virial radius of the Abell S1136 galaxy cluster, and within the boundary of the [ICM](#), with a small centroid shift detected in the X-ray emission. The redshift of PKS 2333-318 ($z = 0.06134$) and Abell S1136 ($z = 0.06250$) are close enough that they may be physically close to each other, or PKS2333-318 could be a background object.

4.1.5 Classification of the Abell S1136 Radio Emission Using the Taxonomy in Section 1.5.1: [Kempner et al. \(2004\)](#)

The discussion in this section uses the taxonomy outlined in Section 1.5.1, with other references as required. [Kempner et al. \(2004\)](#) separate diffuse emission into three broad categories:

1. Emission associated with active radio galaxies: This includes Confined Cluster Core / Radio Galaxy (FRI, WAT, NAT) / Classic Double (FRII)
2. Emission associated with extinct / dying radio galaxies: This includes AGN relic / Radio Phoenix
3. Emission not associated with radio galaxies: This includes Radio Gischt / Mini-Halo / Halo

In these observations, the polarisation of the sources in Abell S1136 is minimal. It might be that the sources in the Abell S1136 cluster are non-polarised; or if the cluster is in a tangled magnetic field, there will be many different polarisation angles in the telescope beam, cancelling each other out, so the net result may be zero polarisation.

It might also be possible that given the low surface brightness of the diffuse emission in the cluster, the time on source may have been insufficient to yield polarisation measurements.

For this reason, the (lack of) polarisation detected in these observations is not included in classifying the emission.

The diffuse emission in Abell S1136 presents in a reverse “S” shape, similar to the characteristics of an Fanaroff-Riley Type I (**FRI**) type radio galaxy. Within the diffuse emission, the filaments that have been discovered in these observations show the following characteristics:

1. the “northern filament” (aka: the “radio channel”):

- (a) The “northern filament” and the “**BCG** filament” appear to be aligned within the broad diffuse emission. The broad diffuse emission appears symmetric about a central core, similar to an **FRI** type radio galaxy
- (b) is ~ 700 to 800 kpc in length
- (c) has a very steep spectral index, steepening from ~ -1.5 to $\lesssim -2.5$ as you move from the centre of the cluster, along the length of the filament
- (d) appears anti-correlated with the X-ray emission
- (e) does not show polarisation in these observations
- (f) appears associated with an **AGN**

2. the “BCG Filament”:

- (a) The “**BCG** filament” and the “northern filament” appear to be aligned within the broad diffuse emission. The broad diffuse emission appears symmetric about a central core, similar to an **FRI** type radio galaxy
- (b) is ~ 700 to 800 kpc in length, nearly equal in length to the “northern filament”, indicating symmetry
- (c) has a very steep spectral index, steepening from ~ -1.5 to $\lesssim -2.5$ as you move from the centre of the cluster, along the length of the filament
- (d) does not show polarisation in these observations
- (e) appears associated with an **AGN**

3. the “southern filament”:

- (a) is situated ~ 1 Mpc from the cluster centre and appears to lie tangentially
- (b) is ~ 400 kpc in length
- (c) has a very steep spectral index, which remains constant at ~ -2 to ~ -2.3 along the length of the filament
- (d) does not show polarisation in these observations
- (e) appears coincident with the southern “bright lobe” of radio emission labelled as Source “C” in Figure 4.1. However, source “C” does not appear to have a corresponding optical or infrared counterpart, and might either be a high redshift background AGN, or a bright lobe of emission in the WAT. The association of the “southern filament” to the galaxy cluster needs to be examined further.

Using Kempner et al. (2004), the location, size, morphology, spectral index, and relationship to hot gas, means the classification of the sub-structure in the Abell S1136 diffuse emission would not be associated with a VLBI Core, a Confined Cluster Core Source, a standard Radio Galaxy, or a Classical Double.

The emission could, therefore, be classified as one of the following:

1. the “northern filament” (aka the “radio channel”) appears to be located well *within* the diffuse emission at the centre of the galaxy cluster. It seems to be associated with either the AGN labelled “A” or “B”, in Figure 4.1. This would classify the “northern filament” as either:
 - (a) an AGN Relic
 - (b) a Radio Phoenix
 - (c) given the proximity of this filament to an AGN, in this taxonomy it is not considered that the “northern filament” is a Radio Gischt, a Mini-Halo, or a Radio Halo (types *not* associated with radio galaxies)
 - (d) filamentary sub-structure that, thanks to the higher sensitivity and resolution of new generation low-frequency radio telescopes, is now visible in the diffuse arms of an FRI
2. the “BCG Filament”, as with the “northern filament”, appears to be located well *within* the diffuse emission at the centre of the

galaxy cluster, and seems to be associated with either the **AGN** labelled as Source “A” or “B”, in Figure 4.1. This would classify the “BCG Filament” as either:

- (a) an AGN Relic
- (b) a Radio Phoenix
- (c) given the proximity of this filament to an **AGN**, in this taxonomy it is not considered that the “BCG filament” is a Radio Gischt, a Mini-Halo, or a Radio Halo (types *not* associated with radio galaxies)
- (d) filamentary sub-structure that is now visible in the diffuse arms of an **FRI**, thanks to the higher sensitivity and resolution of new generation low-frequency radio telescopes

3. the “southern filament” is a special case. As mentioned previously, the bright lobe of emission coincident with this filament might be a high redshift background **AGN**. It would appear that the “southern filament” is associated with Abell S1136, but may or may not be associated with Source “C”. Therefore, this filament can be classified as follows:

- (a) If Source “C” is not a high redshift background **AGN**, and is in the Abell S1136 cluster, the emission in the “southern filament” might be:
 - i. an AGN relic
 - ii. a radio phoenix
 - iii. filamentary sub-structure that is now visible in the diffuse arms of an **FRI**, thanks to the higher sensitivity and resolution of new generation low-frequency radio telescopes
- (b) If Source “C” is a high redshift background **AGN**, and not in the Abell S1136 cluster, the emission in the “southern filament” might be:
 - i. a Radio Gischt
 - ii. a Mini-Halo
 - iii. a Radio Halo

4.1.6 Classification of the Abell S1136 Radio Emission Using Feretti et al. (2012)

Sources of diffuse radio emission are generally allocated into groups of halos, relicts and mini-halos Feretti and Giovannini (1996); Feretti et al. (2012); Kempner et al. (2004), dependant on the cluster type (merging or cool-core), and the location of the source within the cluster.

The discussion in this section uses the classification methods from Feretti et al. (2012), as an alternative method with which to classify the diffuse structure in the Abell S1136 galaxy cluster. The discussion below is divided into “Radio Relics”, “Radio Halos”, and “Radio Mini-Halos”. Feretti et al. (2012) further separate the classification of relicts into two distinct components and offer an updated discussion on Halos and Mini-Halos.

4.1.6.1 Radio Relics (aka. “Gischt”)

Radio relicts, first mentioned in Section 1.4.1, are diffuse emission, low surface brightness, extended radio sources that do not have an optical counterpart, and they exhibit steep spectrum in the radio regime; they typically present on scales of $\gtrsim 1\text{Mpc}$, but unlike a radio halo, they are located at the cluster periphery (Govoni et al., 2001b; Feretti et al., 2012). Classically, relicts tend to appear as an elongated radio structure, with emission that is linearly polarised at ~ 10 to 30 percent (Giovannini and Feretti, 2004a; Feretti et al., 2012; Govoni et al., 2001b). Relics that appear roundish and more regular have also been discovered and can be associated with the cluster centre or the periphery. Examples of both classes can be seen in Giovannini and Feretti (2004b).

Feretti et al. (2012) discuss a morphology for radio relicts which is based only on the observable morphology, and divide the relic emission into two categories: (1) “elongated relicts”, and (2) “roundish relicts”. A summary of the classification from Feretti et al. (2012) is presented below, with discussion on the classification of the Abell S1136 diffuse emission, using this system, at the end of the section.

Elongated Relics Located in the cluster periphery, elongated relicts are characterised by their long narrow shape, and lie roughly tangential to the cluster centre. There is little evidence of filamentary sub-structure. An excellent example was detected by van Weeren et al. (2010). Figure

4.2 shows the long narrow, slightly curved, northern relic in CIZAJ2242.8+530 hugging the edge of the cluster ICM. The relic is strongly polarised and has a very steep spectrum, as shown in Figure 4.3.

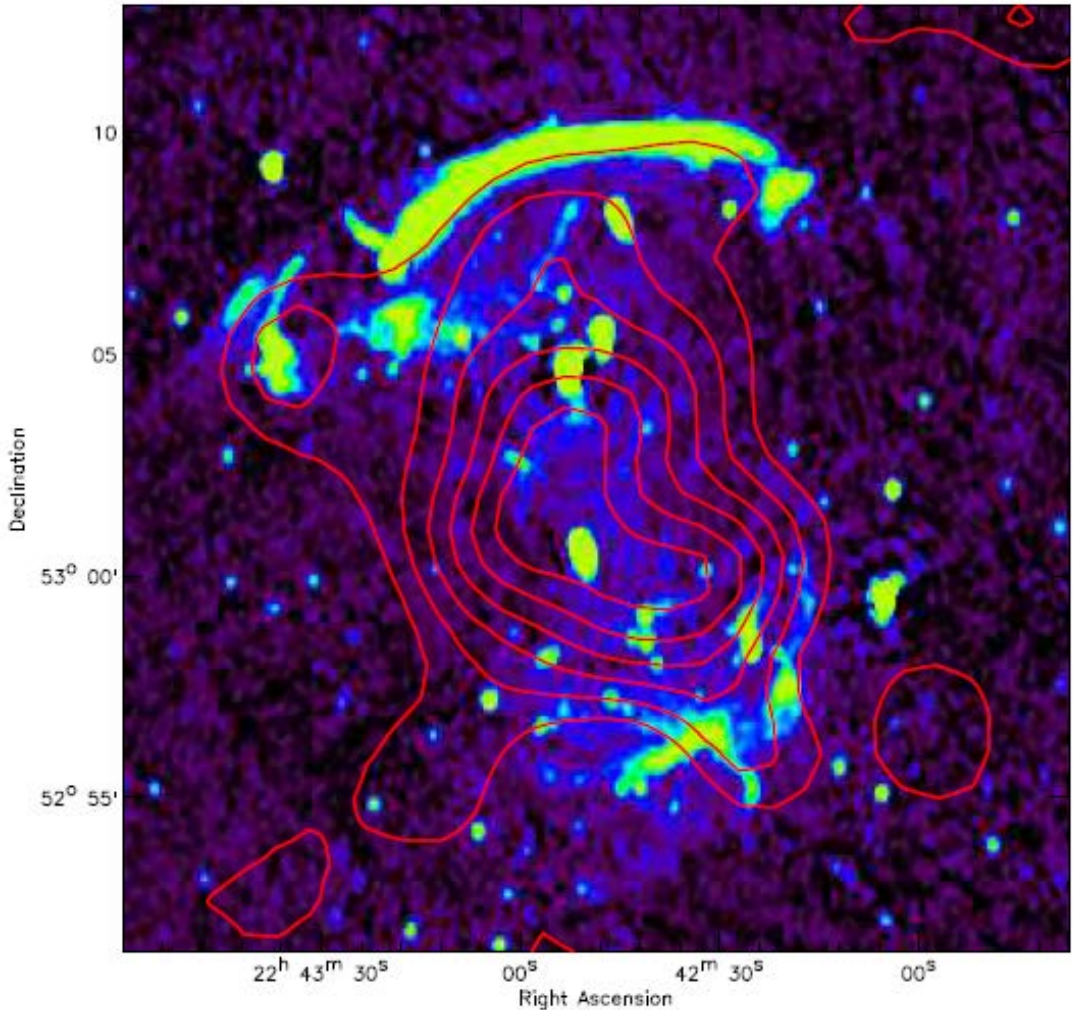


Figure 4.2: Reproduced from [van Weeren et al. \(2010\)](#): “WSRT radio image at 1.4 GHz. The image has a resolution of 16.5 arcsec \times 12.9 arcsec and the rms noise is 19 $\mu\text{Jy beam}^{-1}\text{beam}^{-1}$. Red contours (linearly spaced) represent the X-ray emission from ROSAT showing the hot ICM.”

Roundish Relics Although having a distinctly different shape, roundish relics present as a diffuse extended radio source, located at the cluster periphery, but connected in some way to an AGN. [Feretti et al. \(2012\)](#) defined a roundish relic to include the sources named Radio Phoenix in [Kempner et al. \(2004\)](#), and relic sources located near a First Ranked Galaxy (FRG) ([Giovannini and Feretti, 2004a](#)). Sizes can range from ~ 100 kpc, as in Abell 2063 and Abell 4038, to ~ 350 kpc, as in Abell 85. As with elongated relics, there is no optical counterpart. It is unlikely

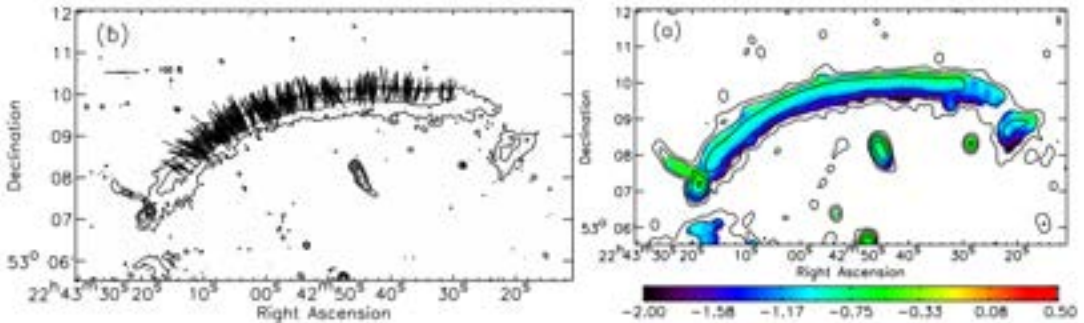


Figure 4.3: Reproduced from Feretti et al. (2012): “Left panel: Contours of the radio emission of the northern relic in CIZAJ2242.8+5301, obtained with the GMRT at 610 MHz. Superimposed lines represent the polarization electric field vectors obtained with the VLA at 4.9 GHz. The length of the vectors are proportional in length to the polarization fraction. Right panel: Radio spectral index map of the same relic, obtained with a power-law fit to measurements at 5 frequencies between 2.3 and 0.61 GHz. Contours of the radio emission are from WSRT 1.4 GHz.”

that a roundish relic is merely an elongated relic viewed face on, as the population of elongated relics already known is too high to imply projection effects.

When observed at high resolution, roundish relics show evidence of filaments in the substructure (Govoni et al., 2001b). Given these sources lie close to an AGN, one hypothesis is that a roundish relic is the radio lobe from previous AGN activity that has switched off, and been re-accelerated by energy from a shock wave. Another possibility, presented by Mathews and Brighenti (2008), is the connection between X-ray cavities and radio lobes; whereby a radio bubble is blown into the cluster gas, which then expands to the cluster outskirts, where cosmic rays impact into the surrounding medium, creating small relics located near the AGN.

4.1.6.2 Radio Halos

Radio halos are diffuse, extended sources, located at or near the cluster centre, and are found in clusters undergoing a merger process (Feretti, 2002; Giovannini and Feretti, 2002; Feretti et al., 2012; Kempner et al., 2004). Sizes for radio halos are typically $\gtrsim 1$ Mpc. They are typically low surface brightness objects, with a flux density in the range of $\sim 1 - 0.1 \mu\text{Jy arcsec}^{-2}$ at 1.4 GHz. They have a regular morphology and have minimal polarisation, mostly only a few percents.

The prototypical radio halo is at the centre of the Coma Cluster (Large et al., 1959; Willson, 1970).

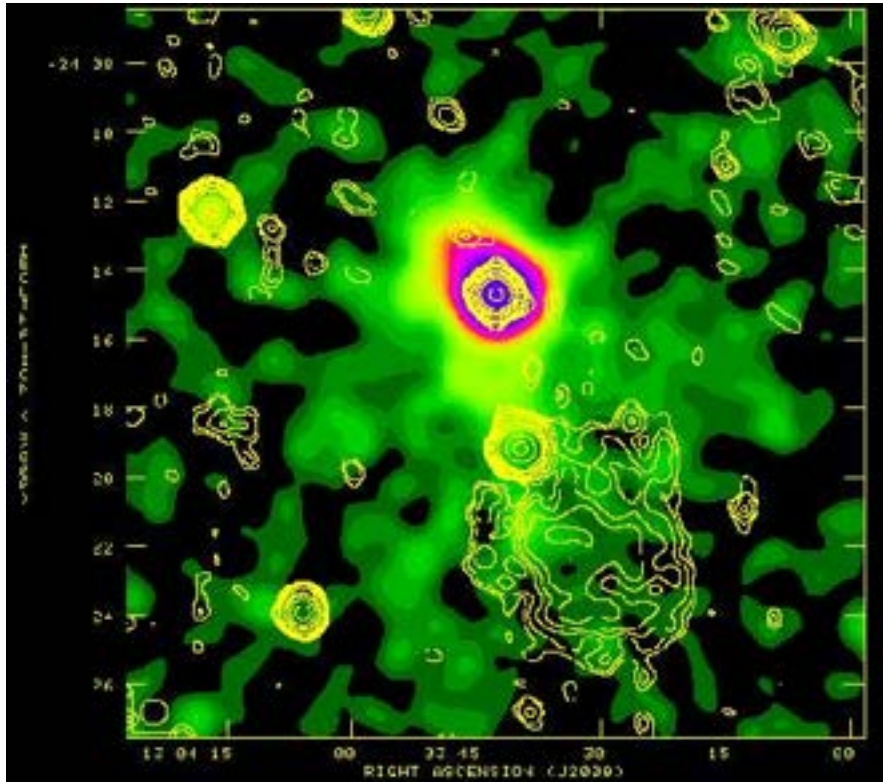


Figure 4.4: Reproduced from [Giovannini and Feretti \(2004a\)](#): “Radio image (contours) of the radio Relic in the cluster A1664 ([Govoni et al., 2001b](#)) from NVSS data, overimposed to the cluster ROSAT X-ray image (colour).”

An analysis of radio halos in National Radio Astronomy Observatory (NRAO) Very Large Array (VLA) Sky Survey (NVSS) sample data, by [Giovannini et al. \(1999b\)](#), discovered the occurrence of radio halos increases with the host clusters X-ray luminosity, reaching about 25 % in clusters with $L_x > 5 \times 10^{44}$ erg/s ([Giovannini and Feretti, 2002](#)). With improved statistics, [Cassano et al. \(2011\)](#) confirmed this relationship, and found radio halos in ~ 30 % of galaxy clusters with $L_x > 5 \times 10^{44}$ erg/s.

Table 2 from [Feretti et al. \(2012\)](#) shows the spectral index of radio halos, including the cluster X-ray temperature in KeV, and includes measurements of various clusters across multiple frequency measurements (a minimum of 2 and a maximum of 3). The data is taken from a listing of all clusters in September 2011 known to host a radio halo, the “September2011-Halo collection” shown in Table 1 [Feretti et al. \(2012\)](#). The lowest and highest X-ray temperatures in a cluster with a radio halo were measured at 5.2 KeV in Abell 521 ([Giovannini et al., 2009](#)), and 13.3 KeV in Abell 2163 ([Feretti et al., 2001](#)).

4.1.6.3 Radio Mini-Halos

Relaxed cool-core clusters are the hosts for radio mini-halos. They usually surround a powerful radio galaxy and are centrally located. The Perseus cluster is the prototype of the mini-halo class. Sizes for a mini-halo extend to $\gtrsim 500$ kpc from the central AGN, with typical low surface brightness and a steep spectral index. A mini-halo is considered to be just that; a mini version of a radio halo. However, their classification is difficult. In general, a mini-halo can be distinguished from other steep spectrum sources in clusters (for example radio bubbles), as the gas in the ICM of a mini-halo is thought to be inherently mixed with the radio emission that has originated from the magnetic fields and relativistic particles. Feretti et al. (2012) note that they do not consider a mini-halo as a source where the gas in the ICM is separated from the non-thermal diffuse emission - as described above in Halos, where the diffuse emission creates a cavity in the ICM.

Radio mini-halos have steep spectra, the same as a radio halo, with some evidence of radial spectral steepening as seen in Perseus cluster (Gitti et al., 2002b), Abell 2626 (Gitti et al., 2004), and Ophiucus (Murgia et al., 2010b).

Some clusters that host a mini-halo have also been observed to have a cold front associated with the sloshing of the X-ray gas in the core. It has been hypothesised that gas sloshing may generate turbulence in the core, which might be the process which re-accelerates the relativistic electrons necessary to form a mini-halo (Mazzotta and Giacintucci, 2008; ZuHone et al., 2011).

Table 5 from Feretti et al. (2012) shows the “September2011-Mini-halos collection”, which includes the luminosity of the X-ray gas in the cluster mini-halo. As with the data given for radio halos in the previous section, the mini-halo data is taken from a listing of all clusters in September 2011 known to host a radio mini-halo. The lowest and highest X-ray luminosity in a cluster with a radio mini-halo was measured in the $L_x[0.1-2.4\text{keV}]$ band; the lowest was Abell 2626 at $1.18 \times 10^{44}\text{erg/sec}$ (Gitti et al., 2004), and the highest was in the most X-ray-luminous cluster RXJ1347.5-1145 at $51.95 \times 10^{44}\text{erg/sec}$ (Gitti et al., 2007). The mean and median values for the data are $16.18 \times 10^{44}\text{erg/sec}$ and $10.33 \times 10^{44}\text{erg/sec}$ for 10 mini-halos.

Figure 4.5, reproduced from Ferrari et al. (2011), shows the mini-halo

in the galaxy cluster RXJ1347.5-1145, using data from the Giant Metrewave Radio Telescope ([GMRT](#)) at 614 MHz.

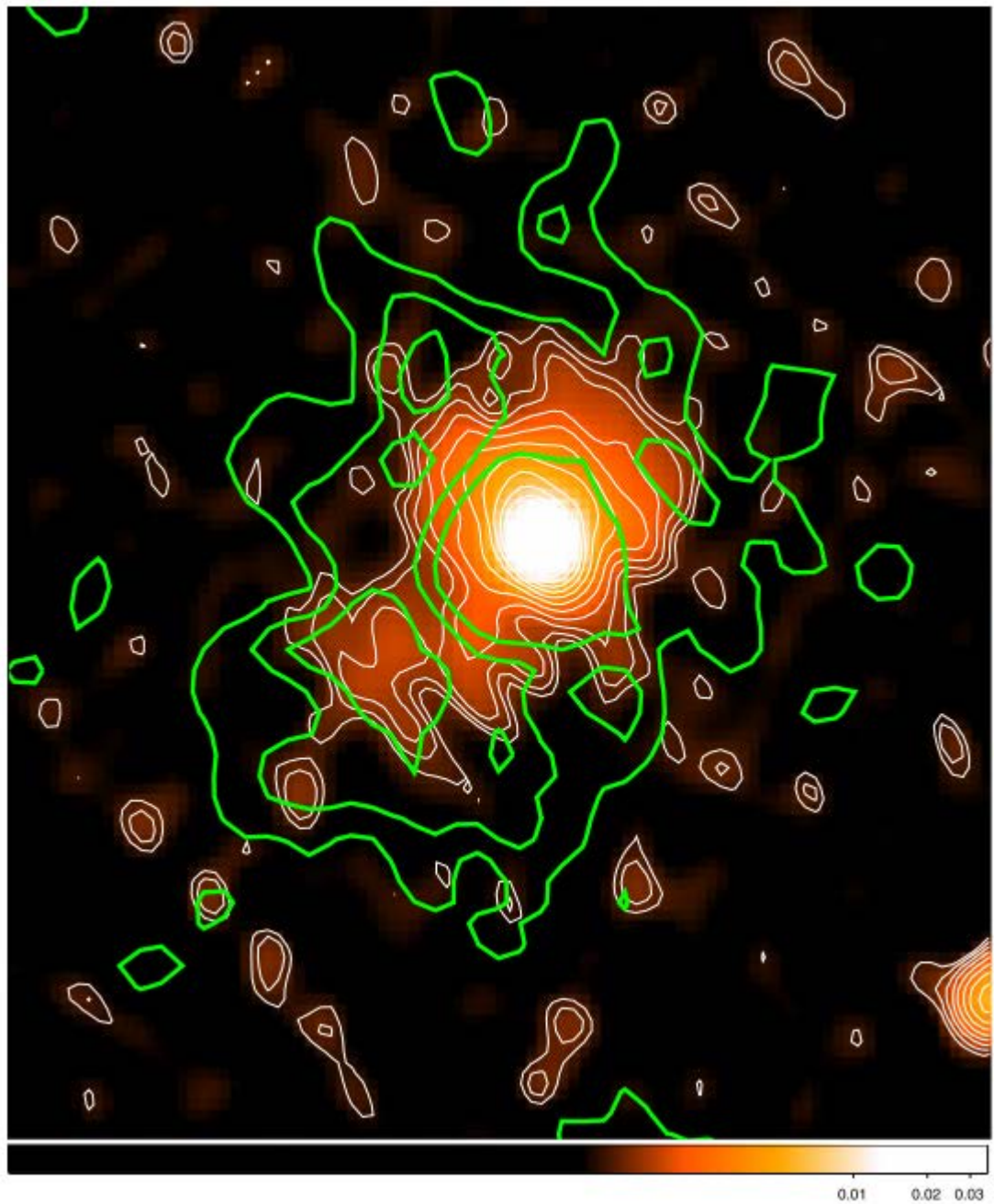


Figure 4.5: RXJ1347.5-1145, reproduced from [Feretti et al. \(2012\)](#): “GMRT 614 MHz total intensity map and contours (white) of the mini-halo in RXJ1347.5-1145. The resolution is $4.8'' \times 3.5''$. The first contour levels are drawn at $-0.3, 0.3 \text{ mJy beam}^{-1}$ and the rest are spaced by a factor $\sqrt{2}$. Contours of the MUSTANG SZE image ([Mason et al., 2010](#)) of the cluster are overlaid in green.”

4.1.6.4 Discussion on Abell S1136 Diffuse Emission Using Feretti et al. (2012a)

As discussed previously, in these observations, the polarisation of the sources in Abell S1136 is minimal. It might be that the sources in the cluster are non-polarised, or if the cluster is in a tangled magnetic field there will be many different polarisation angles in the telescope beam, cancelling each other out; so the net result may be zero polarisation. It might also be possible that given the low surface brightness of the diffuse emission in the cluster, the time on source may have been insufficient to yield polarisation measurements.

For this reason, as with the classification using Kempner et al. (2004), the (lack of) polarisation detected in these observations is not included in classifying the emission using the schema from Feretti et al. (2012).

Within the Abell S1136 diffuse emission, the filaments that have been discovered in these observations show the following characteristics:

1. the “northern filament” (aka: the “radio channel”):
 - (a) The “northern filament” and the “Brightest Cluster Galaxy (BCG) filament” appear symmetric about a central core, similar in nature to an Fanaroff-Riley Type I (FRI) type radio galaxy
 - (b) is ~ 600 kpc in length
 - (c) has a very steep spectral index, steepening from ~ -1.5 to $\lesssim -2.5$ as you move from the centre of the cluster, along the length of the filament
 - (d) appears anti-correlated with the X-ray emission
 - (e) does not show polarisation in these observations
 - (f) appears associated with an Active Galactic Nuclei (AGN)
2. the “BCG Filament”:
 - (a) The “BCG filament” and the “northern filament” appear symmetric about a central core, similar in nature to an FRI type radio galaxy
 - (b) is ~ 500 kpc in length, nearly equal in length to the “northern filament”, indicating symmetry
 - (c) has a very steep spectral index, steepening from ~ -1.5 to $\lesssim -2.5$ as you move from the centre of the cluster, along the length of the filament

- (d) does not show polarisation in these observations
 - (e) appears associated with an **AGN**
3. the “southern filament”:
- (a) is ~ 300 kpc in length
 - (b) has a very steep spectral index, which remains constant at ~ -2 to ~ -2.3 along the length of the filament
 - (c) does not show polarisation in these observations
 - (d) appears coincident with the southern “bright lobe” of radio emission labelled as Source “C” in Figure 4.1. However, source “C” does not appear to have a corresponding optical or infrared counterpart, and might either be a high redshift background **AGN**, or a bright lobe of emission in the Wide Angle Tail (**WAT**). The association of the “southern filament” to the galaxy cluster needs to be examined further.

In this schema, the location, size, morphology, and spectral index, are considered to classify the filamentary sub-structure as follows:

1. the “northern filament” (aka the “radio channel”) appears to be located well within the diffuse emission at the centre of the galaxy cluster. It seems to be associated with either the **AGN** labelled “A” or “B”, in Figure 4.1.

Based on the morphology of this filament, we can exclude the likelihood of this being a “roundish relic”.

The Abell S1136 galaxy cluster is already known to host a “Radio Halo” when observed at 168 MHz ([Duchesne et al., 2017](#)), however when observed with the Australian Square Kilometre Array Pathfinder (**ASKAP**) at 864.5 MHz, the low surface brightness radio emission and sub-structure seen with these observations, does not appear consistent with the existence of a ‘Mini-Halo’ in the centre of the cluster.

The most sensible classification for the “northern filament” is that of a “Radio Relic”. However, “Radio Relics” as we have known them exist in the cluster periphery, and lie perpendicular to the cluster centre. This raises the question, are we now seeing with higher sensitivity radio observations that “Radio Relics” also present as filamentary sub-structure, and can be located in the cluster centre, extending radially from the core?

- the “BCG filament”, as with the “northern filament”, appears to be located well within the diffuse emission at the centre of the galaxy cluster, and seems to be associated with either the AGN labelled as Source “A” or “B”, in Figure 4.1.

Apart from the direction in which the filament is extending from the centre of the cluster, the “BCG filament” is similar to the “northern filament”, with comparable features.

In this schema, the classification of the “BCG filament” is, therefore, the same as the “northern filament”.

- the “southern filament”, as mentioned previously, is a particular case. The bright lobe of emission coincident with this filament might be a high redshift background AGN. It would appear that the “southern filament” is associated with Abell S1136, but may or may not be associated with Source “C” in Figure 4.1.

Ignoring Source “C”, the “southern” filament lies ~ 1 Mpc from the cluster centre and appears to lie tangentially. As with the “northern filament” and the “BCG filament”, the morphology would exclude this filament as a “roundish relic” or a “Radio Halo”.

With the location, size, and morphology of the “southern filament”, the most sensible classification is that of a “Radio Relic”; albeit slightly smaller than expected at ~ 400 kpc.

The other possibility, if Source “C” is located in the cluster and is not a background source, is that Source “C” might be hosting a “Radio Mini-Halo”; however, this would mean the mini-halo is off centre in the cluster. As with the “northern filament” and the “BCG filament”, are we now seeing with higher sensitivity radio observations that “Radio Mini-Halos” can exist off centre in a galaxy cluster?

4.1.7 Classification of the Abell S1136 Radio Emission when Compared with the Recent Literature

Other possibilities for the classification of the filamentary sub-structure in Abell S1136 include those presented in Section 4.1.7.

- Does Abell S1136 have a cold front associated with the “northern” and “BCG” filaments, similar to Abell 2626?

2. Does the elongated morphology of the filaments describe particle re-acceleration by turbulence, which is causing particle re-acceleration by stirring either the X-ray gas and the magnetic field (unobserved in this work), and causing instability in the cluster, similar to that proposed for Abell 2142 ([Venturi et al., 2007](#))?
3. If there is re-acceleration by turbulence, is it caused by an interaction between Abell S1136 and PKS 2333-318?
4. Another possibility for the “southern filament” is that it is similar to the “GReET” discovered by [de Gasperin et al. \(2017\)](#) in Abell 1033, with the “southern filament” being evident as non-thermal fossil radio plasma gently re-energised by perturbations in the Intra-Cluster Medium ([ICM](#)).
5. Is there central sloshing of the X-ray gas, similar to Abell 2142 ([Venturi et al., 2017b](#)) and Abell 2626 ([Clarke and Ensslin, 2001](#)), in a process *similar* to what has been suggested for mini-halos ([Feretti et al., 2012](#)).

It is clear from these observations, and from those discussed in Section 1.6 “[Evidence of Filamentary Structure in Recent Literature](#)”, that higher resolution observations of galaxy cluster diffuse emission are showing us that cluster radio emission is more complex than we thought, and classification of filamentary sub-substructure in diffuse radio emission is difficult using current models, and current observations.

Chapter 5

Conclusions and Future Work

5.1 Conclusions

In this thesis, I have presented my observations of the diffuse radio emission from the galaxy cluster Abell S1136, first observed by [Olowin \(1988\)](#) in the Southern Extension to the [Abell et al. \(1989\)](#) All-Sky Catalog. These observations were made with the Australian Square Kilometre Array Pathfinder ([ASKAP](#)) telescope, as part of the Early Science program of the Evolutionary Map of the Universe ([EMU](#)) ([Norris et al., 2011](#)); a wide-field, radio continuum survey, planned for the Australian Square Kilometre Array Pathfinder ([ASKAP](#)) ([Norris et al., 2011](#)).

The diffuse emission in the Abell S1136 galaxy cluster, previously identified as a radio halo in surveys with Murchison Wide Field Array ([MWA](#)), appears to extend in a reverse “S” shape from the Active Galactic Nuclei ([AGNs](#)) in the core of the cluster, shown in Figure [4.1](#). This emission appears consistent with a Fanaroff-Riley Type I ([FRI](#)) type radio galaxy with a Wide Angle Tail ([WAT](#)). The diffuse emission breaks up into several filamentary structures, which is interpreted as synchrotron emission from shock-excited electrons.

I found there is evidence of filamentary structure in three distinct areas of the cluster centre, which I have labelled as:

1. The “Northern Filament.”
2. The “BCG Filament.”
3. The “Southern Filament.”

The “northern filament” and the “Brightest Cluster Galaxy ([BCG](#)) filament” are similar in size at ~ 500 to 600 kpc. The “southern filament” is smaller at ~ 250 to 300 kpc.

All three filaments have a very steep spectral index; the “northern filament” and the “BCG filament” both have a spectral index starting at ~ -1.5 , steepening to and exceeding $\lesssim -2.0$. The “southern filament” has a spectral index that remains nearly constant for the length at an average of ~ -2.1 .

The bright lobe of emission coincident with the “southern filament” has either a very faint, or no optical counterpart; and a very faint or no infrared emitting counterpart. Since an extra-galactic source seen in radio but not optical is almost certainly an AGN, this bright lobe might either be related to another source in the Abell S1136 cluster or be a background source at higher redshift.

Analysis of radio and X-ray data shows Abell S1136 to be a relaxed cluster that is likely in equilibrium. The X-ray and radio emission was found to be coincident with the centre of the galaxy cluster, located on the BCG ESO 470-20 ([Lauberts and Valentijn, 1989](#)). The ‘northern filament’ showed as being a possible “radio channel”, either punching its way through the hot gas of the Intra-Cluster Medium (ICM) or being constrained in some way by the ICM. In the analysis presented here, Abell S1136 does not have a cool core. There is a small centroid shift, which indicates the possibility of a slightly disturbed system, and possible interaction between Abell S1136 and PKS 2333-318.

The filamentary sub-structure in Abell S1136 is quite unusual, and difficult to interpret in the framework of currently proposed models. The taxonomies presented in Sections 4.1.5 and 4.1.6, do not cover the filamentary structure we are now seeing in Abell S1136, or the discoveries discussed in [Evidence of Filamentary Structure in Recent Literature](#) in Section 1.6.

The main result from this thesis is that it raises questions about what is causing these sub-structures:

1. Does the elongated morphology of the filaments describe particle re-acceleration by turbulence, generated either by stirring the gas and magnetic fields on a larger scale?
2. Does Abell S1136 have a cold front associated with the “northern” and “BCG” filaments, similar to Abell 2626?
3. Is the “southern filament” associated with the Abell S1136 galaxy cluster, or is it a high redshift background source?
4. Is the “southern filament” a “GReeT” similar to that seen in Abell 1033?

5. Is there an interaction with Abell S1136 and PKS 2333-318, which is causing particle re-acceleration by stirring either the X-ray gas and the magnetic field (unobserved in this work), and causing instability in the cluster, similar to that proposed for Abell 2142 (Venturi et al., 2007)?

5.2 Future Work

More work is needed to understand the nature of the emission in Abell S1136 and classify the filamentary sub-structure.

In all the results presented above, I noticed that the majority of the galaxy clusters being observed are in the Northern Hemisphere. Additionally, as detailed by De Propris et al. (2002) in a study of galaxy clusters in The 2dF Galaxy Redshift Survey, “There is a deficiency of clusters at redshift $z \sim 0.05$ that may correspond to a large underdensity in the Southern hemisphere”.

The Abell S1136 has a preferred redshift of $z \sim 0.0625$. To see if there is indeed a deficiency of clusters at redshift $z \sim 0.05$, I think it would be interesting to do a follow-up study of Southern Hemisphere clusters, using data from the full survey of the Evolutionary Map of the Universe (EMU).

With regards to Abell S1136 specifically, future work includes the following:

1. Perform follow up observations of Abell S1136 with “BIGCAT”¹, the upgrade to the Australia Telescope Compact Array (ATCA) being led by my primary supervisor Ray Norris. This upgrade will take the ATCA into the next generation, with a GPU back-end and observing bandwidth doubled from 4GHz to 8GHz.
2. Currently there is not a lot of “deep” optical or infrared data available for Abell S1136. Deeper observations in the optical and infrared regime are required to determine the nature of the source labelled “C” in Figure 4.1, to see if it is associated with Abell S1136, or if it is a background source.
3. There is also the need to determine the magnetic field structure within Abell S1136, which will help understand if there is polarisation at a level not evident in these observations.

¹https://theconversation.com/a-brain-transplant-for-one-of-australias-top-telescopes-129138?utm_source=twitter&utm_medium=twitterbutton

4. With regards to PKS 2333-318, it would be interesting to run a side study, and see if there is indeed interaction between this source and Abell S1136.

The work in this thesis raises the further question: “Is the filamentary sub-structure discovered in Abell S1136 true of all diffuse emission in galaxy clusters, or is S1136 special?”.

Hopefully, the [EMU](#) project will tell us the answer. It is estimated that the [EMU](#) project will increase the number of known radio galaxies from ~ 2.5 million to ~ 70 million. This will enable observations of never before seen galaxies and galaxy clusters, allowing us to analyse in greater detail the associated radio emission properties.

References

- Abell, G. O. (1958a). The Distribution of Rich Clusters of Galaxies. *ApJS*, 3:211.
- Abell, G. O. (1958b). The Distribution of Rich Clusters of Galaxies. *ApJS*, 3:211.
- Abell, G. O., Corwin, Jr., H. G., and Olowin, R. P. (1989). A catalog of rich clusters of galaxies. *ApJS*, 70:1-138.
- Arnaud, M., Pointecouteau, E., and Pratt, G. W. (2005). The structural and scaling properties of nearby galaxy clusters. II. The M-T relation. *A&A*, 441(3):893-903.
- Bagchi, J. (2002). Discovery of giant ‘radio arcs’ in cluster Abell 3376: evidence for shock acceleration in a violent cluster merger? *arXiv e-prints*, pages astro-ph/0210553.
- Baum, W. A. (1966). Multicolour Photometry of Spiral Arms. In Loden, K., Loden, L. O., and Sinnerstad, U., editors, *Spectral Classification and Multicolour Photometry*, volume 24 of *IAU Symposium*, page 288.
- Bautz, L. P. and Morgan, W. W. (1970a). On the Classification of the Forms of Clusters of Galaxies. *ApJ*, 162:L149.
- Bautz, L. P. and Morgan, W. W. (1970b). Preliminary Classification of Clusters of Galaxies. In *BAAS*, volume 2, page 294.
- Bedran, M. L. (2002). A comparison between the Doppler and cosmological redshifts. *American Journal of Physics*, 70(4):406-408.
- Bhardwaj, A., Elsner, R. F., Randall Gladstone, G., Cravens, T. E., Lisse, C. M., Dennerl, K., Branduardi-Raymont, G.,

Wargelin, B. J., Hunter Waite, J., Robertson, I., et al. (2007). X-rays from solar system objects. *Planet. Space Sci.*, 55(9):1135-1189.

Blanton, E. L., Clarke, T. E., Sarazin, C. L., Randall, S. W., and McNamara, B. R. (2010). Active galactic nucleus feedback in clusters of galaxies. *Proceedings of the National Academy of Science*, 107(16):7174-7178.

Boehringer, H., Voges, W., Fabian, A. C., Edge, A. C., and Neumann, D. M. (1993). A ROSAT HRI study of the interaction of the X-ray emitting gas and radio lobes of NGC 1275. *MNRAS*, 264:L25-L28.

Bogdanov, S., Deller, A. T., Miller-Jones, J. C. A., Archibald, A. M., Hessels, J. W. T., Jaodand, A., Patruno, A., Bassa, C., and D'Angelo, C. (2018). Simultaneous Chandra and VLA Observations of the Transitional Millisecond Pulsar PSR J1023+0038: Anti-correlated X-Ray and Radio Variability. *ApJ*, 856(1):54.

Böhringer, H., Schuecker, P., Guzzo, L., Collins, C. A., Voges, W., Cruddace, R. G., Ortiz-Gil, A., Chincarini, G., De Grandi, S., Edge, A. C., et al. (2004). The ROSAT-ESO Flux Limited X-ray (REFLEX) Galaxy cluster survey. V. The cluster catalogue. *A&A*, 425:367-383.

Bonafede, A., Brüggen, M., Rafferty, D., Zhuravleva, I., Riseley, C. J., van Weeren, R. J., Farnes, J. S., Vazza, F., Savini, F., Wilber, A., et al. (2018). LOFAR discovery of radio emission in MACS J0717.5+3745. *MNRAS*, 478(3):2927-2938.

Bonafede, A., Feretti, L., Murgia, M., Govoni, F., Giovannini, G., Dallacasa, D., Dolag, K., and Taylor, G. B. (2010). The Coma cluster magnetic field from Faraday rotation measures. *A&A*, 513:A30.

Bonafede, A., Intema, H. T., Bruggen, M., Russell, H. R., Ogrean, G., Basu, K., Sommer, M., van Weeren, R. J., Cassano, R., Fabian, A. C., et al. (2014). A giant radio halo in the cool core cluster CL1821+643. *MNRAS*, 444:L44-L48.

- Bowman, J. D., Cairns, I., Kaplan, D. L., Murphy, T., Oberoi, D., Staveley-Smith, L., Arcus, W., Barnes, D. G., Bernardi, G., Briggs, F. H., et al. (2013). Science with the Murchison Widefield Array. *PASA*, 30:e031.
- Bridle, A. H., Hough, D. H., Lonsdale, C. J., Burns, J. O., and Laing, R. A. (1994). Deep VLA Imaging of Twelve Extended 3CR Quasars. *AJ*, 108:766.
- Burns, J. O., Sulkanen, M. E., Gisler, G. R., and Perley, R. A. (1992). Where Have All the Cluster Halos Gone? *ApJ*, 388:L49.
- Carlberg, R. G., Yee, H. K. C., and Ellingson, E. (1997). The Average Mass and Light Profiles of Galaxy Clusters. *ApJ*, 478(2):462-475.
- Cassano, R. (2010). The radio-X-ray luminosity correlation of radio halos at low radio frequency. Application of the turbulent re-acceleration model. *A&A*, 517:A10.
- Cassano, R., Brunetti, G., and Venturi, T. (2011). The Connection between Radio Halos and Cluster Mergers and the Statistical Properties of the Radio Halo Population. *Journal of Astrophysics and Astronomy*, 32:519-527.
- Cavaliere, A. G., Gursky, H., and Tucker, W. H. (1971). Extragalactic X-ray Sources and Associations of Galaxies. *Nature*, 231(5303):437-438.
- Clarke, T. E. and Ensslin, T. A. (2001). Cluster mergers and diffuse radio emission in Abell 2256 and Abell 754. In Neumann, D. M. and Tran, J. T. V., editors, *Clusters of Galaxies and the High Redshift Universe Observed in X-rays*, page 56.
- Clarke, T. E., Kronberg, P. P., and Böhringer, H. (2001). A New Radio-X-Ray Probe of Galaxy Cluster Magnetic Fields. *ApJ*, 547(2):L111-L114.
- Clausius, R. (1870). Ueber einen auf die Wärme anwendbaren mechanischen Satz. *Annalen der Physik*, 217(9):124-130.

- Clausius, R. (2003). On a Mechanical Theorem Applicable to Heat. *The Kinetic Theory Of Gases. Series: History of Modern Physical Sciences*, 1:172-178.
- Collins, G. W., I. (1978). *The virial theorem in stellar astrophysics*, volume 7 of *Astronomy and Astrophysics*. Pachart Publishing House.
- Condon, J. J., Cotton, W. D., Greisen, E. W., Yin, Q. F., Perley, R. A., Taylor, G. B., and Broderick, J. J. (1998). The NRAO VLA Sky Survey. *AJ*, 115(5):1693-1716.
- Conselice, C. J., Wilkinson, A., Duncan, K., and Mortlock, A. (2016). The Evolution of Galaxy Number Density at $z < 8$ and Its Implications. *ApJ*, 830(2):83.
- Cornwell, T. J. (1988). Radio-interferometric imaging of very large objects. *A&A*, 202:316-321.
- Dai, X., Griffin, R. D., Kochanek, C. S., Nugent, J. M., and Bregman, J. N. (2015). The SWIFT AGN and Cluster Survey. I. Number Counts of AGNs and Galaxy Clusters. *ApJS*, 218(1):8.
- Davis, T. M. and Lineweaver, C. H. (2004). Expanding Confusion: Common Misconceptions of Cosmological Horizons and the Superluminal Expansion of the Universe. *PASA*, 21(1):97-109.
- de Gasperin, F., Intema, H. T., Shimwell, T. W., Brunetti, G., Brüggen, M., Enßlin, T. A., van Weeren, R. J., Bonafede, A., and Röttgering, H. J. A. (2017). Gentle reenergization of electrons in merging galaxy clusters. *Science Advances*, 3(10):e1701634.
- De Propris, R., Couch, W. J., Colless, M., Dalton, G. B., Collins, C., Baugh, C. M., Bland -Hawthorn, J., Bridges, T., Cannon, R., Cole, S., et al. (2002). The 2dF Galaxy Redshift Survey: a targeted study of catalogued clusters of galaxies. *MNRAS*, 329(1):87-101.
- de Swart, J. G., Bertone, G., and van Dongen, J. (2017). How dark matter came to matter. *Nature Astronomy*, 1:0059.
- de Vaucouleurs, G. (1959). Classification and Morphology of External Galaxies. *Handbuch der Physik*, 53:275.

- De Vaucouleurs, G. (1959). Classification and Morphology of External Galaxies. *Handbuch der Physik*, 53:275.
- de Vaucouleurs, G. (1963). Revised Classification of 1500 Bright Galaxies. *ApJS*, 8:31.
- De Young, D. S. (2003). Relic radio ‘bubbles’ and cluster cooling flows. *MNRAS*, 343(3):719–724.
- Dewdney, P. E., Hall, P. J., Schilizzi, R. T., and Lazio, T. J. L. W. (2009). The Square Kilometre Array. *IEEE Proceedings*, 97(8):1482–1496.
- Doppler, C. and Studnica, F. J. (1903). *Ueber das farbige licht der doppelsterne und einiger anderer gestirne des himmels*. Prag, K. Bohm gesellschaft der wissenschaften.
- Dressler, A. (1980). Galaxy morphology in rich clusters: implications for the formation and evolution of galaxies. *ApJ*, 236:351–365.
- Duchesne, S. W., Johnston-Hollitt, M., Offringa, A. R., Pratt, G. W., Zheng, Q., and Dehghan, S. (2017). Diffuse galaxy cluster emission at 168 MHz within the Murchison Widefield Array Epoch of Reionization 0-hour field. *arXiv e-prints*, page arXiv:1707.03517.
- Ebeling, H., Voges, W., Boehringer, H., Edge, A. C., Huchra, J. P., and Briel, U. G. (1996). Erratum: Properties of the X-ray-brightest Abell-type clusters of galaxies (XBACs) from ROSAT All-SKY Survey data - I. The sample. *MNRAS*, 283:1103.
- Eke, V. R., Baugh, C. M., Cole, S., Frenk, C. S., Norberg, P., Peacock, J. A., Baldry, I. K., Bland-Hawthorn, J., Bridges, T., Cannon, R., et al. (2004). Galaxy groups in the 2dFGRS: the group-finding algorithm and the 2PIGG catalogue. *MNRAS*, 348(3):866–878.
- Enßlin, T. A. and Brüggen, M. (2002). On the formation of cluster radio relics. *MNRAS*, 331(4):1011–1019.
- Enßlin, T. A. and Gopal-Krishna (2001). Reviving fossil radio plasma in clusters of galaxies by adiabatic compression in environmental shock waves. *A&A*, 366:26–34.

- Fanaroff, B. L. and Riley, J. M. (1974). The morphology of extragalactic radio sources of high and low luminosity. *MNRAS*, 167:31P-36P.
- Feretti, L. (2000). Observational Properties of Diffuse Halos in Clusters. *arXiv e-prints*, pages astro-ph/0006379.
- Feretti, L. (2002). Observational Properties of Diffuse Halos in Clusters. In Pramesh Rao, A., Swarup, G., and Gopal-Krishna, editors, *The Universe at Low Radio Frequencies*, volume 199 of *IAU Symposium*, page 133.
- Feretti, L., Fusco-Femiano, R., Giovannini, G., and Govoni, F. (2001). The giant radio halo in Abell 2163. *A&A*, 373:106-112.
- Feretti, L. and Giovannini, G. (1996). Diffuse Cluster Radio Sources (Review). In Ekers, R. D., Fanti, C., and Padrielli, L., editors, *Extragalactic Radio Sources*, volume 175 of *IAU Symposium*, page 333.
- Feretti, L., Giovannini, G., Govoni, F., and Murgia, M. (2012). Clusters of galaxies: observational properties of the diffuse radio emission. *A&A Rev.*, 20:54.
- Fernie, J. D. (1969). The Period-Luminosity Relation: A Historical Review. *PASP*, 81(483):707.
- Ferrari, C., Intema, H. T., Orrù, E., Govoni, F., Murgia, M., Mason, B., Bourdin, H., Asad, K. M., Mazzotta, P., Wise, M. W., et al. (2011). Discovery of the correspondence between intra-cluster radio emission and a high pressure region detected through the Sunyaev-Zel'dovich effect. *A&A*, 534:L12.
- Friedman, A. (1999). On the Possibility of a World with Constant Negative Curvature of Space. *General Relativity and Gravitation*, 31:31-2009.
- Friedmann, A. (1922). Über die Krümmung des Raumes. *Zeitschrift für Physik*, 10:377-386.
- Gardini, A. and Ricker, P. M. (2004). Simulations of Hot Bubbles in the ICM. *Modern Physics Letters A*, 19(31):2317-2329.

- Giacconi, R., Reidy, W. P., Vaiana, G. S., van Speybroeck, L. P., and Zehnpfennig, T. F. (1969). Grazing-Incidence Telescopes for X-Ray Astronomy. *Space Sci. Rev.*, 9(1):3-57.
- Giacintucci, S. (2011). Diffuse radio sources in colliding galaxy clusters . Low frequency follow up of the GMRT Radio Halo Survey. *Mem. Soc. Astron. Italiana*, 82:541.
- Giovannini, G., Bonafede, A., Feretti, L., Govoni, F., Murgia, M., Ferrari, F., and Monti, G. (2009). Radio halos in nearby ($z < 0.4$) clusters of galaxies. *A&A*, 507(3):1257-1270.
- Giovannini, G. and Feretti, L. (2002). *Diffuse Radio Sources and Cluster Mergers: Radio Halos and Relics*, volume 272 of *Astrophysics and Space Science Library*, pages 197-227. Kluwer Academic Publishers.
- Giovannini, G. and Feretti, L. (2004a). Radio Relics in Clusters of Galaxies. *Journal of Korean Astronomical Society*, 37(5):323-328.
- Giovannini, G. and Feretti, L. (2004b). Radio Relics in Clusters of Galaxies. *Journal of Korean Astronomical Society*, 37(5):323-328.
- Giovannini, G., Tordi, M., and Feretti, L. (1999a). Radio halo and relic candidates from the NRAO VLA Sky Survey. , 4(2):141-155.
- Giovannini, G., Tordi, M., and Feretti, L. (1999b). Radio halo and relic candidates from the NRAO VLA Sky Survey. , 4(2):141-155.
- Gitti, M. (2013). The puzzling radio source in the cool core cluster A2626. *MNRAS*, 436:L84-L88.
- Gitti, M., Brunetti, G., Feretti, L., and Setti, G. (2004). Particle acceleration in cooling flow clusters of galaxies: The case of Abell 2626. *A&A*, 417:1-11.
- Gitti, M., Brunetti, G., and Setti, G. (2002a). Modeling the interaction between ICM and relativistic plasma in cooling flows: The case of the Perseus cluster. *A&A*, 386:456-463.

- Gitti, M., Brunetti, G., and Setti, G. (2002b). Modeling the interaction between ICM and relativistic plasma in cooling flows: The case of the Perseus cluster. *A&A*, 386:456-463.
- Gitti, M., Ferrari, C., Domainko, W., Feretti, L., and Schindler, S. (2007). Discovery of diffuse radio emission at the center of the most X-ray-luminous cluster RX J1347.5-1145. *A&A*, 470(3):L25-L28.
- Gooch, R. (1995). *Space and the Spaceball*, volume 77 of *Astronomical Society of the Pacific Conference Series*, page 144. Astronomical Society of the Pacific.
- Górski, K. M., Hivon, E., Banday, A. J., Wandelt, B. D., Hansen, F. K., Reinecke, M., and Bartelmann, M. (2005). HEALPix: A Framework for High-Resolution Discretization and Fast Analysis of Data Distributed on the Sphere. *ApJ*, 622(2):759-771.
- Govoni, F., Enßlin, T. A., Feretti, L., and Giovannini, G. (2001a). A comparison of radio and X-ray morphologies of four clusters of galaxies containing radio halos. *A&A*, 369:441-449.
- Govoni, F., Feretti, L., Giovannini, G., Böhringer, H., Reiprich, T. H., and Murgia, M. (2001b). Radio and X-ray diffuse emission in six clusters of galaxies. *A&A*, 376:803-819.
- Govoni, F., Murgia, M., Markevitch, M., Feretti, L., Giovannini, G., Taylor, G. B., and Carretti, E. (2009). A search for diffuse radio emission in the relaxed, cool-core galaxy clusters A1068, A1413, A1650, A1835, A2029, and Ophiuchus. *A&A*, 499(2):371-383.
- Grandi, S. A. (1983). Spectroscopic observations of southern N-galaxy candidates. *MNRAS*, 204:691-697.
- Heywood, I., Bannister, K. W., Marvil, J., Allison, J. R., Ball, L., Bell, M. E., Bock, D. C. J., Brothers, M., Bunton, J. D., Chippendale, A. P., et al. (2016). Wide-field broad-band radio imaging with phased array feeds: a pilot multi-epoch continuum survey with ASKAP-BETA. *MNRAS*, 457(4):4160-4178.

- Hilton, M., Collins, C., De Propris, R., Baldry, I. K., Baugh, C. M., Bland-Hawthorn, J., Bridges, T., Cannon, R., Cole, S., Colless, M., et al. (2005). The 2dF Galaxy Redshift Survey: correlation with the ROSAT-ESO flux-limited X-ray galaxy cluster survey. *MNRAS*, 363(2):661-674.
- Homan, D. C. (2005). *Polarization of AGN Jets*, volume 340 of *Astronomical Society of the Pacific Conference Series*, page 133. Astronomical Society of the Pacific.
- Homan, D. C., Attridge, J. M., and Wardle, J. F. C. (2001). Parsec-Scale Circular Polarization Observations of 40 Blazars. *ApJ*, 556(1):113-120.
- Hubble, E. (1926a). No. 324. Extra-galactic nebulae. *Contributions from the Mount Wilson Observatory / Carnegie Institution of Washington*, 324:1-49.
- Hubble, E. (1929). A Relation between Distance and Radial Velocity among Extra-Galactic Nebulae. *Proceedings of the National Academy of Science*, 15(3):168-173.
- Hubble, E. P. (1926b). Extragalactic nebulae. *ApJ*, 64:321-369.
- Hubble, E. P. (1927). The classification of spiral nebulae. *The Observatory*, 50:276-281.
- Hudson, D. S., Mittal, R., Reiprich, T. H., Nulsen, P. E. J., Andernach, H., and Sarazin, C. L. (2010). What is a cool-core cluster? a detailed analysis of the cores of the X-ray flux-limited HIFLUGCS cluster sample. *A&A*, 513:A37.
- Huggins, W. (1868). Further Observations on the Spectra of Some of the Stars and Nebulae, with an Attempt to Determine Therefrom Whether These Bodies are Moving towards or from the Earth, Also Observations on the Spectra of the Sun and of Comet II., 1868. *Philosophical Transactions of the Royal Society of London Series I*, 158:529-564.
- Humason, M. L., Mayall, N. U., and Sandage, A. R. (1956). Redshifts and magnitudes of extragalactic nebulae. *AJ*, 61:97-162.

- Hurley-Walker, N., Callingham, J. R., Hancock, P. J., Franzen, T. M. O., Hindson, L., Kapińska, A. D., Morgan, J., Offringa, A. R., Wayth, R. B., Wu, C., et al. (2017). GaLactic and Extragalactic All-sky Murchison Widefield Array (GLEAM) survey - I. A low-frequency extragalactic catalogue. *MNRAS*, 464(1):1146–1167.
- Ignesti, A., Gitti, M., Brunetti, G., O'Sullivan, E., Sarazin, C., and Wong, K. (2018). The mystery of the “Kite” radio source in Abell 2626: Insights from new Chandra observations. *A&A*, 610:A89.
- Intema, H. T., Jagannathan, P., Mooley, K. P., and Frail, D. A. (2017). The GMRT 150 MHz all-sky radio survey. First alternative data release TGSS ADR1. *A&A*, 598:A78.
- J., J. H. (1936). The realm of the nebulae. *Nature*, 138(3499):859–860.
- Johnston, S., Bailes, M., Bartel, N., Baugh, C., Bietenholz, M., Blake, C., Braun, R., Brown, J., Chatterjee, S., Darling, J., et al. (2007). Science with the Australian Square Kilometre Array Pathfinder. *PASA*, 24(4):174–188.
- Johnston, S., Taylor, R., Bailes, M., Bartel, N., Baugh, C., Bietenholz, M., Blake, C., Braun, R., Brown, J., Chatterjee, S., et al. (2008). Science with ASKAP. The Australian square-kilometre-array pathfinder. *Experimental Astronomy*, 22(3):151–273.
- Johnston-Hollitt, M. (2003). *Detection of magnetic fields and diffuse radio emission in Abell 3667 and other rich southern clusters of galaxies*. PhD thesis, University of Adelaide.
- Johnston-Hollitt, M., Clay, R. W., Ekers, R. D., Wieringa, M. H., and Hunstead, R. W. (2002). The Dual Radio Relics of A3667. In Pramesh Rao, A., Swarup, G., and Gopal-Krishna, editors, *The Universe at Low Radio Frequencies*, volume 199 of *IAU Symposium*, page 157.
- Jones, D. H., Read, M. A., Saunders, W., Colless, M., Jarrett, T., Parker, Q. A., Fairall, A. P., Mauch, T., Sadler, E. M., Watson, F. G., et al. (2009). The 6dF Galaxy Survey: final

- redshift release (DR3) and southern large-scale structures. *MNRAS*, 399(2):683-698.
- Jones, T. W., Nolting, C., O'Neill, B. J., and Mendygral, P. J. (2017). Using collisions of AGN outflows with ICM shocks as dynamical probes. *Physics of Plasmas*, 24(4):041402.
- Kalberla, P. M. W., Burton, W. B., Hartmann, D., Arnal, E. M., Bajaja, E., Morras, R., and Pöppel, W. G. L. (2005). The Leiden/Argentine/Bonn (LAB) Survey of Galactic HI. Final data release of the combined LDS and IAR surveys with improved stray-radiation corrections. *A&A*, 440(2):775-782.
- Kempner, J. C., Blanton, E. L., Clarke, T. E., Enßlin, T. A., Johnston-Hollitt, M., and Rudnick, L. (2004). Conference Note: A Taxonomy of Extended Radio Sources in Clusters of Galaxies. In Reiprich, T., Kempner, J., and Soker, N., editors, *The Riddle of Cooling Flows in Galaxies and Clusters of galaxies*, page 335.
- Kempner, J. C. and Sarazin, C. L. (2001a). Radio Halo and Relic Candidates from the Westerbork Northern Sky Survey. *ApJ*, 548(2):639-651.
- Kempner, J. C. and Sarazin, C. L. (2001b). Radio Halo and Relic Candidates from the Westerbork Northern Sky Survey. *ApJ*, 548(2):639-651.
- Kraushaar, W., Clark, G. W., Garmire, G., Helmken, H., Higbie, P., and Agogino, M. (1965). Explorer XI Experiment on Cosmic Gamma Rays. *ApJ*, 141:845.
- Kraushaar, W. L. and Clark, G. W. (1962). Search for Primary Cosmic Gamma Rays with the Satellite Explorer XI. *Phys. Rev. Lett.*, 8(3):106-109.
- Land, K. and Slosar, A. (2007). Correlation between galactic HI and the cosmic microwave background. *Phys. Rev. D*, 76(8):087301.
- Lane, W. M., Clarke, T. E., Taylor, G. B., Perley, R. A., and Kassim, N. E. (2003). Hydra A: A New Picture. In *American Astronomical Society Meeting Abstracts*, volume 203 of *American Astronomical Society Meeting Abstracts*, page 47.04.

Lane, W. M., Clarke, T. E., Taylor, G. B., Perley, R. A., and Kassim, N. E. (2005). Hydra A: A New Picture. In Sjouwerman, L. O. and Dyer, K. K., editors, *X-Ray and Radio Connections*, page 7.19.

Large, M. I., Mathewson, D. S., and Haslam, C. G. T. (1959). A High-Resolution Survey of the Coma Cluster of Galaxies at 408 Mc./s. *Nature*, 183(4676):1663-1664.

Lasker, B. M., Doggett, J., McLean, B., Sturch, C., Djorgovski, S., de Carvalho, R. R., and Reid, I. N. (1996). The Palomar-ST ScI Digitized Sky Survey (POSS-II): Preliminary Data Availability. In Jacoby, G. H. and Barnes, J., editors, *Astronomical Data Analysis Software and Systems V*, volume 101 of *Astronomical Society of the Pacific Conference Series*, page 88.

Lasker, B. M., Lattanzi, M. G., McLean, B. J., Bucciarelli, B., Drimmel, R., Garcia, J., Greene, G., Guglielmetti, F., Hanley, C., Hawkins, G., et al. (2008). The Second-Generation Guide Star Catalog: Description and Properties. *AJ*, 136(2):735-766.

Lasker, B. M., Sturch, C. R., McLean, B. J., Russell, J. L., Jenkner, H., and Shara, M. M. (1990). The Guide Star Catalog. I. Astronomical Foundations and Image Processing. *AJ*, 99:2019.

Lauberts, A. and Valentijn, E. A. (1989). *The surface photometry catalogue of the ESO-Uppsala galaxies*. Garching: European Southern Observatory.

Lavaux, G. and Hudson, M. J. (2011). The 2M++ galaxy redshift catalogue. *MNRAS*, 416(4):2840-2856.

Leavitt, H. S. (1908). 1777 variables in the Magellanic Clouds. *Annals of Harvard College Observatory*, 60:87-108.3.

Lemaître, G. (1927). Un Univers homogène de masse constante et de rayon croissant rendant compte de la vitesse radiale des nébuleuses extra-galactiques. *Annales de la Société Scientifique de Bruxelles*, 47:49-59.

- Liang, H., Hunstead, R. W., Birkinshaw, M., and Andreani, P. (2000). A Powerful Radio Halo in the Hottest Known Cluster of Galaxies 1E 0657-56. *ApJ*, 544(2):686-701.
- Lin, Y.-T. and Mohr, J. J. (2004). K-band Properties of Galaxy Clusters and Groups: Brightest Cluster Galaxies and Intracluster Light. *ApJ*, 617:879-895.
- Lisenfeld, U. and Völk, H. J. (2000). On the radio spectral index of galaxies. *A&A*, 354:423-430.
- Luminet, J.-P. (2015). Lemaitre's Big Bang. *arXiv e-prints*, page arXiv:1503.08304.
- Mandal, S., Intema, H. T., van Weeren, R. J., Shimwell, T. W., Botteon, A., Brunetti, G., de Gasperin, F., Brüggen, M., Di Gennaro, G., Kraft, R., et al. (2020). Revived fossil plasma sources in galaxy clusters. *A&A*, 634:A4.
- Mason, B. S., Dicker, S. R., Korngut, P. M., Devlin, M. J., Cotton, W. D., Koch, P. M., Molnar, S. M., Sievers, J., Aguirre, J. E., Benford, D., et al. (2010). Implications of a High Angular Resolution Image of the Sunyaev-Zel'Dovich Effect in RXJ1347-1145. *ApJ*, 716(1):739-745.
- Mathews, W. G. and Brighenti, F. (2008). Creation of the X-Ray Cavity Jet and Its Radio Lobe in M87/Virgo with Cosmic Rays: Relevance to Relic Radio Sources. *ApJ*, 676(2):880-888.
- Mauch, T. and Sadler, E. M. (2007). Radio sources in the 6dFGS: local luminosity functions at 1.4GHz for star-forming galaxies and radio-loud AGN. *MNRAS*, 375(3):931-950.
- Mazzotta, P. and Giacintucci, S. (2008). Do Radio Core-Halos and Cold Fronts in Non-Major-Merging Clusters Originate from the Same Gas Sloshing? *ApJ*, 675(1):L9.
- McConnell, D. (2017). Observing with askap: Optimisation for survey speed.
- McConnell, D., Allison, J. R., Bannister, K., Bell, M. E., Bignall, H. E., Chippendale, A. P., Edwards, P. G., Harvey-Smith, L., Hegarty, S., Heywood, I., et al. (2016). The Australian Square Kilometre Array Pathfinder:

Performance of the Boolardy Engineering Test Array. *PASA*, 33:e042.

Mcconnell, D., Hotan, A., Chippendale, A., Lenc, E., and Mahony, E. (2019). ASKAP Science Observation Guide. Technical Report March, CSIRO.

McNamara, B. R., Wise, M., Nulsen, P. E. J., David, L. P., Sarazin, C. L., Bautz, M., Markevitch, M., Vikhlinin, A., Forman, W. R., Jones, C., et al. (2000). Chandra X-Ray Observations of the Hydra A Cluster: An Interaction between the Radio Source and the X-Ray-emitting Gas. *ApJ*, 534(2):L135-L138.

Meisenheimer, K., Roser, H. J., Hiltner, P. R., Yates, M. G., Longair, M. S., Chini, R., and Perley, R. A. (1989). The synchrotron spectra of radio hot spots. *A&A*, 219:63-86.

Merloni, A., Predehl, P., Becker, W., Böhringer, H., Boller, T., Brunner, H., Brusa, M., Dennerl, K., Freyberg, M., Friedrich, P., et al. (2012). eROSITA Science Book: Mapping the Structure of the Energetic Universe. *arXiv e-prints*, page arXiv:1209.3114.

Morgan, W. W. (1958a). A Preliminary Classification of the Forms of Galaxies According to Their Stellar Population. *PASP*, 70(415):364.

Morgan, W. W. (1958b). A Preliminary Classification of the Forms of Galaxies According to Their Stellar Population. *PASP*, 70(415):364.

Morgan, W. W. (1959a). Preliminary Classification of the Forms of Galaxies According to Their Stellar Population. II. *PASP*, 71(422):394.

Morgan, W. W. (1959b). Preliminary Classification of the Forms of Galaxies According to Their Stellar Population. II. *PASP*, 71(422):394.

Morgan, W. W. (1971). A Unitary Classification for N Galaxies. *AJ*, 76:1000.

Morgan, W. W. and Mayall, N. U. (1957). A Spectral Classification of Galaxies. *PASP*, 69(409):291.

Murgia, M., Eckert, D., Govoni, F., Ferrari, C., Pandey-Pommier, M., Nevalainen, J., and Paltani, S. (2010a). GMRT observations of the Ophiuchus galaxy cluster. *A&A*, 514:A76.

Murgia, M., Eckert, D., Govoni, F., Ferrari, C., Pandey-Pommier, M., Nevalainen, J., and Paltani, S. (2010b). GMRT observations of the Ophiuchus galaxy cluster. *A&A*, 514:A76.

NASA (2019). Introduction to the electromagnetic spectrum.

Norris, R. P. (2017). Extragalactic radio continuum surveys and the transformation of radio astronomy. *Nature Astronomy*, 1:671-678.

Norris, R. P., Hopkins, A. M., Afonso, J., Brown, S., Condon, J. J., Dunne, L., Feain, I., Hollow, R., Jarvis, M., Johnston-Hollitt, M., et al. (2011). EMU: Evolutionary Map of the Universe. *PASA*, 28:215-248.

Ochsenbein, F., e. (2000). The VizieR database of astronomical catalogues.

O'Dea, C. and Baum, S. (1991). PKS0745-191: the archetypal cooling flow radio source? In Colless, M. M., Babul, A., Edge, A. C., Johnstone, R. M., and Raychaudhury, S., editors, *Clusters and Superclusters of Galaxies*, page 37.

Offringa, A. R., Trott, C. M., Hurley-Walker, N., Johnston-Hollitt, M., McKinley, B., Barry, N., Beardsley, A. P., Bowman, J. D., Briggs, F., Carroll, P., et al. (2016). Parametrizing Epoch of Reionization foregrounds: a deep survey of low-frequency point-source spectra with the Murchison Widefield Array. *MNRAS*, 458(1):1057-1070.

Olowin, R. P. (1988). The all-sky abell catalog of rich clusters of galaxies. *Publications of the Astronomical Society of the Pacific*, 100(633):1354-1359.

Owen, F. N., Eilek, J. A., and Kassim, N. E. (2000a). M87 at 90 Centimeters: A Different Picture. *ApJ*, 543(2):611-619.

- Owen, F. N., Eilek, J. A., and Kassim, N. E. (2000b). M87 at 90 Centimeters: A Different Picture. *ApJ*, 543(2):611-619.
- Owen, F. N. and Ledlow, M. J. (1994). *The FRI/II Break and the Bivariate Luminosity Function in Abell Clusters of Galaxies*, volume 54 of *Astronomical Society of the Pacific Conference Series*, page 319. Astronomical Society of the Pacific.
- Panko, E. (2015). The Morphology of Galaxy Clusters. In Biernacka, M., Bajan, K., Stachowski, G., and Flin, P., editors, *Introduction to Cosmology*, pages 85-88.
- Peebles, P. J. E., Schramm, D. N., Turner, E. L., and Kron, R. G. (1994). The Evolution of the Universe. *Scientific American*, 271:52.
- Perley, R. A., Willis, A. G., and Scott, J. S. (1979). The structure of the radio jets in 3C 449. *Nature*, 281:437-442.
- Planck Collaboration, Ade, P. A. R., Aghanim, N., Arnaud, M., Ashdown, M., Aumont, J., Baccigalupi, C., Banday, A. J., Barreiro, R. B., Bartlett, J. G., et al. (2016). Planck 2015 results. XIII. Cosmological parameters. *A&A*, 594:A13.
- Porter, S. C. and Raychaudhury, S. (2005). The Pisces-Cetus supercluster: a remarkable filament of galaxies in the 2dF Galaxy Redshift and Sloan Digital Sky surveys. *MNRAS*, 364(4):1387-1396.
- Puccetti, S., Capalbi, M., Giommi, P., Perri, M., Stratta, G., Angelini, L., Burrows, D. N., Campana, S., Chincarini, G., Cusumano, G., et al. (2011). The Swift serendipitous survey in deep XRT GRB fields (SwiftFT). I. The X-ray catalog and number counts. *A&A*, 528:A122.
- Rayner, D. P., Norris, R. P., and Sault, R. J. (2000). Radio circular polarization of active galaxies. *MNRAS*, 319(2):484-496.
- Read, A. M., Filipović, M. D., Pietsch, W., and Jones, P. A. (2001). Radio jets and diffuse X-ray emission around the peculiar galaxy pair ESO 295-IG022. *A&A*, 369:467-472.

- Reiprich, T. (2017). Galaxy clusters from eeHIFLUGCS, to eROSITA, to Athena. In Ness, J.-U. and Migliari, S., editors, *The X-ray Universe 2017*, page 189.
- Rengelink, R. B., Tang, Y., de Bruyn, A. G., Miley, G. K., Bremer, M. N., Roettgering, H. J. A., and Bremer, M. A. R. (1997). The Westerbork Northern Sky Survey (WENSS), I. A 570 square degree Mini-Survey around the North Ecliptic Pole. *A&AS*, 124:259–280.
- Rizza, E., Loken, C., Bliton, M., Roettiger, K., Burns, J. O., and Owen, F. N. (2000). X-Ray and Radio Interactions in the Cores of Cooling Flow Clusters. *AJ*, 119(1):21–31.
- Rottgering, H. J. A., Wieringa, M. H., Hunstead, R. W., and Ekers, R. D. (1997). The extended radio emission in the luminous X-ray cluster A3667. *MNRAS*, 290(4):577–584.
- Rudnick, L. and Lemmertman, J. A. (2009). An Objective Survey of Mpc-scale Radio Emission in $0.03 < z < 0.3$ Bright X-ray Clusters. *ApJ*, 697(2):1341–1357.
- Safi-Harb, S. and Kotani, T. (2003). SS 433: Radio/X-ray anti-correlation and fast time variability. In Durouchoux, P., Fuchs, Y., and Rodriguez, J., editors, *New Views on Microquasars*, page 279.
- Sault, R. J., Teuben, P. J., and Wright, M. C. H. (1995). A Retrospective View of MIRIAD. In Shaw, R. A., Payne, H. E., and Hayes, J. J. E., editors, *Astronomical Data Analysis Software and Systems IV*, volume 77 of *Astronomical Society of the Pacific Conference Series*, page 433.
- Schilizzi, R. T., Dewdney, P. E. F., and Lazio, T. J. W. (2010). The square kilometre array. In *Proc. SPIE*, volume 7733 of *Society of Photo-Optical Instrumentation Engineers (SPIE) Conference Series*, page 773318.
- Shapley, H. (1930). Note on a Remote Cloud of Galaxies in Centaurus. *Harvard College Observatory Bulletin*, 874:9–12.
- Shimmins, A. J. and Bolton, J. G. (1974). The Parkes 2700 MHz Survey (Sixth Part): Catalogue for the Declination zone

-30° to -35°. *Australian Journal of Physics Astrophysical Supplement*, 32:1.

Slee, O. B., Roy, A. L., Murgia, M., Andernach, H., and Ehle, M. (2001). Four Extreme Relic Radio Sources in Clusters of Galaxies. *AJ*, 122(3):1172-1193.

Springel, V., White, S. D. M., Jenkins, A., Frenk, C. S., Yoshida, N., Gao, L., Navarro, J., Thacker, R., Croton, D., Helly, J., et al. (2005). Simulations of the formation, evolution and clustering of galaxies and quasars. *Nature*, 435(7042):629-636.

Taylor, G. B. (2003). Observed properties of jets in young radio galaxies. *New A Rev.*, 47(6-7):585-588.

Taylor, G. B., Fabian, A. C., and Allen, S. W. (2002a). Magnetic fields in the Centaurus cluster. *MNRAS*, 334(4):769-776.

Taylor, G. B., Fabian, A. C., and Allen, S. W. (2002b). Magnetic fields in the Centaurus cluster. *MNRAS*, 334(4):769-776.

Taylor, M. B. (2005). *TOPCAT & STIL: Starlink Table/VOTable Processing Software*, volume 347 of *Astronomical Society of the Pacific Conference Series*, page 29. Astronomical Society of the Pacific.

Tingay, S. J., Goeke, R., Bowman, J. D., Emrich, D., Ord, S. M., Mitchell, D. A., Morales, M. F., Booler, T., Crosse, B., Wayth, R. B., et al. (2013). The Murchison Widefield Array: The Square Kilometre Array Precursor at Low Radio Frequencies. *PASA*, 30:e007.

Trove (1994). The digitized sky survey [electronic resource], space telescope science institute, nasa.

van Weeren, R. J., Brüggen, M., Röttgering, H. J. A., Hoeft, M., Nuza, S. E., and Intema, H. T. (2011). Radio continuum observations of new radio halos and relics from the NVSS and WENSS surveys. Relic orientations, cluster X-ray luminosity, and redshift distributions. *A&A*, 533:A35.

van Weeren, R. J., de Gasperin, F., Akamatsu, H., Brüggen, M., Feretti, L., Kang, H., Stroe, A., and Zandanel, F. (2019).

Diffuse Radio Emission from Galaxy Clusters. *Space Sci. Rev.*, 215(1):16.

van Weeren, R. J., Röttgering, H. J. A., Brüggen, M., and Hoeft, M. (2010). Particle Acceleration on Megaparsec Scales in a Merging Galaxy Cluster. *Science*, 330(6002):347.

Venturi, T. (2011). Observational properties of diffuse radio sources in galaxy clusters . Current knowledge and open questions. *Mem. Soc. Astron. Italiana*, 82:499.

Venturi, T., Bardelli, S., Dallacasa, D., Di Gennaro, G., Gastaldello, F., Giacintucci, S., and Rossetti, M. (2017a). Extended Radio Emission in the Peripherical Regions of the Shapley Concentration Core. *Galaxies*, 5(1):16.

Venturi, T., Giacintucci, S., Brunetti, G., Cassano, R., Bardelli, S., Dallacasa, D., and Setti, G. (2007). GMRT radio halo survey in galaxy clusters at $z = 0.2\text{--}0.4$. I. The REFLEX sub-sample. *A&A*, 463(3):937–947.

Venturi, T., Giacintucci, S., Dallacasa, D., Cassano, R., Brunetti, G., Bardelli, S., and Setti, G. (2008). GMRT radio halo survey in galaxy clusters at $z = 0.2\text{--}0.4$. II. The eBCS clusters and analysis of the complete sample. *A&A*, 484(2):327–340.

Venturi, T., Rossetti, M., Brunetti, G., Farnsworth, D., Gastaldello, F., Giacintucci, S., Lal, D. V., Rudnick, L., Shimwell, T. W., Eckert, D., et al. (2017b). The two-component giant radio halo in the galaxy cluster Abell 2142. *A&A*, 603:A125.

Wang, Y., Kratochvil, J. M., Linde, A., and Shmakova, M. (2004). Current observational constraints on cosmic doomsday. *JCAP*, 2004(12):006.

Wayth, R. B., Lenc, E., Bell, M. E., Callingham, J. R., Dwarakanath, K. S., Franzen, T. M. O., For, B. Q., Gaensler, B., Hancock, P., Hindson, L., et al. (2015). GLEAM: The Galactic and Extragalactic All-Sky MWA Survey. *PASA*, 32:e025.

- Wayth, R. B., Tingay, S. J., Trott, C. M., Emrich, D., Johnston-Hollitt, M., McKinley, B., Gaensler, B. M., Beardsley, A. P., Booler, T., Crosse, B., et al. (2018). The Phase II Murchison Widefield Array: Design overview. *PASA*, 35:33.
- Westfold, K. C. (1959). The Polarization of Synchrotron Radiation. *ApJ*, 130:241.
- Whiting, M. and Humphreys, B. (2012). Source-Finding for the Australian Square Kilometre Array Pathfinder. *PASA*, 29(3):371-381.
- Willson, M. A. G. (1970). Radio observations of the cluster of galaxies in Coma Berenices - the 5C4 survey. *MNRAS*, 151:1.
- Wright, E. L. (2006). A Cosmology Calculator for the World Wide Web. *PASP*, 118(850):1711-1715.
- Wright, E. L., Eisenhardt, P. R. M., Mainzer, A. K., Ressler, M. E., Cutri, R. M., Jarrett, T., Kirkpatrick, J. D., Padgett, D., McMillan, R. S., Skrutskie, M., et al. (2010). The Wide-field Infrared Survey Explorer (WISE): Mission Description and Initial On-orbit Performance. *AJ*, 140(6):1868-1881.
- ZuHone, J., Markevitch, M., and Brunetti, G. (2011). Testing the connection between radio mini-halos and core gas sloshing with MHD simulations. *Mem. Soc. Astron. Italiana*, 82:632.
- Zwicky, F. (1937). On the Masses of Nebulae and of Clusters of Nebulae. *ApJ*, 86:217.

Appendix A

Data Processing Parameters

A.1 Data Processing Parameters

In this section I show the ASKAPsoft pipeline processing parameters for the 2017 ASKAP 16 antenna observations and the 2019 ASKAP 33 antenna observations.

Table A.1: Processing parameters for ASKAP 16 antenna observation. The second column shows the parameter name used by ASKAPsoft.

Explanation	Parse name	Value
Only continuum (i.e. 288 1-MHz channels)	DO_PREFLAG_SCIENCE	true
Number of w planes	DO_SPLIT_TIMEWISE	true
Scales used bu multiscale CLEAN, in pixels	NUM_CHAN_TO_AVERAGE	1
	DO_SPECTRAL_IMAGING	false
	GRIDDER_NWPLANES	557
	CLEAN_SCALES	“[0,6,15,30,45,60]”
	CLEAN_NUM_MAJORCYCLES	“[5,15]”
	CLEAN_THRESHOLD_MINORCYCLE	“[30%, 0.25mJy, 0.03mJy]”
	CLEAN_MINORCYCLE_NITER	“[400,3000]”
	SELFCAL_METHOD	“CleanModel”
	SELFCAL_INTERVAL	“[200,60]”
	PRECONDITIONER_WIENER_ROBUSTNESS	0.0
Use a Wiener filter for the main image and a Gaussian taper for the alt image	RESTORE_PRECONDITIONER_LIST	“[Wiener,GaussianTaper]”
Both the main and the alt image have robustness = 0	RESTORE_PRECONDITIONER_WIENER_ROBUSTNESS	0.0
Taper the alt image with a 30×30 arcsec gaussian	RESTORE_PRECONDITIONER_GAUSS_TAPER	“[30arcsec, 30arcsec, 0deg]”
Cut off the beams at 0.23 of peak when mosaicing them	NUM_PIXELS_CONTCUBE	6144
	LINMOS_CUTOFF	0.23
	TRANSITION_SB	true
	ARCHIVE_SPECTRAL_MS	false
	DO_CONTCUBE_IMAGING	true

Table A.2: Processing parameters for ASKAP 33 antenna observation. The second column shows the parameter name used by ASKAPsoft.

Explanation	Parse name	Value
Only continuum (i.e. 288 1-MHz channels)	DO_PREFLAG_SCIENCE	true
Number of w planes	DO_SPLIT_TIMEWISE	true
Scales used bu multiscale CLEAN, in pixels	NUM_CHAN_TO_AVERAGE	1
	DO_SPECTRAL_IMAGING	false
	GRIDDER_NWPLANES	557
	CLEAN_SCALES	“[0,6,15,30,45,60]”
	CLEAN_NUM_MAJORCYCLES	“[5,15]”
	CLEAN_THRESHOLD_MINORCYCLE	“[30%, 0.25mJy, 0.03mJy]”
	CLEAN_MINORCYCLE_NITER	“[400,3000]”
	SELFCAL_METHOD	“CleanModel”
	SELFCAL_INTERVAL	“[200,60]”
	PRECONDITIONER_WIENER_ROBUSTNESS	0.0
Use a Wiener filter for the main image and a Gaussian taper for the alt image	RESTORE_PRECONDITIONER_LIST	“[Wiener,GaussianTaper]”
Both the main and the alt image have robustness = 0	RESTORE_PRECONDITIONER_WIENER_ROBUSTNESS	0.0
Taper the alt image with a 30×30 arcsec gaussian	RESTORE_PRECONDITIONER_GAUSS_TAPER	“[30arcsec, 30arcsec, 0deg]”
Cut off the beams at 0.23 of peak when mosaicing them	NUM_PIXELS_CONTCUBE	6144
	LINMOS_CUTOFF	0.23
	TRANSITION_SB	true
	ARCHIVE_SPECTRAL_MS	false
	DO_CONTCUBE_IMAGING	true

Appendix B

Paper in Preparation

B.1 EMU Observations of Filamentary Structures in the Abell S1136 Galaxy Cluster

In this appendix, I include a draft paper on which I am first author, written as part of my Master of Research. The paper was started as a result of my presentation of this work at the 17th International Meeting of the Evolutionary Map of the Universe project, held in Catania, Italy, from 28 October to 30 October 2019, and the interest shown in this work.

Appendix C

Abell S1136 Poster Presentation

In this appendix, I include a poster which was presented on 25 November 2019, at the inaugural “Physics in Research Showcase”, at Macquarie University in Sydney. The poster was used to showcase the work on the Abell S1136 draft paper in Appendix [B.1](#).

Appendix D

Catalogue of Abell Clusters

VII/110A/table4 (c)Southern “Abell Catalog” (1364 rows), and VII/110A/table5 (c)Supplementary southern clusters (1174 rows), downloaded from VizieR¹. data was downloaded in .fits format and converted in astropy to latex format. Abell S1136 is shown on page 196 and has been highlighted in green for easier location.

Table D.1: Abell Southern Clusters

ACO	RAB1950	DEB1950	Xcen	Ycen	BMtype	Count	m10	z	Rich	Dclass	_RA_icrs	_DE_icrs
	"h:m:s"	"d:m:s"	mm	mm		ct	mag				"h:m:s"	"d:m:s"
1	00 00.0	-30 54	-4	-46	I	-8	16.9	0.0	0	5	00 02 33.5	-30 37 18
2	00 00.2	-30 12	-2	-9	I-II	11	15.9	0.0	0	4	00 02 45.5	-29 55 18
3	00 00.6	-28 10	3	100	I	11	16.8	0.0	0	5	00 03 09.5	-27 53 18
4	00 01.3	-70 16	3	-13	I-II	-8	17.7	0.0	0	5	00 03 49.7	-69 59 17
5	00 02.1	-45 54	130	-50	II	-7	16.0	0.0395	0	4	00 04 38.8	-45 37 18
6	00 02.2	-30 46	21	-39	I	7	15.4	0.027	0	3	00 04 45.2	-30 29 18
7	00 02.6	-17 03	31	160	I?	78	20.3	0.0	1	6	00 05 09.4	-16 46 18
8	00 04.4	-67 57	19	112	I	-18	17.0	0.0	0	5	00 06 53.7	-67 40 18
9	00 04.6	-44 39	157	16	I-II	-12	16.0	0.0	0	4	00 07 08.1	-44 22 18
10	00 06.0	-29 17	66	40	I	28	19.5	0.0	0	6	00 08 32.6	-29 00 18
11	00 06.0	-39 54	59	8	I-II	-11	19.5	0.0	0	6	00 08 32.0	-39 37 18
12	00 06.8	-35 38	71	-29	III-III?	3	15.1	0.0	0	3	00 09 20.1	-35 21 18
13	00 08.4	-51 29	68	-80	III	53	20.1	0.0	1	6	00 10 54.2	-51 12 18
14	00 09.6	-51 36	77	-87	III:	70	20.2	0.0	1	6	00 12 05.8	-51 19 19
15	00 10.2	-17 30	-140	136	II-III	11	16.8	0.0	0	5	00 12 44.7	-17 13 19
16	00 10.3	-52 05	81	156	III	113	20.6	0.0	2	6	00 12 47.5	-51 48 19
17	00 11.2	-38 02	116	107	II	-23	18.0	0.0	0	6	00 13 42.9	-37 45 19
18	00 11.8	-65 27	62	-24	II-III	19	18.3	0.0	0	6	00 14 13.5	-65 10 19
19	00 13.1	-68 07	63	99	II	17	17.7	0.0	0	5	00 15 29.5	-67 50 19
20	00 14.1	-70 00	61	-1	II	28	18.2	0.0	0	6	00 16 27.6	-69 43 20
21	00 14.1	-84 21	18	35	II	-8	16.0	0.0	0	4	00 15 56.6	-84 04 20
22	00 14.8	-43 58	44	56	III?	79	20.2	0.0	1	6	00 17 17.3	-43 41 20
23	00 15.6	-64 38	86	18	III	-9	19.4	0.0	0	6	00 17 59.5	-64 21 20
24	00 15.8	-68 27	75	80	III	12	19.3	0.0	0	6	00 18 09.3	-68 10 20
25	00 16.5	-64 34	91	22	III	2	19.3	0.0	0	6	00 18 53.0	-64 17 20
26	00 16.6	-20 44	-57	-37	II-III	85	19.7	0.0	2	6	00 19 07.8	-20 27 21
27	00 16.7	-69 43	75	13	II	19	18.1	0.0	0	6	00 19 01.8	-69 26 20

¹<https://vizier.u-strasbg.fr/viz-bin/VizieR>

Table D.1 continued from previous page

ACO	RAB1950	DEB1950	Xcen	Ycen	BMtype	Count	m10	z	Rich	Dclass	_RA_icrs	_DE_icrs
28	00 16.9	-17 28	-54	138	II	3	15.6	0.0	0	4	00 19 26.1	-17 11 21
29	00 17.1	-67 40	85	122	II	-8	16.5	0.0	0	5	00 19 26.9	-67 23 21
30	00 17.7	-81 06	35	-57	II	-20	16.8	0.0	0	5	00 19 41.5	-80 49 21
31	00 18.1	-67 57	89	106	III	1	19.3	0.0	0	6	00 20 26.0	-67 40 21
32	00 19.6	-39 49	-67	11	III	14	18.6	0.0	0	6	00 22 04.7	-39 32 22
33	00 20.0	-65 56	106	-53	II-III	11	18.0	0.0	0	6	00 22 20.1	-65 39 22
34	00 20.0	-67 21	101	137	III	-16	19.6	0.0	0	6	00 22 19.1	-67 04 22
35	00 20.3	-39 25	-60	32	II	12	16.4	0.0	0	5	00 22 46.6	-39 08 22
36	00 21.2	-39 09	-51	47	II-III	29	18.1	0.0	0	6	00 23 40.5	-38 52 22
37	00 21.2	-42 32	-50	-134	I-II	-1	15.9	0.0	0	4	00 23 39.8	-42 15 22
38	00 21.3	-38 32	-50	80	I-II	16	18.1	0.0	0	6	00 23 46.6	-38 15 22
39	00 21.5	-20 27	4	-22	III	52	19.7	0.0	1	6	00 24 01.3	-20 10 23
40	00 22.4	-37 02	-39	160	I-II	21	18.6	0.0	0	6	00 24 52.6	-36 45 23
41	00 23.0	-33 18	-14	91	II	26	15.3	0.0498	0	3	00 25 29.2	-33 01 23
42	00 23.2	-65 00	-120	-4	I-II	26	18.1	0.0	0	6	00 25 30.7	-64 43 23
43	00 23.3	-19 29	27	30	II	18	18.0	0.0	0	6	00 25 49.3	-19 12 23
44	00 23.3	-27 40	0	127	II:	54	19.9	0.0	1	6	00 25 48.0	-27 23 23
45	00 23.3	-57 15	-73	-121	II	20	16.7	0.0241	0	4	00 25 40.7	-56 58 23
46	00 23.6	-37 38	-25	128	III	9	16.9	0.0	0	5	00 26 04.2	-37 21 23
47	00 24.0	-51 54	-76	166	II	6	17.1	0.0	0	5	00 26 24.5	-51 37 24
48	00 24.2	-54 13	-71	43	II-III	29	18.1	0.0	0	6	00 26 35.6	-53 56 24
49	00 24.4	-53 38	-70	74	II	-43	17.1	0.0	0	5	00 26 47.7	-53 21 24
50	00 24.8	-47 06	-49	156	III:	78	20.4	0.0	1	6	00 27 13.7	-46 49 24
51	00 25.3	-36 59	-7	163	I	26	16.8	0.0	0	5	00 27 46.0	-36 42 24
52	00 25.3	-54 28	-62	29	II	26	17.5	0.0	0	5	00 27 41.0	-54 11 24
53	00 25.4	-44 32	-29	28	II-III	1	18.6	0.0	0	6	00 27 50.2	-44 15 24
54	00 25.9	-52 10	-37	-114	III	48	19.9	0.0	0	6	00 28 17.7	-51 53 24
55	00 25.9	-52 16	-60	148	I-II	-40	17.5	0.0	0	5	00 28 17.6	-51 59 24
56	00 26.0	-63 27	-113	79	II	12	16.7	0.0	0	5	00 28 18.1	-63 10 24
57	00 26.0	-65 58	-98	-55	II-III	20	18.3	0.0	0	6	00 28 16.2	-65 41 24
58	00 26.1	-69 18	120	31	I-II	1	16.5	0.0	0	5	00 28 19.0	-69 01 24
59	00 28.2	-47 48	-2	-147	I-II	4	16.8	0.0	0	5	00 30 36.4	-47 31 26
60	00 32.0	-18 53	-128	62	II-III	73	20.2	0.0	1	6	00 34 30.5	-18 36 28
61	00 32.0	-39 24	61	32	II-III	21	17.6	0.0	0	5	00 34 25.9	-39 07 28
62	00 32.5	-47 36	20	129	II?	71	20.1	0.0	1	6	00 34 53.1	-47 19 28
63	00 33.5	-52 28	2	137	II	-44	17.0	0.0417	0	5	00 35 50.7	-52 11 29
64	00 36.7	-39 08	-160	44	I-II	10	16.6	0.0	0	5	00 39 06.9	-38 51 31
65	00 38.2	-62 40	-38	126	II-III	11	18.6	0.0	0	6	00 40 23.8	-62 23 32
66	00 38.5	-53 53	42	60	II	15	16.6	0.0	0	5	00 40 48.1	-53 36 32
67	00 38.6	-44 46	-166	10	II-III:	93	21.0	0.0	2	6	00 40 58.4	-44 29 33
68	00 38.7	-28 07	-65	-167	II-III:	100	20.0	0.0	2	6	00 41 09.6	-27 50 33
69	00 39.1	-38 10	-137	97	I	-5	16.8	0.0	0	5	00 41 30.6	-37 53 33
70	00 39.6	-28 19	-77	92	II-III	15	17.3	0.0	0	5	00 42 03.4	-28 02 33
71	00 41.0	-38 30	-117	80	I-II	19	19.3	0.0	0	6	00 43 24.1	-38 13 34
72	00 41.4	-34 12	-75	46	II-III	65	19.7	0.0	1	6	00 43 49.4	-33 55 35
73	00 41.8	-39 38	-107	19	I-II	21	17.5	0.0	0	5	00 44 11.5	-39 21 35
74	00 43.4	-50 13	-147	-13	II	21	15.7	0.0283	0	4	00 45 42.3	-49 56 36
75	00 43.6	-69 06	-44	50	III	26	18.1	0.0	0	6	00 45 36.2	-68 49 36
76	00 44.3	-55 54	83	-49	I-II	19	19.3	0.0	0	6	00 46 32.4	-55 37 37
77	00 44.5	-55 01	86	-2	I	29	16.8	0.0	0	5	00 46 45.0	-54 44 37
78	00 45.2	-48 31	-136	79	I	-4	15.9	0.0	0	4	00 47 30.7	-48 14 38
79	00 45.3	-64 48	5	11	II	16	17.5	0.0	0	5	00 47 23.4	-64 31 38
80	00 45.9	-58 41	49	72	III	28	17.8	0.0	0	5	00 48 05.5	-58 24 38
81	00 46.0	-49 23	-126	33	II-III	26	16.7	0.0	0	5	00 48 17.9	-49 06 39
82	00 46.2	-65 11	10	-10	II	-11	16.5	0.0	0	5	00 48 16.4	-64 54 39
83	00 46.5	-34 31	-19	29	II	12	17.0	0.0	0	5	00 48 54.3	-34 14 39

Table D.1 continued from previous page

ACO	RAB1950	DEB1950	Xcen	Ycen	BMtype	Count	m10	z	Rich	Dclass	_RA_icrs	_DE_icrs
84	00 46.9	-29 48	8	13	I	11	17.4	0.11	0	5	00 49 19.8	-29 31 40
85	00 47.6	-47 39	-116	126	II	-6	16.0	0.0196	0	4	00 49 54.4	-47 22 40
86	00 47.7	-48 05	-115	103	II	4	16.4	0.0	0	5	00 50 00.1	-47 48 40
87	00 48.7	-55 26	117	-26	II-III	2	19.1	0.0	0	6	00 50 55.0	-55 09 41
88	00 49.4	-34 12	15	46	II-III	9	17.5	0.0	0	5	00 51 47.9	-33 55 42
89	00 49.8	-37 48	-25	118	II-III	18	17.3	0.0	0	5	00 52 10.4	-37 31 42
90	00 50.5	-39 14	-16	42	II-III	25	18.6	0.0	0	6	00 52 51.6	-38 57 43
91	00 50.9	-25 18	81	-15	II-III	68	20.1	0.0	1	6	00 53 20.7	-25 01 43
92	00 51.1	-48 26	-84	85	II-III	27	16.2	0.0	0	4	00 53 22.8	-48 09 43
93	00 51.1	-57 41	127	-148	I-II	17	18.6	0.0	0	6	00 53 16.0	-57 24 43
94	00 51.6	-59 32	87	24	II-III:	43	20.0	0.0	0	6	00 53 44.0	-59 15 44
95	00 51.7	-55 48	139	-47	II-III	4	18.6	0.0	0	6	00 53 53.4	-55 31 44
96	00 52.5	-46 56	-73	166	II	2	16.4	0.0	0	5	00 54 47.3	-46 39 45
97	00 52.5	-66 08	43	-61	I-II	23	16.9	0.0	0	5	00 54 29.1	-65 51 45
98	00 52.6	-20 04	-134	-3	II	25	18.0	0.0	0	6	00 55 04.1	-19 47 45
99	00 52.9	-49 43	-66	17	II-III	3	16.7	0.0	0	5	00 55 09.4	-49 26 45
100	00 53.3	-29 05	83	50	II	-28	17.5	0.0	0	5	00 55 43.1	-28 48 46
101	00 53.3	-50 12	-62	-9	II	26	15.6	0.0	0	4	00 55 33.0	-49 55 46
102	00 53.4	-37 41	14	125	II	29	16.3	0.0	0	4	00 55 45.6	-37 24 46
103	00 53.4	-85 01	60	-9	II-III	19	17.7	0.0	0	5	00 53 06.0	-84 44 44
104	00 53.6	-79 50	-87	4	I-II	25	18.0	0.0	0	5	00 54 43.7	-79 33 45
105	00 54.0	-29 22	91	35	II	-59	16.8	0.0	0	5	00 56 24.8	-29 05 46
106	00 54.2	-38 11	22	98	II-III	-34	16.8	0.0	0	5	00 56 33.2	-37 54 47
107	00 54.3	-84 09	74	35	I-II	-9	16.1	0.0	0	4	00 54 22.1	-83 52 45
108	00 54.9	-29 43	101	15	I-II	29	17.8	0.0	0	5	00 57 18.6	-29 26 47
109	00 54.9	-31 12	99	-64	I-II	-4	15.8	0.0316	0	4	00 57 18.0	-30 55 47
110	00 55.3	-52 32	-42	-134	III	20	17.7	0.0	0	5	00 57 30.6	-52 15 48
111	00 56.0	-44 01	-2	55	III	45	19.7	0.0	0	6	00 58 17.9	-43 44 48
112	00 56.5	-67 05	62	-113	II	16	16.1	0.0321	0	4	00 58 24.8	-66 48 49
113	00 58.3	-40 30	63	-27	I-II	12	16.1	0.0545	0	4	01 00 37.2	-40 13 51
114	00 59.1	-29 35	-118	23	I	-5	19.4	0.0	0	6	01 01 29.9	-29 18 52
115	00 59.5	-49 59	-9	3	I	-24	16.7	0.0	0	5	01 01 43.1	-49 42 52
116	00 59.5	-52 08	-8	-112	II	25	15.6	0.0	0	4	01 01 41.4	-51 51 52
117	00 59.6	-48 02	-8	108	III	18	19.2	0.0	0	6	01 01 50.4	-47 45 52
118	01 00.4	-17 23	-35	141	II-III	-42	16.1	0.0	0	4	01 02 52.2	-17 06 54
119	01 00.6	-29 28	-101	30	I-II	39	19.8	0.0	0	6	01 02 59.8	-29 11 54
120	01 01.5	-43 09	91	-170	I-II	-17	15.4	0.0	0	3	01 03 46.9	-42 52 55
121	01 01.7	-42 50	53	118	II:	98	20.6	0.0	2	6	01 03 59.1	-42 33 55
122	01 03.3	-41 56	111	-105	I-II	-35	17.3	0.0	0	5	01 05 35.2	-41 39 57
123	01 03.4	-38 41	118	69	III	27	19.5	0.0	0	6	01 05 43.0	-38 24 57
124	01 03.8	-49 30	29	29	II-III	-4	17.1	0.0	0	5	01 06 00.0	-49 13 57
125	01 04.2	-51 10	31	-61	I-II	13	16.4	0.0	0	5	01 06 22.5	-50 53 58
126	01 04.7	-57 52	-83	114	III	4	19.3	0.0	0	6	01 06 45.8	-57 35 58
127	01 05.6	-40 18	137	-19	I-II	-13	18.0	0.0	0	6	01 07 53.6	-40 02 00
128	01 05.6	-81 17	-52	-71	I-II	0	16.7	0.0	0	5	01 06 08.1	-81 00 59
129	01 06.6	-49 22	53	35	II	6	16.8	0.0	0	5	01 08 47.2	-49 06 01
130	01 06.9	-49 43	56	17	II-III	17	17.8	0.0	0	5	01 09 04.8	-49 27 01
131	01 07.4	-67 59	73	107	I-II	-17	15.9	0.0	0	4	01 09 09.6	-67 43 02
132	01 08.0	-51 25	62	-75	I-II	20	19.2	0.0	0	6	01 10 09.0	-51 09 03
133	01 08.5	-31 01	-8	-52	II	10	17.5	0.0	0	5	01 10 51.8	-30 45 04
134	01 08.7	-27 43	-6	124	II-III	26	17.7	0.0	0	5	01 11 05.3	-27 27 04
135	01 08.7	-48 09	74	101	III	26	19.3	0.0	0	6	01 10 53.5	-47 53 04
136	01 09.5	-30 00	3	1	I-II	-7	19.4	0.0	0	6	01 11 52.1	-29 44 05
137	01 09.9	-61 48	-42	-95	I	-13	15.4	0.0263	0	3	01 11 50.0	-61 32 05
138	01 10.5	-19 16	93	38	II	-3	15.8	0.0	0	4	01 12 56.6	-19 00 06
139	01 11.1	-30 20	21	-16	I-II	-2	19.4	0.0	0	6	01 13 27.7	-30 04 07

Table D.1 continued from previous page

ACO	RAB1950	DEB1950	Xcen	Ycen	BMtype	Count	m10	z	Rich	Dclass	_RA_icrs	_DE_icrs
140	01 11.3	-52 39	88	-141	II-III	28	17.4	0.0	0	5	01 13 24.7	-52 23 07
141	01 11.4	-32 01	25	-107	I	12	15.4	0.0206	0	3	01 13 44.8	-31 45 07
142	01 12.1	-47 51	105	115	II	13	16.8	0.0	0	5	01 14 16.7	-47 35 08
143	01 13.7	-62 32	-92	132	II	16	17.8	0.0	0	5	01 15 34.9	-62 16 10
144	01 15.5	-38 19	-30	93	II	26	16.8	0.0	0	5	01 17 46.5	-38 03 13
145	01 15.6	-54 26	71	29	II-III	71	20.1	0.0	1	6	01 17 39.2	-54 10 13
146	01 15.7	-30 34	74	-29	III	15	19.1	0.0	0	6	01 18 02.8	-30 18 13
147	01 16.0	-51 51	-118	-100	III:	60	20.4	0.0	1	6	01 18 05.8	-51 35 14
148	01 16.7	-54 18	80	35	III	56	19.9	0.0	1	6	01 18 45.0	-54 02 15
149	01 18.0	-48 53	155	58	III	20	18.9	0.0	0	6	01 20 08.0	-48 37 17
150	01 18.4	-47 35	-105	129	II:	54	19.8	0.0	1	6	01 20 33.0	-47 19 17
151	01 18.7	-30 43	109	-38	I-II	21	17.5	0.0	0	5	01 21 02.3	-30 27 18
152	01 18.8	-51 53	-94	-101	III	58	20.2	0.0	1	6	01 20 52.8	-51 37 18
153	01 18.9	-59 49	17	11	II	3	17.1	0.0	0	5	01 20 48.7	-59 33 18
154	01 20.3	-28 48	-140	64	I-II	-10	19.4	0.0	0	6	01 22 39.0	-28 32 20
155	01 22.4	-46 10	-19	-61	III	70	19.7	0.0	1	6	01 24 33.1	-45 54 23
156	01 23.5	-39 44	52	16	I-II	25	16.8	0.0	0	5	01 25 43.8	-39 28 25
157	01 23.9	-59 58	50	2	III	4	19.4	0.0	0	6	01 25 46.2	-59 42 25
158	01 25.0	-81 21	-12	-72	I-II	-44	16.7	0.0	0	5	01 24 57.0	-81 05 25
159	01 27.0	-27 17	-61	146	III	21	16.9	0.0	0	5	01 29 20.9	-27 01 31
160	01 27.9	-33 10	-92	99	I	-47	16.8	0.0	0	5	01 30 11.3	-32 54 32
161	01 28.5	-58 25	85	84	II	17	17.8	0.0	0	5	01 30 22.6	-58 09 33
162	01 29.7	-51 36	-4	-85	III	22	15.6	0.0	0	4	01 31 43.4	-51 20 35
163	01 30.2	-42 22	117	-126	II	23	16.4	0.0	0	5	01 32 22.2	-42 06 36
164	01 31.4	-68 02	-64	106	I-II	-18	16.1	0.0	0	4	01 32 53.3	-67 46 37
165	01 31.6	-32 47	-51	120	II-III	12	16.8	0.0	0	5	01 33 52.9	-32 31 38
166	01 32.1	-31 51	-1	-99	II	3	16.5	0.0	0	5	01 34 23.4	-31 35 39
167	01 32.1	-33 05	-45	104	I	23	17.3	0.0	0	5	01 34 22.6	-32 49 39
168	01 32.2	-28 01	0	107	I-II	15	17.5	0.0	0	5	01 34 31.7	-27 45 40
169	01 32.6	-64 30	22	28	II	-39	17.1	0.0	0	5	01 34 14.5	-64 14 40
170	01 32.7	-57 16	119	144	II	12	17.3	0.0	0	5	01 34 34.7	-57 00 40
171	01 33.7	-69 21	-51	35	II-III	20	17.1	0.0	0	5	01 35 05.2	-69 05 41
172	01 34.2	-68 55	-49	59	II	7	17.0	0.0	0	5	01 35 36.5	-68 39 42
173	01 34.7	-47 56	90	-158	II?	54	19.7	0.0	1	6	01 36 45.9	-47 40 44
174	01 34.8	-27 31	32	134	III	2	19.3	0.0	0	6	01 37 07.7	-27 15 44
175	01 35.1	-20 12	-126	-7	III	50	19.8	0.0	1	6	01 37 29.8	-19 56 45
176	01 35.6	-73 50	108	57	II	-16	16.2	0.0	0	4	01 36 36.7	-73 34 44
177	01 37.7	-27 58	66	109	I-II	-9	19.3	0.0	0	6	01 40 01.0	-27 42 49
178	01 38.1	-17 47	-90	123	III	66	19.8	0.0	1	6	01 40 30.8	-17 31 50
179	01 39.3	-17 20	-75	147	III	46	19.7	0.0	0	6	01 41 43.0	-17 04 52
180	01 39.9	-42 22	-45	-129	III	20	16.6	0.0	0	5	01 42 01.9	-42 06 53
181	01 40.5	-20 06	-59	-1	III	14	19.4	0.0	0	6	01 42 53.3	-19 50 55
182	01 41.2	-36 37	54	-86	II	5	16.6	0.0175	0	5	01 43 24.4	-36 21 56
183	01 41.2	-62 31	79	131	II-III	27	17.7	0.0	0	5	01 42 50.7	-62 15 55
184	01 41.4	-58 41	-90	69	I-II	-28	17.5	0.0	0	5	01 43 10.6	-58 25 56
185	01 41.7	-61 55	-81	-103	II	-68	16.8	0.0	0	5	01 43 21.9	-61 39 56
186	01 42.0	-35 33	63	-29	II	9	16.0	0.0	0	4	01 44 13.1	-35 17 57
187	01 42.9	-49 24	-154	31	I-II	8	18.6	0.0	0	6	01 44 53.8	-49 08 59
188	01 43.3	-56 42	27	-88	III:	103	20.8	0.0	2	6	01 45 07.3	-56 26 59
189	01 43.5	-29 06	134	48	II-III	-22	16.8	0.0	0	5	01 45 47.4	-28 51 00
190	01 44.1	-18 27	-12	87	III	21	19.5	0.0	0	6	01 46 29.9	-18 12 02
191	01 44.1	-73 12	-110	92	II	4	16.3	0.0	0	4	01 45 03.0	-72 57 00
192	01 44.8	-37 03	91	-110	III	13	17.4	0.0	0	5	01 46 59.4	-36 48 03
193	01 44.9	-28 43	-120	70	III	5	19.2	0.0	0	6	01 47 11.5	-28 28 03
194	01 46.4	-63 07	107	98	I-II	25	17.3	0.0	0	5	01 47 58.6	-62 52 05
195	01 46.6	-56 07	53	-58	I?	53	20.1	0.0	1	6	01 48 25.0	-55 52 06

Table D.1 continued from previous page

ACO	RAB1950	DEB1950	Xcen	Ycen	BMtype	Count	m10	z	Rich	Dclass	_RA_icrs	_DE_icrs
196	01 46.6	-62 17	-50	-121	II	5	17.5	0.0	0	5	01 48 12.6	-62 02 05
197	01 47.8	-33 04	131	103	III	-19	19.5	0.0	0	6	01 50 01.9	-32 49 09
198	01 49.2	-69 41	22	17	III	9	17.4	0.0	0	5	01 50 23.1	-69 26 10
199	01 49.5	-17 02	57	163	I-II	-11	17.1	0.0	0	5	01 51 54.3	-16 47 12
200	01 49.9	-19 47	59	15	III	1	19.5	0.0	0	6	01 52 16.6	-19 32 13
201	01 50.2	-44 31	-20	26	III	-59	16.7	0.0	0	5	01 52 15.2	-44 16 13
202	01 50.7	-18 59	70	58	II	16	16.8	0.0	0	5	01 53 05.0	-18 44 15
203	01 51.1	-33 53	-104	59	II-III	28	17.7	0.0	0	5	01 53 18.7	-33 38 15
204	01 53.3	-49 03	-64	53	III	12	19.1	0.0	0	6	01 55 15.1	-48 48 20
205	01 53.5	-58 47	-5	66	III	7	18.6	0.0	0	6	01 55 11.2	-58 32 20
206	01 54.0	-37 47	-67	-149	II	22	19.4	0.0	0	6	01 56 08.9	-37 32 21
207	01 55.6	-18 38	133	76	III	34	19.9	0.0	0	6	01 57 58.8	-18 23 25
208	01 55.7	-58 34	10	77	III	8	18.6	0.0	0	6	01 57 22.8	-58 19 24
209	01 55.9	-78 43	67	65	I-II	26	18.0	0.0	0	5	01 55 47.3	-78 28 23
210	01 56.2	-64 38	-93	19	I	-89	16.1	0.0	0	4	01 57 37.3	-64 23 25
211	01 56.3	-81 38	49	-91	II	0	16.8	0.0	0	5	01 55 15.0	-81 23 23
212	01 57.5	-65 19	-84	-17	II	10	17.1	0.0	0	5	01 58 52.4	-65 04 28
213	01 58.0	-22 51	97	116	I-II	26	19.4	0.0	0	6	02 00 19.8	-22 36 30
214	01 58.8	-40 23	-117	-22	II	24	17.2	0.0	0	5	02 00 53.5	-40 08 31
215	01 59.0	-40 50	-114	-46	II	-10	16.1	0.0	0	4	02 01 05.0	-40 35 32
216	01 59.5	-37 16	-113	146	II-III	28	18.0	0.0	0	6	02 01 38.3	-37 01 33
217	01 59.6	-44 54	70	4	I-II	13	16.0	0.0	0	4	02 01 36.4	-44 39 33
218	01 59.8	-48 29	-7	84	I-II	-7	17.4	0.0	0	5	02 01 44.0	-48 14 33
219	01 59.9	-36 03	-5	-55	I-II	14	18.7	0.0	0	6	02 02 03.4	-35 48 34
220	02 00.8	-32 05	2	158	II-III	112	20.0	0.0	2	6	02 03 00.6	-31 50 36
221	02 03.5	-42 16	112	146	III	21	18.3	0.0	0	6	02 05 32.5	-42 01 42
222	02 04.0	-51 02	29	-53	III	23	19.2	0.1716	0	6	02 05 51.1	-50 47 43
223	02 04.7	-37 32	-58	132	I-II	-8	16.8	0.0	0	5	02 06 49.1	-37 17 45
224	02 05.0	-45 09	121	-10	II:	26	18.3	0.0	0	6	02 06 58.8	-44 54 45
225	02 05.6	-61 27	71	-79	I-II	-10	16.1	0.0	0	4	02 07 05.7	-61 12 46
226	02 08.0	-29 37	-119	21	III	41	19.8	0.0	0	6	02 10 13.6	-29 22 52
227	02 08.2	-33 54	84	60	III:	8	18.7	0.0	0	6	02 10 21.9	-33 39 53
228	02 08.5	-43 07	160	97	II	-32	17.9	0.0	0	5	02 10 30.4	-42 52 53
229	02 08.8	-37 00	-14	161	II-III	23	18.3	0.0	0	6	02 10 54.8	-36 45 54
230	02 10.0	-48 05	85	104	II-III	10	16.0	0.2197	0	4	02 11 53.7	-47 50 57
231	02 10.7	-28 09	-88	100	II-III	7	19.4	0.0	0	6	02 12 56.4	-27 54 59
232	02 10.9	-32 19	-83	-123	III	9	19.3	0.0	0	6	02 13 04.8	-32 04 59
233	02 11.1	-34 37	117	22	II-III:	17	18.7	0.0	0	6	02 13 14.7	-34 23 00
234	02 11.9	-48 54	100	59	III	26	19.3	0.0	0	6	02 13 46.0	-48 40 01
235	02 12.0	-34 03	-135	51	I	104	20.1	0.0	2	6	02 14 09.1	-33 49 02
236	02 13.3	-68 23	-115	85	I-II	26	16.5	0.0	0	5	02 14 19.3	-68 09 03
237	02 13.4	-33 13	-119	94	III	120	19.8	0.0	2	6	02 15 33.6	-32 59 05
238	02 13.8	-30 03	-50	-1	II-III	29	19.5	0.0	0	6	02 16 00.4	-29 49 06
239	02 14.9	-48 03	129	103	I	20	16.4	0.0635	0	5	02 16 46.4	-47 49 08
240	02 15.0	-82 14	-85	-125	III	14	18.8	0.0	0	5	02 13 07.2	-82 00 04
241	02 16.6	-65 03	24	-2	I-II	5	16.7	0.0	0	5	02 17 49.2	-64 49 12
242	02 17.1	-31 53	-13	-99	III	58	19.8	0.0	1	6	02 19 16.3	-31 39 14
243	02 17.2	-29 41	-12	18	III	30	19.9	0.0	0	6	02 19 24.2	-29 27 15
244	02 17.8	-26 11	68	-63	I-II	-6	15.8	0.0	0	4	02 20 03.1	-25 57 16
245	02 17.8	-28 35	-4	78	III	20	19.3	0.0	0	6	02 20 01.1	-28 21 16
246	02 18.0	-27 19	-2	145	II	21	17.4	0.0	0	5	02 20 14.2	-27 05 17
247	02 18.3	-40 08	83	-8	I-II	-15	16.8	0.0	0	5	02 20 19.7	-39 54 17
248	02 18.9	-62 35	41	131	II	4	17.0	0.0	0	5	02 20 14.4	-62 21 18
249	02 19.8	-37 05	-46	-111	II:	83	20.0	0.0	2	6	02 21 52.7	-36 51 21
250	02 20.5	-51 20	-82	-70	I-II	-3	16.1	0.0484	0	4	02 22 15.6	-51 06 22
251	02 20.5	-55 54	59	-47	III	13	19.3	0.0	0	6	02 22 06.9	-55 40 22

Table D.1 continued from previous page

ACO	RAB1950	DEB1950	Xcen	Ycen	BMtype	Count	m10	z	Rich	Dclass	_RA_icrs	_DE_icrs
252	02 21.3	-44 06	11	51	II-III	9	16.8	0.0	0	5	02 23 14.2	-43 52 24
253	02 21.7	-44 53	15	9	II-III	1	16.8	0.0	0	5	02 23 37.1	-44 39 25
254	02 22.2	-67 35	49	-138	II	6	16.6	0.0	0	5	02 23 11.8	-67 21 26
255	02 22.4	-19 17	-60	39	III	46	20.4	0.0	0	6	02 24 44.1	-19 03 28
256	02 22.4	-30 37	48	-32	III	44	19.9	0.0	0	6	02 24 34.7	-30 23 28
257	02 22.5	-64 05	59	49	II	12	17.5	0.0	0	5	02 23 43.7	-63 51 27
258	02 23.6	-29 50	62	9	II	8	16.1	0.0	0	4	02 25 47.2	-29 36 31
259	02 23.6	-59 17	-63	39	III	26	18.6	0.0	0	6	02 25 03.8	-59 03 30
260	02 23.7	-36 04	-5	-56	III	73	20.0	0.0	1	6	02 25 47.1	-35 50 31
261	02 23.9	-63 27	69	82	II	18	17.6	0.0574	0	5	02 25 09.3	-63 13 30
262	02 24.2	-63 50	70	62	I-II	18	17.4	0.0	0	5	02 25 25.8	-63 36 31
263	02 24.3	-23 39	150	72	I	16	15.3	0.0	0	3	02 26 34.5	-23 25 33
264	02 24.9	-36 17	9	-67	II-III	45	19.7	0.0	0	6	02 26 58.7	-36 03 34
265	02 25.0	-19 24	-28	32	II	23	16.5	0.0	0	5	02 27 19.8	-19 10 35
266	02 25.3	-28 54	84	59	III	-1	19.6	0.0	0	6	02 27 29.9	-28 40 35
267	02 25.3	-47 26	48	-128	I-II	-16	17.7	0.0	0	5	02 27 08.6	-47 12 35
268	02 27.3	-17 16	2	147	I-II	15	15.9	0.0	0	4	02 29 39.3	-17 02 41
269	02 27.5	-22 26	3	-130	II-III	21	16.8	0.0	0	5	02 29 47.2	-22 12 41
270	02 27.6	-27 08	-79	-114	II-III	21	19.1	0.0	0	6	02 29 49.2	-26 54 41
271	02 28.1	-39 07	-84	48	I	19	18.1	0.0	0	6	02 30 07.0	-38 53 42
272	02 28.1	-42 22	-81	-126	III	12	19.0	0.0	0	6	02 30 03.0	-42 08 42
273	02 29.1	-17 52	25	115	I	-6	15.8	0.0	0	4	02 31 26.7	-17 38 45
274	02 29.7	-58 09	-21	100	I-II	-4	15.4	0.0309	0	3	02 31 10.4	-57 55 46
275	02 30.2	-50 59	-1	-51	II	-4	16.8	0.0	0	5	02 31 55.4	-50 45 47
276	02 30.5	-79 48	-72	9	II	29	17.4	0.0	0	5	02 29 20.2	-79 34 44
277	02 31.6	-49 48	12	13	II	-5	16.0	0.0	0	4	02 33 21.1	-49 34 51
278	02 32.4	-33 54	91	108	III:	45	19.7	0.0	0	6	02 34 30.0	-33 40 54
279	02 32.5	-37 45	-39	121	II	-10	16.7	0.0	0	5	02 34 31.8	-37 31 54
280	02 32.9	-59 51	1	9	I-II	-63	16.8	0.0	0	5	02 34 16.6	-59 37 54
281	02 33.2	-41 47	-31	-94	II	11	16.9	0.0	0	5	02 35 08.7	-41 33 56
282	02 33.3	-66 12	112	-69	II-III	0	16.8	0.0	0	5	02 34 18.0	-65 58 55
283	02 33.8	-50 32	31	-27	II	9	16.8	0.0212	0	5	02 35 31.2	-50 18 57
284	02 33.9	-59 23	8	34	III	27	18.0	0.0	0	6	02 35 17.5	-59 09 57
285	02 34.1	-66 32	-120	-83	III	18	18.0	0.0	0	6	02 35 04.1	-66 18 57
286	02 34.7	-45 04	-130	-4	II-III	25	18.8	0.0	0	6	02 36 33.8	-44 51 00
287	02 34.8	-20 39	95	-35	II-III	44	20.5	0.0	0	6	02 37 06.0	-20 26 01
288	02 35.3	-57 21	19	143	I-II	-59	16.5	0.0	0	5	02 36 46.4	-57 08 01
289	02 36.6	-42 04	3	-110	III	29	18.1	0.0	0	6	02 38 31.6	-41 51 05
290	02 37.8	-47 56	69	111	III	0	19.1	0.0	0	6	02 39 34.7	-47 43 08
291	02 42.9	-29 15	20	42	I	19	18.6	0.0	0	6	02 45 03.3	-29 02 23
292	02 42.9	-47 42	116	122	I-II	21	17.0	0.0	0	5	02 44 39.8	-47 29 23
293	02 43.1	-45 26	-50	-22	II-III	-16	18.0	0.0	0	6	02 44 55.4	-45 13 23
294	02 43.7	-32 37	-51	126	II-III	68	20.1	0.0	1	6	02 45 47.7	-32 24 26
295	02 43.9	-53 14	-11	95	III?	85	20.2	0.0	2	6	02 45 29.1	-53 01 25
296	02 44.7	-42 35	-36	132	I	-15	16.4	0.0	0	5	02 46 35.3	-42 22 28
297	02 45.6	-42 02	92	-108	II	6	16.1	0.0	0	4	02 47 29.9	-41 49 31
298	02 45.7	-56 42	2	-89	II	68	20.1	0.0	1	6	02 47 08.5	-56 29 30
299	02 47.0	-67 29	54	136	III	-10	19.4	0.0	0	6	02 47 46.7	-67 16 33
300	02 47.1	-41 29	109	-81	I-II	-39	17.2	0.0	0	5	02 49 00.3	-41 16 35
301	02 47.5	-31 24	71	-74	I	5	14.7	0.0223	0	3	02 49 36.5	-31 11 37
302	02 47.7	-35 51	-6	-45	III	65	19.7	0.0	1	6	02 49 43.5	-35 38 37
303	02 48.3	-71 35	48	-85	II	5	16.8	0.0586	0	5	02 48 38.0	-71 22 36
304	02 49.8	-43 00	14	109	I-II	2	19.3	0.0	0	6	02 51 39.7	-42 47 43
305	02 50.5	-55 27	39	-24	III	65	19.7	0.0	1	6	02 51 58.0	-55 14 44
306	02 52.0	-41 29	-103	-80	II	17	17.5	0.0	0	5	02 53 53.4	-41 16 50
307	02 52.4	-51 11	-69	-62	II	5	15.9	0.0	0	4	02 54 01.0	-50 58 50

Table D.1 continued from previous page

ACO	RAB1950	DEB1950	Xcen	Ycen	BMtype	Count	m10	z	Rich	Dclass	_RA_icrs	_DE_icrs
308	02 52.7	-52 08	-65	-113	I-II	2	16.5	0.0	0	5	02 54 16.9	-51 55 51
309	02 52.7	-62 06	-114	-114	II	-6	16.2	0.0	0	4	02 53 49.5	-61 53 50
310	02 53.0	-49 40	-65	20	III	17	19.3	0.0	0	6	02 54 39.8	-49 27 52
311	02 53.6	-66 37	-15	-85	I-II	15	16.8	0.0263	0	5	02 54 23.9	-66 24 53
312	02 53.7	-61 55	132	-108	II	-3	16.2	0.0	0	4	02 54 49.8	-61 42 54
313	02 55.3	-49 25	-45	33	III	16	19.3	0.0	0	6	02 56 57.7	-49 12 59
314	02 56.4	-42 59	79	109	II	27	17.7	0.0	0	5	02 58 14.4	-42 47 03
315	02 57.6	-51 13	-25	-64	I	-12	16.1	0.0618	0	4	02 59 11.6	-51 01 06
316	02 58.3	-37 14	107	-118	II	6	15.5	0.0201	0	4	03 00 16.1	-37 02 09
317	03 00.3	-49 45	-1	15	II	26	17.3	0.0	0	5	03 01 55.9	-49 33 15
318	03 00.9	-18 00	-105	109	II	29	19.4	0.0	0	6	03 03 12.3	-17 48 18
319	03 01.0	-32 21	143	139	II?	60	20.6	0.0	1	6	03 03 03.7	-32 09 17
320	03 01.9	-41 07	-3	-59	I-II	24	18.4	0.0	0	6	03 03 46.1	-40 55 20
321	03 03.6	-46 58	-116	-104	II	19	17.5	0.0	0	5	03 05 18.3	-46 46 25
322	03 04.4	-79 35	9	24	I	28	16.6	0.0	0	5	03 02 39.2	-79 23 22
323	03 07.4	-56 51	-81	-98	III:	63	19.9	0.0	1	6	03 08 43.2	-56 39 36
324	03 08.3	-47 31	-72	-133	II	9	16.7	0.0585	0	5	03 09 58.3	-47 19 40
325	03 08.3	-51 52	64	-99	II	3	16.5	0.0	0	5	03 09 49.4	-51 40 40
326	03 08.3	-52 26	63	-129	II	14	17.4	0.0	0	5	03 09 48.2	-52 14 40
327	03 09.4	-72 18	-37	146	II	9	16.5	0.0	0	5	03 09 24.6	-72 06 41
328	03 11.0	-46 55	-48	-100	II	21	17.2	0.0	0	5	03 12 40.9	-46 43 49
329	03 11.0	-49 49	91	9	I-II	-3	16.8	0.0531	0	5	03 12 35.2	-49 37 48
330	03 11.6	-51 26	93	-76	II	0	17.0	0.0	0	5	03 13 07.6	-51 14 50
331	03 11.8	-68 37	-83	74	II-III	22	18.0	0.0	0	6	03 12 15.5	-68 25 49
332	03 12.0	-39 17	102	37	II	-14	15.6	0.0	0	4	03 13 53.1	-39 05 52
333	03 13.1	-29 26	104	29	II	24	15.6	0.0	0	4	03 15 11.6	-29 14 56
334	03 14.6	-45 18	-15	-14	II	5	16.0	0.0	0	4	03 16 19.0	-45 07 00
335	03 15.4	-46 42	-8	-89	II	-99	16.1	0.0	0	4	03 17 04.3	-46 31 03
336	03 15.8	-44 53	-4	9	II	5	15.9	0.0744	0	4	03 17 31.6	-44 42 04
337	03 16.0	-29 49	137	8	I	-10	16.1	0.0	0	4	03 18 04.8	-29 38 06
338	03 16.7	-52 26	-112	-131	II	-1	17.1	0.0384	0	5	03 18 10.0	-52 15 07
339	03 17.9	-54 03	-4	53	III	15	15.3	0.0546	0	3	03 19 17.8	-53 52 11
340	03 18.3	-27 17	-1	-120	II-III	-99	16.4	0.0	0	5	03 20 25.5	-27 06 13
341	03 18.5	-48 17	-105	92	I-II	-3	16.8	0.0	0	5	03 20 06.7	-48 06 13
342	03 18.8	-44 10	25	46	I-II	21	18.9	0.0	0	6	03 20 32.2	-43 59 14
343	03 19.0	-43 27	28	86	II	23	18.1	0.0	0	6	03 20 45.4	-43 16 15
344	03 20.0	-44 02	37	54	II-III	27	18.1	0.0	0	6	03 21 44.3	-43 51 18
345	03 20.1	-45 43	37	-36	II	9	16.1	0.0	0	4	03 21 47.2	-45 32 19
346	03 20.8	-49 30	-83	28	I-II	8	16.0	0.067	0	4	03 22 21.7	-49 19 21
347	03 20.9	-29 28	-73	32	III	108	19.9	0.0	2	6	03 22 58.7	-29 17 22
348	03 22.3	-64 44	-103	10	II	18	17.5	0.0	0	5	03 23 02.7	-64 33 25
349	03 22.4	-67 11	-32	153	II	0	16.6	0.0	0	5	03 22 55.4	-67 00 24
350	03 22.7	-74 30	14	27	III	28	18.1	0.0	0	5	03 22 10.6	-74 19 24
351	03 23.7	-34 30	-140	27	I	17	19.3	0.0	0	6	03 25 40.1	-34 19 31
352	03 24.8	-32 56	-130	112	II-III	19	17.5	0.0	0	5	03 26 48.0	-32 45 35
353	03 24.9	-51 35	-46	-84	II	-11	15.8	0.041	0	4	03 26 22.1	-51 24 35
354	03 26.6	-57 54	112	112	III	26	16.7	0.0	0	5	03 27 46.3	-57 43 40
355	03 27.4	-66 32	-70	-82	I-II	-42	17.2	0.0	0	5	03 27 57.1	-66 21 42
356	03 28.0	-46 09	109	-62	I-II	10	16.0	0.0	0	4	03 29 38.9	-45 58 46
357	03 29.2	-26 16	130	-68	I	-1	16.6	0.0	0	5	03 31 19.7	-26 05 51
358	03 30.8	-49 59	4	3	II-III	26	17.1	0.0	0	5	03 32 18.5	-49 48 55
359	03 31.5	-22 27	15	-130	III	13	19.5	0.0	0	6	03 33 41.7	-22 16 59
360	03 31.8	-49 18	13	38	II	-12	16.1	0.0	0	4	03 33 19.8	-49 07 59
361	03 32.0	-32 50	-49	119	I	27	16.8	0.0	0	5	03 33 59.3	-32 40 00
362	03 32.1	-64 25	-47	32	I-II	-74	16.0	0.0	0	4	03 32 48.5	-64 14 58
363	03 32.2	-33 49	-46	66	II-III	5	16.4	0.0	0	5	03 34 10.0	-33 39 01

Table D.1 continued from previous page

ACO	RAB1950	DEB1950	Xcen	Ycen	BMtype	Count	m10	z	Rich	Dclass	_RA_icrs	_DE_icrs
364	03 33.0	-39 40	50	18	I-II	9	16.8	0.0	0	5	03 34 49.3	-39 30 03
365	03 33.5	-42 35	52	-139	I-II	-3	16.5	0.0	0	5	03 35 14.5	-42 25 05
366	03 33.6	-53 45	-139	68	II	-5	16.1	0.0598	0	4	03 34 56.6	-53 35 05
367	03 33.8	-45 20	-98	-18	I-II	-13	16.0	0.0666	0	4	03 35 27.4	-45 10 06
368	03 34.0	-33 08	-26	102	I-II	19	17.2	0.0	0	5	03 35 58.7	-32 58 07
369	03 34.6	-59 07	-93	47	I-II	12	17.5	0.0	0	5	03 35 39.9	-58 57 08
370	03 35.2	-32 38	-12	129	II	23	16.7	0.0	0	5	03 37 11.2	-32 28 11
371	03 35.9	-60 24	-82	-21	II-III	4	17.1	0.0	0	5	03 36 52.8	-60 14 12
372	03 36.0	-55 35	-116	-29	I-II	7	15.9	0.0758	0	4	03 37 14.9	-55 25 13
373	03 36.6	-35 37	2	-31	I	-18	10.1	0.0046	0	0	03 38 30.9	-35 27 16
374	03 38.7	-50 23	71	-21	III	13	17.4	0.0	0	5	03 40 09.9	-50 13 23
375	03 39.0	-51 46	71	-94	II	2	16.5	0.0	0	5	03 40 24.5	-51 36 24
376	03 39.1	-38 00	116	106	I-II	11	17.1	0.0	0	5	03 40 57.1	-37 50 25
377	03 39.5	-55 22	-90	-17	I-II	19	15.4	0.0425	0	3	03 40 44.7	-55 12 25
378	03 39.6	-64 43	-4	16	II	-67	16.8	0.0	0	5	03 40 14.3	-64 33 25
379	03 41.9	-19 29	149	27	I-II	27	18.0	0.0	0	6	03 44 08.3	-19 19 36
380	03 42.0	-75 10	79	-13	I-II	-70	16.8	0.0	0	5	03 41 07.2	-75 00 30
381	03 42.7	-62 43	16	124	I-II	27	18.0	0.0	0	5	03 43 29.0	-62 33 36
382	03 42.8	-66 10	13	-62	II	4	17.4	0.0	0	5	03 43 17.1	-66 00 36
383	03 43.6	-36 57	78	-103	II-III	26	17.8	0.0	0	5	03 45 28.1	-36 47 41
384	03 44.0	-41 20	-103	-72	I	6	15.5	0.0	0	4	03 45 45.0	-41 10 43
385	03 45.1	-31 58	100	163	I	14	16.6	0.0	0	5	03 47 05.1	-31 48 47
386	03 45.4	-31 05	-55	-55	III	17	18.1	0.0	0	6	03 47 24.2	-30 55 48
387	03 45.4	-61 39	-19	-87	II	-35	17.0	0.0	0	5	03 46 14.8	-61 29 46
388	03 45.5	-34 47	-160	10	II-III?	80	19.9	0.0	2	6	03 47 25.1	-34 37 48
389	03 45.5	-85 47	76	-57	II	8	17.1	0.0	0	5	03 35 53.3	-85 37 27
390	03 45.7	-54 11	-43	48	I-II	-65	16.5	0.0605	0	5	03 46 58.7	-54 01 48
391	03 45.8	-23 41	68	71	III?	71	20.1	0.0	1	6	03 47 57.3	-23 31 50
392	03 45.8	-69 24	80	31	I-II	7	17.1	0.0	0	5	03 45 54.1	-69 14 46
393	03 46.7	-45 42	24	-35	I	11	16.1	0.0454	0	4	03 48 18.5	-45 32 52
394	03 47.1	-29 50	-35	8	II-III	12	17.7	0.0	0	5	03 49 07.7	-29 40 54
395	03 47.3	-51 49	-108	-98	II	-15	16.8	0.0	0	5	03 48 40.7	-51 39 54
396	03 47.4	-64 43	40	16	II-III	26	18.0	0.0	0	6	03 47 59.6	-64 33 53
397	03 50.4	-31 30	21	-77	II-III	20	18.0	0.0	0	6	03 52 23.2	-31 21 06
398	03 53.2	-46 17	84	-67	II-III	27	17.6	0.0	0	5	03 54 46.3	-46 08 16
399	03 53.2	-53 57	16	60	I-II	11	16.4	0.0394	0	5	03 54 27.7	-53 48 15
400	03 53.7	-36 43	-69	-92	II?	79	20.9	0.0	1	6	03 55 33.3	-36 34 19
401	03 54.2	-59 06	42	49	II-III	10	17.5	0.0	0	5	03 55 10.6	-58 57 19
402	03 54.3	-44 21	97	36	II:	-56	16.6	0.0	0	5	03 55 56.0	-44 12 20
403	03 54.4	-34 20	-63	31	III	61	21.4	0.0	1	6	03 56 18.8	-34 11 21
404	03 55.1	-54 01	31	56	I	23	15.5	0.0365	0	4	03 56 21.1	-53 52 23
405	03 56.0	-82 22	-64	-130	I-II	2	16.8	0.0	0	5	03 51 32.9	-82 13 15
406	03 57.0	-64 05	98	46	II	12	17.3	0.0	0	5	03 57 35.8	-63 56 28
407	03 57.2	-50 16	-26	-12	III	1	19.3	0.0	0	6	03 58 36.7	-50 07 31
408	03 57.4	-61 50	57	-98	III	29	18.0	0.0	0	5	03 58 10.6	-61 41 30
409	03 57.4	-68 29	-114	78	I-II	8	17.0	0.0	0	5	03 57 32.4	-68 20 29
410	03 57.7	-59 44	64	15	II	-29	15.7	0.0	0	4	03 58 37.3	-59 35 32
411	04 00.3	-65 07	112	-11	I-II	-17	15.9	0.038	0	4	04 00 47.2	-64 58 41
412	04 00.6	-57 02	91	158	II-III	-1	16.1	0.0467	0	4	04 01 40.5	-56 53 43
413	04 02.1	-63 56	128	52	II	-7	17.1	0.037	0	5	04 02 41.1	-63 47 48
414	04 02.3	-24 27	0	29	II-III	70	19.7	0.0	1	6	04 04 25.3	-24 18 52
415	04 02.9	-60 57	95	-53	II	1	15.4	0.0	0	3	04 03 43.0	-60 48 51
416	04 03.2	-43 59	-86	55	I-II	-13	16.6	0.0648	0	5	04 04 49.5	-43 50 54
417	04 03.3	-66 06	124	-65	II-III	19	18.0	0.0	0	6	04 03 40.4	-65 57 52
418	04 04.2	-39 00	104	54	II:	12	15.2	0.0	0	3	04 05 58.4	-38 51 58
419	04 04.5	-47 59	38	109	III	15	19.2	0.0	0	6	04 05 58.8	-47 50 59

Table D.1 continued from previous page

ACO	RAB1950	DEB1950	Xcen	Ycen	BMtype	Count	m10	z	Rich	Dclass	_RA_icrs	_DE_icrs
420	04 04.7	-47 15	-68	-120	II-III	-57	16.6	0.0	0	5	04 06 12.4	-47 06 59
421	04 05.8	-27 33	-87	132	III	20	19.2	0.0	0	6	04 07 51.1	-27 25 05
422	04 05.9	-22 22	-76	-131	II:	65	20.2	0.0	1	6	04 08 03.6	-22 14 05
423	04 05.9	-44 34	-60	24	III	-3	16.8	0.0	0	5	04 07 29.9	-44 26 04
424	04 06.0	-43 33	-60	78	II	-2	16.7	0.0589	0	5	04 07 37.9	-43 25 05
425	04 07.1	-60 12	125	-15	I-II	-1	17.1	0.0	0	5	04 07 57.1	-60 04 07
426	04 07.7	-60 57	126	-55	I	-18	15.4	0.0	0	3	04 08 29.8	-60 49 10
427	04 07.8	-19 21	-55	36	II-III	73	20.8	0.0	1	6	04 10 01.1	-19 13 13
428	04 07.8	-75 09	-60	-8	II	20	17.6	0.0	0	5	04 06 40.6	-75 01 06
429	04 08.1	-61 34	126	-88	II	-3	15.9	0.0	0	4	04 08 50.9	-61 26 11
430	04 09.2	-58 07	-122	99	III:	91	20.1	0.0	2	6	04 10 10.8	-57 59 16
431	04 11.4	-48 40	99	70	I-II	16	17.4	0.0	0	5	04 12 50.2	-48 32 25
432	04 12.7	-69 30	-38	28	II	-70	16.7	0.0	0	5	04 12 36.8	-69 22 27
433	04 13.2	-50 55	109	-50	I	2	16.3	0.0668	0	5	04 14 32.3	-50 47 32
434	04 14.9	-43 02	27	106	II	7	16.6	0.0	0	5	04 16 31.8	-42 54 39
435	04 16.9	-17 35	61	130	II?	58	20.9	0.0	1	6	04 19 08.7	-17 27 49
436	04 17.1	-42 19	49	145	II	0	17.1	0.0	0	5	04 18 45.0	-42 11 48
437	04 17.2	-44 20	48	37	II	-8	17.4	0.0	0	5	04 18 46.9	-44 12 48
438	04 17.2	-46 30	47	-79	III	3	18.0	0.0	0	6	04 18 42.3	-46 22 48
439	04 17.5	-19 31	68	27	III	96	20.0	0.0	2	6	04 19 42.4	-19 23 51
440	04 17.8	-28 00	55	107	I-II	-67	16.2	0.0	0	4	04 19 49.7	-27 52 52
441	04 18.2	-18 42	75	70	II	102	20.4	0.0	2	6	04 20 25.3	-18 34 54
442	04 19.0	-51 34	-95	-83	I-II	-48	16.8	0.0	0	5	04 20 17.6	-51 26 55
443	04 19.1	-20 31	87	-27	II?	0	21.6	0.0	0	6	04 21 17.1	-20 23 57
444	04 20.3	-43 16	79	93	III	49	19.9	0.0	0	6	04 21 54.7	-43 09 01
445	04 20.7	-74 49	-16	11	II	-1	16.6	0.0	0	5	04 19 33.4	-74 41 57
446	04 21.5	-46 00	86	-54	II	27	17.3	0.0	0	5	04 23 00.9	-45 53 05
447	04 21.8	-30 50	99	-46	III	28	18.1	0.0	0	6	04 23 45.5	-30 43 07
448	04 21.8	-33 54	-26	60	I-II	0	17.8	0.0	0	5	04 23 40.9	-33 47 07
449	04 22.3	-27 51	108	115	I-II	-16	15.7	0.0	0	4	04 24 19.6	-27 44 09
450	04 23.1	-68 45	11	68	I-II	9	16.8	0.0	0	5	04 23 03.5	-68 38 08
451	04 23.9	-37 49	40	119	III	78	20.1	0.0	1	6	04 25 40.4	-37 42 15
452	04 24.0	-28 45	127	66	II	-17	16.6	0.0	0	5	04 26 00.3	-28 38 16
453	04 24.1	-32 47	1	120	I	29	16.8	0.0	0	5	04 26 00.4	-32 40 16
454	04 24.4	-43 28	120	81	II	-15	16.5	0.0	0	5	04 25 59.9	-43 21 17
455	04 24.7	-48 34	-50	79	I-II	-4	16.8	0.0	0	5	04 26 06.5	-48 27 18
456	04 25.2	-45 53	122	-49	III	41	19.8	0.0	0	6	04 26 42.7	-45 46 20
457	04 25.5	-49 14	-42	44	II	-29	16.9	0.0	0	5	04 26 52.8	-49 07 21
458	04 25.6	-29 56	-122	9	II-III	20	17.2	0.0	0	5	04 27 34.5	-29 49 23
459	04 26.6	-28 15	-113	99	II	0	16.1	0.0	0	4	04 28 36.8	-28 08 27
460	04 26.8	-62 25	14	140	III:	133	20.6	0.0	3	6	04 27 24.5	-62 18 25
461	04 26.9	-50 39	-30	-32	I-II	12	16.6	0.0539	0	5	04 28 12.9	-50 32 26
462	04 27.5	-32 53	39	114	II	24	17.4	0.0	0	5	04 29 24.0	-32 46 30
463	04 28.0	-53 56	30	57	I-II	26	15.1	0.0394	0	3	04 29 09.4	-53 49 31
464	04 28.5	-36 45	47	-93	I	27	15.9	0.0	0	4	04 30 17.8	-36 38 34
465	04 29.5	-29 52	-77	14	I-II	4	15.1	0.0	0	3	04 31 28.3	-29 45 38
466	04 29.7	-27 55	-76	117	I-II	17	17.3	0.0	0	5	04 31 43.1	-27 48 39
467	04 30.1	-67 01	50	160	II	-50	16.5	0.0	0	5	04 30 14.5	-66 54 37
468	04 30.2	-46 13	-89	-64	II	1	16.5	0.0675	0	5	04 31 41.3	-46 06 40
469	04 30.7	-20 54	-32	-47	III	20	18.9	0.0	0	5	04 32 52.2	-20 47 44
470	04 31.3	-31 55	-56	-97	II	13	16.6	0.0	0	5	04 33 13.2	-31 48 45
471	04 33.5	-28 37	-31	81	I-II	22	16.7	0.0	0	5	04 35 29.9	-28 30 55
472	04 34.0	-36 01	-154	-56	II	-41	16.8	0.0	0	5	04 35 48.6	-35 54 56
473	04 34.4	-22 33	14	-135	I-II	2	16.7	0.0	0	5	04 36 31.9	-22 26 59
474	04 34.7	-20 22	19	-18	I-II	26	17.5	0.0	0	5	04 36 52.7	-20 16 00
475	04 34.8	-50 37	38	-31	II	-6	16.7	0.0	0	5	04 36 05.9	-50 30 58

Table D.1 continued from previous page

ACO	RAB1950	DEB1950	Xcen	Ycen	BMtype	Count	m10	z	Rich	Dclass	_RA_icrs	_DE_icrs
476	04 34.9	-39 45	-118	14	II	-1	15.9	0.0	0	4	04 36 36.0	-39 39 00
477	04 35.6	-49 43	46	17	II	5	16.4	0.0	0	5	04 36 56.2	-49 37 02
478	04 36.2	-31 46	0	-89	II	2	16.1	0.0	0	4	04 38 07.1	-31 40 05
479	04 36.5	-51 32	51	-80	I	-4	16.0	0.0363	0	4	04 37 45.2	-51 26 05
480	04 36.6	-85 55	-14	-47	II-III	26	17.8	0.0	0	5	04 24 54.6	-85 48 39
481	04 36.8	-29 20	7	42	II	2	16.4	0.0	0	5	04 38 46.7	-29 14 08
482	04 37.1	-55 58	-150	-57	III	50	20.4	0.0	1	6	04 38 07.3	-55 52 07
483	04 38.0	-33 08	-114	99	I-II	26	17.2	0.0	0	5	04 39 52.9	-33 02 13
484	04 38.3	-35 43	-108	-38	II	5	15.9	0.0	0	4	04 40 06.7	-35 37 14
485	04 38.5	-73 15	53	92	I-II	5	17.2	0.0	0	5	04 37 36.4	-73 09 09
486	04 38.7	-45 27	-9	-23	II	4	16.7	0.0	0	5	04 40 12.1	-45 21 15
487	04 38.9	-44 44	-8	16	I	-7	15.0	0.0372	0	3	04 40 25.7	-44 38 16
488	04 39.4	-29 47	38	18	I-II	22	16.6	0.0	0	5	04 41 21.9	-29 41 19
489	04 40.0	-37 02	-89	-109	I	3	15.8	0.0	0	4	04 41 46.4	-36 56 21
490	04 40.2	-27 06	49	161	II	13	17.3	0.0	0	5	04 42 13.6	-27 00 22
491	04 40.5	-32 56	-86	111	I-II	-16	16.6	0.0	0	5	04 42 23.0	-32 50 23
492	04 40.8	-21 18	95	-70	II	-3	16.8	0.0	0	5	04 42 57.2	-21 12 25
493	04 41.2	-21 54	99	-101	II	10	16.8	0.0	0	5	04 43 20.5	-21 48 26
494	04 41.7	-21 23	105	-74	I-II	29	19.6	0.0	0	6	04 43 51.1	-21 17 29
495	04 41.7	-47 32	17	-134	I-II	0	16.4	0.0	0	5	04 43 07.0	-47 26 27
496	04 43.7	-36 01	-50	-54	II	-10	15.6	0.0	0	4	04 45 29.8	-35 55 36
497	04 44.6	-44 49	46	11	I	-22	15.6	0.0329	0	4	04 46 06.9	-44 43 39
498	04 44.8	-37 50	-37	-151	II-III	27	19.3	0.0	0	6	04 46 32.6	-37 44 40
499	04 45.8	-29 20	113	41	I-II	27	18.6	0.0	0	5	04 47 46.2	-29 14 45
500	04 46.2	-62 33	-138	129	II	-11	14.8	0.019	0	3	04 46 43.9	-62 27 44
501	04 48.9	-51 13	156	-68	III	2	16.9	0.0768	0	5	04 50 08.6	-51 07 56
502	04 49.2	-37 39	32	127	III	21	19.1	0.0	0	6	04 50 56.6	-37 33 59
503	04 50.1	-47 42	-90	124	II-III:	67	20.4	0.0	1	6	04 51 29.7	-47 37 02
504	04 54.1	-55 16	-23	-14	III	86	19.9	0.0	2	6	04 55 07.4	-55 11 18
505	04 56.7	-46 41	-110	-90	II	-12	15.6	0.0	0	4	04 58 07.6	-46 36 30
506	04 59.0	-24 29	-111	28	III	121	21.0	0.0	2	6	05 01 04.4	-24 24 41
507	04 59.4	-34 31	124	24	II-III	0	19.4	0.0	0	6	05 01 13.4	-34 26 42
508	05 01.7	-38 52	-108	61	II	22	17.1	0.0	0	5	05 03 23.6	-38 47 51
509	05 03.1	-37 17	-95	146	II	-51	16.8	0.0	0	5	05 04 50.4	-37 12 57
510	05 05.1	-39 31	-72	27	II-III	20	17.3	0.0	0	5	05 06 46.2	-39 27 06
511	05 06.6	-62 03	-12	160	II	15	17.4	0.0	0	5	05 07 07.3	-61 59 10
512	05 07.3	-37 53	-50	115	I-II	21	15.8	0.0	0	4	05 09 01.1	-37 49 15
513	05 09.9	-42 49	-22	-150	II	-52	16.5	0.0	0	5	05 11 27.3	-42 45 26
514	05 10.2	-40 21	-19	-18	II-III	-23	17.1	0.0	0	5	05 11 50.3	-40 17 27
515	05 11.3	-41 50	-8	-97	I-II	16	15.9	0.0	0	4	05 12 53.3	-41 46 32
516	05 13.3	-27 12	61	-118	II	93	20.9	0.0	2	6	05 15 18.1	-27 08 41
517	05 14.2	-25 19	72	-21	II	85	19.8	0.0	2	6	05 16 14.8	-25 15 45
518	05 14.2	-50 38	-136	-36	I-II	29	17.2	0.0	0	5	05 15 25.9	-50 34 44
519	05 14.9	-22 41	84	125	II-III	86	20.1	0.0	2	6	05 17 00.4	-22 37 48
520	05 15.4	-54 35	142	16	I-II:	83	20.9	0.0	2	6	05 16 25.6	-54 31 48
521	05 17.3	-37 09	56	154	I	0	14.5	0.015	0	2	05 19 02.0	-37 05 58
522	05 17.5	-56 17	-96	-68	I-II	19	16.8	0.0	0	5	05 18 25.4	-56 13 57
523	05 18.4	-26 29	123	-80	II-III	90	19.8	0.0	2	6	05 20 25.0	-26 26 03
524	05 19.8	-61 20	-146	-75	II	-7	15.1	0.0	0	3	05 20 21.5	-61 17 06
525	05 20.2	-49 59	-86	1	II-III	24	18.6	0.0	0	5	05 21 27.4	-49 56 09
526	05 21.8	-46 06	124	-60	II-III	19	19.3	0.0	0	6	05 23 13.3	-46 03 17
527	05 23.6	-32 45	16	-146	I	5	16.4	0.0	0	5	05 25 27.3	-32 42 25
528	05 24.1	-45 01	-113	-3	I-II	21	16.5	0.0	0	5	05 25 33.7	-44 58 27
529	05 24.4	-55 21	-46	-17	II-III	25	17.1	0.0	0	5	05 25 22.3	-55 18 27
530	05 25.3	-56 16	-38	-66	II-III	11	17.4	0.0	0	5	05 26 12.9	-56 13 31
531	05 25.6	-49 30	-39	28	II	17	17.5	0.0	0	5	05 26 52.4	-49 27 33

Table D.1 continued from previous page

ACO	RAB1950	DEB1950	Xcen	Ycen	BMtype	Count	m10	z	Rich	Dclass	_RA_icrs	_DE_icrs
532	05 25.7	-51 18	-37	-68	I-II	12	16.6	0.0	0	5	05 26 53.3	-51 15 33
533	05 27.9	-50 32	-19	-27	II	22	17.3	0.0	0	5	05 29 07.4	-50 29 43
534	05 29.6	-49 17	-5	40	II	-7	15.9	0.0	0	4	05 30 52.8	-49 14 50
535	05 31.6	-36 23	-48	-74	II	-5	15.4	0.0	0	3	05 33 20.9	-36 21 00
536	05 32.5	-30 50	119	-45	I	11	14.7	0.0	0	2	05 34 24.1	-30 48 04
537	05 33.5	-59 26	-61	32	I	-22	15.7	0.0	0	4	05 34 11.4	-59 24 06
538	05 34.2	-42 50	-39	-151	I-II	-11	15.5	0.0	0	3	05 35 44.2	-42 48 11
539	05 34.6	-39 48	-36	12	III	74	19.7	0.0	1	6	05 36 14.4	-39 46 13
540	05 38.5	-40 52	4	-45	I	22	15.3	0.0358	0	3	05 40 06.2	-40 50 30
541	05 39.5	-59 44	-20	16	I-II	-97	16.2	0.0	0	4	05 40 09.7	-59 42 32
542	05 43.7	-48 07	120	101	I	24	15.6	0.0519	0	4	05 45 01.4	-48 05 52
543	05 44.6	-47 12	131	149	II	-11	17.4	0.0	0	5	05 45 57.7	-47 10 56
544	05 44.8	-29 53	-4	8	II	28	19.4	0.0	0	6	05 46 43.4	-29 51 58
545	05 44.9	-32 36	101	127	II	28	15.5	0.0	0	3	05 46 45.1	-32 34 58
546	05 46.7	-32 41	-151	125	II	23	16.5	0.0	0	5	05 48 32.9	-32 40 06
547	05 46.8	-47 26	-121	137	I	-54	16.7	0.0	0	5	05 48 09.1	-47 25 05
548	05 47.5	-42 57	-163	109	II	14	17.3	0.0	0	5	05 49 01.6	-42 56 09
549	05 48.8	-32 17	40	-121	I-II	-57	16.5	0.0403	0	5	05 50 39.6	-32 16 15
550	05 49.1	-34 48	-122	12	II	3	15.5	0.0	0	3	05 50 53.3	-34 47 16
551	05 49.4	-49 41	-93	18	III	25	18.1	0.0	0	5	05 50 39.1	-49 40 16
552	05 50.3	-57 07	58	155	II	-7	16.1	0.0	0	4	05 51 08.5	-57 06 19
553	05 52.4	-39 13	-119	44	III	24	19.1	0.0	0	6	05 54 03.2	-39 12 30
554	05 54.1	-20 37	-39	-31	II-III	96	19.7	0.0	2	5	05 56 14.6	-20 36 39
555	05 55.5	-37 29	-51	-130	I	-2	16.0	0.0	0	4	05 57 12.5	-37 28 44
556	05 56.1	-43 51	-78	63	II	29	17.2	0.0	0	5	05 57 35.6	-43 50 46
557	05 56.1	-47 06	-36	157	I-II	14	17.4	0.0	0	5	05 57 27.8	-47 05 46
558	05 57.4	-59 52	101	5	II	17	14.8	0.0	0	3	05 58 02.6	-59 51 50
559	05 59.6	-39 00	-44	55	II	-5	15.0	0.0	0	3	06 01 15.6	-39 00 02
560	06 00.0	-58 36	124	72	I	-10	15.3	0.0	0	3	06 00 44.3	-58 36 02
561	06 00.3	-60 35	117	-35	I	-8	15.7	0.0	0	4	06 00 53.2	-60 35 03
562	06 00.6	-27 46	-89	120	I-II	-9	16.1	0.0	0	4	06 02 34.6	-27 46 07
563	06 01.6	-32 44	17	124	II	17	16.1	0.0	0	4	06 03 26.8	-32 44 11
564	06 04.3	-42 45	2	122	II	-30	16.4	0.0	0	4	06 05 50.0	-42 45 22
565	06 04.4	-50 24	35	-21	III	19	18.1	0.0	0	5	06 05 37.0	-50 24 22
566	06 05.7	-45 11	14	-8	II	7	15.6	0.0	0	4	06 07 08.5	-45 11 28
567	06 05.7	-62 48	83	117	I	-26	16.8	0.0	0	5	06 06 05.7	-62 48 26
568	06 07.2	-27 30	-12	135	I-II	-2	16.4	0.0	0	4	06 09 11.0	-27 30 36
569	06 08.3	-47 37	74	128	I	-13	16.4	0.0405	0	5	06 09 38.6	-47 37 39
570	06 09.1	-32 33	10	-136	II	0	16.0	0.0	0	4	06 10 57.1	-32 33 44
571	06 09.8	-33 07	-161	100	I	-1	16.2	0.0	0	4	06 11 38.2	-33 07 47
572	06 10.0	-43 59	57	55	II	-10	16.0	0.0	0	4	06 11 29.3	-43 59 47
573	06 10.2	-32 57	114	110	I-II	9	16.0	0.0	0	4	06 12 02.5	-32 57 49
574	06 11.1	-45 04	65	-3	I	19	15.4	0.014	0	3	06 12 32.8	-45 04 52
575	06 11.6	-33 40	-141	70	I	8	16.7	0.0	0	5	06 13 25.3	-33 40 55
576	06 13.0	-44 33	84	24	I-II	-52	16.7	0.0	0	5	06 14 28.1	-44 34 00
577	06 13.5	-34 06	148	47	I-II	27	18.0	0.0	0	5	06 15 18.6	-34 07 03
578	06 13.6	-29 15	64	41	I-II	-17	16.1	0.0	0	4	06 15 32.4	-29 16 04
579	06 14.9	-39 47	-159	10	III	15	18.0	0.0	0	5	06 16 32.2	-39 48 09
580	06 15.1	-51 50	122	-100	I	-7	16.0	0.0	0	4	06 16 14.9	-51 51 08
581	06 15.7	-23 40	20	72	II	18	16.1	0.0	0	4	06 17 46.5	-23 41 13
582	06 19.7	-62 54	-102	112	III:	99	20.8	0.0	2	6	06 20 05.6	-62 55 27
583	06 20.4	-26 21	74	-72	III	29	19.2	0.0	0	5	06 22 24.8	-26 22 33
584	06 21.9	-53 34	149	72	I-II	1	16.0	0.0473	0	4	06 22 57.6	-53 35 38
585	06 22.2	-64 54	169	-5	I	1	14.7	0.0241	0	2	06 22 23.7	-64 55 37
586	06 22.5	-76 32	158	-100	II	0	17.5	0.0	0	5	06 20 25.6	-76 33 34
587	06 23.0	-56 58	143	-111	II	12	17.3	0.0	0	5	06 23 51.4	-56 59 42

Table D.1 continued from previous page

ACO	RAB1950	DEB1950	Xcen	Ycen	BMtype	Count	m10	z	Rich	Dclass	_RA_icrs	_DE_icrs
588	06 23.6	-32 16	-6	147	I-II	7	17.2	0.0	0	5	06 25 27.8	-32 17 47
589	06 26.7	-32 27	28	137	I-II	1	16.5	0.0	0	4	06 28 33.5	-32 29 00
590	06 29.0	-41 57	-29	163	I	48	19.8	0.0	0	5	06 30 34.1	-41 59 10
591	06 32.5	-34 54	90	4	I-II	-24	16.2	0.0	0	4	06 34 17.6	-34 56 25
592	06 37.8	-53 55	12	58	II-III:	63	20.6	0.0	1	6	06 38 51.2	-53 57 47
593	06 38.4	-37 43	86	122	I-II	0	15.1	0.0	0	3	06 40 06.8	-37 45 51
594	06 41.5	-63 54	28	61	III	48	20.1	0.0	0	5	06 41 49.4	-63 57 01
595	06 43.7	-36 57	-48	-102	I	1	16.0	0.0	0	4	06 45 26.4	-37 00 14
596	06 43.8	-37 17	-47	-120	I-II	4	19.5	0.0	0	5	06 45 31.8	-37 20 14
597	06 47.5	-32 58	-6	111	I-II	5	16.0	0.0	0	4	06 49 21.3	-33 01 30
598	06 48.9	-67 45	-38	122	I-II	-32	17.1	0.0	0	5	06 48 47.8	-67 48 32
599	06 54.3	-55 29	-116	-26	I-II	-18	15.7	0.0	0	4	06 55 17.2	-55 32 57
600	06 54.8	-60 06	-25	-4	III	19	19.3	0.0	0	5	06 55 28.7	-60 09 59
601	06 59.8	-49 40	-3	20	I-II	16	16.1	0.0441	0	4	07 01 05.7	-49 44 21
602	07 08.2	-50 05	69	-5	II	3	16.4	0.0	0	4	07 09 29.3	-50 09 57
603	07 09.4	-73 26	127	75	III	25	18.2	0.0	0	5	07 08 22.6	-73 30 57
604	07 16.4	-49 04	-122	51	II	8	16.7	0.0	0	5	07 17 44.9	-49 09 31
605	07 31.8	-84 52	21	10	II-III	25	17.8	0.0	0	5	07 22 43.8	-84 58 13
606	07 56.4	-53 08	-32	-167	I-II	9	16.8	0.0	0	5	07 57 39.8	-53 16 10
607	07 57.8	-84 58	-116	-16	III	23	18.0	0.0	0	5	07 49 04.9	-85 05 56
608	08 03.1	-57 37	-79	128	II-III	22	17.5	0.0	0	5	08 04 09.1	-57 45 35
609	08 12.6	-79 29	-117	20	II-III	0	17.5	0.0	0	5	08 10 05.0	-79 38 04
610	08 24.3	-27 12	-20	151	I	-53	16.8	0.0	0	4	08 26 24.0	-27 21 54
611	08 24.7	-19 54	6	5	II	18	17.3	0.0	0	5	08 26 56.2	-20 03 56
612	08 28.9	-18 06	61	101	II	1	17.8	0.0	0	5	08 31 10.3	-18 16 10
613	08 45.9	-22 55	-28	112	I-II	10	16.8	0.0	0	5	08 48 06.6	-23 06 07
614	09 19.3	-17 17	-100	147	III	103	20.1	0.0	2	6	09 21 38.3	-17 29 49
615	09 20.7	-22 07	132	154	I-II	1	16.8	0.0	0	5	09 22 58.4	-22 19 53
616	09 31.3	-27 00	-9	-105	II:	113	20.8	0.0	2	6	09 33 31.2	-27 13 22
617	09 35.6	-20 07	106	-5	II:	23	15.4	0.0	0	3	09 37 55.3	-20 20 33
618	09 37.3	-29 17	25	40	II	-41	17.5	0.0	0	5	09 39 29.9	-29 30 37
619	09 41.6	-30 31	76	-25	III?	76	20.0	0.0	1	6	09 43 47.4	-30 44 48
620	09 46.7	-25 48	-91	-43	I	-6	16.8	0.0	0	5	09 48 58.0	-26 02 00
621	09 57.0	-32 50	-36	117	III	14	19.6	0.0	0	6	09 59 11.8	-33 04 24
622	09 58.6	-37 57	-19	-158	I-II	-13	16.0	0.0	0	4	10 00 43.5	-38 11 27
623	09 58.7	-18 49	135	63	I	-32	16.8	0.0	0	5	10 01 04.3	-19 03 28
624	09 59.1	-38 03	11	104	II	-13	15.7	0.0	0	4	10 01 13.5	-38 17 28
625	10 00.6	-21 51	-106	-100	III	59	19.8	0.0	1	6	10 02 56.4	-22 05 32
626	10 02.4	-32 02	26	159	I-II	16	17.4	0.0	0	5	10 04 37.3	-32 16 36
627	10 03.2	-35 16	32	-15	I-II	-9	19.4	0.0	0	6	10 05 22.8	-35 30 37
628	10 04.0	-39 30	62	26	I	-27	15.1	0.0	0	3	10 06 07.1	-39 44 39
629	10 05.5	-32 15	61	147	III	18	19.4	0.0	0	6	10 07 43.6	-32 29 42
630	10 07.3	-33 26	79	83	I-II	-5	17.0	0.0	0	5	10 09 31.0	-33 40 46
631	10 07.5	-39 42	98	15	I	-15	15.6	0.0	0	3	10 09 37.7	-39 56 46
632	10 16.1	-34 00	-90	57	II-III	9	17.4	0.0	0	5	10 18 20.1	-34 15 03
633	10 19.9	-36 35	-47	-80	I-II	25	16.9	0.0	0	5	10 22 06.9	-36 50 10
634	10 27.3	-28 33	72	77	II-III	77	19.8	0.0	1	6	10 29 37.5	-28 48 23
635	10 27.6	-33 15	36	94	III?	76	19.9	0.0	1	6	10 29 52.7	-33 30 24
636	10 27.8	-35 04	38	0	I-II	1	13.2	0.0087	0	1	10 30 03.5	-35 19 24
637	10 29.7	-29 08	90	44	II-III	94	20.0	0.0	2	6	10 32 01.5	-29 23 28
638	10 36.7	-33 50	138	64	III	64	20.0	0.0	1	6	10 39 00.0	-34 05 39
639	10 38.4	-45 56	-55	-49	I-II	14	14.8	0.0204	0	2	10 40 33.9	-46 11 41
640	10 40.4	-30 33	-44	-28	II	-10	15.8	0.0	0	4	10 42 44.4	-30 48 44
641	10 40.4	-33 12	-85	97	I-II	21	19.9	0.0	0	6	10 42 43.0	-33 27 44
642	10 40.7	-47 22	97	140	II	6	16.7	0.0	0	5	10 42 51.3	-47 37 45
643	10 42.2	-40 22	-83	-19	I-II	-13	16.1	0.0	0	4	10 44 27.0	-40 37 47

Table D.1 continued from previous page

ACO	RAB1950	DEB1950	Xcen	Ycen	BMtype	Count	m10	z	Rich	Dclass	_RA_icrs	_DE_icrs
644	10 42.8	-19 10	-106	47	III	55	19.8	0.0	1	6	10 45 14.1	-19 25 48
645	10 43.8	-18 12	-92	100	III:	127	20.8	0.0	2	6	10 46 14.6	-18 27 49
646	10 43.8	-29 05	-5	50	I-II	-5	16.4	0.0	0	5	10 46 09.7	-29 20 49
647	10 45.7	-32 35	-26	130	I-II	25	17.5	0.0	0	6	10 48 02.3	-32 50 52
648	10 46.9	-42 35	-34	-137	I-II	9	16.7	0.0	0	5	10 49 08.7	-42 50 53
649	11 00.3	-25 30	2	-25	I-II	-52	16.7	0.0	0	5	11 02 43.7	-25 46 10
650	11 02.5	-48 01	21	108	II	15	17.0	0.0	0	5	11 04 45.6	-48 17 12
651	11 04.9	-22 45	58	123	I-II	26	17.1	0.0	0	6	11 07 21.2	-23 01 15
652	11 05.8	-33 19	-73	91	I	23	18.6	0.0	0	6	11 08 11.6	-33 35 16
653	11 07.5	-27 21	2	145	I-II	94	19.8	0.0	2	6	11 09 56.0	-27 37 17
654	11 08.4	-45 48	-36	-41	II	19	16.7	0.0	0	5	11 10 42.7	-46 04 18
655	11 08.5	-46 39	-34	-86	II	-16	15.4	0.0	0	3	11 10 48.2	-46 55 18
656	11 08.9	-32 20	18	-123	I-II	123	19.7	0.0	2	6	11 11 18.6	-32 36 19
657	11 09.8	-28 37	29	75	II:	111	20.0	0.0	2	6	11 12 14.0	-28 53 20
658	11 09.9	-23 57	118	57	II	19	18.0	0.0	0	6	11 12 21.4	-24 13 20
659	11 15.1	-22 55	-86	112	II-III	12	19.0	0.0	0	6	11 17 34.4	-23 11 24
660	11 16.4	-39 04	1	51	II	16	17.3	0.0	0	5	11 18 47.7	-39 20 25
661	11 18.7	-40 35	23	-31	I-II	12	16.8	0.0	0	5	11 21 05.7	-40 51 27
662	11 19.3	-29 48	140	12	II	95	19.9	0.0	2	6	11 21 45.2	-30 04 28
663	11 21.2	-41 44	48	-92	I	1	17.3	0.0	0	5	11 23 36.0	-42 00 29
664	11 23.1	-44 49	-162	6	I-II	7	16.9	0.0	0	5	11 25 29.4	-45 05 30
665	11 23.4	-35 07	122	-7	I	12	15.8	0.0318	0	4	11 25 50.5	-35 23 30
666	11 25.5	-22 42	43	124	II-III	29	17.5	0.0	0	6	11 27 59.7	-22 58 32
667	11 25.7	-37 33	100	131	II	-16	16.7	0.0	0	5	11 28 08.3	-37 49 32
668	11 26.4	-23 53	52	61	I-II	3	16.8	0.0	0	5	11 28 53.6	-24 09 32
669	11 29.7	-50 28	-3	-25	II-III	-3	16.0	0.0	0	4	11 32 05.4	-50 44 34
670	11 35.0	-47 22	-47	-127	II	20	16.8	0.0	0	5	11 37 26.2	-47 38 37
671	11 36.5	-44 08	-35	47	I-II	26	17.3	0.0	0	5	11 38 57.4	-44 24 38
672	11 37.5	-23 37	-82	77	III	57	19.8	0.0	1	6	11 40 01.0	-23 53 38
673	11 37.8	-46 25	-22	-76	I-II	12	16.0	0.0	0	4	11 40 15.3	-46 41 38
674	11 39.5	-30 33	108	-32	III	18	18.1	0.0	0	6	11 42 00.4	-30 49 39
675	11 41.9	-26 29	-29	-76	I-II	29	16.7	0.0	0	5	11 44 25.3	-26 45 40
676	11 44.8	-32 32	96	132	II	-1	17.3	0.0	0	6	11 47 19.1	-32 48 41
677	11 47.5	-32 15	-65	-119	II	-15	16.0	0.0	0	4	11 50 01.7	-32 31 41
678	11 48.1	-33 36	-138	75	II	15	16.3	0.0	0	5	11 50 37.7	-33 52 41
679	11 48.6	-32 53	-133	114	I-II	26	17.5	0.0	0	6	11 51 07.8	-33 09 41
680	11 50.3	-31 15	-34	-66	I-II	23	16.5	0.0	0	5	11 52 50.3	-31 31 42
681	11 53.6	-45 31	127	-30	I-II	14	17.9	0.0	0	5	11 56 08.2	-45 47 42
682	11 53.9	-22 29	-3	-133	I-II	84	20.0	0.0	2	6	11 56 27.2	-22 45 42
683	11 54.1	-31 29	10	-79	I-II	10	16.1	0.0	0	5	11 56 38.9	-31 45 42
684	11 54.7	-30 43	18	-37	II	19	17.5	0.0	0	6	11 57 15.1	-30 59 42
685	12 00.4	-40 52	-81	-46	II	26	18.0	0.0	0	6	12 02 58.2	-41 08 42
686	12 03.1	-19 39	113	19	III	30	19.7	0.0	0	6	12 05 40.2	-19 55 42
687	12 04.1	-28 00	129	106	II	-4	15.9	0.0	0	4	12 06 40.6	-28 16 42
688	12 08.1	-22 02	-85	-108	III	19	19.3	0.0	0	6	12 10 40.9	-22 18 42
689	12 08.5	-46 24	0	-74	I-II	0	15.8	0.0	0	4	12 11 06.8	-46 40 42
690	12 11.4	-25 32	63	-27	II	26	17.5	0.0	0	6	12 13 59.5	-25 48 41
691	12 12.2	-30 48	-48	-41	II	6	17.8	0.0	0	6	12 14 48.1	-31 04 41
692	12 16.0	-33 37	-93	74	I-II	11	19.4	0.0	0	6	12 18 37.1	-33 53 40
693	12 21.5	-39 41	136	16	I	8	16.7	0.0	0	5	12 24 09.3	-39 57 37
694	12 22.9	-40 19	149	-19	III	22	18.0	0.0	0	6	12 25 33.8	-40 35 37
695	12 23.9	-41 45	156	-96	II	-62	16.8	0.0	0	5	12 26 34.3	-42 01 36
696	12 27.2	-19 38	-114	19	I-II	12	17.5	0.0	0	6	12 29 48.7	-19 54 35
697	12 29.5	-33 59	58	55	I	20	18.6	0.0	0	6	12 32 09.8	-34 15 33
698	12 32.7	-23 09	56	101	I	10	17.5	0.0	0	6	12 35 20.0	-23 25 31
699	12 33.8	-43 08	-23	101	I-II	20	16.9	0.0	0	5	12 36 31.4	-43 24 31

Table D.1 continued from previous page

ACO	RAB1950	DEB1950	Xcen	Ycen	BMtype	Count	m10	z	Rich	Dclass	_RA_icrs	_DE_icrs
700	12 34.0	-33 38	109	72	II	-1	17.0	0.0	0	5	12 36 40.6	-33 54 31
701	12 34.1	-35 16	107	-14	I-II	28	17.3	0.0	0	6	12 36 47.1	-35 32 30
702	12 35.1	-42 24	-9	140	I	-8	16.7	0.0	0	5	12 37 49.5	-42 40 30
703	12 35.4	-34 29	122	27	II	17	17.3	0.0	0	6	12 38 05.1	-34 45 30
704	12 35.5	-38 34	10	78	II?	63	19.8	0.0	1	6	12 38 12.3	-38 50 30
705	12 36.8	-43 25	6	86	III	-60	16.7	0.0	0	5	12 39 32.3	-43 41 29
706	12 38.4	-33 06	-109	101	II-III	-4	19.6	0.0	0	6	12 41 05.3	-33 22 27
707	12 40.7	-42 40	46	126	II	-7	15.1	0.0	0	3	12 43 27.1	-42 56 26
708	12 41.7	-33 09	-72	99	I	-11	19.4	0.0	0	6	12 44 24.0	-33 25 25
709	12 43.6	-42 20	75	143	II	2	16.4	0.0	0	5	12 46 21.7	-42 36 23
710	12 45.7	-21 32	119	-83	II	0	16.6	0.0	0	5	12 48 21.2	-21 48 21
711	12 46.8	-19 33	-132	25	II-III	0	18.1	0.0	0	6	12 49 26.7	-19 49 20
712	12 46.8	-43 48	103	63	I	-23	15.5	0.0	0	4	12 49 35.2	-44 04 20
713	12 48.5	-22 16	-108	-120	I	3	16.0	0.0	0	4	12 51 09.7	-22 32 19
714	12 48.8	-26 11	-16	-63	I	-7	13.4	0.0	0	1	12 51 28.9	-26 27 18
715	12 50.4	-27 25	1	-130	I	16	16.6	0.0	0	5	12 53 05.6	-27 41 17
716	12 51.7	-17 46	-70	122	II-III	16	17.3	0.0	0	6	12 54 20.7	-18 02 16
717	12 55.4	-27 57	61	-158	I	-1	16.8	0.0	0	5	12 58 06.5	-28 13 12
718	12 57.0	-33 24	100	84	I	16	16.0	0.0	0	4	12 59 44.9	-33 40 10
719	13 00.9	-19 15	47	41	II	3	15.9	0.0	0	4	13 03 34.1	-19 31 06
720	13 01.4	-19 46	53	14	II	-7	16.7	0.0	0	5	13 04 04.3	-20 02 05
721	13 03.3	-37 19	-96	-123	II	26	16.0	0.0	0	4	13 06 06.0	-37 35 03
722	13 04.3	-19 59	89	2	I-II	-5	16.8	0.0	0	5	13 06 58.7	-20 15 02
723	13 06.4	-44 31	19	28	II	-12	16.6	0.0	0	5	13 09 17.0	-44 46 59
724	13 10.5	-32 41	-20	127	II	7	17.6	0.0	0	6	13 13 17.1	-32 56 54
725	13 11.4	-29 56	106	4	II	21	17.3	0.0	0	6	13 14 09.8	-30 11 52
726	13 12.4	-33 23	1	90	II	12	16.7	0.059	0	5	13 15 11.8	-33 38 51
727	13 17.6	-40 45	-89	-40	I-II	3	16.8	0.0	0	5	13 20 29.3	-41 00 43
728	13 18.1	-27 03	72	-110	II-III	27	16.5	0.0	0	5	13 20 51.4	-27 18 43
729	13 18.7	-35 32	69	-26	I	19	16.6	0.0499	0	5	13 21 32.2	-35 47 42
730	13 19.2	-26 43	84	-93	I-II	6	16.7	0.0	0	5	13 21 57.4	-26 58 41
731	13 20.2	-34 37	87	23	I-II	29	16.1	0.0	0	4	13 23 01.9	-34 52 40
732	13 21.9	-25 46	119	-42	II	1	17.0	0.0	0	6	13 24 39.3	-26 01 37
733	13 23.0	-36 59	114	-105	II	-21	16.6	0.0	0	5	13 25 52.0	-37 14 35
734	13 25.0	-40 52	-14	-45	I-II	8	16.4	0.0503	0	5	13 27 55.2	-41 07 32
735	13 25.8	-20 41	96	-37	II	21	15.4	0.0	0	4	13 28 31.2	-20 56 31
736	13 28.2	-27 47	38	119	I-II	25	17.3	0.0	0	6	13 30 59.3	-28 02 27
737	13 32.5	-39 49	62	11	I-II	-2	16.6	0.0	0	5	13 35 26.1	-40 04 19
738	13 35.0	-45 03	25	0	I-II	17	16.8	0.0	0	5	13 38 01.2	-45 18 15
739	13 40.0	-34 43	40	17	II	17	16.7	0.0	0	5	13 42 53.7	-34 58 06
740	13 40.6	-37 56	-125	111	I-II	2	15.4	0.0336	0	3	13 43 32.3	-38 11 05
741	13 41.3	-19 33	28	24	II	10	16.0	0.0	0	4	13 44 02.1	-19 48 03
742	13 41.7	-34 03	59	53	I-II	11	15.5	0.0	0	4	13 44 35.5	-34 18 03
743	13 43.3	-39 39	-93	20	I-II	-9	16.0	0.0315	0	4	13 46 16.3	-39 53 59
744	13 44.6	-31 54	94	168	I	-13	16.7	0.0	0	5	13 47 28.4	-32 08 57
745	13 45.3	-36 14	96	-65	III	2	19.5	0.0	0	6	13 48 13.9	-36 28 56
746	13 46.9	-34 44	116	16	II	8	15.8	0.0	0	4	13 49 49.0	-34 58 52
747	13 48.1	-35 53	127	-46	II	4	16.4	0.0	0	5	13 51 02.1	-36 07 50
748	13 49.7	-32 09	151	153	II	-8	16.9	0.0	0	6	13 52 35.4	-32 23 47
749	13 50.1	-34 07	-79	48	II:	103	20.2	0.0	2	6	13 53 01.0	-34 21 46
750	13 50.6	-38 06	-19	105	I-II	16	17.4	0.0	0	6	13 53 34.5	-38 20 45
751	13 51.3	-25 29	-60	-25	I-II	26	18.6	0.0	0	6	13 54 06.9	-25 43 44
752	13 52.2	-19 22	-100	35	II	-3	16.1	0.0	0	5	13 54 57.0	-19 36 42
753	14 00.7	-33 44	5	69	I	18	13.6	0.014	0	1	14 03 38.5	-33 58 23
754	14 03.3	-39 35	113	25	I-II	-9	16.1	0.0281	0	4	14 06 20.5	-39 49 17
755	14 06.5	-25 13	-143	-13	III	3	19.5	0.0	0	6	14 09 20.5	-25 27 10

Table D.1 continued from previous page

ACO	RAB1950	DEB1950	Xcen	Ycen	BMtype	Count	m10	z	Rich	Dclass	_RA_icrs	_DE_icrs
756	14 06.7	-17 38	85	127	I-II	-3	15.8	0.0	0	4	14 09 27.1	-17 52 10
757	14 09.3	-32 54	100	114	I	10	15.6	0.0	0	4	14 12 15.2	-33 08 04
758	14 09.4	-34 05	101	49	II?	16	15.5	0.0	0	4	14 12 22.3	-34 19 03
759	14 13.2	-22 23	-62	141	I-II	11	17.0	0.0	0	6	14 16 01.1	-22 36 54
760	14 15.4	-36 57	-29	158	II-III	73	20.1	0.0	1	6	14 18 26.2	-37 10 49
761	14 15.9	-27 12	-27	-118	II	7	15.4	0.0	0	4	14 18 47.2	-27 25 48
762	14 18.6	-42 10	-94	150	II:	44	20.4	0.0	0	6	14 21 44.7	-42 23 41
763	14 20.0	-30 54	-163	-55	I-II	0	17.1	0.0	0	6	14 22 57.0	-31 07 37
764	14 23.2	-23 44	61	67	II	7	17.0	0.0	0	6	14 26 03.2	-23 57 29
765	14 30.3	-33 33	67	78	II	-22	16.7	0.0	0	5	14 33 19.1	-33 46 10
766	14 31.4	-32 15	-32	-120	II-III	74	19.9	0.0	1	6	14 34 24.0	-32 28 07
767	14 31.7	-32 28	84	136	I	25	17.9	0.0	0	6	14 34 42.2	-32 41 07
768	14 33.1	-31 01	-13	-94	II:	172	20.1	0.0	3	6	14 36 05.0	-31 14 03
769	14 36.4	-28 45	25	67	II-III:	102	19.7	0.0	2	6	14 39 21.2	-28 57 54
770	14 38.6	-37 45	-60	122	II	-8	16.1	0.0	0	4	14 41 43.2	-37 57 47
771	14 38.8	-38 37	-57	75	I-II	14	17.7	0.0	0	5	14 41 56.3	-38 49 47
772	14 39.8	-42 05	-44	-111	I	-4	16.6	0.0	0	5	14 43 01.0	-42 17 44
773	14 44.7	-19 00	32	54	I-II	23	17.5	0.0	0	6	14 47 31.1	-19 12 30
774	14 46.2	-40 09	20	-6	II-III	11	16.7	0.0	0	5	14 49 23.6	-40 21 26
775	14 48.3	-37 47	42	120	I	6	15.4	0.0	0	3	14 51 26.9	-37 59 19
776	14 50.6	-37 21	67	143	I-II	24	17.6	0.0	0	5	14 53 44.7	-37 33 13
777	14 50.8	-30 55	-74	-49	I-II	1	17.5	0.0	0	6	14 53 49.2	-31 07 12
778	14 53.3	-37 24	55	-128	I-II	4	14.6	0.0237	0	2	14 56 27.2	-37 36 05
779	14 54.4	-32 18	71	145	III	-17	19.4	0.0	0	6	14 57 27.2	-32 30 01
780	14 56.8	-17 58	-83	110	I	116	20.0	0.0	2	6	14 59 37.1	-18 09 54
781	14 57.1	-17 53	-78	115	III	82	20.1	0.0	2	6	14 59 55.0	-18 04 53
782	14 57.3	-30 09	2	-7	II:	130	19.8	0.0	3	6	15 00 19.2	-30 20 52
783	14 58.1	-18 03	-66	106	II-III	131	20.0	0.0	3	6	15 00 55.2	-18 14 50
784	15 21.9	-20 45	-27	-39	III	28	19.3	0.0	0	6	15 24 47.5	-20 55 33
785	15 30.8	-85 17	72	-23	II	13	17.2	0.0	0	5	15 44 32.2	-85 26 44
786	15 44.6	-23 30	-15	82	II-III	29	18.0	0.0	0	6	15 47 34.1	-23 39 13
787	15 52.4	-84 13	-78	31	I-II	11	16.6	0.0	0	5	16 04 34.2	-84 21 27
788	15 52.9	-83 03	-94	92	II	24	17.6	0.0	0	5	16 03 25.3	-83 11 28
789	16 05.1	-82 50	-77	108	I-II	26	18.0	0.0	0	5	16 15 36.0	-82 57 42
790	16 38.9	-19 16	-117	40	I	-15	19.3	0.0	0	6	16 41 49.8	-19 21 41
791	16 53.0	-85 50	0	-41	II-III	8	16.9	0.0	0	5	17 10 29.5	-85 54 12
792	16 55.0	-82 07	44	-113	I	12	17.4	0.0	0	5	17 05 22.3	-82 11 19
793	17 06.4	-81 09	73	-65	I-II	16	17.4	0.0	0	5	17 15 58.8	-81 12 32
794	17 23.5	-66 39	-68	-88	II	-31	15.7	0.0	0	3	17 28 37.0	-66 41 28
795	17 26.1	-76 20	-33	-71	II	-32	17.1	0.0	0	5	17 33 12.6	-76 22 12
796	17 46.3	-75 27	32	-23	II	6	16.8	0.0	0	5	17 53 09.1	-75 27 45
797	17 47.4	-65 29	61	-26	II	-13	15.8	0.0	0	4	17 52 24.2	-65 29 44
798	17 55.2	-79 45	-14	15	II-III	25	18.1	0.0	0	5	18 03 55.4	-79 45 02
799	18 16.2	-72 01	17	-107	II?	80	20.0	0.0	2	5	18 22 10.8	-71 59 36
800	18 20.8	-77 12	58	150	I	-20	16.2	0.0	0	4	18 28 13.9	-77 10 13
801	18 23.5	-51 34	-55	-83	II	-30	15.5	0.0511	0	3	18 27 27.4	-51 32 09
802	18 24.2	-46 58	-151	-109	II	8	16.9	0.0	0	5	18 27 56.9	-46 56 06
803	18 27.1	-72 55	58	-157	II-III?	55	20.2	0.0	1	6	18 33 15.1	-72 52 48
804	18 31.9	-67 48	98	114	II-III	92	20.2	0.0	2	6	18 37 09.5	-67 45 30
805	18 42.5	-63 23	133	81	I	8	14.7	0.0139	0	2	18 47 14.4	-63 19 45
806	18 47.4	-54 55	39	5	II	-36	17.1	0.0	0	5	18 51 30.6	-54 51 25
807	18 55.8	-82 22	-35	140	III	2	19.1	0.0	0	6	19 06 20.6	-82 17 36
808	18 56.9	-49 10	-29	45	I-II	17	16.1	0.0	0	4	19 00 42.5	-49 05 46
809	19 02.0	-82 28	-50	-134	II	29	17.8	0.0	0	5	19 12 35.0	-82 23 10
810	19 06.1	-75 23	76	-22	I-II	-5	16.5	0.0	0	5	19 12 43.7	-75 18 01
811	19 13.3	-52 31	-19	134	II	-24	16.6	0.0688	0	5	19 17 14.1	-52 25 37

Table D.1 continued from previous page

ACO	RAB1950	DEB1950	Xcen	Ycen	BMtype	Count	m10	z	Rich	Dclass	_RA_icrs	_DE_icrs
812	19 18.0	-35 21	63	-19	I	-17	18.9	0.0	0	5	19 21 18.3	-35 15 19
813	19 25.1	-59 06	-90	48	III	21	17.8	0.0	0	5	19 29 23.2	-58 59 48
814	19 25.4	-41 16	-50	-67	I	3	17.5	0.0	0	5	19 28 52.1	-41 09 48
815	19 26.5	-52 45	-27	-145	III:	66	20.1	0.0	1	6	19 30 25.0	-52 38 43
816	19 26.8	-63 42	-128	67	III	13	19.0	0.0	0	5	19 31 26.6	-63 35 40
817	19 27.5	-52 11	-21	-115	III	74	19.7	0.0	1	6	19 31 23.3	-52 04 39
818	19 27.8	-71 32	-118	-86	I	105	20.1	0.0	2	6	19 33 25.9	-71 25 34
819	19 28.2	-61 01	-66	-54	II	24	19.5	0.0	0	6	19 32 36.9	-60 54 35
820	19 30.0	-39 47	-4	13	I	18	17.1	0.0	0	5	19 33 24.9	-39 40 29
821	19 31.2	-50 59	10	-51	III:	87	20.6	0.0	2	6	19 35 01.4	-50 52 24
822	19 34.0	-46 29	-21	-79	II-III	23	17.4	0.0	0	5	19 37 38.0	-46 22 13
823	19 35.6	-53 17	-101	91	II-III	21	15.4	0.0518	0	3	19 39 31.2	-53 10 06
824	19 36.8	-45 45	5	-39	II	7	17.1	0.0	0	5	19 40 24.0	-45 38 02
825	19 37.5	-82 58	37	109	III	19	19.2	0.0	0	6	19 48 07.8	-82 50 45
826	19 39.4	-67 07	-86	153	II-III	-9	18.7	0.0	0	5	19 44 20.3	-66 59 49
827	19 43.0	-43 04	66	104	I-II	-10	18.6	0.0	0	6	19 46 29.7	-42 56 38
828	19 43.6	-52 05	-38	157	II	19	16.6	0.0	0	5	19 47 26.5	-51 57 35
829	19 43.7	-43 23	72	87	I-II	23	17.1	0.0	0	5	19 47 12.2	-43 15 35
830	19 45.5	-34 03	103	53	III	128	20.0	0.0	2	6	19 48 44.0	-33 55 28
831	19 48.4	-32 19	-134	143	I	21	19.3	0.0	0	6	19 51 35.2	-32 11 17
832	19 51.1	-41 19	-50	-70	II:	29	17.9	0.0	0	5	19 54 31.4	-41 11 06
833	19 53.7	-83 15	-160	56	II-III	15	17.3	0.0	0	5	20 04 21.1	-83 06 42
834	19 54.6	-34 56	-61	5	II	26	17.8	0.0	0	5	19 57 50.5	-34 47 53
835	19 54.7	-52 46	52	119	II	15	15.6	0.047	0	4	19 58 32.4	-52 37 52
836	19 54.8	-32 48	-61	119	I	-1	14.8	0.0	0	3	19 57 59.3	-32 39 53
837	19 56.0	-83 29	63	78	II:	13	17.3	0.0	0	5	20 06 53.3	-83 20 33
838	19 57.0	-38 59	10	56	I-II:	131	20.1	0.0	3	6	20 00 20.7	-38 50 44
839	19 57.5	-53 04	75	103	I-II:	17	15.1	0.0426	0	3	20 01 20.7	-52 55 41
840	19 59.4	-56 06	84	-59	I-II:	15	13.9	0.0152	0	1	20 03 23.4	-55 57 33
841	20 00.9	-65 46	68	-38	II	76	19.9	0.0	1	6	20 05 34.9	-65 37 27
842	20 01.8	-39 25	58	30	III	155	19.9	0.0	3	6	20 05 08.8	-39 16 26
843	20 02.0	-66 20	72	-69	II:	88	19.9	0.0	2	6	20 06 43.9	-66 11 22
844	20 03.6	-53 17	123	89	I-II	14	16.2	0.0405	0	4	20 07 26.1	-53 08 18
845	20 03.8	-52 43	126	119	III	23	17.5	0.0	0	5	20 07 36.5	-52 34 17
846	20 03.8	-64 54	89	6	III	29	18.8	0.0	0	5	20 08 23.0	-64 45 16
847	20 04.7	-31 35	95	-82	III	23	17.9	0.0	0	5	20 07 50.7	-31 26 15
848	20 05.1	-35 33	54	-28	II	11	18.0	0.0	0	5	20 08 20.3	-35 24 14
849	20 05.2	-54 32	-126	23	I-II	10	16.4	0.0	0	5	20 09 05.3	-54 23 12
850	20 06.1	-54 07	140	43	II-III	6	16.9	0.0	0	5	20 09 57.9	-53 58 09
851	20 06.3	-48 32	52	82	I	6	13.4	0.01	0	1	20 09 55.7	-48 23 08
852	20 07.1	-34 10	77	46	I-II	2	16.7	0.0	0	5	20 10 18.1	-34 01 06
853	20 07.3	-47 21	62	145	II	-6	17.0	0.0	0	5	20 10 53.0	-47 12 05
854	20 07.4	-56 53	140	-105	II	24	15.6	0.0536	0	4	20 11 24.1	-56 44 04
855	20 07.5	-32 03	82	159	I-II	26	18.0	0.0	0	5	20 10 39.1	-31 54 05
856	20 08.0	-65 23	107	-21	II	27	18.0	0.0	0	5	20 12 36.3	-65 14 00
857	20 09.6	-57 38	-85	-141	II-III	15	17.1	0.0	0	5	20 13 38.1	-57 28 55
858	20 11.3	-19 38	-88	22	II-III	13	18.6	0.0	0	5	20 14 11.6	-19 28 51
859	20 12.5	-61 41	-24	-90	I-II	4	16.4	0.0	0	5	20 16 46.7	-61 31 44
860	20 13.3	-86 21	-69	-85	I	22	17.5	0.0	0	5	20 29 47.6	-86 11 19
861	20 15.0	-52 51	-52	115	I-II	2	16.4	0.0	0	5	20 18 46.5	-52 41 36
862	20 15.8	-78 08	-123	86	II-III	14	19.3	0.0	0	6	20 22 41.2	-77 58 28
863	20 15.9	-39 23	-65	35	I-II	6	17.1	0.0	0	5	20 19 12.9	-39 13 34
864	20 16.1	-27 22	-39	143	III	120	20.1	0.0	2	6	20 19 08.2	-27 12 34
865	20 17.3	-33 26	-79	84	II	26	18.1	0.0	0	5	20 20 27.9	-33 16 29
866	20 18.2	-49 52	-104	7	I-II	-4	15.1	0.0183	0	3	20 21 50.5	-49 42 25
867	20 18.5	-41 09	-37	-59	II	23	16.8	0.0	0	5	20 21 51.5	-40 59 24

Table D.1 continued from previous page

ACO	RAB1950	DEB1950	Xcen	Ycen	BMtype	Count	m10	z	Rich	Dclass	_RA_icrs	_DE_icrs
868	20 20.1	-21 06	22	-56	I	13	16.7	0.0	0	5	20 23 00.7	-20 56 19
869	20 21.7	-61 58	34	-105	I-II	3	16.8	0.0	0	5	20 25 57.0	-61 48 11
870	20 21.7	-80 47	-83	-51	III	25	19.3	0.0	0	6	20 29 44.2	-80 37 05
871	20 22.3	-51 28	-67	-78	II-III	9	18.6	0.0	0	5	20 25 59.4	-51 18 10
872	20 22.6	-76 39	-101	-93	I-II	28	17.5	0.0	0	5	20 28 54.9	-76 29 05
873	20 22.7	-33 43	-18	71	I-II	-29	17.3	0.0371	0	5	20 25 51.7	-33 33 10
874	20 23.0	-27 51	43	120	II?	127	20.2	0.0	2	6	20 26 02.2	-27 41 09
875	20 23.9	-77 13	-109	138	II	15	17.4	0.0	0	5	20 30 22.1	-77 03 00
876	20 25.6	-48 42	-42	71	II	-9	16.8	0.0	0	5	20 29 10.5	-48 31 59
877	20 27.4	-53 52	47	62	I-II	28	18.1	0.0	0	5	20 31 10.3	-53 41 52
878	20 27.6	-48 25	-24	86	II-III	23	18.4	0.0	0	5	20 31 09.5	-48 14 52
879	20 29.1	-41 12	70	-62	I-II	24	18.8	0.0	0	5	20 32 25.9	-41 01 47
880	20 30.1	-59 52	93	5	II	9	19.3	0.0	0	6	20 34 10.2	-59 41 42
881	20 31.6	-57 28	111	137	II-III	17	17.5	0.0	0	5	20 35 31.6	-57 17 37
882	20 32.1	-43 37	-1	75	I	-14	16.1	0.029	0	4	20 35 29.5	-43 26 37
883	20 32.1	-58 29	111	78	II-III	11	16.6	0.0	0	5	20 36 04.8	-58 18 36
884	20 32.2	-50 51	16	-44	I-II	20	17.5	0.0	0	5	20 35 49.8	-50 40 36
885	20 32.6	-57 48	116	115	I-II	22	16.0	0.0	0	4	20 36 32.4	-57 37 34
886	20 34.1	-31 49	-92	-97	II-III	9	17.8	0.0	0	5	20 37 11.9	-31 38 30
887	20 34.4	-37 20	130	144	I-II	14	17.5	0.0	0	5	20 37 37.3	-37 09 29
888	20 35.7	-58 02	138	101	II	-3	17.1	0.0	0	5	20 39 38.2	-57 51 23
889	20 36.3	-53 14	-146	91	II-III	7	15.9	0.0437	0	4	20 40 00.5	-53 03 22
890	20 37.2	-40 15	-113	-13	I	14	15.5	0.0	0	3	20 40 29.2	-40 04 20
891	20 37.8	-20 55	-18	-49	I	2	15.4	0.0	0	3	20 40 41.3	-20 44 18
892	20 38.5	-37 50	-103	116	II	16	16.0	0.0254	0	4	20 41 43.4	-37 39 15
893	20 39.9	-73 36	-58	75	II	-65	16.6	0.0503	0	5	20 45 19.1	-73 25 07
894	20 40.6	-26 36	100	-82	I-II	5	15.9	0.0409	0	4	20 43 35.1	-26 25 09
895	20 42.0	-18 25	35	85	II	-42	16.7	0.0	0	5	20 44 50.5	-18 14 04
896	20 42.0	-40 09	-64	-7	II-III	28	18.1	0.0	0	5	20 45 16.2	-39 58 04
897	20 44.2	-38 36	-43	76	I	25	15.6	0.0224	0	4	20 47 25.6	-38 24 56
898	20 44.4	-30 21	25	-16	I-II	3	16.8	0.0282	0	5	20 47 27.0	-30 09 56
899	20 45.2	-39 03	-32	53	I	9	16.4	0.0	0	5	20 48 26.1	-38 51 53
900	20 45.5	-38 11	-29	99	I	12	14.5	0.0243	0	2	20 48 42.8	-37 59 52
901	20 45.9	-41 22	-23	-72	I-II	11	17.3	0.0	0	5	20 49 11.4	-41 10 51
902	20 46.4	-72 05	-5	-108	II-III	98	20.1	0.0	2	6	20 51 30.0	-71 53 46
903	20 47.2	-24 17	-85	41	I-II:	90	19.7	0.0	2	6	20 50 08.0	-24 05 47
904	20 48.5	-42 57	-115	109	II	-2	16.4	0.0	0	5	20 51 49.5	-42 45 42
905	20 48.8	-25 42	-64	-36	III	117	20.1	0.0	2	6	20 51 45.4	-25 30 42
906	20 48.8	-52 09	-97	-114	II	29	15.7	0.0467	0	4	20 52 24.8	-51 57 41
907	20 51.0	-43 15	-89	93	I	3	15.8	0.0	0	4	20 54 19.5	-43 03 34
908	20 51.8	-37 46	38	121	I-II	28	17.6	0.0	0	5	20 54 59.3	-37 34 32
909	20 52.2	-43 43	-77	68	III	25	15.3	0.0	0	3	20 55 32.0	-43 31 30
910	20 53.1	-64 51	114	6	III	132	21.1	0.311	3	6	20 57 22.1	-64 39 26
911	20 55.3	-43 09	-48	99	III	26	17.4	0.0	0	5	20 58 36.5	-42 57 21
912	20 56.2	-50 30	-35	-25	II-III	109	19.8	0.0	2	6	20 59 43.4	-50 18 17
913	20 56.2	-67 19	38	147	I	3	19.8	0.0	0	6	21 00 39.1	-67 07 16
914	20 57.6	-29 05	-92	51	I	-14	17.5	0.0	0	5	21 00 36.1	-28 53 14
915	20 57.7	-41 11	95	-63	II-III	0	16.8	0.0	0	5	21 00 57.1	-40 59 13
916	20 58.4	-41 37	102	-87	I-II	3	15.8	0.0	0	4	21 01 39.6	-41 25 11
917	20 58.5	-38 42	107	70	I	18	15.4	0.0	0	3	21 01 41.5	-38 30 11
918	20 59.7	-38 11	121	97	I-II	7	15.3	0.0	0	3	21 02 52.6	-37 59 07
919	21 01.8	-43 38	16	74	I	6	15.6	0.0487	0	4	21 05 06.0	-43 26 01
920	21 02.8	-57 52	59	115	II	45	19.7	0.0	0	6	21 06 35.2	-57 39 57
921	21 03.5	-45 02	31	-1	II	27	15.3	0.029	0	3	21 06 49.8	-44 49 55
922	21 03.7	-39 51	155	10	I	24	15.1	0.0306	0	3	21 06 54.2	-39 38 55
923	21 04.2	-43 04	40	103	II-III	28	17.4	0.0	0	5	21 07 28.7	-42 51 53

Table D.1 continued from previous page

ACO	RAB1950	DEB1950	Xcen	Ycen	BMtype	Count	m10	z	Rich	Dclass	_RA_icrs	_DE_icrs
924	21 04.5	-47 23	39	-128	I	13	15.7	0.0165	0	4	21 07 53.6	-47 10 52
925	21 06.8	-27 13	16	152	I-II	14	17.2	0.0	0	5	21 09 45.1	-27 00 46
926	21 09.9	-77 08	27	151	II	7	16.9	0.0	0	5	21 15 41.2	-76 55 33
927	21 13.2	-59 37	-131	17	II	29	15.9	0.0602	0	4	21 17 00.6	-59 24 26
928	21 14.7	-45 49	-126	-45	I-II	10	16.8	0.0	0	5	21 18 00.6	-45 36 22
929	21 14.9	-22 59	-80	-159	II	-29	16.1	0.0	0	4	21 17 46.2	-22 46 23
930	21 15.5	-53 25	-100	85	III	25	16.6	0.0	0	5	21 19 02.2	-53 12 20
931	21 15.7	-49 01	134	51	III	53	19.7	0.0	1	6	21 19 05.7	-48 48 19
932	21 16.2	-72 31	84	132	I	11	16.8	0.0	0	5	21 21 02.3	-72 18 16
933	21 16.3	-45 36	-111	-33	I	24	16.9	0.0	0	5	21 19 35.9	-45 23 18
934	21 16.6	-85 14	-23	-13	II	-4	17.1	0.0	0	5	21 27 28.3	-85 01 06
935	21 16.9	-54 41	-82	17	III	67	19.7	0.0	1	6	21 20 28.6	-54 28 16
936	21 17.3	-51 32	140	-84	III?	127	20.1	0.0	2	6	21 20 45.9	-51 19 15
937	21 17.6	-63 48	7	66	III	53	19.8	0.0	1	6	21 21 36.9	-63 35 13
938	21 17.7	-33 11	59	101	II-III	51	20.1	0.0	1	6	21 20 43.9	-32 58 14
939	21 18.1	-46 49	-93	-97	I	-4	16.9	0.0	0	5	21 21 25.4	-46 36 13
940	21 20.4	-21 18	-12	-69	II	-12	15.9	0.0	0	4	21 23 14.3	-21 05 07
941	21 20.8	-56 32	-49	-79	II-III	11	17.6	0.0	0	5	21 24 25.6	-56 19 05
942	21 21.2	-20 24	-1	-20	II	-2	16.7	0.0	0	5	21 24 01.4	-20 11 05
943	21 22.3	-63 15	35	95	II	60	19.7	0.0	1	6	21 26 14.7	-63 02 00
944	21 22.4	-31 07	-68	-57	II-III	14	19.3	0.0	0	6	21 25 23.1	-30 54 01
945	21 23.0	-48 15	-65	94	III	137	20.1	0.0	3	6	21 26 20.5	-48 01 59
946	21 23.3	-32 17	-57	-120	I:	55	20.3	0.0	1	6	21 26 18.1	-32 03 59
947	21 25.8	-39 45	116	-85	III	9	16.1	0.0	0	4	21 28 56.0	-39 31 52
948	21 26.9	-38 39	131	74	III	40	19.7	0.0	0	6	21 30 00.5	-38 25 49
949	21 27.3	-84 10	-14	45	I-II	-50	16.8	0.0	0	5	21 36 18.6	-83 56 40
950	21 28.8	-29 06	4	53	I:	102	19.7	0.0	2	6	21 31 44.3	-28 52 44
951	21 29.0	-19 52	98	7	II	-12	16.1	0.0	0	4	21 31 48.4	-19 38 44
952	21 29.1	-35 25	-78	-20	II	23	16.0	0.0	0	4	21 32 08.5	-35 11 43
953	21 29.8	-72 16	-125	140	I-II	6	16.8	0.0	0	5	21 34 26.6	-72 02 39
954	21 31.0	-63 08	-8	-165	II-III	34	19.7	0.0	0	6	21 34 52.4	-62 54 37
955	21 31.2	-83 34	-9	78	I	27	17.2	0.0569	0	5	21 39 29.5	-83 20 31
956	21 31.3	-52 27	29	138	II-III	127	19.8	0.0	2	6	21 34 43.6	-52 13 37
957	21 32.2	-52 46	38	122	III	12	16.0	0.064	0	4	21 35 37.9	-52 32 34
958	21 32.7	-56 25	38	-73	I-II:	20	16.4	0.0691	0	5	21 36 15.2	-56 11 33
959	21 34.2	-47 16	55	-121	II	7	15.5	0.0	0	4	21 37 28.2	-47 02 29
960	21 34.7	-73 02	-101	101	II	-3	17.3	0.0	0	5	21 39 22.8	-72 48 26
961	21 35.0	-27 56	-36	-156	III	47	20.0	0.0	0	6	21 37 54.4	-27 42 28
962	21 35.3	-27 59	-33	-159	III	26	20.0	0.0	0	6	21 38 12.5	-27 45 27
963	21 37.1	-22 42	-15	124	III	10	14.9	0.0	0	3	21 39 55.9	-22 28 23
964	21 40.3	-39 04	-1	52	I-II	-5	16.0	0.0	0	4	21 43 22.4	-38 50 14
965	21 40.6	-44 00	120	52	II	29	17.5	0.0	0	5	21 43 46.1	-43 46 13
966	21 40.7	-43 36	-151	73	III:	98	19.9	0.0	2	6	21 43 51.6	-43 22 13
967	21 41.3	-62 39	-118	123	II	19	17.5	0.0	0	5	21 45 04.1	-62 25 11
968	21 42.2	-51 50	98	-98	I-II:	20	15.3	0.0534	0	3	21 45 33.2	-51 36 09
969	21 42.5	-42 41	-136	122	III:	53	19.8	0.0	1	6	21 45 38.1	-42 27 09
970	21 42.7	-34 53	70	7	II:	179	19.7	0.0	3	6	21 45 41.7	-34 39 08
971	21 43.0	-46 45	136	-96	I-II	0	15.9	0.0324	0	4	21 46 13.2	-46 31 07
972	21 43.2	-38 05	73	-164	II-III?	180	19.7	0.0	3	6	21 46 14.8	-37 51 07
973	21 43.4	-86 40	6	-89	III	-17	19.4	0.0	0	6	21 55 54.8	-86 25 55
974	21 45.0	-46 15	-106	-66	II-III:	18	15.1	0.0596	0	3	21 48 12.0	-46 01 03
975	21 45.1	-17 52	37	115	I-II	12	18.3	0.0	0	6	21 47 51.5	-17 38 03
976	21 45.6	-64 44	-85	14	I-II	0	16.6	0.0543	0	5	21 49 26.7	-64 30 00
977	21 46.3	-21 24	49	-75	II-III	10	17.4	0.0	0	5	21 49 06.0	-21 10 00
978	21 48.2	-42 47	79	-147	I-II	-62	16.5	0.0	0	5	21 51 18.9	-42 32 55
979	21 49.8	-56 38	164	-91	II:	163	20.3	0.0	3	6	21 53 15.5	-56 23 51

Table D.1 continued from previous page

ACO	RAB1950	DEB1950	Xcen	Ycen	BMtype	Count	m10	z	Rich	Dclass	_RA_icrs	_DE_icrs
980	21 51.7	-72 17	-36	146	II	-2	16.1	0.0	0	4	21 56 04.4	-72 02 45
981	21 52.3	-55 49	-60	-46	III	21	14.5	0.0347	0	2	21 55 43.0	-55 34 45
982	21 54.6	-65 42	-32	-36	II	-64	16.8	0.0	0	5	21 58 25.3	-65 27 40
983	21 57.3	-19 27	-75	32	I	7	16.1	0.0	0	4	22 00 03.6	-19 12 35
984	21 57.8	-66 57	-14	-102	II	-31	17.1	0.0	0	5	22 01 40.0	-66 42 32
985	21 57.9	-18 35	-69	78	II	29	17.3	0.0	0	5	22 00 39.0	-18 20 33
986	21 58.3	-69 53	79	8	II:	88	20.5	0.0	2	6	22 02 22.2	-69 38 31
987	21 59.1	-22 40	-51	-141	I-II	20	15.8	0.0	0	4	22 01 53.6	-22 25 31
988	22 01.1	-58 22	-63	89	I-II	16	15.8	0.0405	0	4	22 04 32.6	-58 07 26
989	22 01.2	-50 19	6	-16	I-II	25	15.3	0.0363	0	3	22 04 25.0	-50 04 26
990	22 02.0	-63 23	9	89	II	-68	16.6	0.0	0	5	22 05 38.2	-63 08 24
991	22 02.1	-66 56	111	163	III	96	20.1	0.0	2	6	22 05 55.4	-66 41 23
992	22 02.7	-38 23	-38	88	III	27	18.5	0.0	0	6	22 05 41.3	-38 08 23
993	22 03.7	-39 29	-27	29	II	19	17.4	0.0	0	5	22 06 42.1	-39 14 21
994	22 04.1	-85 21	29	-19	III	25	19.3	0.0	0	6	22 12 54.1	-85 06 14
995	22 05.1	-74 42	16	17	II-III	17	17.6	0.0	0	5	22 09 34.1	-74 27 16
996	22 05.8	-59 55	-31	6	III	92	19.7	0.1611	2	6	22 09 15.9	-59 40 16
997	22 06.1	-35 22	64	-18	II	-1	15.4	0.0	0	3	22 09 02.0	-35 07 16
998	22 07.2	-57 22	-23	141	II-III	78	19.9	0.0	1	6	22 10 34.2	-57 07 13
999	22 07.7	-21 09	56	-59	I-II	5	16.1	0.0	0	4	22 10 27.7	-20 54 13
1000	22 08.6	-33 56	93	59	I-II	-8	17.4	0.0	0	5	22 11 30.4	-33 41 11
1001	22 09.0	-62 19	-8	-123	II-III	70	19.7	0.0	1	6	22 12 31.9	-62 04 09
1002	22 09.1	-45 43	-143	-41	II-III	25	18.1	0.0	0	6	22 12 11.1	-45 28 09
1003	22 09.9	-62 10	60	153	II	-10	16.1	0.0426	0	4	22 13 25.1	-61 55 07
1004	22 10.6	-43 35	-133	74	I	-3	16.9	0.0	0	5	22 13 38.5	-43 20 07
1005	22 11.2	-36 57	118	-104	II	-18	16.1	0.0	0	4	22 14 08.4	-36 42 05
1006	22 13.7	-17 24	134	142	I	-19	19.6	0.0	0	6	22 16 25.0	-17 09 01
1007	22 13.8	-61 23	20	-73	I-II	75	19.8	0.0	1	6	22 17 15.4	-61 08 00
1008	22 14.9	-26 19	-87	-70	III	106	20.9	0.0	2	6	22 17 42.1	-26 03 58
1009	22 15.9	-85 04	45	-6	II	5	17.3	0.0	0	5	22 23 47.3	-84 48 52
1010	22 16.0	-26 56	-73	-104	III	82	20.1	0.0	2	6	22 18 48.4	-26 40 56
1011	22 16.5	-62 21	100	141	I	3	16.8	0.0426	0	5	22 19 58.3	-62 05 55
1012	22 17.0	-36 43	-77	-91	III	29	19.0	0.0	0	6	22 19 55.0	-36 27 54
1013	22 18.4	-38 06	128	100	II	-8	18.0	0.0	0	6	22 21 19.8	-37 50 52
1014	22 18.9	-80 26	-26	-23	I-II	16	15.4	0.0481	0	3	22 24 10.8	-80 10 49
1015	22 19.1	-42 46	126	-150	III	21	19.2	0.0	0	6	22 22 05.6	-42 30 50
1016	22 19.3	-38 55	-134	58	II	-10	16.9	0.0	0	5	22 22 14.3	-38 39 50
1017	22 20.1	-51 40	-81	-89	II-III	85	21.0	0.0	2	6	22 23 14.8	-51 24 48
1018	22 20.3	-26 37	-21	-86	III	96	20.0	0.0	2	6	22 23 05.6	-26 21 48
1019	22 21.0	-27 16	-14	-119	II?	66	20.0	0.0	1	6	22 23 47.9	-27 00 47
1020	22 21.0	-56 44	-91	-97	II-III	25	15.7	0.0355	0	4	22 24 15.6	-56 28 47
1021	22 21.1	-32 51	-38	118	III	25	19.7	0.0	0	6	22 23 57.5	-32 35 47
1022	22 21.8	-64 30	-132	21	III	4	17.0	0.0936	0	5	22 25 18.7	-64 14 45
1023	22 22.4	-56 05	-81	-60	III	27	15.9	0.0789	0	4	22 25 38.0	-55 49 44
1024	22 22.7	-79 01	-20	52	II-III	18	18.1	0.0	0	5	22 27 32.7	-78 45 42
1025	22 23.1	-19 34	-13	29	II?	96	20.2	0.0	2	6	22 25 49.3	-19 18 43
1026	22 24.1	-27 36	24	-137	III	73	20.1	0.0	1	6	22 26 53.7	-27 20 42
1027	22 24.3	-73 48	89	61	II	4	16.8	0.0	0	5	22 28 22.4	-73 32 40
1028	22 25.1	-36 20	10	-68	III?	93	20.7	0.0	2	6	22 27 59.2	-36 04 40
1029	22 26.5	-54 11	-53	44	III	12	16.5	0.0	0	5	22 29 39.8	-53 55 37
1030	22 26.5	-71 42	-26	-89	I	-11	16.8	0.0	0	5	22 30 21.8	-71 26 36
1031	22 27.5	-32 46	34	122	III	21	18.9	0.0	0	6	22 30 20.3	-32 30 36
1032	22 28.5	-53 25	-38	83	III?	85	19.7	0.0	2	6	22 31 38.0	-53 09 34
1033	22 29.0	-35 17	51	-12	III	24	18.1	0.0	0	6	22 31 51.7	-35 01 33
1034	22 29.5	-30 03	-88	-7	II?	159	20.8	0.0	3	6	22 32 18.4	-29 47 32
1035	22 30.6	-57 24	-128	135	III	0	21.1	0.0	0	6	22 33 48.6	-57 08 30

Table D.1 continued from previous page

ACO	RAB1950	DEB1950	Xcen	Ycen	BMtype	Count	m10	z	Rich	Dclass	_RA_icrs	_DE_icrs
1036	22 31.0	-39 43	-12	17	II-III	3	16.7	0.0	0	5	22 33 54.4	-39 27 30
1037	22 31.1	-47 08	9	154	III	86	19.8	0.0	2	6	22 34 06.4	-46 52 30
1038	22 31.4	-69 56	-5	5	I-II	4	16.7	0.0	0	5	22 35 04.9	-69 40 28
1039	22 31.8	-52 43	-15	120	I-II:	24	16.2	0.0554	0	4	22 34 54.0	-52 27 28
1040	22 32.7	-28 38	-52	75	I:	125	19.9	0.0	2	6	22 35 29.1	-28 22 27
1041	22 32.8	-35 20	92	-15	III:	60	20.0	0.0	1	6	22 35 39.0	-35 04 27
1042	22 32.9	-38 59	7	57	I-II	5	16.7	0.0	0	5	22 35 47.4	-38 43 27
1043	22 33.7	-24 36	-128	23	I	-3	16.7	0.0	0	5	22 36 26.8	-24 20 26
1044	22 33.8	-48 26	33	86	III	126	20.0	0.0	2	6	22 36 48.9	-48 10 25
1045	22 34.0	-38 19	19	92	II-III	27	18.0	0.0	0	6	22 36 52.7	-38 03 25
1046	22 34.1	-44 32	93	24	II	3	17.0	0.0	0	5	22 37 03.3	-44 16 25
1047	22 34.2	-39 26	21	32	I	13	16.6	0.0	0	5	22 37 05.5	-39 10 25
1048	22 36.1	-25 14	167	-14	II	108	19.8	0.0	2	6	22 38 50.8	-24 58 22
1049	22 36.3	-38 30	44	82	II-III	16	17.6	0.0	0	5	22 39 10.4	-38 14 21
1050	22 36.5	-36 25	133	-75	II	26	15.5	0.0	0	4	22 39 21.0	-36 09 21
1051	22 36.6	-38 07	47	103	II-III	29	16.9	0.0	0	5	22 39 28.0	-37 51 21
1052	22 36.6	-45 34	-147	-32	II-III	-24	17.5	0.0	0	5	22 39 33.5	-45 18 21
1053	22 36.6	-62 45	-49	120	II-III	24	18.1	0.0	0	6	22 39 54.8	-62 29 21
1054	22 36.7	-63 58	-47	58	II	25	19.5	0.0	0	6	22 40 03.2	-63 42 20
1055	22 40.4	-40 08	84	-6	II	0	15.4	0.0322	0	3	22 43 16.5	-39 52 15
1056	22 41.9	-38 03	103	105	I-II	15	17.1	0.0	0	5	22 44 44.9	-37 47 13
1057	22 42.5	-71 35	42	-84	I	-11	16.1	0.0	0	4	22 46 08.4	-71 19 12
1058	22 43.3	-73 59	-86	53	II-III	14	18.6	0.0	0	6	22 47 05.8	-73 43 10
1059	22 43.7	-44 01	-82	54	II	-9	16.1	0.0	0	4	22 46 36.4	-43 45 10
1060	22 43.8	-46 17	-78	-68	II	22	15.6	0.0331	0	4	22 46 44.1	-46 01 10
1061	22 43.9	-84 24	86	21	II	-62	16.8	0.0723	0	5	22 49 56.5	-84 08 08
1062	22 44.5	-72 51	-86	114	I-II	21	17.5	0.0	0	5	22 48 11.6	-72 35 09
1063	22 46.0	-44 47	-60	13	I-II	74	19.7	0.0	1	6	22 48 54.3	-44 31 07
1064	22 46.5	-33 07	-20	103	II-III?	27	19.2	0.0	0	6	22 49 17.2	-32 51 07
1065	22 46.5	-37 45	152	120	I	-17	15.6	0.0288	0	4	22 49 19.7	-37 29 07
1066	22 47.3	-46 32	-48	-81	II-III?	25	16.8	0.0496	0	5	22 50 13.2	-46 16 06
1067	22 47.8	-45 36	-42	-30	II-III?	20	15.9	0.0	0	4	22 50 42.4	-45 20 05
1068	22 48.2	-32 14	-2	150	III?	88	20.2	0.0	2	6	22 50 58.4	-31 58 04
1069	22 50.3	-27 19	-120	145	II-III	26	19.2	0.0	0	6	22 53 01.9	-27 03 02
1070	22 51.0	-44 06	-12	50	II-III	12	16.7	0.0	0	5	22 53 52.5	-43 50 01
1071	22 51.3	-17 54	76	115	I-II	-12	16.5	0.0642	0	5	22 53 58.0	-17 38 01
1072	22 52.9	-53 47	-106	64	II-III:	73	20.0	0.0	1	6	22 55 53.4	-53 30 58
1073	22 53.1	-50 38	-59	-32	II:	48	20.1	0.0	0	6	22 56 02.6	-50 21 58
1074	22 55.2	-49 57	-42	6	II-III?	0	21.4	0.0	0	6	22 58 07.4	-49 40 56
1075	22 55.7	-31 01	-54	-52	II-III	15	17.1	0.0	0	5	22 58 26.6	-30 44 55
1076	22 55.7	-41 08	-24	-58	II?	90	21.4	0.0	2	6	22 58 31.5	-40 51 55
1077	22 56.1	-35 03	85	-2	II-III	92	19.7	0.312	2	6	22 58 52.3	-34 46 55
1078	22 57.2	-68 54	119	55	I-II	-14	18.1	0.0	0	6	23 00 31.1	-68 37 53
1079	22 57.6	-53 47	-69	65	II:	43	20.1	0.0	0	6	23 00 33.6	-53 30 53
1080	22 58.8	-44 16	62	40	III	21	16.8	0.0699	0	5	23 01 38.5	-43 59 51
1081	22 59.4	-70 06	-115	-14	I-II	-1	16.8	0.0	0	5	23 02 44.4	-69 49 50
1082	23 00.3	-48 45	3	67	III?	158	20.1	0.0	3	6	23 03 10.8	-48 28 50
1083	23 00.5	-53 54	-46	60	II	41	20.2	0.0	0	6	23 03 26.6	-53 37 49
1084	23 00.8	-42 37	84	129	III	20	17.5	0.0	0	5	23 03 37.0	-42 20 49
1085	23 01.9	-49 06	15	51	II-III	70	20.2	0.0	1	6	23 04 46.6	-48 49 48
1086	23 02.1	-32 54	20	-153	I-II	-2	16.7	0.0	0	5	23 04 50.3	-32 37 48
1087	23 03.8	-68 41	-101	66	II:	21	18.5	0.0	0	6	23 07 01.9	-68 24 46
1088	23 05.7	-52 07	46	-111	II-III:	94	19.9	0.0	2	6	23 08 35.3	-51 50 44
1089	23 06.4	-47 59	56	110	III	63	20.0	0.0	1	6	23 09 51.7	-38 39 43
1090	23 07.1	-38 56	92	60	II	51	20.0	0.0	1	6	23 09 51.7	-38 39 43
1091	23 07.3	-86 14	78	-80	I	26	17.4	0.0	0	5	23 13 22.5	-85 57 41

Table D.1 continued from previous page

ACO	RAB1950	DEB1950	Xcen	Ycen	BMtype	Count	m10	z	Rich	Dclass	_RA_icrs	_DE_icrs
1092	23 07.4	-17 10	16	152	III	24	17.2	0.0	0	5	23 10 02.3	-16 53 43
1093	23 07.7	-76 27	4	-75	II-III	6	17.1	0.0	0	5	23 11 15.8	-76 10 42
1094	23 07.8	-19 11	18	45	III?	40	19.7	0.0	0	6	23 10 26.8	-18 54 42
1095	23 08.6	-55 39	15	-33	III	60	20.1	0.0	1	6	23 11 30.8	-55 22 41
1096	23 08.9	-29 23	100	35	I-II	28	17.6	0.0	0	5	23 11 35.8	-29 06 41
1097	23 09.0	-73 36	10	77	II-III	29	17.4	0.0	0	5	23 12 21.8	-73 19 41
1098	23 09.6	-44 08	-103	47	I	-62	16.8	0.0	0	5	23 12 23.5	-43 51 40
1099	23 10.6	-23 25	55	85	I-II	17	17.0	0.0	0	5	23 13 15.8	-23 08 40
1100	23 10.7	-52 34	35	133	III	85	20.0	0.0	2	6	23 13 33.8	-52 17 39
1101	23 11.2	-43 00	-89	108	III	28	16.3	0.0564	0	4	23 13 58.5	-42 43 39
1102	23 11.6	-54 36	40	22	III	29	19.4	0.0	0	6	23 14 28.8	-54 19 38
1103	23 14.3	-44 34	-57	24	II-III	2	18.0	0.0	0	6	23 17 04.4	-44 17 36
1104	23 14.3	-74 11	29	45	II	0	17.6	0.0	0	5	23 17 36.4	-73 54 36
1105	23 14.3	-75 18	27	-15	I-II	-3	17.4	0.0	0	5	23 17 39.9	-75 01 36
1106	23 14.7	-43 07	-54	102	II-III	-23	17.3	0.0346	0	5	23 17 27.6	-42 50 36
1107	23 14.7	-52 05	121	-110	II-III	69	20.9	0.0	1	6	23 17 32.0	-51 48 36
1108	23 15.2	-47 44	136	121	III	79	20.9	0.0	1	6	23 17 59.5	-47 27 35
1109	23 15.6	-36 34	36	-81	III?	75	19.7	0.0	1	6	23 18 19.0	-36 17 35
1110	23 16.2	-48 16	143	93	III	73	21.0	0.0	1	6	23 18 59.5	-47 59 35
1111	23 16.4	-42 22	-75	-123	III	25	15.4	0.0	0	4	23 19 08.9	-42 05 34
1112	23 16.5	-54 22	77	34	III	0	21.1	0.0	0	6	23 19 20.7	-54 05 34
1113	23 17.4	-24 24	-131	32	II	8	17.5	0.0	0	5	23 20 03.2	-24 07 34
1114	23 18.2	-74 17	43	39	II	21	17.3	0.0	0	5	23 21 26.8	-74 00 33
1115	23 19.2	-55 03	97	-3	III	0	21.3	0.0	0	6	23 22 02.0	-54 46 32
1116	23 19.7	-64 22	-53	32	I-II:	59	20.1	0.0	1	6	23 22 39.1	-64 05 32
1117	23 20.6	-23 06	-94	102	III	19	18.6	0.0	0	6	23 23 14.5	-22 49 31
1118	23 21.5	-51 28	-75	-78	II	-96	16.6	0.0	0	5	23 24 17.2	-51 11 31
1119	23 21.9	-30 12	-17	-10	II-III	29	18.1	0.0	0	6	23 24 33.9	-29 55 30
1120	23 22.0	-38 57	-24	57	II-III	6	18.1	0.0	0	6	23 24 42.3	-38 40 30
1121	23 22.5	-41 29	-17	-78	I	81	20.0	0.0	2	6	23 25 13.0	-41 12 30
1122	23 23.1	-81 36	102	-97	I-II	22	17.5	0.0	0	5	23 26 47.6	-81 19 29
1123	23 24.2	-32 01	11	-107	II-III	24	19.4	0.0	0	6	23 26 52.0	-31 44 29
1124	23 24.4	-49 53	-53	8	I	3	18.0	0.0	0	6	23 27 09.5	-49 36 29
1125	23 25.0	-38 30	9	82	III	56	19.9	0.0	1	6	23 27 41.5	-38 13 28
1126	23 25.5	-32 00	25	-106	I-II	6	19.3	0.0	0	6	23 28 09.8	-31 43 28
1127	23 25.6	-29 24	27	33	I-II	28	17.7	0.0	0	5	23 28 15.2	-29 07 28
1128	23 26.3	-53 55	156	54	III	47	20.2	0.0	0	6	23 29 04.6	-53 38 27
1129	23 27.2	-31 23	45	-73	II	3	16.1	0.0358	0	4	23 29 51.3	-31 06 27
1130	23 27.3	-17 23	1	144	III	9	18.8	0.0	0	6	23 29 54.6	-17 06 27
1131	23 27.6	-79 07	-83	45	II	-3	16.5	0.0	0	5	23 30 55.7	-78 50 26
1132	23 27.9	-54 09	167	41	III	0	20.8	0.0	0	6	23 30 40.1	-53 52 26
1133	23 28.6	-38 12	44	98	II-III	20	19.8	0.0	0	6	23 31 16.6	-37 55 26
1134	23 31.7	-43 45	-159	65	II	26	17.9	0.0	0	5	23 34 23.2	-43 28 24
1135	23 33.3	-42 28	88	-131	III	93	20.1	0.0	2	6	23 35 58.5	-42 11 24
1136	23 33.6	-31 53	118	-101	III	21	16.7	0.0	0	5	23 36 14.3	-31 36 24
1137	23 34.2	-31 41	-138	-88	II-III:	25	19.6	0.0	0	6	23 36 50.1	-31 24 23
1138	23 34.4	-42 01	101	-108	III	103	20.6	0.0	2	6	23 37 04.1	-41 44 23
1139	23 35.8	-50 16	46	-13	II-III	15	19.1	0.0	0	6	23 38 29.7	-49 59 22
1140	23 36.8	-46 15	-106	-67	I	3	16.5	0.0682	0	5	23 39 28.4	-45 58 22
1141	23 38.0	-28 52	-99	63	II	84	19.7	0.0	2	6	23 40 37.1	-28 35 22
1142	23 38.7	-30 30	-85	-20	II-III	20	15.5	0.0701	0	4	23 41 19.2	-30 13 21
1143	23 42.2	-49 23	102	32	II	13	18.2	0.0	0	6	23 44 51.3	-49 06 20
1144	23 42.3	-62 31	-113	131	III	10	19.3	0.0	0	6	23 45 00.9	-62 14 20
1145	23 42.8	-56 19	25	-68	II	27	18.0	0.0	0	6	23 45 28.7	-56 02 20
1146	23 43.4	-23 32	-83	80	I-II	-9	15.9	0.0	0	4	23 45 59.7	-23 15 20
1147	23 43.8	-47 15	-40	-119	I-II	4	16.3	0.0705	0	4	23 46 26.4	-46 58 20

Table D.1 continued from previous page

ACO	RAB1950	DEB1950	Xcen	Ycen	BMtype	Count	m10	z	Rich	Dclass	_RA_icrs	_DE_icrs
1148	23 43.9	-66 30	78	-94	II-III	36	20.1	0.0	0	6	23 46 37.6	-66 13 19
1149	23 44.8	-74 17	-55	38	I-II	21	17.4	0.0	0	5	23 47 35.9	-74 00 19
1150	23 45.2	-35 52	98	-46	I-II	95	19.8	0.0	2	6	23 47 48.6	-35 35 19
1151	23 45.7	-29 11	-8	47	II	218	19.7	0.226	4	6	23 48 17.9	-28 54 19
1152	23 45.9	-44 10	-22	46	III	20	19.5	0.0	0	6	23 48 31.4	-43 53 19
1153	23 46.7	-47 48	146	115	I	-1	19.5	0.0	0	6	23 49 19.6	-47 31 19
1154	23 46.8	-63 23	-83	86	III	12	19.2	0.0	0	6	23 49 28.6	-63 06 19
1155	23 47.6	-29 18	-148	38	I-II	3	15.4	0.0	0	3	23 50 11.6	-29 01 19
1156	23 47.6	-64 37	-75	20	III	-9	19.3	0.0	0	6	23 50 16.5	-64 20 19
1157	23 49.3	-34 42	-124	16	II:	19	14.7	0.0456	0	3	23 51 53.7	-34 25 18
1158	23 49.5	-56 13	75	-65	II	10	17.5	0.0	0	5	23 52 07.8	-55 56 18
1159	23 51.0	-64 31	-55	26	II-III	-8	18.6	0.0	0	6	23 53 38.4	-64 14 18
1160	23 51.4	-44 39	-82	18	II-III:	66	20.6	0.0	1	6	23 53 59.9	-44 22 18
1161	23 53.0	-33 56	-81	61	III	17	16.3	0.0	0	5	23 55 34.9	-33 39 18
1162	23 53.2	-22 52	-87	115	II-III	24	17.4	0.0	0	5	23 55 46.4	-22 35 18
1163	23 53.4	-18 27	67	85	II	8	15.9	0.0	0	4	23 55 58.3	-18 10 18
1164	23 55.0	-37 54	-55	118	III	14	16.4	0.0	0	5	23 57 34.6	-37 37 18
1165	23 56.1	-30 08	-49	-5	I-II	3	15.5	0.0299	0	4	23 58 40.2	-29 51 18
1166	23 57.1	-67 11	-17	152	II	-46	17.1	0.0	0	5	23 59 40.9	-66 54 17
1167	23 57.7	-20 16	-30	-13	III	78	20.0	0.0	1	6	00 00 15.9	-19 59 18
1168	23 57.8	-59 56	-18	6	III:	22	18.1	0.0	0	6	00 00 22.2	-59 39 17
1169	23 58.2	-46 41	91	-90	I-II	12	16.7	0.0	0	5	00 00 45.9	-46 24 17
1170	23 58.5	-37 07	-18	159	I-II	26	17.7	0.0	0	5	00 01 03.8	-36 50 18
1171	23 58.8	-27 49	-19	119	II	8	15.9	0.0	0	4	00 01 21.8	-27 32 18
1172	23 58.8	-39 03	-15	55	I	8	16.1	0.05	0	4	00 01 21.7	-38 46 18
1173	23 59.2	-44 14	-13	43	III	27	15.4	0.0	0	3	00 01 45.6	-43 57 17
1174	23 59.3	-37 16	-10	151	I	-5	19.4	0.0	0	6	00 01 51.6	-36 59 18
2713	00 00.0	-47 26	107	-131	I-II	58	18.7	0.0	1	6	00 02 33.4	-47 09 17
2714	00 00.0	-68 20	-2	90	II-III	45	18.0	0.0	0	6	00 02 32.8	-68 03 17
2715	00 00.2	-34 57	-2	5	III	112	16.9	0.0	2	5	00 02 45.5	-34 40 18
2716	00 00.3	-27 27	2	-128	I-II	44	16.1	0.0	0	4	00 02 51.5	-27 10 18
2717	00 00.7	-36 14	4	-62	I-II	52	15.4	0.0498	1	3	00 03 15.3	-35 57 18
2718	00 01.1	-42 13	111	-120	III:	61	17.8	0.0	1	5	00 03 39.1	-41 56 18
2719	00 01.4	-23 24	15	87	I-II	41	17.5	0.0	0	5	00 03 57.4	-23 07 18
2720	00 02.6	-18 18	28	92	I	80	18.9	0.0	2	6	00 05 09.4	-18 01 18
2721	00 03.6	-35 00	34	3	II	192	16.8	0.114	3	5	00 06 08.8	-34 43 18
2722	00 04.5	-41 15	41	-66	I	51	18.0	0.0	1	5	00 07 02.3	-40 58 18
2723	00 04.6	-77 25	11	-129	I-II	43	18.6	0.0	0	6	00 07 02.3	-77 08 18
2724	00 04.7	-32 08	48	-113	I-II	47	19.3	0.0	0	6	00 07 14.7	-31 51 18
2725	00 04.8	-18 00	58	108	I-II	92	19.6	0.0	2	6	00 07 21.2	-17 43 18
2726	00 04.8	-28 24	53	87	I	47	18.0	0.0	0	6	00 07 20.8	-28 07 18
2727	00 05.1	-82 17	9	146	I-II	68	19.1	0.0	1	6	00 07 26.5	-82 00 18
2728	00 05.5	-61 04	32	-54	I:	56	18.8	0.0	1	6	00 08 00.2	-60 47 18
2729	00 06.9	-17 04	85	157	II-III?	64	18.3	0.0	1	5	00 09 27.0	-16 47 18
2730	00 07.4	-35 58	77	-48	II	79	17.4	0.114	1	5	00 09 55.9	-35 41 18
2731	00 07.7	-57 16	51	-121	III:	39	15.1	0.0312	0	3	00 10 11.7	-56 59 18
2732	00 07.7	-64 43	41	16	II-III	39	17.3	0.0	0	5	00 10 10.3	-64 26 18
2733	00 08.7	-34 43	91	20	III	74	18.6	0.0	1	6	00 11 13.8	-34 26 18
2734	00 08.8	-29 09	99	47	III	58	16.1	0.0	1	4	00 11 20.1	-28 52 19
2735	00 09.3	-68 05	44	102	III	57	18.7	0.0	1	6	00 11 44.2	-67 48 18
2736	00 09.5	-42 31	90	131	III	41	16.8	0.0	0	5	00 12 00.9	-42 14 19
2737	00 09.6	-66 37	48	-86	II-III	33	18.6	0.0	0	6	00 12 02.5	-66 20 19
2738	00 10.1	-50 36	84	-33	III	63	19.1	0.0	1	6	00 12 35.8	-50 19 19
2739	00 10.2	-18 59	-139	56	II-III	90	19.1	0.0	2	6	00 12 44.6	-18 42 19
2740	00 10.2	-63 29	58	81	II-III	42	18.6	0.0	0	6	00 12 39.1	-63 12 19
2741	00 11.2	-32 45	120	123	III	59	18.3	0.0	1	6	00 13 43.4	-32 28 19

Table D.1 continued from previous page

ACO	RAB1950	DEB1950	Xcen	Ycen	BMtype	Count	m10	z	Rich	Dclass	_RA_icrs	_DE_icrs
2742	00 11.4	-23 55	-132	59	II	66	19.3	0.0	1	6	00 13 56.1	-23 38 19
2743	00 11.5	-46 38	104	-89	III	69	19.2	0.0	1	6	00 13 59.9	-46 21 19
2744	00 11.8	-30 40	131	-35	III	137	19.5	0.308	3	6	00 14 19.5	-30 23 19
2745	00 11.8	-42 54	114	111	II-III	62	18.0	0.0	1	6	00 14 18.2	-42 37 19
2746	00 11.8	-66 21	60	-72	II-III	35	18.7	0.0	0	6	00 14 13.2	-66 04 19
2747	00 12.6	-29 39	-124	18	II-III	56	19.1	0.0	1	6	00 15 07.5	-29 22 19
2748	00 13.5	-18 29	-97	84	III	70	19.5	0.0	1	6	00 16 02.3	-18 12 20
2749	00 13.5	-35 14	-118	-14	III	109	17.5	0.0	2	5	00 16 00.7	-34 57 20
2750	00 13.5	-37 25	-115	-129	II	69	17.8	0.0	1	5	00 16 00.5	-37 08 20
2751	00 13.7	-31 40	-110	-87	III	68	17.6	0.0	1	5	00 16 13.1	-31 23 20
2752	00 13.8	-46 40	125	-92	II	70	19.1	0.0	1	6	00 16 17.1	-46 23 20
2753	00 13.8	-50 08	-143	-7	III	76	17.7	0.0	1	5	00 16 16.5	-49 51 20
2754	00 14.6	-53 05	113	102	II	41	19.1	0.0	0	6	00 17 03.7	-52 48 20
2755	00 15.0	-35 28	-100	-25	III	120	16.7	0.0	2	5	00 17 30.4	-35 11 20
2756	00 15.3	-19 35	-74	25	II-III	79	17.1	0.0	1	5	00 17 50.1	-19 18 20
2757	00 15.8	-88 27	-10	-81	III	40	18.1	0.0	0	5	00 15 45.9	-88 10 20
2758	00 15.9	-42 03	-102	-108	III	37	17.0	0.0	0	5	00 18 23.3	-41 46 20
2759	00 16.0	-30 57	-84	-50	III	47	17.1	0.0	0	5	00 18 30.8	-30 40 20
2760	00 16.8	-65 50	89	-48	II	39	17.8	0.0	0	5	00 19 10.2	-65 33 21
2761	00 16.9	-64 48	92	9	II	40	18.7	0.0	0	6	00 19 16.6	-64 31 21
2762	00 17.0	-53 49	-129	61	II	45	16.9	0.1124	0	5	00 19 26.5	-53 32 21
2763	00 17.5	-42 14	-86	-119	II-III?	58	18.3	0.0	1	6	00 19 58.8	-41 57 21
2764	00 18.0	-49 30	-107	27	II	55	16.7	0.0641	1	5	00 20 27.2	-49 13 21
2765	00 19.0	-21 02	-27	-54	II	55	16.8	0.0	1	5	00 21 31.5	-20 45 22
2766	00 20.2	-32 22	-47	141	II-III:	58	19.0	0.0	1	6	00 22 41.8	-32 05 22
2767	00 20.3	-38 24	-61	87	II	55	17.8	0.0	1	5	00 22 46.8	-38 07 22
2768	00 21.5	-17 20	6	145	II	68	18.6	0.0	1	6	00 24 01.7	-17 03 23
2769	00 21.7	-39 55	-46	6	I-II	33	18.4	0.0	0	6	00 24 10.2	-39 38 23
2770	00 21.9	-66 12	114	-67	II-III	33	17.8	0.0	0	5	00 24 12.6	-65 55 22
2771	00 22.1	-40 24	-42	-20	I-II	33	16.8	0.0	0	5	00 24 34.0	-40 07 23
2772	00 22.5	-38 16	-37	95	I-II	58	17.7	0.0	1	5	00 24 58.3	-37 59 23
2773	00 22.7	-43 43	-56	71	I-II	37	18.5	0.0	0	6	00 25 09.1	-43 26 23
2774	00 23.2	-65 57	-116	-55	II-III	69	18.5	0.0	1	6	00 25 30.0	-65 40 23
2775	00 23.5	-69 13	109	37	III	51	19.1	0.0	1	6	00 25 45.0	-68 56 23
2776	00 23.8	-50 42	-55	-37	II	53	19.1	0.0	1	6	00 26 12.9	-50 25 23
2777	00 24.8	-50 32	-47	-26	II	88	18.0	0.0	2	6	00 27 12.6	-50 15 24
2778	00 26.1	-30 31	33	-24	III	51	16.8	0.0	1	5	00 28 35.1	-30 14 25
2779	00 26.6	-53 23	-53	88	I	42	18.0	0.0	0	6	00 28 58.9	-53 06 25
2780	00 26.8	-29 40	40	20	III	54	17.1	0.0	1	5	00 29 17.1	-29 23 25
2781	00 27.6	-20 21	81	-18	III	78	19.1	0.0	1	6	00 30 06.7	-20 04 26
2782	00 27.9	-53 40	-42	73	II	48	16.3	0.0	0	5	00 30 16.3	-53 23 26
2783	00 28.1	-34 41	42	18	II-III	32	18.6	0.0	0	6	00 30 33.9	-34 24 26
2784	00 28.3	-29 43	58	20	II-III:	53	18.7	0.0	1	6	00 30 46.9	-29 26 26
2785	00 28.8	-62 56	-94	109	II-III:	32	19.0	0.0	0	6	00 31 04.8	-62 39 26
2786	00 29.2	-41 40	29	-88	II	64	18.7	0.0	1	6	00 31 37.9	-41 23 26
2787	00 29.6	-55 28	-28	-24	I-II	59	17.5	0.0	1	5	00 31 56.8	-55 11 26
2788	00 29.7	-27 47	76	123	III	41	19.3	0.0	0	6	00 32 11.1	-27 30 27
2789	00 31.2	-69 32	-102	24	I	48	17.8	0.0	0	5	00 33 20.8	-69 15 27
2790	00 31.4	-50 21	8	-17	II-III	88	17.5	0.0	2	5	00 33 46.4	-50 04 28
2791	00 31.6	-21 51	-156	115	III	73	18.9	0.0	1	6	00 34 06.0	-21 34 28
2792	00 33.6	-60 18	-32	-15	II-III	33	19.0	0.0	0	6	00 35 52.2	-60 01 29
2793	00 34.0	-82 52	58	111	II-III	30	17.6	0.0	0	5	00 35 14.9	-82 35 29
2794	00 34.1	-31 18	124	-73	II-III	57	18.6	0.0	1	6	00 36 33.6	-31 01 29
2795	00 34.5	-52 10	11	154	II-III	44	18.6	0.0	0	6	00 36 50.5	-51 53 30
2796	00 34.5	-64 45	-57	13	II	33	17.7	0.0	0	5	00 36 42.0	-64 28 29
2797	00 34.8	-62 56	-57	111	II	46	18.1	0.0	0	6	00 37 01.5	-62 39 30

Table D.1 continued from previous page

ACO	RAB1950	DEB1950	Xcen	Ycen	BMtype	Count	m10	z	Rich	Dclass	_RA_icrs	_DE_icrs
2798	00 35.1	-28 49	-131	65	I-II	58	17.3	0.1126	1	5	00 37 34.0	-28 32 30
2799	00 35.1	-39 24	93	31	I-II	63	16.0	0.0	1	4	00 37 31.1	-39 07 30
2800	00 35.5	-25 22	-106	-19	III	59	15.6	0.0	1	4	00 37 58.7	-25 05 30
2801	00 36.1	-29 21	-119	36	I	74	18.1	0.0	1	6	00 38 33.7	-29 04 31
2802	00 36.5	-31 53	138	165	III	74	19.0	0.0	1	6	00 38 57.0	-31 36 31
2803	00 37.0	-20 15	-64	-11	II-III	105	19.1	0.0	2	6	00 39 29.7	-19 58 32
2804	00 37.2	-29 11	-106	45	I-II	56	17.3	0.0	1	5	00 39 39.6	-28 54 32
2805	00 37.2	-52 27	32	137	II-III	40	18.4	0.0	0	6	00 39 31.4	-52 10 31
2806	00 37.9	-56 26	34	-76	I-II	37	15.1	0.0271	0	3	00 40 10.8	-56 09 32
2807	00 38.2	-34 53	-110	9	II-III	36	18.2	0.0	0	6	00 40 37.8	-34 36 32
2808	00 38.2	-50 31	65	-27	III	54	18.1	0.0	1	6	00 40 32.0	-50 14 32
2809	00 39.1	-44 07	103	49	II	36	18.1	0.0	0	6	00 41 28.5	-43 50 33
2810	00 39.3	-61 22	4	-72	III	44	16.6	0.0	0	5	00 41 30.4	-61 05 33
2811	00 39.7	-28 49	-76	66	I-II	73	17.3	0.0	1	5	00 42 09.3	-28 32 33
2812	00 40.1	-38 26	-127	83	I-II	55	18.6	0.0	1	6	00 42 30.3	-38 09 34
2813	00 40.9	-20 54	-15	-47	III	155	19.4	0.0	3	6	00 43 23.1	-20 37 34
2814	00 40.9	-28 54	-62	61	II	52	17.1	0.0	1	5	00 43 21.1	-28 37 34
2815	00 43.0	-17 09	11	153	III	110	19.1	0.0	2	6	00 45 29.8	-16 52 36
2816	00 43.3	-18 22	16	88	II-III	48	16.7	0.0	0	5	00 45 47.5	-18 05 36
2817	00 43.4	-54 07	80	47	I-II	47	18.6	0.0	0	6	00 45 40.0	-53 50 36
2818	00 43.5	-50 24	-145	-23	I	56	19.2	0.0	1	6	00 45 48.2	-50 07 36
2819	00 43.7	-63 52	-4	62	I-II	90	15.8	0.0	2	4	00 45 49.5	-63 35 36
2820	00 45.5	-57 03	88	-109	II	51	18.0	0.0	1	5	00 47 43.0	-56 46 38
2821	00 45.8	-64 28	8	29	I-II	30	17.8	0.0	0	5	00 47 53.5	-64 11 38
2822	00 45.9	-38 44	-65	68	I-II	67	18.6	0.0	1	6	00 48 16.9	-38 27 39
2823	00 45.9	-41 08	-63	-60	II-III	39	17.3	0.0	0	5	00 48 15.9	-40 51 39
2824	00 46.1	-21 37	48	-87	III	46	15.3	0.0486	0	3	00 48 34.4	-21 20 39
2825	00 46.2	-46 02	-91	-55	I-II?	56	18.4	0.0	1	6	00 48 31.6	-45 45 39
2826	00 47.5	-62 42	20	123	I	44	19.0	0.0	0	6	00 49 36.7	-62 25 40
2827	00 48.4	-50 33	-103	-29	II	54	18.8	0.0	1	6	00 50 40.4	-50 16 41
2828	00 48.8	-39 48	-34	12	I-II	37	18.2	0.0	0	6	00 51 09.8	-39 31 41
2829	00 48.9	-28 48	32	66	II	50	17.3	0.0	1	5	00 51 19.8	-28 31 41
2830	00 48.9	-48 51	163	57	II?	58	19.0	0.0	1	6	00 51 11.3	-48 34 41
2831	00 49.1	-55 39	120	-38	II	32	19.5	0.0	0	6	00 51 18.6	-55 22 41
2832	00 49.6	-23 52	65	62	I-II	45	19.5	0.0	0	6	00 52 03.3	-23 35 42
2833	00 50.5	-55 58	129	-55	III	36	19.1	0.0	0	6	00 52 41.8	-55 41 43
2834	00 50.6	-50 53	-84	-46	III	44	19.1	0.0	0	6	00 52 51.5	-50 36 43
2835	00 50.7	-47 08	-89	155	I-II	53	19.0	0.0	1	6	00 52 59.7	-46 51 43
2836	00 51.4	-47 53	-82	115	II	41	16.1	0.0	0	4	00 53 41.0	-47 36 44
2837	00 51.6	-80 32	-86	-34	I-II	47	18.0	0.0	0	5	00 52 40.7	-80 15 43
2838	00 51.8	-39 31	-4	26	II	39	18.1	0.0	0	6	00 54 09.2	-39 14 44
2839	00 52.0	-51 15	-71	-65	II-III	45	18.0	0.0	0	6	00 54 14.7	-50 58 44
2840	00 52.1	-40 06	-1	-5	II	54	17.4	0.0	1	5	00 54 26.9	-39 49 44
2841	00 52.8	-49 13	-67	44	I	35	16.8	0.0	0	5	00 55 03.8	-48 56 45
2842	00 53.6	-24 23	113	33	II-III	70	18.9	0.0	1	6	00 56 02.6	-24 06 46
2843	00 54.2	-27 47	118	-149	III	34	18.8	0.0	0	6	00 56 37.4	-27 30 47
2844	00 54.2	-30 20	92	-17	II-III	50	17.8	0.0	1	5	00 56 36.4	-30 03 47
2845	00 54.4	-39 04	23	51	II-III	78	18.4	0.0	1	6	00 56 44.8	-38 47 47
2846	00 54.7	-29 58	98	3	II:	53	18.5	0.0	1	6	00 57 06.5	-29 41 47
2847	00 56.3	-34 36	90	23	I-II	38	18.0	0.0	0	6	00 58 40.4	-34 19 49
2848	00 56.3	-41 01	42	-54	II	34	18.3	0.0	0	6	00 58 37.4	-40 44 49
2849	00 56.6	-21 16	-83	-67	III	31	19.1	0.0	0	6	00 59 03.3	-20 59 49
2850	00 56.9	-29 19	125	36	II-III	102	18.6	0.0	2	6	00 59 18.4	-29 02 50
2851	00 57.6	-30 41	-134	-36	II	30	17.8	0.0	0	5	00 59 59.8	-30 24 50
2852	00 57.8	-39 53	59	6	II-III	45	18.5	0.0	0	6	01 00 07.6	-39 36 50
2853	00 58.1	-39 25	62	31	II-III	75	18.9	0.0	1	6	01 00 25.8	-39 08 51

Table D.1 continued from previous page

ACO	RAB1950	DEB1950	Xcen	Ycen	BMtype	Count	m10	z	Rich	Dclass	_RA_icrs	_DE_icrs
2854	00 58.6	-50 48	-16	-40	I-II	64	15.6	0.0	1	4	01 00 48.8	-50 31 51
2855	00 58.9	-44 12	25	45	II-III:	75	19.2	0.0	1	6	01 01 11.0	-43 55 52
2856	00 59.3	-38 56	75	57	II-III	53	18.7	0.0	1	6	01 01 37.7	-38 39 52
2857	00 59.7	-40 13	77	-12	I	66	18.8	0.0	1	6	01 02 01.0	-39 56 53
2858	01 00.0	-56 00	-48	-53	II-III	85	19.5	0.0	2	6	01 02 07.8	-55 43 53
2859	01 00.4	-67 51	38	117	II	43	16.4	0.0	0	5	01 02 14.6	-67 34 53
2860	01 01.8	-40 03	99	-4	I	41	16.0	0.0268	0	4	01 04 06.6	-39 46 55
2861	01 02.2	-51 49	14	-95	III	32	19.3	0.0	0	6	01 04 22.7	-51 32 55
2862	01 02.7	-17 00	-6	161	II	87	18.1	0.0	2	6	01 05 10.2	-16 43 56
2863	01 02.8	-48 45	21	69	II-III	58	18.6	0.0	1	6	01 05 00.9	-48 28 56
2864	01 02.9	-67 12	95	-123	II	39	16.5	0.0	0	5	01 04 44.3	-66 55 56
2865	01 03.8	-36 11	-94	-63	III	43	17.7	0.0	0	5	01 06 08.2	-35 54 58
2866	01 04.0	-17 46	11	120	I-II	82	17.8	0.0	2	5	01 06 27.8	-17 29 58
2867	01 04.0	-34 15	-92	95	II-III	59	18.0	0.0	1	6	01 06 21.1	-33 58 58
2868	01 04.3	-56 00	-16	-53	III	92	18.0	0.0	2	6	01 06 24.0	-55 43 58
2869	01 05.0	-44 19	83	33	II-III:	55	19.4	0.0	1	6	01 07 15.3	-44 02 59
2870	01 05.5	-47 11	46	153	I	33	15.0	0.025	0	3	01 07 43.2	-46 55 00
2871	01 05.6	-37 00	-70	-108	I	92	16.8	0.0	2	5	01 07 55.4	-36 44 00
2872	01 05.9	-43 29	93	83	III:	71	19.2	0.0	1	6	01 08 09.6	-43 13 00
2873	01 06.3	-43 58	97	56	III	61	18.9	0.0	1	6	01 08 33.2	-43 42 01
2874	01 06.4	-40 37	-123	-31	I	79	18.0	0.0	1	6	01 08 41.2	-40 21 01
2875	01 06.4	-65 58	119	-59	III	37	18.4	0.0	0	6	01 08 14.6	-65 42 00
2876	01 07.0	-57 33	-67	131	III	48	19.3	0.0	0	6	01 09 03.2	-57 17 01
2877	01 07.6	-46 10	105	-65	I	30	14.1	0.0241	0	2	01 09 49.3	-45 54 02
2878	01 07.7	-29 57	-18	4	I-II	32	17.7	0.0	0	5	01 10 04.4	-29 41 02
2879	01 08.3	-36 27	-42	-77	II-III?	69	18.6	0.0	1	6	01 10 37.1	-36 11 03
2880	01 08.7	-49 36	71	23	I-II	37	18.6	0.0	0	6	01 10 52.3	-49 20 04
2881	01 08.8	-17 21	72	142	II	36	15.4	0.0	0	3	01 11 15.5	-17 05 04
2882	01 10.0	-60 54	-42	-48	II	32	17.7	0.0	0	5	01 11 57.4	-60 38 05
2883	01 10.1	-36 37	-23	-86	II	65	17.8	0.0	1	5	01 12 24.6	-36 21 06
2884	01 10.8	-37 52	-16	-153	II-III?	64	18.6	0.0	1	6	01 13 05.8	-37 36 06
2885	01 11.6	-39 14	-71	44	II-III	37	18.0	0.0	0	6	01 13 52.8	-38 58 08
2886	01 11.9	-49 09	101	46	III	45	18.1	0.0	0	6	01 14 03.7	-48 53 08
2887	01 12.1	-36 33	-2	-82	II	95	17.7	0.0	2	5	01 14 24.3	-36 17 08
2888	01 12.3	-56 59	-29	163	III	45	19.3	0.0	0	6	01 14 19.6	-56 43 08
2889	01 12.6	-48 46	107	66	I-II	65	17.6	0.0667	1	5	01 14 45.8	-48 30 09
2890	01 13.6	-21 18	129	-71	II	91	18.1	0.0	2	6	01 16 01.5	-21 02 11
2891	01 14.5	-38 08	-40	104	II	57	18.0	0.0	1	6	01 16 46.8	-37 52 12
2892	01 14.7	-37 20	25	-123	II:	66	17.6	0.0	1	5	01 16 59.3	-37 04 12
2893	01 15.0	-51 08	122	-63	II:	63	19.0	0.0	1	6	01 17 06.9	-50 52 12
2894	01 15.2	-22 54	112	113	I-II	36	19.3	0.0	0	6	01 17 36.6	-22 38 13
2895	01 15.7	-27 16	114	-119	II:	62	19.3	0.0	1	6	01 18 04.5	-27 00 13
2896	01 16.0	-37 22	-25	144	I	44	17.4	0.0317	0	5	01 18 17.0	-37 06 14
2897	01 16.2	-56 54	-1	168	II-III	36	19.1	0.0	0	6	01 18 12.0	-56 38 14
2898	01 16.4	-35 20	45	-17	III	88	17.6	0.0	2	5	01 18 42.1	-35 04 14
2899	01 17.9	-64 55	-62	5	II-III	59	18.3	0.0	1	6	01 19 39.9	-64 39 16
2900	01 18.9	-51 45	152	-97	II-III	31	18.6	0.0	0	6	01 20 58.9	-51 29 18
2901	01 19.1	-44 09	-51	46	III:	45	18.9	0.0	0	6	01 21 17.6	-43 53 18
2902	01 19.3	-20 41	-60	-34	II-III:	38	19.2	0.0	0	6	01 21 43.1	-20 25 19
2903	01 19.7	-55 59	99	-56	III	60	18.9	0.0	1	6	01 21 41.8	-55 43 19
2904	01 20.0	-29 34	125	23	II-III?	40	19.0	0.0	0	6	01 22 20.7	-29 18 20
2905	01 20.9	-46 17	-34	-68	II-III	60	19.3	0.0	1	6	01 23 03.4	-46 01 21
2906	01 21.2	-27 20	-82	-123	I-II	46	18.9	0.0	0	6	01 23 33.7	-27 04 22
2907	01 21.7	-25 06	-77	-3	II-III	73	19.1	0.0	1	6	01 24 04.7	-24 50 22
2908	01 21.7	-33 37	105	74	III	75	18.5	0.0	1	6	01 24 00.1	-33 21 22
2909	01 22.1	-37 39	40	129	III	55	17.7	0.0	1	5	01 24 21.5	-37 23 23

Table D.1 continued from previous page

ACO	RAB1950	DEB1950	Xcen	Ycen	BMtype	Count	m10	z	Rich	Dclass	_RA_icrs	_DE_icrs
2910	01 23.6	-33 43	125	68	II-III:	84	18.2	0.0	2	6	01 25 53.7	-33 27 25
2911	01 23.8	-38 14	58	97	I-II	72	16.1	0.0202	1	4	01 26 02.8	-37 58 26
2912	01 24.7	-50 15	-49	-13	II-III	100	17.7	0.0	2	5	01 26 46.5	-49 59 27
2913	01 25.6	-34 18	149	31	III	34	17.1	0.0	0	5	01 27 53.0	-34 02 28
2914	01 26.4	-47 09	-36	152	II-III	78	18.0	0.0	1	6	01 28 31.0	-46 53 30
2915	01 26.5	-29 16	-67	40	II	55	16.7	0.0	1	5	01 28 49.9	-29 00 30
2916	01 26.9	-46 31	21	-80	III	45	18.6	0.0	0	6	01 29 01.5	-46 15 30
2917	01 27.7	-53 34	-93	79	II	60	18.6	0.0	1	6	01 29 41.7	-53 18 32
2918	01 28.0	-49 13	-18	42	III	68	18.9	0.0	1	6	01 30 04.5	-48 57 32
2919	01 28.6	-27 21	-42	142	II	52	18.9	0.0	1	6	01 30 56.6	-27 05 33
2920	01 29.2	-34 52	-76	8	II-III	53	18.6	0.0	1	6	01 31 28.0	-34 36 34
2921	01 29.7	-24 59	20	2	I-II	60	18.6	0.0	1	6	01 32 03.8	-24 43 35
2922	01 30.0	-29 51	-25	8	I-II	115	18.1	0.0	2	6	01 32 19.0	-29 35 36
2923	01 30.0	-31 21	-25	-72	I-II	50	16.8	0.0	1	5	01 32 18.1	-31 05 36
2924	01 30.9	-27 12	-15	150	II-III	49	18.0	0.0	0	6	01 33 14.4	-26 56 37
2925	01 31.3	-45 28	63	-25	I	68	19.3	0.0	1	6	01 33 25.2	-45 12 38
2926	01 31.6	-27 47	-7	120	I-II	61	17.7	0.0	1	5	01 33 56.0	-27 31 39
2927	01 32.3	-27 37	1	128	II-III	86	19.0	0.0	2	6	01 34 38.0	-27 21 40
2928	01 32.8	-27 45	8	121	II-III	73	18.3	0.0	1	6	01 35 07.8	-27 29 41
2929	01 34.2	-28 09	25	100	II-III	38	19.2	0.0	0	6	01 36 31.4	-27 53 43
2930	01 34.7	-34 58	-16	3	I-II	34	18.0	0.0	0	6	01 36 56.9	-34 42 44
2931	01 36.8	-31 12	53	-64	II	66	18.0	0.0	1	6	01 39 05.1	-30 56 48
2932	01 37.9	-29 20	67	35	I-II	98	18.0	0.0	2	6	01 40 12.1	-29 04 50
2933	01 38.8	-54 49	-5	13	III	77	16.7	0.0208	1	5	01 40 42.0	-54 33 51
2934	01 38.9	-31 58	75	-106	II-III?	42	19.0	0.0	0	6	01 41 10.2	-31 42 52
2935	01 40.6	-23 37	-117	75	II	52	19.1	0.0	1	6	01 42 57.3	-23 21 55
2936	01 41.1	-37 36	-32	129	III:	64	19.3	0.0	1	6	01 43 17.7	-37 20 56
2937	01 41.4	-46 28	-101	-80	I-II	55	18.5	0.0	1	6	01 43 27.5	-46 12 56
2938	01 42.3	-22 29	-97	136	I-II	50	19.3	0.0	1	6	01 44 39.8	-22 13 58
2939	01 42.4	-17 17	-35	150	III	45	19.3	0.0	0	6	01 44 48.7	-17 01 58
2940	01 43.0	-25 00	-87	1	III	72	19.0	0.0	1	6	01 45 20.2	-24 44 59
2941	01 43.1	-53 16	29	97	III	85	18.0	0.0	2	6	01 45 00.7	-53 00 59
2942	01 45.4	-22 05	2	-108	I-II	32	18.0	0.0	0	6	01 47 45.7	-21 50 04
2943	01 46.0	-32 10	-105	-115	I-II	64	18.5	0.0	1	6	01 48 14.9	-31 55 05
2944	01 47.3	-26 10	-35	-61	I	37	18.4	0.0	0	6	01 49 36.9	-25 55 08
2945	01 48.2	-27 20	-83	144	III	46	19.1	0.0	0	6	01 50 30.0	-27 05 10
2946	01 49.1	-24 47	-14	13	II	48	19.4	0.0	0	6	01 51 25.6	-24 32 11
2947	01 49.5	-25 25	-8	-21	I-II	67	18.9	0.0	1	6	01 51 49.1	-25 10 12
2948	01 50.0	-32 57	-115	109	III	59	19.1	0.0	1	6	01 52 13.7	-32 42 13
2949	01 51.4	-27 29	14	-131	II-III	45	19.1	0.0	0	6	01 53 41.4	-27 14 16
2950	01 51.6	-26 47	17	-94	I-II	43	18.0	0.0	0	6	01 53 53.9	-26 32 16
2951	01 51.6	-58 25	-19	86	III	37	18.9	0.0	0	6	01 53 18.8	-58 10 16
2952	01 52.2	-35 56	-90	-51	III	45	17.9	0.0	0	5	01 54 22.9	-35 41 18
2953	01 52.2	-78 55	56	55	I-II	57	17.8	0.0	1	5	01 52 07.2	-78 40 15
2954	01 53.5	-71 43	36	-92	II	121	16.1	0.0	2	4	01 54 27.9	-71 28 19
2955	01 54.6	-17 17	-147	147	II	56	16.9	0.0	1	5	01 56 59.8	-17 02 23
2956	01 54.8	-24 14	57	43	I-II	92	19.3	0.0	2	6	01 57 07.3	-23 59 23
2957	01 56.2	-79 31	63	22	I	40	18.0	0.0	0	5	01 55 52.7	-79 16 23
2958	01 56.3	-19 24	-124	32	III	57	19.3	0.0	1	6	01 58 40.3	-19 09 26
2959	01 56.4	-50 02	-36	1	III	41	18.4	0.0	0	6	01 58 18.9	-49 47 26
2960	01 57.5	-38 16	-133	91	I-II	35	18.3	0.0	0	6	01 59 37.8	-38 01 29
2961	01 57.8	-31 29	29	-78	I	31	18.0	0.0	0	6	02 00 01.6	-31 14 29
2962	01 58.4	-33 07	-21	102	II-III	57	17.0	0.0	1	5	02 00 36.1	-32 52 31
2963	01 58.6	-36 14	-19	-65	III	41	17.5	0.0	0	5	02 00 45.4	-35 59 31
2964	01 58.8	-25 19	104	-17	II-III	47	18.9	0.0	0	6	02 01 06.0	-25 04 32
2965	01 59.2	-40 39	-112	-36	III	41	18.1	0.0	0	6	02 01 17.1	-40 24 32

Table D.1 continued from previous page

ACO	RAB1950	DEB1950	Xcen	Ycen	BMtype	Count	m10	z	Rich	Dclass	_RA_icrs	_DE_icrs
2966	01 59.4	-21 15	-85	-66	II-III	68	18.2	0.0	1	6	02 01 44.8	-21 00 33
2967	02 00.6	-28 30	64	81	II-III	34	18.1	0.0	0	6	02 02 51.5	-28 15 36
2968	02 01.5	-27 27	75	137	III	42	17.6	0.0	0	5	02 03 46.1	-27 12 38
2969	02 01.5	-41 20	-88	-72	I	83	17.3	0.0	2	5	02 03 33.9	-41 05 37
2970	02 02.9	-35 55	26	-49	II-III	72	18.1	0.0	1	6	02 05 02.9	-35 40 41
2971	02 03.0	-31 52	87	-100	III	37	18.0	0.0	0	6	02 05 12.4	-31 37 41
2972	02 03.4	-27 21	98	142	I-II	47	17.7	0.0	0	5	02 05 40.0	-27 06 42
2973	02 04.2	-26 19	-95	-70	II-III	76	19.1	0.0	1	6	02 06 28.7	-26 04 44
2974	02 04.3	-27 30	109	134	II-III	63	18.7	0.0	1	6	02 06 33.7	-27 15 44
2975	02 04.4	-28 59	108	54	III	43	18.1	0.0	0	6	02 06 38.6	-28 44 44
2976	02 04.5	-25 47	-93	-41	II	102	18.8	0.0	2	6	02 06 47.0	-25 32 44
2977	02 04.9	-26 01	-88	-54	I	93	18.9	0.0	2	6	02 07 10.8	-25 46 45
2978	02 05.9	-32 09	120	-116	II:	41	18.0	0.0	0	5	02 08 05.8	-31 54 48
2979	02 06.6	-26 36	-66	-85	II	43	18.0	0.0	0	6	02 08 52.1	-26 21 49
2980	02 07.1	-43 12	-126	96	III	59	18.8	0.0	1	6	02 09 06.6	-42 57 50
2981	02 07.7	-27 36	-53	-138	II-III	30	18.0	0.0	0	5	02 09 57.2	-27 21 52
2982	02 08.6	-37 19	-16	144	II	50	19.2	0.0	1	6	02 10 42.6	-37 04 54
2983	02 08.7	-33 20	92	90	III	51	17.5	0.0	1	5	02 10 52.3	-33 05 54
2984	02 09.4	-40 31	-9	-28	I	54	17.5	0.0	1	5	02 11 27.1	-40 16 55
2985	02 09.5	-17 17	43	147	II-III	101	18.4	0.0	2	6	02 11 52.6	-17 02 56
2986	02 09.8	-28 41	-98	71	III	43	19.1	0.0	0	6	02 12 02.1	-28 26 57
2987	02 10.8	-53 43	-14	71	II-III	30	18.2	0.0	0	6	02 12 32.5	-53 28 58
2988	02 11.0	-47 22	-81	-126	I-II	72	18.0	0.0649	1	5	02 12 54.4	-47 07 59
2989	02 11.2	-27 48	-82	119	III	67	19.2	0.0	1	6	02 13 26.6	-27 34 00
2990	02 12.0	-30 42	-71	-36	I-II	33	17.5	0.0	0	5	02 14 12.1	-30 28 02
2991	02 12.3	-26 03	1	-55	II	44	18.1	0.0	0	6	02 14 33.9	-25 49 03
2992	02 12.6	-26 54	5	-101	I	30	17.0	0.0	0	5	02 14 51.2	-26 40 03
2993	02 12.8	-36 46	-123	-96	II-III	55	19.5	0.0	1	6	02 14 54.3	-36 32 04
2994	02 12.9	-21 19	85	-70	III	76	19.1	0.0	1	6	02 15 13.4	-21 05 04
2995	02 12.9	-25 04	9	-2	I-II	69	17.8	0.0378	1	5	02 15 10.6	-24 50 04
2996	02 13.0	-51 51	102	-100	II	43	18.6	0.0	0	6	02 14 47.0	-51 37 04
2997	02 13.9	-52 03	11	160	III	30	19.3	0.0	0	6	02 15 40.4	-51 49 06
2998	02 14.4	-48 30	123	79	I-II	50	18.8	0.0	1	6	02 16 15.9	-48 16 07
2999	02 15.1	-28 36	-36	77	II-III	56	19.1	0.0	1	6	02 17 19.4	-28 22 09
3000	02 15.3	-19 39	-150	19	II-III	71	19.3	0.0	1	6	02 17 38.5	-19 25 10
3001	02 15.4	-17 42	119	123	II	40	18.2	0.0	0	6	02 17 45.9	-17 28 10
3002	02 16.4	-50 16	-117	-13	II-III	31	18.5	0.0	0	6	02 18 12.6	-50 02 12
3003	02 16.7	-29 12	-17	45	III	54	19.3	0.0	1	6	02 18 54.7	-28 58 13
3004	02 17.0	-48 14	-117	95	I-II	36	16.6	0.0635	0	5	02 18 51.6	-48 00 14
3005	02 17.5	-19 20	-122	36	II-III	84	19.0	0.0	2	6	02 19 50.5	-19 06 16
3006	02 17.7	-41 16	76	-68	III	42	17.9	0.0	0	5	02 19 42.5	-41 02 16
3007	02 18.8	-23 19	83	91	I-II	39	19.4	0.0	0	6	02 21 05.3	-23 05 19
3008	02 19.7	-40 15	97	-15	II-III	40	18.1	0.0	0	6	02 21 43.3	-40 01 21
3009	02 20.3	-48 48	-87	66	I	54	16.1	0.0631	1	4	02 22 07.8	-48 34 22
3010	02 20.4	-63 55	48	59	II-III	55	18.0	0.0	1	6	02 21 39.3	-63 41 21
3011	02 20.5	-17 01	-85	160	II-III	72	18.7	0.0	1	6	02 22 52.0	-16 47 23
3012	02 21.3	-27 02	37	160	II	62	18.0	0.0	1	6	02 23 32.0	-26 48 25
3013	02 21.5	-41 14	-148	-68	I-II	46	18.8	0.0	0	6	02 23 29.8	-41 00 25
3014	02 22.0	-42 20	115	-128	III	51	18.6	0.0	1	6	02 23 58.3	-42 06 26
3015	02 23.2	-49 46	-61	14	I-II	88	19.0	0.0	2	6	02 24 59.5	-49 32 29
3016	02 23.4	-42 14	32	151	II-III	42	19.1	0.0	0	6	02 25 22.2	-42 00 30
3017	02 23.9	-42 08	-124	-115	II?	55	18.7	0.0	1	6	02 25 52.2	-41 54 31
3018	02 24.8	-64 15	72	39	II-III	38	18.2	0.0	0	6	02 26 00.0	-64 01 32
3019	02 25.0	-56 21	-149	-76	II-III:	80	19.4	0.0	2	6	02 26 34.4	-56 07 33
3020	02 25.5	-50 16	-41	-13	I-II	59	18.9	0.0	1	6	02 27 16.0	-50 02 35
3021	02 25.9	-67 14	-55	150	II	36	17.6	0.0	0	5	02 26 53.3	-67 00 35

Table D.1 continued from previous page

ACO	RAB1950	DEB1950	Xcen	Ycen	BMtype	Count	m10	z	Rich	Dclass	_RA_icrs	_DE_icrs
3022	02 26.1	-24 39	-99	19	III	44	19.4	0.0	0	6	02 28 21.5	-24 25 37
3023	02 26.3	-28 27	96	83	III	34	19.5	0.0	0	6	02 28 30.1	-28 13 38
3024	02 26.3	-38 34	-103	76	III	57	18.3	0.0	1	6	02 28 19.9	-38 20 38
3025	02 27.2	-27 48	107	118	II-III	42	19.3	0.0	0	6	02 29 24.6	-27 34 40
3026	02 28.0	-37 01	41	-108	III	88	19.2	0.0	2	6	02 30 03.4	-36 47 42
3027	02 28.4	-33 19	48	90	III	44	16.1	0.0	0	4	02 30 31.2	-33 05 43
3028	02 28.7	-27 49	124	117	III	76	18.8	0.0	1	6	02 30 54.4	-27 35 44
3029	02 28.9	-38 55	-76	58	II	72	18.4	0.0	1	6	02 30 55.1	-38 41 44
3030	02 28.9	-49 22	-11	36	II	42	18.1	0.0	0	6	02 30 40.6	-49 08 44
3031	02 30.0	-56 15	-114	-69	III	66	19.5	0.0	1	6	02 31 32.9	-56 01 47
3032	02 32.4	-21 49	64	-98	III	45	19.1	0.0	0	6	02 34 41.2	-21 35 54
3033	02 34.2	-41 59	140	162	II-III	31	18.1	0.0	0	6	02 36 08.2	-41 45 59
3034	02 34.4	-32 43	-78	-144	I	51	19.3	0.0	1	6	02 36 30.9	-32 29 59
3035	02 35.0	-66 50	-112	-100	III	40	19.2	0.0	0	6	02 35 56.3	-66 36 59
3036	02 35.1	-45 34	-125	-31	III	62	18.8	0.0	1	6	02 36 57.0	-45 21 01
3037	02 36.0	-86 04	10	-58	II:	30	18.2	0.0	0	5	02 28 50.2	-85 50 51
3038	02 36.3	-52 37	-73	127	II:	60	18.0	0.0	1	6	02 37 56.6	-52 24 04
3039	02 38.1	-33 17	-113	91	II-III:	71	18.9	0.0	1	6	02 40 11.8	-33 04 10
3040	02 38.6	-55 38	-50	-32	II	69	17.3	0.0923	1	5	02 40 07.4	-55 25 10
3041	02 39.2	-28 51	-23	63	I-II	62	18.7	0.0	1	6	02 41 22.2	-28 38 13
3042	02 41.1	-27 07	0	156	I	77	18.4	0.0	1	6	02 43 17.6	-26 54 18
3043	02 41.5	-29 01	3	54	I	61	19.4	0.0	1	6	02 43 39.7	-28 48 19
3044	02 41.6	-28 05	5	104	II-III	65	17.5	0.0	1	5	02 43 46.6	-27 52 20
3045	02 42.0	-51 40	97	-90	II	32	16.7	0.0	0	5	02 43 38.8	-51 27 20
3046	02 43.4	-34 29	-53	29	III	51	18.2	0.0	1	6	02 45 27.7	-34 16 25
3047	02 43.4	-46 40	-46	-88	I	45	16.8	0.0	0	5	02 45 11.4	-46 27 24
3048	02 43.8	-20 41	-53	-36	III	110	19.5	0.0	2	6	02 46 05.2	-20 28 26
3049	02 43.9	-53 24	-11	85	III	46	19.4	0.0	0	6	02 45 28.7	-53 11 25
3050	02 44.2	-54 20	-8	37	II	50	19.4	0.0	1	6	02 45 44.6	-54 07 26
3051	02 44.7	-57 51	85	114	III	43	18.9	0.0	0	6	02 46 05.8	-57 38 27
3052	02 45.2	-27 46	49	120	I	44	17.5	0.0	0	5	02 47 22.5	-27 33 30
3053	02 45.3	-34 10	-32	46	III	70	18.4	0.0	1	6	02 47 21.8	-33 57 30
3054	02 46.5	-27 57	64	110	I-II	31	17.0	0.0	0	5	02 48 40.2	-27 44 34
3055	02 46.6	-48 01	-124	107	I-II	40	17.8	0.0	0	5	02 48 20.4	-47 48 33
3056	02 47.4	-28 10	74	99	I	81	19.3	0.0	2	6	02 49 33.9	-27 57 36
3057	02 47.5	-48 37	-112	73	II	31	18.3	0.0	0	6	02 49 13.1	-48 24 36
3058	02 48.8	-55 09	26	-6	III?	54	19.4	0.0	1	6	02 50 17.3	-54 56 39
3059	02 49.2	-46 31	7	-80	I-II	40	17.4	0.0	0	5	02 50 58.3	-46 18 41
3060	02 49.9	-48 54	-93	60	II-III	42	18.0	0.0	0	6	02 51 36.0	-48 41 43
3061	02 50.0	-64 56	-36	6	II	44	18.8	0.0	0	6	02 50 57.4	-64 43 42
3062	02 50.2	-25 35	-72	-30	II-III	48	18.1	0.0	0	6	02 52 24.1	-25 22 45
3063	02 50.2	-36 56	22	-103	III	67	18.0	0.0	1	6	02 52 11.7	-36 43 44
3064	02 51.2	-33 40	32	72	II-III	74	19.4	0.0	1	6	02 53 15.5	-33 27 47
3065	02 51.3	-53 46	47	67	III?	80	18.6	0.0	2	6	02 52 49.8	-53 33 47
3066	02 52.8	-79 16	-19	41	III	44	19.1	0.0	0	6	02 51 23.5	-79 03 47
3067	02 53.1	-54 19	61	37	III	88	18.0	0.0	2	6	02 54 36.0	-54 06 52
3068	02 53.5	-44 32	48	26	II	61	18.6	0.0	1	6	02 55 18.6	-44 19 54
3069	02 53.7	-22 52	-29	115	I-II	43	18.1	0.0	0	6	02 55 56.4	-22 39 55
3070	02 54.4	-24 55	-21	5	I	53	17.5	0.0	1	5	02 56 36.3	-24 42 57
3071	02 55.2	-47 12	-47	152	I-II	40	19.4	0.0	0	6	02 56 55.8	-46 59 59
3072	02 55.6	-47 48	64	-149	III	37	18.8	0.0	0	6	02 57 18.6	-47 36 00
3073	02 55.9	-21 16	97	-68	III	43	18.1	0.0	0	5	02 58 09.7	-21 04 02
3074	02 56.4	-52 55	85	111	II	31	16.3	0.0	0	5	02 57 56.2	-52 43 02
3075	02 56.8	-23 12	9	97	I-II	38	19.4	0.0	0	6	02 59 01.8	-23 00 05
3076	02 57.0	-45 15	81	-13	I-II	49	18.6	0.0	0	6	02 58 46.7	-45 03 05
3077	02 58.3	-51 39	-18	-86	II	36	17.2	0.0	0	5	02 59 52.5	-51 27 08

Table D.1 continued from previous page

ACO	RAB1950	DEB1950	Xcen	Ycen	BMtype	Count	m10	z	Rich	Dclass	_RA_icrs	_DE_icrs
3078	02 58.9	-52 02	-14	-107	I	40	16.8	0.06	0	5	03 00 27.5	-51 50 10
3079	02 59.2	-44 35	104	22	I-II	39	19.3	0.0	0	6	03 00 59.3	-44 23 11
3080	02 59.7	-66 15	18	-66	I-II	36	18.1	0.0	0	6	03 00 28.8	-66 03 11
3081	03 00.2	-41 10	-21	-62	I-II	37	19.2	0.0	0	6	03 02 04.4	-40 58 15
3082	03 01.2	-27 49	-35	118	II-III	91	18.7	0.0	2	6	03 03 20.7	-27 37 18
3083	03 01.8	-22 34	71	130	I	40	19.5	0.0	0	6	03 04 02.0	-22 22 20
3084	03 02.1	-37 09	-109	-115	I-II	58	19.0	0.0	1	6	03 04 03.6	-36 57 21
3085	03 02.2	-49 07	15	49	III	56	18.6	0.0	1	6	03 03 50.6	-48 55 20
3086	03 02.6	-24 50	78	8	III	43	18.6	0.0	0	6	03 04 47.6	-24 38 23
3087	03 03.8	-29 58	-4	3	I-II	41	18.5	0.0	0	6	03 05 54.0	-29 46 26
3088	03 04.9	-28 52	9	62	I-II	83	18.6	0.0	2	6	03 07 01.1	-28 40 30
3089	03 06.2	-36 54	-64	-102	I-II	30	15.6	0.0	0	4	03 08 09.3	-36 42 34
3090	03 06.8	-48 25	57	86	I-II	34	18.6	0.0	0	6	03 08 26.9	-48 13 35
3091	03 07.2	-29 13	36	42	II-III	56	18.1	0.0	1	6	03 09 18.5	-29 01 37
3092	03 07.3	-65 46	60	-41	II	40	18.0	0.0	0	6	03 08 03.8	-65 34 35
3093	03 09.2	-47 35	80	129	I	93	16.2	0.0585	2	4	03 10 52.0	-47 23 43
3094	03 09.3	-27 07	-109	-111	I-II	80	16.1	0.0	2	4	03 11 26.6	-26 55 44
3095	03 10.3	-27 20	-96	-123	I-II	49	16.1	0.0	0	4	03 12 26.2	-27 08 47
3096	03 10.3	-44 29	-56	30	II	35	17.6	0.0	0	5	03 12 03.3	-44 17 46
3097	03 11.1	-63 18	90	90	III	36	19.1	0.0	0	6	03 12 01.6	-63 06 48
3098	03 11.8	-38 30	101	79	I	38	16.7	0.0	0	5	03 13 42.3	-38 18 52
3099	03 12.1	-58 54	10	61	II-III	69	18.8	0.0	1	6	03 13 17.5	-58 42 51
3100	03 12.2	-47 59	106	108	I	46	15.9	0.0	0	4	03 13 50.6	-47 47 52
3101	03 12.3	-32 23	1	140	III	110	19.5	0.0	2	6	03 14 20.2	-32 11 53
3102	03 12.5	-44 49	-35	13	I-II	33	18.0	0.0	0	6	03 14 14.3	-44 37 54
3103	03 12.5	-69 23	-77	33	II-III	30	18.0	0.0	0	6	03 12 52.0	-69 11 51
3104	03 12.6	-45 36	-33	-30	I	37	16.0	0.0	0	4	03 14 18.9	-45 24 54
3105	03 12.7	-42 41	-33	127	II-III	52	18.7	0.0	1	6	03 14 29.8	-42 29 54
3106	03 13.3	-58 17	19	94	I-II	44	17.5	0.0645	0	5	03 14 31.1	-58 05 55
3107	03 13.6	-42 57	-24	112	II	61	16.8	0.0	1	5	03 15 23.2	-42 45 57
3108	03 13.6	-47 49	-150	116	II	73	16.0	0.0632	1	4	03 15 14.6	-47 37 57
3109	03 14.9	-44 02	-12	54	I	32	16.8	0.0673	0	5	03 16 39.2	-43 51 02
3110	03 15.0	-51 05	122	-60	I-II	37	16.0	0.0755	0	4	03 16 31.5	-50 54 01
3111	03 16.1	-45 55	-1	-46	I-II	54	16.1	0.0	1	4	03 17 47.7	-45 44 05
3112	03 16.2	-44 25	0	34	I	116	15.9	0.0703	2	4	03 17 56.3	-44 14 06
3113	03 16.2	-49 00	-124	53	I	55	17.6	0.0	1	5	03 17 47.7	-48 49 06
3114	03 16.4	-39 18	-122	36	I-II	45	18.1	0.0	0	6	03 18 16.4	-39 07 07
3115	03 16.9	-20 56	96	-50	II	40	18.5	0.0	0	6	03 19 08.4	-20 45 09
3116	03 17.2	-43 07	11	103	I-II	47	17.8	0.0	0	5	03 18 58.3	-42 56 09
3117	03 19.2	-72 09	-41	-114	II	32	18.0	0.0	0	5	03 19 08.1	-71 58 13
3118	03 19.5	-34 22	80	34	III	43	17.7	0.0	0	5	03 21 28.8	-34 11 17
3119	03 19.5	-68 16	-46	94	II-III	41	18.0	0.0	0	6	03 19 56.0	-68 05 15
3120	03 20.4	-51 30	-83	-80	I	40	17.3	0.0696	0	5	03 21 53.3	-51 19 19
3121	03 20.4	-70 40	-38	-34	II	38	18.0	0.0	0	6	03 20 32.3	-70 29 17
3122	03 20.5	-41 31	-77	-81	I-II	100	15.6	0.0	2	4	03 22 18.3	-41 20 20
3123	03 21.5	-52 12	-74	-117	I-II	37	16.0	0.065	0	4	03 22 57.4	-52 01 23
3124	03 21.6	-44 41	52	18	III	39	18.2	0.0	0	6	03 23 18.8	-44 30 24
3125	03 26.0	-53 41	63	123	III	46	15.6	0.0593	0	4	03 27 22.6	-53 30 38
3126	03 27.4	-55 53	67	-47	III	75	16.8	0.0862	1	5	03 28 40.3	-55 42 43
3127	03 27.5	-17 27	-33	139	II-III	93	19.5	0.0	2	6	03 29 47.2	-17 16 45
3128	03 28.8	-52 44	88	122	I-II	140	15.1	0.0554	3	3	03 30 12.4	-52 33 48
3129	03 29.7	-30 46	28	-38	III	55	17.8	0.0	1	5	03 31 44.2	-30 35 52
3130	03 30.0	-47 16	-3	148	III	36	18.0	0.0	0	6	03 31 36.4	-47 05 52
3131	03 30.1	-51 14	-2	-65	II	31	18.0	0.0	0	6	03 31 33.7	-51 03 53
3132	03 30.5	-44 22	-131	33	II:	56	18.2	0.0	1	5	03 32 11.8	-44 11 54
3133	03 31.1	-46 07	-116	-61	III	33	16.0	0.0	0	4	03 32 44.4	-45 56 56

Table D.1 continued from previous page

ACO	RAB1950	DEB1950	Xcen	Ycen	BMtype	Count	m10	z	Rich	Dclass	_RA_icrs	_DE_icrs
3134	03 31.5	-40 57	34	-51	II-III	50	17.8	0.0	1	5	03 33 17.5	-40 46 58
3135	03 32.2	-39 10	43	44	II	111	15.3	0.0	2	3	03 34 02.2	-39 00 01
3136	03 32.4	-72 00	14	-106	II	68	17.9	0.1203	1	5	03 32 14.1	-71 49 58
3137	03 33.0	-18 16	36	95	II-III	46	18.3	0.0	0	6	03 35 16.1	-18 06 04
3138	03 33.2	-34 42	-35	18	III	32	19.2	0.0	0	6	03 35 08.6	-34 32 04
3139	03 34.4	-23 49	-71	63	II-III:	100	19.6	0.0	2	6	03 36 34.0	-23 39 09
3140	03 34.5	-40 48	64	-43	I-II	45	18.2	0.0	0	6	03 36 17.3	-40 38 09
3141	03 34.9	-28 13	90	99	II-III	55	16.6	0.0	1	5	03 36 58.8	-28 03 11
3142	03 34.9	-39 58	70	2	I-II	78	16.7	0.0	1	5	03 36 42.6	-39 48 10
3143	03 35.3	-71 38	26	-86	I-II	32	18.1	0.0	0	6	03 35 10.1	-71 28 08
3144	03 35.8	-55 11	-118	-8	I-II	54	15.6	0.0423	1	4	03 37 04.1	-55 01 12
3145	03 36.0	-38 11	83	97	II-III	36	17.8	0.0	0	5	03 37 51.2	-38 01 14
3146	03 36.4	-33 21	0	91	II	35	17.1	0.0	0	5	03 38 22.1	-33 11 16
3147	03 36.4	-62 45	-23	122	I-II	47	19.2	0.0	0	6	03 37 12.9	-62 35 14
3148	03 36.7	-32 53	6	117	I	83	17.4	0.0	2	5	03 38 40.7	-32 43 17
3149	03 36.9	-69 45	37	15	III	31	19.3	0.0	0	6	03 37 01.4	-69 35 14
3150	03 37.5	-33 23	13	89	I-II	55	19.5	0.0	1	6	03 39 28.0	-33 13 20
3151	03 38.4	-28 52	131	63	I-II	52	15.9	0.0	1	4	03 40 27.7	-28 42 23
3152	03 38.4	-32 44	24	124	I-II	51	16.8	0.0	1	5	03 40 22.7	-32 34 23
3153	03 39.1	-34 25	31	34	I-II	64	16.8	0.0	1	5	03 41 02.3	-34 15 25
3154	03 40.0	-32 13	41	151	II-III	48	16.1	0.0	0	4	03 41 59.3	-32 03 29
3155	03 40.3	-70 15	51	-13	I-II	33	18.1	0.0	0	6	03 40 19.8	-70 05 26
3156	03 40.6	-31 06	-110	-56	III	77	18.6	0.0	1	6	03 42 36.7	-30 56 31
3157	03 41.5	-30 06	-100	-2	I-II?	106	18.6	0.209	2	6	03 43 31.9	-29 56 34
3158	03 41.7	-53 48	-75	68	I-II	85	15.6	0.059	2	4	03 43 00.6	-53 38 33
3159	03 42.1	-32 51	65	117	I-II	98	16.9	0.0	2	5	03 44 04.2	-32 41 36
3160	03 42.9	-22 36	35	128	III	59	18.7	0.0	1	6	03 45 04.8	-22 26 39
3161	03 43.0	-35 48	73	-42	II	36	16.2	0.0	0	4	03 44 53.9	-35 38 39
3162	03 43.1	-29 34	-81	26	II-III	77	18.8	0.0	1	6	03 45 08.4	-29 24 40
3163	03 44.3	-51 40	115	-91	I-II	43	18.9	0.0	0	6	03 45 41.7	-51 30 43
3164	03 44.7	-57 12	-49	-113	I-II	33	15.5	0.0611	0	4	03 45 49.7	-57 02 44
3165	03 44.8	-29 11	-62	48	III	31	17.2	0.0	0	5	03 46 50.7	-29 01 46
3166	03 44.8	-32 58	95	110	I	79	17.3	0.0	1	5	03 46 45.7	-32 48 46
3167	03 45.7	-28 35	-53	78	I	51	19.2	0.0	1	6	03 47 45.4	-28 25 49
3168	03 45.9	-21 55	71	166	II-III	100	19.3	0.0	2	6	03 48 05.3	-21 45 50
3169	03 46.4	-33 38	112	74	I-II	101	17.4	0.0	2	5	03 48 20.6	-33 28 52
3170	03 46.6	-53 59	-36	59	III	53	18.9	0.0	1	6	03 47 53.0	-53 49 51
3171	03 46.7	-34 12	115	43	I	65	17.5	0.0	1	5	03 48 37.8	-34 02 53
3172	03 47.0	-39 03	-75	52	III	90	18.2	0.0	2	6	03 48 48.4	-38 53 54
3173	03 47.3	-33 53	122	60	II-III	35	16.8	0.0	0	5	03 49 14.2	-33 43 55
3174	03 47.8	-17 39	-43	128	II-III	68	18.6	0.0	1	6	03 50 03.9	-17 29 57
3175	03 48.0	-18 11	-40	99	I-II	64	18.0	0.0	1	6	03 50 15.4	-18 01 58
3176	03 48.8	-27 30	-15	136	II-III	62	18.6	0.0	1	6	03 50 52.5	-27 21 01
3177	03 48.9	-23 17	-163	91	II:	49	18.2	0.0	0	6	03 51 03.6	-23 08 01
3178	03 49.5	-20 07	-21	-5	I-II	52	19.1	0.0	1	6	03 51 43.1	-19 58 04
3179	03 50.8	-48 45	-83	68	III	41	18.0	0.0	0	6	03 52 17.4	-48 36 07
3180	03 51.0	-39 05	-33	51	III	110	18.7	0.0	2	6	03 52 47.8	-38 56 08
3181	03 51.7	-30 50	18	-43	III	71	18.2	0.0	1	6	03 53 42.0	-30 41 11
3182	03 52.4	-31 10	24	-60	II-III	52	17.3	0.0	1	5	03 54 23.4	-31 01 14
3183	03 52.5	-32 10	25	-113	III	40	17.0	0.0	0	5	03 54 28.1	-32 01 14
3184	03 52.7	-37 53	-15	115	II-III	96	19.6	0.0	2	6	03 54 31.6	-37 44 15
3185	03 52.8	-18 38	21	74	II-III	80	19.3	0.0	2	6	03 55 02.6	-18 29 16
3186	03 53.1	-74 09	-117	41	I-II	62	18.3	0.0	1	5	03 52 20.7	-74 00 11
3187	03 55.3	-28 12	60	100	III	57	18.8	0.0	1	6	03 57 21.1	-28 03 25
3188	03 55.7	-27 11	66	153	III	67	17.0	0.0	1	5	03 57 46.4	-27 02 26
3189	03 56.0	-39 45	18	15	II:	65	19.6	0.0	1	6	03 57 46.1	-39 36 27

Table D.1 continued from previous page

ACO	RAB1950	DEB1950	Xcen	Ycen	BMtype	Count	m10	z	Rich	Dclass	_RA_icrs	_DE_icrs
3190	03 56.3	-22 31	63	-134	II-III	85	19.4	0.0	2	6	03 58 28.0	-22 22 29
3191	03 56.3	-62 58	99	106	II-III	33	17.2	0.0	0	5	03 56 59.6	-62 49 26
3192	03 56.7	-30 03	75	-1	II	141	17.1	0.0	3	5	03 58 42.6	-29 54 30
3193	03 56.9	-52 29	-28	-131	I	41	15.4	0.034	0	3	03 58 13.0	-52 20 29
3194	03 57.2	-30 19	79	-15	III	83	16.5	0.0	2	5	03 59 12.2	-30 10 32
3195	03 57.3	-35 19	-30	-21	III	30	16.6	0.0	0	5	03 59 11.0	-35 10 32
3196	03 57.6	-20 07	80	-5	II	41	18.0	0.0	0	6	03 59 48.7	-19 58 34
3197	03 58.0	-30 34	89	-28	II	62	17.5	0.0	1	5	03 59 59.7	-30 25 35
3198	03 58.6	-27 45	100	122	II	50	18.3	0.0	1	6	04 00 39.4	-27 36 37
3199	03 58.8	-24 01	-41	53	II-III	46	18.8	0.0	0	6	04 00 56.1	-23 52 38
3200	03 58.8	-31 18	97	-69	III	91	17.5	0.0	2	5	04 00 46.7	-31 09 38
3201	03 59.0	-19 47	99	12	II-III	47	18.6	0.0	0	6	04 01 13.0	-19 38 39
3202	03 59.0	-53 48	61	67	II	65	15.6	0.0388	1	4	04 00 14.9	-53 39 37
3203	03 59.7	-33 12	-4	96	III	80	18.8	0.0	2	6	04 01 37.9	-33 03 41
3204	03 59.9	-46 57	-112	-105	II-III	32	17.7	0.0	0	5	04 01 25.8	-46 48 41
3205	04 00.2	-26 57	121	164	II-III?	54	17.5	0.0	1	5	04 02 16.3	-26 48 43
3206	04 00.4	-79 04	-76	47	II	32	18.0	0.0	0	5	03 58 00.7	-78 55 36
3207	04 00.8	-27 20	127	143	II-III	77	19.2	0.212	1	6	04 02 51.8	-27 11 46
3208	04 00.9	-27 20	-17	-125	II-III	81	18.9	0.0	2	6	04 02 57.8	-27 11 46
3209	04 01.5	-53 39	82	74	III	32	19.3	0.0	0	6	04 02 44.9	-53 30 47
3210	04 01.5	-56 26	76	-75	I-II	61	18.4	0.0	1	6	04 02 36.3	-56 17 46
3211	04 01.6	-27 12	136	150	III	37	18.8	0.0	0	6	04 03 39.9	-27 03 49
3212	04 02.0	-33 13	21	95	II-III	95	18.0	0.0	2	6	04 03 55.7	-33 04 50
3213	04 02.2	-27 10	-1	-118	II-III	69	19.2	0.0	1	6	04 04 15.9	-27 01 51
3214	04 03.1	-41 37	89	-86	III	55	19.1	0.0	1	6	04 04 48.0	-41 28 54
3215	04 03.2	-53 01	23	-160	II-III	39	18.0	0.0	0	6	04 04 28.4	-52 52 53
3216	04 03.7	-65 21	-116	-22	II-III	92	18.0	0.0	2	6	04 04 08.8	-65 12 54
3217	04 04.5	-30 41	-101	-36	III	54	18.8	0.0	1	6	04 06 29.0	-30 33 00
3218	04 05.6	-27 06	39	-112	II-III	60	19.4	0.0	1	6	04 07 39.7	-26 58 04
3219	04 05.6	-65 44	-104	-40	II-III	62	18.7	0.0	1	6	04 05 59.9	-65 36 01
3220	04 06.2	-78 49	-62	62	III	53	18.0	0.0	1	5	04 03 51.2	-78 40 58
3221	04 06.4	-27 26	-80	139	II-III	44	19.3	0.0	0	6	04 08 27.2	-27 18 07
3222	04 06.6	-27 39	-79	126	II-III	102	19.4	0.0	2	6	04 08 38.9	-27 31 08
3223	04 06.6	-30 57	-76	-51	I	100	15.4	0.0	2	3	04 08 34.5	-30 49 08
3224	04 07.2	-27 36	-71	129	III	40	19.3	0.0	0	6	04 09 15.0	-27 28 10
3225	04 08.4	-59 44	-122	13	II	37	15.6	0.0433	0	4	04 09 16.7	-59 36 13
3226	04 09.6	-28 09	-42	100	III	64	18.1	0.0	1	6	04 11 38.1	-28 01 19
3227	04 09.6	-45 14	-24	-12	III	52	19.3	0.0	1	6	04 11 10.1	-45 06 19
3228	04 09.7	-48 59	84	55	I-II	60	18.8	0.0	1	6	04 11 07.7	-48 51 19
3229	04 10.5	-62 51	-100	-154	I-II	42	16.8	0.0	0	5	04 11 08.3	-62 43 20
3230	04 11.0	-63 49	-80	64	II	112	18.0	0.0	2	6	04 11 33.2	-63 41 22
3231	04 11.4	-64 44	-75	14	II	65	18.2	0.057	1	6	04 11 52.0	-64 36 23
3232	04 11.9	-35 28	-134	-25	II	40	18.0	0.0	0	6	04 13 45.3	-35 20 28
3233	04 12.0	-45 17	-1	-14	III	70	19.4	0.0	1	6	04 13 33.6	-45 09 28
3234	04 12.0	-46 01	-2	-53	II-III	31	17.3	0.0	0	5	04 13 32.1	-45 53 28
3235	04 12.6	-45 41	1	-34	II	69	18.4	0.0	1	6	04 14 08.7	-45 33 30
3236	04 12.7	-46 20	5	-70	II	64	18.8	0.0	1	6	04 14 13.3	-46 12 31
3237	04 14.5	-32 20	-108	144	II	69	18.7	0.0	1	6	04 16 25.9	-32 12 38
3238	04 15.3	-42 37	32	128	II-III	43	18.2	0.0	0	6	04 16 56.6	-42 29 41
3239	04 15.7	-39 04	-46	53	II-III?	81	18.4	0.0	2	6	04 17 27.0	-38 56 43
3240	04 15.9	-45 20	35	-17	II-III?	71	18.8	0.0	1	6	04 17 27.0	-45 12 43
3241	04 16.5	-64 55	-51	4	I:	54	17.7	0.0	1	5	04 16 55.6	-64 47 43
3242	04 16.7	-63 43	-52	70	II-III	49	17.8	0.0	0	5	04 17 14.2	-63 35 44
3243	04 17.2	-42 32	51	133	III	67	18.7	0.0	1	6	04 18 50.5	-42 24 48
3244	04 17.8	-60 56	-57	-51	II-III	34	18.0	0.0	0	6	04 18 33.4	-60 48 49
3245	04 17.9	-45 12	54	-10	II-III	64	18.2	0.0	1	6	04 19 27.0	-45 04 51

Table D.1 continued from previous page

ACO	RAB1950	DEB1950	Xcen	Ycen	BMtype	Count	m10	z	Rich	Dclass	_RA_icrs	_DE_icrs
3246	04 19.6	-46 03	69	-56	III	50	18.0	0.0	1	6	04 21 07.0	-45 55 58
3247	04 19.7	-46 36	69	-85	II-III	52	17.7	0.0	1	5	04 21 11.8	-46 28 58
3248	04 20.6	-65 10	-23	-7	III	67	18.1	0.0	1	6	04 20 59.0	-65 02 59
3249	04 20.7	-18 57	-158	58	III	38	19.3	0.0	0	6	04 22 54.9	-18 50 04
3250	04 20.8	-33 22	-36	89	I-II	41	18.1	0.0	0	6	04 22 41.8	-33 15 03
3251	04 22.1	-63 55	-15	59	II-III	74	18.4	0.0	1	6	04 22 35.7	-63 48 06
3252	04 22.2	-46 13	93	-66	II-III	80	18.7	0.0	2	6	04 23 42.3	-46 06 08
3253	04 23.6	-36 20	-7	-70	II	70	17.8	0.0	1	5	04 25 24.9	-36 13 14
3254	04 24.0	-46 51	108	-99	II:	44	18.3	0.0	0	5	04 25 28.7	-46 44 15
3255	04 25.7	-46 31	125	-83	II:	43	18.2	0.0	0	6	04 27 11.2	-46 24 22
3256	04 26.0	-36 11	20	-62	I-II	43	17.4	0.0	0	5	04 27 48.9	-36 04 24
3257	04 26.1	-34 08	22	47	I-II	94	18.0	0.0	2	6	04 27 58.2	-34 01 24
3258	04 26.2	-44 45	132	12	I-II	53	19.4	0.0	1	6	04 27 45.0	-44 38 24
3259	04 27.0	-38 13	73	98	III	130	17.9	0.0	3	5	04 28 45.4	-38 06 28
3260	04 28.2	-21 07	-64	-58	III	42	19.1	0.0	0	6	04 30 22.0	-21 00 33
3261	04 28.5	-60 26	12	-23	III	86	18.9	0.0	2	6	04 29 15.4	-60 19 32
3262	04 28.7	-37 18	48	-123	II	50	19.0	0.0	1	6	04 30 28.8	-37 11 35
3263	04 28.9	-38 11	93	99	III	94	18.1	0.0	2	6	04 30 39.3	-38 04 35
3264	04 30.1	-49 25	-1	34	II	53	16.5	0.0	1	5	04 31 27.7	-49 18 39
3265	04 30.4	-36 43	67	-92	I	71	17.5	0.0	1	5	04 32 11.7	-36 36 42
3266	04 30.5	-61 35	24	-84	I-II	91	15.3	0.0594	2	3	04 31 09.7	-61 28 40
3267	04 31.0	-34 09	76	45	I-II	81	18.4	0.0	2	6	04 32 51.8	-34 02 44
3268	04 31.0	-35 41	75	-37	I-II	88	17.3	0.0	2	5	04 32 49.3	-35 34 44
3269	04 31.1	-32 41	79	124	II	36	16.6	0.0	0	5	04 33 00.1	-32 34 45
3270	04 31.5	-45 57	-77	-49	II-III	52	19.3	0.0	1	6	04 32 59.8	-45 50 45
3271	04 31.8	-49 39	13	21	I-II	74	18.0	0.0	1	6	04 33 08.9	-49 32 46
3272	04 31.8	-59 48	34	10	II-III	65	18.6	0.0	1	6	04 32 35.5	-59 41 45
3273	04 32.0	-36 07	85	-60	II-III	35	18.0	0.0	0	6	04 33 48.5	-36 00 48
3274	04 32.2	-35 29	88	-26	I-II	34	18.0	0.0	0	6	04 34 01.6	-35 22 49
3275	04 32.2	-35 49	87	-44	II-III	41	17.5	0.0	0	5	04 34 01.0	-35 42 49
3276	04 33.2	-34 03	101	50	I-II	70	18.2	0.0	1	6	04 35 03.8	-33 56 53
3277	04 33.9	-35 45	106	-42	II-III	58	18.3	0.0	1	6	04 35 43.0	-35 38 56
3278	04 34.8	-58 06	58	100	II-III?	68	17.8	0.0	1	5	04 35 41.8	-57 59 58
3279	04 36.4	-46 10	-31	-61	II-III	40	17.7	0.0	0	5	04 37 52.7	-46 04 05
3280	04 36.5	-49 05	55	50	III	64	18.3	0.0	1	6	04 37 51.7	-48 59 05
3281	04 39.4	-38 24	-72	88	I-II	54	18.8	0.0	1	6	04 41 08.0	-38 18 18
3282	04 39.5	-45 17	-2	-13	I-II	56	18.3	0.0	1	6	04 41 00.4	-45 11 18
3283	04 39.7	-48 36	84	76	III	41	19.1	0.0	0	6	04 41 04.6	-48 30 19
3284	04 39.8	-45 09	1	-6	I	64	19.1	0.0	1	6	04 41 18.7	-45 03 19
3285	04 40.6	-37 27	-59	138	II-III	30	17.6	0.0	0	5	04 42 21.6	-37 21 23
3286	04 41.9	-24 48	-53	13	II-III:	63	18.9	0.0	1	5	04 43 58.7	-24 42 29
3287	04 42.5	-61 48	100	-101	III:	74	19.0	0.0	1	6	04 43 06.3	-61 42 29
3288	04 42.7	-18 07	122	101	III	48	18.0	0.0	0	5	04 44 55.1	-18 01 33
3289	04 43.1	-33 34	-57	77	I	41	17.6	0.0	0	5	04 44 57.9	-33 28 34
3290	04 45.9	-44 58	58	3	II-III	40	18.1	0.0	0	6	04 47 24.5	-44 52 45
3291	04 46.1	-39 53	-2	8	II-III	47	18.5	0.0	0	6	04 47 46.8	-39 47 46
3292	04 48.4	-44 46	83	13	I-II	67	18.7	0.0	1	6	04 49 54.7	-44 40 55
3293	04 51.0	-34 52	31	7	I-II	42	19.3	0.0	0	6	04 52 49.3	-34 47 06
3294	04 51.3	-62 49	-80	-152	III:	63	18.0	0.0	1	5	04 51 47.6	-62 44 05
3295	04 51.6	-32 01	40	160	I	54	17.5	0.0	1	5	04 53 29.8	-31 56 09
3296	04 53.4	-36 18	56	-70	I-II	61	17.8	0.0	1	5	04 55 10.7	-36 13 16
3297	04 56.4	-30 13	-34	-10	III	112	17.1	0.0	2	5	04 58 20.3	-30 08 29
3298	04 57.4	-57 46	-48	119	III	58	19.2	0.0	1	6	04 58 15.8	-57 41 31
3299	04 57.7	-88 51	-62	-14	II	39	18.0	0.0	0	5	04 10 43.2	-88 44 51
3300	04 57.9	-24 44	-125	14	II-III:	55	18.8	0.0	1	5	04 59 58.1	-24 39 36
3301	04 59.1	-38 45	135	65	I	172	15.4	0.0	3	3	05 00 48.0	-38 40 40

Table D.1 continued from previous page

ACO	RAB1950	DEB1950	Xcen	Ycen	BMtype	Count	m10	z	Rich	Dclass	_RA_icrs	_DE_icrs
3302	04 59.4	-49 07	-7	48	III	55	19.5	0.0	1	6	05 00 43.3	-49 02 41
3303	04 59.8	-51 21	-4	-71	II-III	77	17.6	0.0	1	5	05 01 01.1	-51 16 42
3304	04 59.9	-35 55	126	-51	II-III	70	18.8	0.0	1	5	05 01 41.0	-35 50 44
3305	05 00.2	-39 17	-123	38	I-II	85	18.9	0.0	2	5	05 01 52.9	-39 12 45
3306	05 01.2	-49 36	7	21	II-III?	108	18.0	0.0	2	5	05 02 29.8	-49 31 48
3307	05 01.8	-29 40	29	18	I	63	17.8	0.0	1	5	05 03 44.9	-29 35 52
3308	05 01.9	-29 17	31	39	III	65	19.5	0.0	1	6	05 03 51.5	-29 12 53
3309	05 02.0	-34 01	153	49	I-II	46	18.4	0.0	0	5	05 03 50.1	-33 56 53
3310	05 02.6	-33 18	-107	90	III	71	18.9	0.0	1	5	05 04 27.2	-33 13 55
3311	05 02.9	-49 33	22	24	II-III	49	18.5	0.0	0	5	05 04 11.8	-49 28 55
3312	05 03.0	-57 00	42	-109	III	118	17.1	0.0	2	5	05 03 54.1	-56 55 55
3313	05 03.4	-32 25	-101	138	II-III	64	18.1	0.0	1	5	05 05 16.6	-32 20 59
3314	05 04.3	-45 33	-39	-28	II-III	52	18.7	0.0	1	5	05 05 45.6	-45 29 02
3315	05 05.5	-29 42	72	15	I-II	40	19.4	0.0	0	6	05 07 26.7	-29 38 08
3316	05 05.5	-47 49	48	116	I-II?	63	18.8	0.0	1	5	05 06 52.1	-47 45 07
3317	05 06.0	-49 11	50	43	III	49	18.2	0.0	0	5	05 07 18.5	-49 07 09
3318	05 06.7	-28 29	87	81	II-III	74	18.6	0.0	1	5	05 08 40.5	-28 25 13
3319	05 07.0	-25 06	-13	-5	III	55	18.6	0.0	1	5	05 09 03.3	-25 02 15
3320	05 07.1	-56 34	73	-86	III	40	19.6	0.0	0	6	05 08 01.3	-56 30 13
3321	05 08.1	-36 12	-45	-64	III	74	19.6	0.0	1	6	05 09 52.1	-36 08 19
3322	05 09.1	-45 23	6	-19	I	75	18.9	0.0	1	5	05 10 33.7	-45 19 22
3323	05 09.4	-29 03	-149	51	I	42	16.1	0.0	0	4	05 11 21.5	-28 59 25
3324	05 10.2	-44 16	17	41	I-II	37	18.6	0.0	0	5	05 11 42.2	-44 12 27
3325	05 11.5	-30 09	-123	-8	II	32	17.7	0.0	0	5	05 13 25.8	-30 05 34
3326	05 11.5	-49 45	97	11	II:	65	19.2	0.0	1	6	05 12 46.6	-49 41 32
3327	05 12.2	-39 13	1	43	I-II	41	18.1	0.0	0	5	05 13 52.4	-39 09 36
3328	05 12.3	-42 22	39	143	II	62	18.5	0.0	1	5	05 13 52.1	-42 18 36
3329	05 13.2	-44 47	46	13	I	58	18.6	0.0	1	5	05 14 40.8	-44 43 40
3330	05 13.4	-49 07	115	45	II	52	17.0	0.0903	1	5	05 14 42.2	-49 03 40
3331	05 14.0	-50 24	-138	-24	II	35	17.7	0.0	0	5	05 15 14.6	-50 20 43
3332	05 15.0	-42 16	29	-120	I	45	17.4	0.0	0	5	05 16 34.2	-42 12 48
3333	05 16.0	-86 46	16	-95	II	32	19.4	0.0	0	6	04 59 32.0	-86 42 13
3334	05 17.2	-58 36	91	73	I-II	82	16.9	0.0953	2	5	05 17 58.2	-58 32 55
3335	05 19.9	-31 03	-26	-54	II	59	18.4	0.0	1	5	05 21 48.1	-31 00 10
3336	05 19.9	-40 52	79	-46	I	33	16.6	0.0	0	5	05 21 30.8	-40 49 09
3337	05 20.8	-49 14	-82	42	III	30	19.1	0.0	0	6	05 22 05.4	-49 11 12
3338	05 21.3	-48 19	-79	90	II-III	31	17.3	0.0446	0	5	05 22 37.8	-48 16 14
3339	05 22.8	-27 03	-90	-109	III	55	19.6	0.0	1	6	05 24 48.1	-27 00 22
3340	05 23.5	-30 57	15	-49	I-II	87	18.4	0.0	2	5	05 25 24.2	-30 54 25
3341	05 23.7	-31 38	17	-86	II	87	14.6	0.0	2	2	05 25 35.1	-31 35 26
3342	05 24.0	-30 38	21	-32	I-II	85	18.9	0.0	2	5	05 25 54.7	-30 35 27
3343	05 24.5	-47 15	-107	-124	I-II	64	18.2	0.0	1	5	05 25 52.3	-47 12 28
3344	05 24.6	-30 32	28	-27	I	69	19.0	0.0	1	5	05 26 30.8	-30 29 30
3345	05 25.7	-47 52	-40	116	II	40	19.3	0.0	0	6	05 27 02.7	-47 49 33
3346	05 25.9	-47 24	-93	-129	I-II	86	19.0	0.0	2	5	05 27 15.9	-47 21 34
3347	05 26.2	-47 11	-37	152	I-II	112	18.2	0.0	2	5	05 27 34.4	-47 08 36
3348	05 26.8	-47 40	-31	126	I-II	74	18.4	0.0	1	5	05 28 09.2	-47 37 38
3349	05 28.2	-47 26	-72	-130	II	81	17.8	0.0	2	5	05 29 33.7	-47 23 44
3350	05 29.4	-49 58	-6	3	III	30	17.9	0.0	0	5	05 30 38.9	-49 55 49
3351	05 30.1	-38 24	-83	87	II-III	114	16.1	0.0	2	4	05 31 47.2	-38 21 53
3352	05 30.9	-47 36	6	131	II-III	83	18.9	0.0	2	5	05 32 15.2	-47 33 56
3353	05 31.5	-29 01	110	53	I-II	39	19.2	0.0	0	6	05 33 27.0	-28 59 00
3354	05 32.7	-28 32	125	80	II	54	15.3	0.0	1	3	05 34 39.7	-28 30 05
3355	05 32.9	-32 20	-35	143	III	46	18.8	0.0	0	5	05 34 45.7	-32 18 06
3356	05 33.3	-38 10	-49	99	II	30	15.9	0.0	0	4	05 34 59.6	-38 08 07
3357	05 34.3	-36 55	-39	167	III	49	19.4	0.0	0	6	05 36 01.9	-36 53 12

Table D.1 continued from previous page

ACO	RAB1950	DEB1950	Xcen	Ycen	BMtype	Count	m10	z	Rich	Dclass	_RA_icrs	_DE_icrs
3358	05 36.1	-20 39	-3	-34	II	86	17.2	0.0	2	5	05 38 14.7	-20 37 20
3359	05 36.1	-45 20	0	-18	III:	78	17.6	0.0	1	5	05 37 32.5	-45 18 19
3360	05 38.8	-43 25	26	86	III	85	16.7	0.0	2	5	05 40 18.8	-43 23 31
3361	05 39.6	-48 11	84	98	I-II	48	17.6	0.0	0	5	05 40 55.3	-48 09 34
3362	05 40.4	-61 44	-14	-91	I-II	30	17.1	0.0	0	5	05 40 54.0	-61 42 35
3363	05 43.8	-47 58	122	108	I	139	17.7	0.0	3	5	05 45 07.8	-47 56 52
3364	05 45.7	-31 54	5	-100	II	75	18.4	0.0	1	5	05 47 34.2	-31 53 02
3365	05 46.1	-21 57	116	-104	II	68	16.6	0.0	1	5	05 48 12.9	-21 56 04
3366	05 46.5	-41 16	84	-68	II-III	40	19.2	0.0	0	6	05 48 05.2	-41 15 04
3367	05 47.3	-24 29	-61	30	I-II	33	15.6	0.0	0	3	05 49 21.4	-24 28 09
3368	05 48.4	-22 33	-47	133	I-II	32	16.1	0.0	0	4	05 50 30.0	-22 32 14
3369	05 49.7	-29 04	53	52	II-III	68	19.3	0.0	1	5	05 51 38.6	-29 03 19
3370	05 53.0	-32 20	-80	145	I	49	16.9	0.0	0	5	05 54 51.5	-32 19 33
3371	05 54.0	-18 19	-40	92	III	123	19.2	0.0	2	5	05 56 11.6	-18 18 39
3372	05 54.0	-34 48	-68	13	I-II	35	16.2	0.0	0	4	05 55 47.3	-34 47 38
3373	05 54.4	-18 09	-35	101	III	151	19.3	0.0	3	5	05 56 35.8	-18 08 40
3374	05 54.8	-21 16	-30	-65	II	34	16.1	0.0	0	4	05 56 55.7	-21 15 42
3375	05 58.7	-18 58	19	57	II-III	145	19.3	0.0	3	5	06 00 52.8	-18 57 59
3376	05 59.1	-40 03	-50	-1	I	42	15.3	0.0455	0	3	06 00 43.6	-40 03 00
3377	05 59.6	-20 45	31	-38	I-II	140	19.3	0.0	3	5	06 01 44.4	-20 45 03
3378	06 04.1	-35 18	43	-14	I	78	18.9	0.0	1	5	06 05 52.4	-35 18 22
3379	06 04.6	-42 17	5	147	II	115	16.3	0.0	2	4	06 06 09.0	-42 17 23
3380	06 05.7	-49 29	48	28	I-II	40	15.6	0.0567	0	4	06 06 57.6	-49 29 28
3381	06 08.1	-33 35	88	77	I	69	14.7	0.0282	1	2	06 09 55.4	-33 35 39
3382	06 08.4	-37 47	50	119	III	51	18.6	0.0	1	5	06 10 06.0	-37 47 40
3383	06 08.5	-18 54	-124	60	III	82	18.2	0.0	2	5	06 10 40.9	-18 54 42
3384	06 12.1	-17 57	-77	113	I	43	19.3	0.0	0	5	06 14 18.1	-17 57 58
3385	06 16.6	-52 00	-112	-108	II:	46	17.4	0.0	0	5	06 17 44.4	-52 01 15
3386	06 20.3	-42 37	-114	128	II-III	74	19.3	0.0	1	5	06 21 50.5	-42 38 32
3387	06 20.7	-25 36	79	-32	III	72	19.1	0.0	1	5	06 22 43.8	-25 37 35
3388	06 21.3	-43 10	-105	97	III:	44	19.5	0.0	0	5	06 22 49.3	-43 11 36
3389	06 21.6	-64 56	-86	3	II-III	35	14.5	0.0248	0	2	06 21 47.4	-64 57 35
3390	06 23.3	-37 19	-9	-124	II	63	14.7	0.0	1	2	06 25 01.1	-37 20 45
3391	06 25.2	-53 39	-87	70	I	40	16.1	0.0531	0	4	06 26 15.4	-53 40 52
3392	06 25.3	-35 27	12	-24	I	77	15.5	0.0	1	3	06 27 04.4	-35 28 54
3393	06 25.3	-62 52	-68	115	III	55	19.3	0.0	1	6	06 25 42.0	-62 53 51
3394	06 25.8	-22 12	94	-116	III	60	19.0	0.0	1	5	06 27 54.6	-22 13 57
3395	06 26.5	-54 22	-76	29	II	54	15.9	0.0498	1	4	06 27 31.1	-54 23 58
3396	06 27.3	-41 42	-31	-90	I-II	62	18.6	0.0	1	5	06 28 52.6	-41 44 02
3397	06 28.5	-52 12	-14	-118	I-II	45	16.9	0.0	0	5	06 29 38.2	-52 14 07
3398	06 35.1	-62 35	-9	132	II	58	19.2	0.0	1	5	06 35 32.3	-62 37 34
3399	06 36.0	-48 27	52	83	III	33	18.6	0.0	0	5	06 37 19.2	-48 29 40
3400	06 39.4	-46 00	67	-54	I?	59	18.6	0.0	1	5	06 40 49.5	-46 02 55
3401	06 40.3	-63 25	24	89	II-III	50	19.2	0.0	1	5	06 40 40.1	-63 27 56
3402	06 40.4	-49 44	89	13	I-II	45	18.8	0.0	0	5	06 41 40.0	-49 46 58
3403	06 40.6	-49 57	90	1	I-II	49	17.6	0.0	0	5	06 41 51.4	-49 59 59
3404	06 44.5	-54 09	64	43	I-II	64	17.1	0.0	1	5	06 45 32.9	-54 12 16
3405	06 47.1	-74 38	39	20	III	35	18.2	0.0	0	5	06 45 41.0	-74 41 22
3406	06 57.0	-49 08	-27	48	II-III	42	18.3	0.0	0	5	06 58 18.8	-49 12 09
3407	07 03.7	-49 00	31	54	I	57	15.4	0.0	1	3	07 05 01.8	-49 04 38
3408	07 07.2	-49 08	62	46	I-II	41	15.6	0.0	0	3	07 08 31.8	-49 12 52
3409	08 22.0	-17 27	-27	137	III	39	17.8	0.0	0	5	08 24 16.6	-17 36 46
3410	08 36.1	-17 46	-115	120	II-III	50	19.3	0.0	1	6	08 38 23.1	-17 56 35
3411	08 39.5	-17 18	-72	146	II	55	19.3	0.0	1	6	08 41 47.7	-17 28 46
3412	08 39.8	-17 25	-68	140	II-III	70	19.3	0.0	1	6	08 42 05.7	-17 35 47
3413	08 46.6	-18 53	18	60	III	30	19.4	0.0	0	6	08 48 52.6	-19 04 10

Table D.1 continued from previous page

ACO	RAB1950	DEB1950	Xcen	Ycen	BMtype	Count	m10	z	Rich	Dclass	_RA_icrs	_DE_icrs
3414	09 02.4	-19 09	-46	46	III	57	19.0	0.0	1	6	09 04 41.5	-19 21 00
3415	09 09.6	-20 59	44	-53	II-III	111	18.6	0.0	2	6	09 11 52.4	-21 11 21
3416	09 13.3	-20 32	90	-29	II	125	18.7	0.0	2	6	09 15 35.1	-20 44 32
3417	09 17.0	-20 45	-131	-39	II	76	18.6	0.0	1	6	09 19 17.2	-20 57 43
3418	09 19.5	-21 41	-96	-88	I-II:	47	18.1	0.0	0	6	09 21 46.6	-21 53 50
3419	09 26.2	-22 31	-74	135	III:	94	19.3	0.0	2	6	09 28 28.5	-22 44 08
3420	09 29.9	-24 40	-27	20	II-III	50	16.1	0.0	1	4	09 32 09.1	-24 53 18
3421	09 36.3	-29 04	14	53	III	53	18.9	0.0	1	6	09 38 30.0	-29 17 35
3422	09 38.0	-27 29	33	135	II	60	19.1	0.0	1	6	09 40 13.6	-27 42 39
3423	09 38.8	-27 51	43	116	II-III	74	18.9	0.0	1	6	09 41 01.4	-28 04 41
3424	09 40.1	-27 17	60	146	II-III	94	19.1	0.0	2	6	09 42 20.0	-27 30 44
3425	09 41.1	-23 28	-160	81	I-II	73	19.1	0.0	1	6	09 43 23.2	-23 41 47
3426	09 41.7	-30 36	75	-31	III	80	19.2	0.0	2	6	09 43 53.4	-30 49 48
3427	09 48.4	-22 25	-71	138	I-II	110	19.3	0.0	2	6	09 50 42.8	-22 39 04
3428	09 50.7	-33 30	-106	80	I	46	17.3	0.0	0	5	09 52 52.2	-33 44 10
3429	09 57.1	-24 44	36	15	I	35	16.6	0.0	0	5	09 59 24.1	-24 58 24
3430	09 58.0	-22 25	48	138	II-III	56	18.6	0.0	1	6	10 00 19.8	-22 39 26
3431	09 58.5	-24 03	53	51	I-II	152	18.1	0.0	3	6	10 00 48.7	-24 17 27
3432	09 59.2	-32 48	-11	119	I	56	17.3	0.0	1	5	10 01 24.2	-33 02 29
3433	10 00.2	-31 02	23	-56	III	105	17.9	0.0	2	5	10 02 25.7	-31 16 31
3434	10 01.3	-35 01	12	-1	III	55	18.9	0.0	1	5	10 03 28.7	-35 15 33
3435	10 02.5	-31 21	49	-71	III	169	18.6	0.0	3	6	10 04 43.9	-31 35 36
3436	10 03.0	-31 30	56	-80	III	88	17.4	0.0	2	5	10 05 13.8	-31 44 37
3437	10 09.6	-29 44	-135	14	III	115	19.5	0.0	2	6	10 11 52.1	-29 58 51
3438	10 12.4	-28 19	-102	94	II-III	111	19.4	0.0	2	6	10 14 41.5	-28 33 56
3439	10 13.5	-27 11	-31	-116	III:	56	19.1	0.0	1	6	10 15 48.4	-27 25 58
3440	10 13.5	-29 06	-88	49	II-III	155	19.2	0.0	3	6	10 15 47.2	-29 20 58
3441	10 15.7	-21 20	80	-71	II-III	45	17.9	0.0	0	6	10 18 04.3	-21 35 03
3442	10 16.7	-25 54	9	-47	II-III	59	18.6	0.0	1	6	10 19 01.7	-26 09 04
3443	10 18.9	-33 28	-60	87	II	109	16.4	0.0	2	5	10 21 09.0	-33 43 09
3444	10 21.5	-27 00	66	-107	II-III	57	19.5	0.0	1	6	10 23 49.6	-27 15 13
3445	10 22.1	-29 32	10	27	II-III	81	19.4	0.0	2	6	10 24 24.2	-29 47 14
3446	10 24.8	-37 55	5	-152	III	64	19.1	0.0	1	6	10 27 00.9	-38 10 19
3447	10 24.9	-38 07	7	-162	II-III	63	19.2	0.0	1	6	10 27 06.7	-38 22 19
3448	10 26.8	-33 37	28	78	II-III	58	17.8	0.0	1	5	10 29 04.3	-33 52 23
3449	10 26.8	-33 53	28	64	III	43	19.4	0.0	0	6	10 29 04.1	-34 08 23
3450	10 30.5	-33 20	69	89	II-III	51	19.3	0.0	1	6	10 32 47.1	-33 35 29
3451	10 31.1	-31 34	114	-83	III	72	19.6	0.0	1	6	10 33 24.3	-31 49 30
3452	10 45.2	-29 21	12	36	II-III	35	18.0	0.0	0	6	10 47 33.8	-29 36 51
3453	10 46.8	-36 19	-15	-70	III	38	18.9	0.0	0	6	10 49 06.5	-36 34 53
3454	10 47.4	-81 35	30	-84	II-III	52	18.7	0.0	1	5	10 47 34.9	-81 50 53
3455	10 50.1	-33 57	22	57	I-II	30	17.4	0.0	0	6	10 52 26.4	-34 12 58
3456	10 51.3	-32 08	38	153	I-II	45	18.0	0.0	0	6	10 53 39.5	-32 23 59
3457	10 52.2	-23 23	-99	88	I-II	48	19.3	0.0	0	6	10 54 37.4	-23 39 00
3458	10 56.9	-27 34	-134	129	II	90	18.9	0.0	2	6	10 59 18.4	-27 50 06
3459	10 57.7	-30 41	-109	-37	I?	42	19.0	0.0	0	6	11 00 05.2	-30 57 07
3460	10 59.8	-27 02	-88	159	II-III	41	18.8	0.0	0	6	11 02 13.0	-27 18 09
3461	11 01.9	-33 00	-59	-160	III	57	18.7	0.0	1	6	11 04 17.0	-33 16 12
3462	11 02.6	-28 14	-54	96	I	97	18.5	0.0	2	6	11 05 01.0	-28 30 12
3463	11 04.2	-43 55	-77	59	II-III	38	19.4	0.0	0	6	11 06 30.5	-44 11 14
3464	11 05.2	-27 02	-26	62	III	48	19.0	0.0	0	6	11 07 37.8	-27 18 15
3465	11 05.6	-19 24	-82	32	III	60	18.9	0.0	1	6	11 08 04.3	-19 40 15
3466	11 05.9	-30 35	-15	-29	I	30	17.6	0.0	0	6	11 08 18.7	-30 51 16
3467	11 06.2	-31 00	-12	-51	III	73	18.7	0.0	1	6	11 08 36.6	-31 16 16
3468	11 07.6	-32 05	-54	158	III	67	18.9	0.0	1	6	11 10 00.4	-32 21 17
3469	11 08.1	-31 58	-48	164	III	63	19.2	0.0	1	6	11 10 30.6	-32 14 18

Table D.1 continued from previous page

ACO	RAB1950	DEB1950	Xcen	Ycen	BMtype	Count	m10	z	Rich	Dclass	_RA_icrs	_DE_icrs
3470	11 08.7	-18 31	-45	81	III?	65	19.3	0.0	1	6	11 11 10.9	-18 47 19
3471	11 08.8	-29 53	18	8	II-III	103	18.8	0.0	2	6	11 11 13.4	-30 09 19
3472	11 13.3	-29 55	68	5	I-II	77	19.0	0.0	1	6	11 15 44.1	-30 11 23
3473	11 13.4	-43 28	11	84	II-III	52	18.0	0.0	1	5	11 15 45.2	-43 44 23
3474	11 13.8	-43 06	15	103	II	48	17.0	0.0	0	5	11 16 09.5	-43 22 23
3475	11 14.4	-43 43	21	70	II-III	64	18.0	0.0	1	5	11 16 45.4	-43 59 24
3476	11 15.1	-32 50	32	118	II-III	42	17.7	0.0	0	6	11 17 31.5	-33 06 24
3477	11 16.0	-19 37	48	21	II:	65	18.4	0.0	1	6	11 18 29.3	-19 53 25
3478	11 16.0	-25 05	-75	-3	II	32	18.1	0.0	0	6	11 18 27.9	-25 21 25
3479	11 16.5	-27 09	-67	-114	II	54	19.6	0.0	1	6	11 18 57.4	-27 25 25
3480	11 18.6	-30 56	129	-49	I-II	62	19.0	0.0	1	6	11 21 02.7	-31 12 27
3481	11 19.0	-31 54	-128	-103	I-II	61	18.5	0.0	1	6	11 21 26.5	-32 10 27
3482	11 20.4	-32 42	91	124	I-II	33	18.0	0.0	0	6	11 22 50.6	-32 58 28
3483	11 21.5	-20 39	117	-35	III	70	19.0	0.0	1	6	11 23 59.6	-20 55 29
3484	11 24.0	-22 08	23	155	I-II	63	18.9	0.0	1	6	11 26 29.6	-22 24 31
3485	11 24.7	-31 12	-63	-65	II-III	43	19.5	0.0	0	6	11 27 09.7	-31 28 31
3486	11 26.5	-36 17	-106	-69	II-III	54	18.7	0.0	1	6	11 28 56.8	-36 33 33
3487	11 29.5	-30 55	-8	-49	II-III	45	18.5	0.0	0	6	11 31 58.6	-31 11 34
3488	11 38.2	-27 29	-73	-130	I	41	17.5	0.0	0	6	11 40 42.6	-27 45 38
3489	11 38.4	-30 57	95	-53	II-III	34	17.3	0.0	0	6	11 40 54.2	-31 13 38
3490	11 42.8	-34 10	73	45	I	91	16.4	0.0	2	5	11 45 18.6	-34 26 40
3491	11 46.6	-36 15	112	-68	II	42	18.4	0.0	0	6	11 49 07.1	-36 31 41
3492	11 53.8	-33 14	-74	96	I-II	31	17.3	0.0	0	6	11 56 20.8	-33 30 42
3493	11 54.5	-22 40	127	127	I-II	59	18.4	0.0	1	6	11 57 03.2	-22 56 42
3494	11 54.6	-31 53	16	-100	I-II	40	17.7	0.0	0	6	11 57 09.0	-32 09 42
3495	11 56.3	-28 45	36	68	III	79	17.5	0.0	1	6	11 58 51.4	-29 01 42
3496	11 57.3	-22 46	-110	121	III	49	18.8	0.0	0	6	11 59 51.6	-23 02 42
3497	11 57.5	-31 07	50	-59	I-II	40	16.0	0.0	0	4	12 00 03.5	-31 23 42
3498	11 59.3	-28 24	72	86	III	66	17.5	0.0	1	6	12 01 51.8	-28 40 42
3499	12 00.3	-27 37	85	128	II-III	104	18.0	0.0	2	6	12 02 52.0	-27 53 42
3500	12 00.4	-29 52	83	8	I-II	36	16.7	0.0	0	5	12 02 58.0	-30 08 42
3501	12 00.9	-28 21	91	89	II-III	42	16.8	0.0	0	5	12 03 28.1	-28 37 42
3502	12 01.6	-27 58	100	109	I-II	77	18.5	0.0	1	6	12 04 10.2	-28 14 42
3503	12 01.6	-28 54	99	59	II-III	72	18.5	0.0	1	6	12 04 10.2	-29 10 42
3504	12 06.0	-33 00	63	108	I-II	35	18.1	0.0	0	6	12 08 35.1	-33 16 42
3505	12 06.1	-34 10	63	46	I-II	53	16.0	0.0	1	4	12 08 41.2	-34 26 42
3506	12 10.3	-28 23	-71	88	I-II	46	18.0	0.0	0	6	12 12 53.6	-28 39 41
3507	12 10.4	-25 48	50	-40	I	75	17.4	0.0	1	6	12 12 59.4	-26 04 41
3508	12 13.2	-32 44	-36	-145	II	35	17.7	0.0	0	6	12 15 48.5	-33 00 40
3509	12 13.7	-32 59	150	106	II	43	16.5	0.0	0	5	12 16 18.6	-33 15 40
3510	12 15.7	-30 09	-8	-6	I-II	41	18.1	0.0	0	6	12 18 18.6	-30 25 40
3511	12 17.1	-43 22	84	87	I-II	47	18.9	0.0	0	6	12 19 44.8	-43 38 39
3512	12 19.1	-21 18	51	-69	II-III?	56	19.6	0.0	1	6	12 21 42.1	-21 34 38
3513	12 19.8	-42 46	111	119	II-III?	40	18.8	0.0	0	6	12 22 27.5	-43 02 38
3514	12 20.2	-25 15	-96	-12	III	59	18.1	0.0	1	6	12 22 48.7	-25 31 38
3515	12 21.0	-44 16	-145	39	III	32	17.2	0.0	0	5	12 23 40.1	-44 32 38
3516	12 21.8	-25 30	-77	-26	II-III	35	18.0	0.0	0	6	12 24 25.0	-25 46 37
3517	12 29.2	-17 34	-89	131	III	57	18.5	0.0	1	6	12 31 48.6	-17 50 33
3518	12 29.7	-19 00	-82	54	III	49	18.5	0.0	0	6	12 32 18.9	-19 16 33
3519	12 30.0	-38 07	-46	102	III	49	19.0	0.0	0	6	12 32 40.9	-38 23 33
3520	12 32.2	-24 16	50	41	II-III	77	18.0	0.0	1	6	12 34 50.2	-24 32 32
3521	12 33.9	-17 18	-29	146	III	39	19.0	0.0	0	6	12 36 31.0	-17 34 31
3522	12 36.4	-19 13	3	43	II-III	32	18.5	0.0	0	6	12 39 01.6	-19 29 29
3523	12 36.6	-17 16	5	147	III	41	18.9	0.0	0	6	12 39 13.2	-17 32 29
3524	12 37.4	-33 57	-120	55	I	36	17.0	0.0	0	5	12 40 05.4	-34 13 28
3525	12 45.1	-21 15	111	-67	II-III	32	19.2	0.0	0	6	12 47 45.0	-21 31 22

Table D.1 continued from previous page

ACO	RAB1950	DEB1950	Xcen	Ycen	BMtype	Count	m10	z	Rich	Dclass	_RA_icrs	_DE_icrs
3526	12 46.1	-41 02	-142	-58	I-II:	33	12.9	0.011	0	0	12 48 51.8	-41 18 21
3527	12 47.2	-36 29	-11	-79	I	43	19.4	0.0	0	6	12 49 56.2	-36 45 20
3528	12 51.6	-28 45	-124	67	II	70	15.9	0.0553	1	4	12 54 18.2	-29 01 16
3529	12 52.7	-17 53	-57	116	II-III	43	18.0	0.0	0	6	12 55 20.8	-18 09 15
3530	12 52.9	-30 05	-108	-4	I-II	34	15.6	0.0	0	4	12 55 36.9	-30 21 14
3531	12 54.4	-32 39	71	125	II	34	16.7	0.0	0	5	12 57 08.1	-32 55 13
3532	12 54.6	-30 06	-88	-5	II-III	36	15.8	0.0	0	4	12 57 19.2	-30 22 13
3533	12 55.0	-21 09	-27	-60	II-III	44	19.1	0.0	0	6	12 57 40.1	-21 25 12
3534	12 55.1	-18 41	-26	72	II-III	31	18.0	0.0	0	6	12 57 45.3	-18 57 12
3535	12 55.1	-28 13	-83	97	III	30	16.2	0.0	0	5	12 57 48.6	-28 29 12
3536	12 57.5	-18 28	4	84	II:	40	19.0	0.0	0	6	13 00 09.5	-18 44 09
3537	12 58.3	-32 10	-159	152	I-II	35	13.9	0.0167	0	2	13 01 02.6	-32 26 09
3538	12 58.4	-21 21	14	-71	II-III	89	18.7	0.0	2	6	13 01 04.5	-21 37 08
3539	13 00.4	-17 31	41	135	I-II	32	18.0	0.0	0	6	13 03 03.4	-17 47 06
3540	13 00.5	-33 00	32	-161	II-III	34	18.5	0.0	0	6	13 03 15.4	-33 16 06
3541	13 01.0	-23 59	-135	54	II-III	50	18.0	0.0	1	6	13 03 41.8	-24 15 06
3542	13 05.9	-34 18	-71	40	I	45	16.1	0.0	0	4	13 08 41.0	-34 34 00
3543	13 06.7	-23 15	-66	95	III	47	18.6	0.0	0	6	13 09 24.2	-23 30 59
3544	13 08.3	-32 44	-45	124	I-II	54	19.1	0.0	1	6	13 11 04.7	-32 59 56
3545	13 08.6	-33 49	-42	66	I-II	39	18.0	0.0385	0	6	13 11 23.3	-34 04 56
3546	13 10.3	-29 43	-171	13	I	39	17.6	0.0	0	6	13 13 03.6	-29 58 54
3547	13 10.5	-37 04	111	155	II?	50	19.5	0.0	1	6	13 13 19.4	-37 19 54
3548	13 10.6	-43 49	60	65	II	39	16.5	0.0	0	5	13 13 29.7	-44 04 53
3549	13 11.6	-29 11	-157	42	I-II	65	16.7	0.0	1	5	13 14 21.5	-29 26 52
3550	13 14.8	-22 00	-41	-107	II-III	52	18.6	0.0	1	6	13 17 30.6	-22 15 48
3551	13 15.4	-30 40	-111	-37	I-II	126	17.2	0.0	2	6	13 18 10.9	-30 55 47
3552	13 16.1	-31 33	-102	-84	I	60	17.3	0.0	1	6	13 18 53.4	-31 48 46
3553	13 16.4	-36 55	43	-100	I-II	36	15.9	0.0	0	4	13 19 14.6	-37 10 45
3554	13 16.7	-33 13	49	98	I-II	59	16.0	0.0153	1	4	13 19 30.5	-33 28 45
3555	13 18.0	-28 43	-83	69	II	61	16.0	0.0	1	4	13 20 46.3	-28 58 43
3556	13 21.3	-31 24	-43	-75	I	49	16.0	0.0	0	4	13 24 06.2	-31 39 38
3557	13 22.1	-28 37	-34	74	I-II	36	16.1	0.0	0	5	13 24 52.8	-28 52 37
3558	13 25.1	-31 14	1	-66	I	226	14.7	0.0482	4	3	13 27 54.8	-31 29 32
3559	13 27.1	-29 16	24	40	I	141	15.3	0.0471	3	4	13 29 53.9	-29 31 29
3560	13 29.0	-32 58	-83	110	I	184	14.7	0.0109	3	3	13 31 50.5	-33 13 25
3561	13 30.3	-42 36	-20	131	II	36	16.1	0.0	0	4	13 33 15.8	-42 51 23
3562	13 30.7	-31 25	65	-76	I	129	15.1	0.0499	2	3	13 33 31.8	-31 40 23
3563	13 30.7	-42 18	-16	147	II-III:	33	16.8	0.0	0	5	13 33 39.7	-42 33 22
3564	13 31.5	-34 58	-54	4	II	53	15.3	0.0	1	3	13 34 22.3	-35 13 21
3565	13 33.8	-33 43	-29	71	I	64	13.7	0.0109	1	1	13 36 39.9	-33 58 17
3566	13 36.1	-35 18	-4	-14	II	100	15.5	0.0	2	4	13 38 59.4	-35 33 13
3567	13 36.9	-36 12	5	-62	I-II	50	17.6	0.0	1	6	13 39 48.2	-36 27 12
3568	13 38.3	-34 23	21	36	II-III	64	19.1	0.0	1	6	13 41 11.1	-34 38 09
3569	13 39.8	-35 30	37	-24	I-II	72	17.5	0.0	1	6	13 42 42.2	-35 45 06
3570	13 43.9	-37 40	-91	127	I-II	31	15.5	0.0372	0	4	13 46 50.8	-37 54 58
3571	13 44.6	-32 37	92	129	I	126	15.4	0.0	2	4	13 47 28.9	-32 51 57
3572	13 45.3	-33 08	100	101	I-II	49	15.4	0.0	0	4	13 48 11.4	-33 22 56
3573	13 45.5	-34 26	100	32	I	75	18.3	0.0	1	6	13 48 24.5	-34 40 55
3574	13 46.3	-30 03	-24	-1	I	31	13.0	0.0141	0	1	13 49 09.4	-30 17 54
3575	13 49.7	-32 38	150	127	II	49	15.5	0.0	0	4	13 52 35.8	-32 52 47
3576	13 49.9	-30 03	19	-1	I	110	18.0	0.0	2	6	13 52 45.9	-30 17 46
3577	13 51.5	-27 36	-57	-138	II	103	15.4	0.0	2	4	13 54 20.4	-27 50 43
3578	13 54.7	-24 29	-18	29	I-II	52	14.7	0.0	1	3	13 57 30.6	-24 43 36
3579	13 54.9	-22 45	-15	122	II	43	18.4	0.0	0	6	13 57 41.5	-22 59 36
3580	14 00.1	-23 29	49	82	I	50	18.4	0.0	1	6	14 02 54.5	-23 43 25
3581	14 04.6	-26 47	101	-95	I	42	15.2	0.0	0	3	14 07 27.5	-27 01 15

Table D.1 continued from previous page

ACO	RAB1950	DEB1950	Xcen	Ycen	BMtype	Count	m10	z	Rich	Dclass	_RA_icrs	_DE_icrs
3582	14 05.7	-18 40	71	72	II-III	72	18.1	0.0	1	6	14 08 27.7	-18 54 12
3583	14 07.6	-22 04	92	-110	II-III	48	17.4	0.0	0	6	14 10 24.3	-22 18 08
3584	14 08.1	-19 44	101	14	II-III	59	17.6	0.0	1	6	14 10 52.7	-19 58 07
3585	14 11.3	-22 46	-85	119	III	57	19.1	0.0	1	6	14 14 07.2	-22 59 59
3586	14 11.5	-23 45	-82	67	III	68	18.8	0.0	1	6	14 14 20.0	-23 58 58
3587	14 11.9	-29 42	6	16	II-III:	80	19.6	0.0	2	6	14 14 48.8	-29 55 57
3588	14 11.9	-33 39	-139	71	II	40	17.8	0.0	0	6	14 14 52.3	-33 52 57
3589	14 12.5	-46 29	111	-78	III?	41	19.1	0.0	0	6	14 15 42.8	-46 42 56
3590	14 14.9	-32 22	39	-127	III:	85	17.7	0.0	2	6	14 17 51.6	-32 35 50
3591	14 15.1	-24 40	-38	18	II	70	19.1	0.0	1	6	14 17 57.1	-24 53 50
3592	14 15.8	-22 03	-30	158	II-III	31	19.3	0.0	0	6	14 18 37.1	-22 16 48
3593	14 16.4	-19 15	-60	41	II	32	16.0	0.1196	0	4	14 19 11.1	-19 28 47
3594	14 17.6	-17 31	-45	134	III	82	19.6	0.0	2	6	14 20 21.9	-17 44 44
3595	14 18.0	-86 42	-109	-125	II-III	99	18.8	0.0	2	5	14 32 24.3	-86 55 28
3596	14 22.4	-19 31	15	27	II	64	17.0	0.0	1	6	14 25 11.8	-19 44 31
3597	14 24.0	-18 54	36	59	II-III	46	16.8	0.0	0	5	14 26 47.4	-19 07 27
3598	14 24.6	-17 29	45	135	III	121	19.2	0.0	2	6	14 27 22.4	-17 42 26
3599	14 24.9	-23 20	83	89	I-II	58	18.0	0.0	1	6	14 27 45.0	-23 33 25
3600	14 26.1	-27 40	-95	125	III	31	19.6	0.0	0	6	14 29 00.9	-27 53 22
3601	14 28.8	-21 17	95	-69	II	58	18.4	0.0	1	6	14 31 37.7	-21 30 15
3602	14 29.5	-44 07	14	49	II-III	65	18.4	0.0	1	5	14 32 43.6	-44 20 12
3603	14 30.3	-31 35	-42	-86	II-III	39	15.9	0.0	0	4	14 33 17.1	-31 48 10
3604	14 30.6	-28 12	-41	95	III	85	18.9	0.0	2	6	14 33 31.9	-28 25 10
3605	14 32.1	-28 07	-26	101	I	34	17.3	0.0	0	6	14 35 02.0	-28 20 06
3606	14 33.2	-28 05	-13	103	II	129	17.8	0.0	2	6	14 36 08.1	-28 18 03
3607	14 36.9	-24 25	-41	34	III	48	19.3	0.0	0	6	14 39 47.2	-24 37 53
3608	14 39.5	-30 45	60	-40	II	41	17.5	0.0	0	6	14 42 29.6	-30 57 45
3609	14 45.4	-27 38	-141	127	II	150	19.6	0.0	3	6	14 48 21.2	-27 50 28
3610	14 45.7	-21 13	44	-65	I-II	75	19.3	0.0	1	6	14 48 33.1	-21 25 27
3611	14 46.3	-20 41	51	-37	II-III	96	19.3	0.0	2	6	14 49 08.7	-20 53 26
3612	14 51.8	-27 52	-64	115	II	73	17.6	0.0	1	6	14 54 46.1	-28 04 09
3613	14 51.8	-30 25	-62	-21	II-III	38	17.5	0.0	0	6	14 54 48.8	-30 37 09
3614	14 55.2	-29 49	-23	11	II:	45	17.6	0.0	0	6	14 58 12.6	-30 00 59
3615	14 55.7	-80 22	-12	-18	I-II	36	18.2	0.0	0	5	15 02 56.3	-80 33 51
3616	15 06.3	-28 32	107	80	II-III	141	19.5	0.0	3	6	15 09 18.4	-28 43 24
3617	15 12.3	-19 43	-150	14	III	43	18.7	0.0	0	6	15 15 09.8	-19 54 05
3618	15 17.1	-28 23	-39	88	I	61	19.3	0.0	1	6	15 20 07.4	-28 33 49
3619	15 21.1	-32 14	8	-118	I-II	39	19.4	0.0	0	6	15 24 12.5	-32 24 35
3620	15 23.8	-18 30	-5	81	II-III	68	19.3	0.0	1	6	15 26 39.3	-18 40 27
3621	15 25.7	-24 42	19	18	II-III	34	18.7	0.0	0	6	15 28 40.0	-24 52 20
3622	15 28.9	-18 36	59	76	III	102	19.3	0.0	2	6	15 31 45.7	-18 46 09
3623	15 35.1	-23 45	-133	69	II-III	39	19.2	0.0	0	6	15 38 03.7	-23 54 47
3624	15 46.0	-83 21	-100	74	II-III	38	17.0	0.0	0	5	15 56 44.6	-83 29 54
3625	15 53.4	-86 40	-42	-95	II-III	55	18.0	0.0	1	5	16 13 00.6	-86 48 09
3626	16 09.9	-83 40	-61	65	I	33	17.7	0.0	0	5	16 21 34.1	-83 47 21
3627	16 11.2	-60 47	-115	-46	I	59	14.2	0.0143	1	1	16 15 32.8	-60 54 30
3628	16 24.6	-75 04	-20	-3	II	57	18.0	0.0	1	5	16 31 01.3	-75 10 33
3629	16 28.9	-82 22	-41	139	I	32	18.0	0.0854	0	5	16 39 15.0	-82 28 07
3630	16 33.0	-75 54	9	-48	I-II	30	17.5	0.0	0	5	16 39 43.3	-75 59 58
3631	18 26.0	-78 50	63	61	II	36	17.9	0.0	0	5	18 34 08.9	-78 47 49
3632	18 36.0	-46 22	-41	-72	II:	49	18.8	0.0	0	5	18 39 42.9	-46 19 15
3633	18 49.8	-44 56	86	3	II:	64	18.4	0.0	1	5	18 53 26.7	-44 52 16
3634	18 54.9	-55 00	97	-1	I-II	38	19.6	0.0	0	5	18 59 00.2	-54 55 53
3635	18 55.2	-42 16	-131	145	II-III:	139	19.3	0.0	3	5	18 58 44.6	-42 11 53
3636	18 57.3	-45 10	-104	-9	I-II	185	18.7	0.0	3	5	19 00 56.7	-45 05 44
3637	19 10.8	-73 48	102	61	II-III	34	18.9	0.0	0	5	19 16 59.4	-73 42 42

Table D.1 continued from previous page

ACO	RAB1950	DEB1950	Xcen	Ycen	BMtype	Count	m10	z	Rich	Dclass	_RA_icrs	_DE_icrs
3638	19 22.0	-43 03	-140	102	I-II	84	17.0	0.0	2	5	19 25 32.0	-42 57 02
3639	19 24.2	-51 03	-49	-55	I	80	19.2	0.0	2	6	19 28 02.5	-50 56 52
3640	19 26.7	-79 41	-11	19	III	45	18.3	0.0	0	5	19 34 52.7	-79 34 33
3641	19 30.6	-43 01	-56	107	I-II	46	19.1	0.0	0	5	19 34 07.0	-42 54 27
3642	19 32.0	-61 44	-40	-89	I-II	70	19.4	0.0	1	6	19 36 27.5	-61 37 19
3643	19 38.3	-53 24	-80	85	II-III	32	19.5	0.0	0	6	19 42 13.1	-53 16 55
3644	19 38.3	-80 06	17	-4	II-III	39	17.6	0.0	0	5	19 46 35.0	-79 58 47
3645	19 39.7	-57 04	-62	-111	II-III	47	19.0	0.0	0	6	19 43 48.7	-56 56 49
3646	19 40.2	-40 39	-159	-37	I-II	83	19.6	0.0	2	6	19 43 37.5	-40 31 49
3647	19 40.3	-57 11	-58	-117	I-II	60	19.1	0.0	1	6	19 44 25.0	-57 03 47
3648	19 40.4	-45 36	39	-31	III	67	18.9	0.0	1	5	19 43 59.2	-45 28 48
3649	19 46.7	-27 40	-113	127	II	135	18.5	0.0	3	5	19 49 46.9	-27 32 24
3650	19 46.7	-86 57	-75	-123	II-III	42	18.6	0.0	0	5	20 07 06.9	-86 48 50
3651	19 48.2	-55 13	-1	-10	II	75	15.4	0.0588	1	3	19 52 10.9	-55 05 16
3652	19 48.2	-63 52	-2	64	II-III	31	17.5	0.0	0	5	19 52 46.1	-63 44 15
3653	19 48.8	-52 09	4	153	I-II	42	16.8	0.0475	0	5	19 52 37.8	-52 01 14
3654	19 56.0	-35 03	-46	-2	II-III	110	18.1	0.0	2	5	19 59 14.5	-34 54 48
3655	19 56.3	-82 23	-112	-146	II-III	34	19.2	0.0	0	6	20 05 59.4	-82 14 34
3656	19 57.2	-38 40	10	73	I-II	35	13.5	0.0185	0	1	20 00 32.1	-38 31 43
3657	19 58.5	-29 21	27	39	III	75	17.9	0.0	1	5	20 01 36.2	-29 12 39
3658	19 59.4	-29 33	36	24	III	56	17.7	0.0	1	5	20 02 30.4	-29 24 35
3659	19 59.5	-30 16	36	-10	II-III	139	17.2	0.0	3	5	20 02 37.4	-30 07 35
3660	20 02.0	-52 25	112	137	II-III	32	19.4	0.0	0	6	20 05 48.0	-52 16 24
3661	20 02.9	-42 05	67	-109	II-III:	74	19.2	0.0	1	6	20 06 19.3	-41 56 21
3662	20 03.2	-68 03	75	-161	II-III	39	17.7	0.0	0	5	20 08 06.8	-67 54 17
3663	20 03.5	-52 42	124	121	III	84	19.3	0.0	2	6	20 07 18.5	-52 33 18
3664	20 05.7	-80 48	74	-46	III	64	18.2	0.0369	1	5	20 14 01.1	-80 39 02
3665	20 06.0	-53 19	-124	89	III	120	19.0	0.237	2	6	20 09 49.7	-53 10 09
3666	20 07.8	-80 57	77	-55	III	80	18.6	0.0	2	5	20 16 10.8	-80 47 54
3667	20 08.5	-56 58	-95	-106	I-II	85	15.3	0.053	2	3	20 12 30.1	-56 49 00
3668	20 08.6	-41 38	125	-86	I-II	96	17.6	0.0	2	5	20 11 59.7	-41 29 00
3669	20 09.4	-38 19	140	90	II	42	19.2	0.0	0	6	20 12 42.1	-38 09 58
3670	20 11.2	-29 54	-94	8	I	102	18.7	0.0	2	5	20 14 17.8	-29 44 51
3671	20 11.6	-39 38	-109	21	I-II	55	17.5	0.0	1	5	20 14 55.9	-39 28 49
3672	20 16.7	-41 43	-55	-90	III	38	18.6	0.0	0	5	20 20 04.7	-41 33 31
3673	20 17.3	-46 55	118	-104	III	40	19.6	0.0	0	6	20 20 50.3	-46 45 28
3674	20 17.8	-30 12	-18	-7	II	161	19.3	0.0	3	6	20 20 53.6	-30 02 27
3675	20 18.1	-53 06	-27	103	II-III	54	18.6	0.0	1	5	20 21 52.5	-52 56 25
3676	20 22.0	-40 31	-1	-25	II-III	33	18.1	0.0404	0	5	20 25 19.9	-40 21 12
3677	20 23.2	-33 31	-12	81	I	60	16.8	0.033	1	5	20 26 21.4	-33 21 08
3678	20 24.1	-31 41	54	-87	II	62	18.1	0.0	1	5	20 27 12.9	-31 31 05
3679	20 24.2	-70 34	125	-33	II	45	19.5	0.0	0	6	20 29 17.0	-70 24 01
3680	20 24.9	-69 42	132	10	I-II	44	19.6	0.0	0	6	20 29 51.7	-69 31 59
3681	20 25.3	-33 35	11	77	I-II	58	17.4	0.0	1	5	20 28 27.2	-33 25 01
3682	20 26.0	-37 08	20	-112	II	66	16.2	0.0	1	4	20 29 14.1	-36 57 58
3683	20 26.1	-32 47	19	121	I-II	34	18.0	0.0	0	5	20 29 14.1	-32 36 58
3684	20 26.2	-78 16	-94	83	II	32	17.5	0.0	0	5	20 32 59.6	-78 05 51
3685	20 28.3	-56 36	51	-85	I-II	30	18.1	0.062	0	5	20 32 11.9	-56 25 49
3686	20 28.9	-26 35	-40	-83	I-II	36	18.3	0.0	0	5	20 31 54.2	-26 24 48
3687	20 29.1	-63 12	-24	98	III	46	16.3	0.0759	0	4	20 33 23.9	-63 01 45
3688	20 29.5	-40 10	75	-6	II-III	63	18.1	0.0	1	5	20 32 48.2	-39 59 46
3689	20 29.9	-56 11	63	-63	II-III	31	17.8	0.0	0	5	20 33 46.2	-56 00 43
3690	20 30.7	-35 26	71	-21	II-III	42	17.1	0.0	0	5	20 33 53.1	-35 15 42
3691	20 30.9	-38 12	92	98	I-II	115	16.5	0.0	2	5	20 34 09.0	-38 01 41
3692	20 31.1	-51 41	7	-88	II	46	17.0	0.0	0	5	20 34 46.0	-51 30 40
3693	20 31.2	-34 40	76	20	I-II	77	16.8	0.0	1	5	20 34 22.0	-34 29 40

Table D.1 continued from previous page

ACO	RAB1950	DEB1950	Xcen	Ycen	BMtype	Count	m10	z	Rich	Dclass	_RA_icrs	_DE_icrs
3694	20 31.5	-34 15	80	43	I-II	41	17.0	0.0	0	5	20 34 39.4	-34 04 39
3695	20 31.6	-36 00	80	-51	I	123	16.1	0.0	2	4	20 34 47.8	-35 49 39
3696	20 32.0	-35 05	86	-2	II	58	16.7	0.0	1	5	20 35 10.4	-34 54 37
3697	20 32.7	-57 06	81	-113	I-II	31	18.0	0.0	0	5	20 36 36.2	-56 55 34
3698	20 33.0	-25 27	8	-21	I-II	71	14.9	0.0	1	3	20 35 58.5	-25 16 34
3699	20 33.5	-37 34	121	132	II	30	18.2	0.0	0	5	20 36 43.7	-37 23 32
3700	20 33.9	-34 14	-159	39	II-III	43	17.7	0.0	0	5	20 37 03.1	-34 03 31
3701	20 34.9	-71 27	-57	-76	I-II	75	19.1	0.0	1	6	20 40 01.0	-71 16 24
3702	20 35.3	-36 41	-138	-92	III	54	19.4	0.0	1	6	20 38 30.2	-36 30 26
3703	20 35.9	-61 31	-117	-85	II	52	16.4	0.0708	1	5	20 40 02.5	-61 20 22
3704	20 37.3	-31 46	-56	-93	II	40	17.7	0.0	0	5	20 40 23.5	-31 35 20
3705	20 38.5	-35 25	-105	-21	III	100	16.5	0.0	2	5	20 41 40.1	-35 14 15
3706	20 39.0	-38 31	-97	80	II	41	16.1	0.02	0	4	20 42 14.3	-38 20 14
3707	20 39.3	-25 48	85	-40	II-III	84	18.4	0.0	2	5	20 42 16.4	-25 37 13
3708	20 39.4	-55 05	-115	-4	II-III	54	19.0	0.0	1	5	20 43 10.5	-54 54 11
3709	20 39.5	-32 50	-30	-150	I-II	37	18.9	0.0	0	5	20 42 36.6	-32 39 12
3710	20 41.4	-87 59	-84	72	III	73	19.1	0.0	1	6	21 05 54.6	-87 47 30
3711	20 43.5	-29 37	14	23	I-II	53	18.9	0.0	1	5	20 46 32.2	-29 25 59
3712	20 44.1	-32 47	23	-146	I	40	17.8	0.0	0	5	20 47 11.9	-32 35 57
3713	20 44.4	-34 10	-42	46	III	35	19.1	0.0	0	6	20 47 31.6	-33 58 56
3714	20 45.0	-27 11	-109	-119	II-III	75	19.6	0.0	1	6	20 47 59.3	-26 59 54
3715	20 46.8	-30 41	52	-33	I	78	19.3	0.0	1	6	20 49 51.1	-30 29 48
3716	20 47.9	-52 54	-55	110	I-II:	66	14.9	0.0456	1	3	20 51 32.8	-52 42 44
3717	20 51.1	-37 37	30	130	II-III	40	18.1	0.0	0	6	20 54 17.2	-37 25 34
3718	20 52.2	-55 07	-17	-3	II	118	17.8	0.0	2	5	20 55 55.0	-54 55 30
3719	20 52.7	-42 51	-74	115	II-III	60	19.1	0.0	1	6	20 56 00.5	-42 39 29
3720	20 53.2	-47 13	-64	149	II:	74	19.2	0.0	1	6	20 56 37.8	-47 01 27
3721	20 53.6	-43 17	-64	92	III	56	19.1	0.0	1	6	20 56 55.0	-43 05 26
3722	20 54.1	-66 34	-117	-88	II-III	36	19.4	0.0	0	6	20 58 30.0	-66 22 23
3723	20 54.3	-43 27	-57	84	III	64	18.9	0.0	1	6	20 57 37.2	-43 15 24
3724	20 55.3	-42 36	-48	129	III	72	19.2	0.0	1	6	20 58 35.7	-42 24 21
3725	20 55.3	-47 04	-46	158	II-III	57	18.5	0.0	1	6	20 58 43.1	-46 52 20
3726	20 56.4	-22 04	27	161	III	117	19.6	0.0	2	6	20 59 17.0	-21 52 18
3727	20 56.4	-36 43	88	-91	III	68	18.3	0.0	1	6	20 59 33.2	-36 31 17
3728	20 56.4	-82 56	-68	106	II-III	66	17.5	0.0	1	5	21 05 12.4	-82 44 09
3729	20 56.8	-24 32	33	28	II?	74	18.8	0.0	1	5	20 59 43.4	-24 20 17
3730	20 56.9	-35 18	94	-16	II?	40	18.5	0.0	0	6	21 00 01.3	-35 06 16
3731	20 57.7	-38 51	98	62	I-II	43	17.6	0.0	0	5	21 00 53.8	-38 39 13
3732	20 57.8	-55 52	25	-43	II-III:	45	19.4	0.0	0	6	21 01 31.3	-55 40 12
3733	20 59.0	-28 15	-76	95	I-II	59	15.4	0.0386	1	3	21 01 59.0	-28 03 10
3734	20 59.1	-27 30	-76	136	III	36	17.3	0.0	0	5	21 02 04.2	-27 18 09
3735	20 59.7	-42 35	-4	130	III	89	18.3	0.0	2	6	21 02 58.8	-42 23 07
3736	21 00.0	-43 31	-2	80	III	35	18.0	0.0487	0	6	21 03 18.2	-43 19 06
3737	21 00.1	-33 01	-133	105	III	44	19.3	0.0	0	6	21 03 10.1	-32 49 06
3738	21 00.3	-43 49	1	64	III	40	19.3	0.0	0	6	21 03 36.6	-43 37 05
3739	21 01.0	-41 35	-133	-84	III	90	18.7	0.0	2	6	21 04 15.1	-41 23 03
3740	21 02.8	-39 01	-121	55	I	92	17.9	0.0	2	5	21 05 59.2	-38 48 58
3741	21 03.0	-82 22	5	-128	I	29	17.4	0.0	0	5	21 11 10.8	-82 09 49
3742	21 03.3	-47 21	28	-125	II-III	35	15.1	0.0165	0	3	21 06 41.8	-47 08 56
3743	21 03.4	-27 19	-25	147	II-III	65	19.2	0.0	1	6	21 06 21.6	-27 06 56
3744	21 04.3	-25 41	-142	-35	II-III	70	14.5	0.0	1	2	21 07 13.8	-25 28 54
3745	21 04.3	-47 37	35	130	II-III	96	18.8	0.0	2	6	21 07 42.0	-47 24 53
3746	21 05.1	-36 13	-75	-64	II	44	18.2	0.0	0	6	21 08 13.2	-36 00 51
3747	21 05.4	-43 42	50	70	I-II	44	15.0	0.0306	0	3	21 08 41.4	-43 29 50
3748	21 06.0	-78 26	14	81	III	50	18.8	0.0	1	5	21 12 13.4	-78 13 43
3749	21 06.9	-46 01	62	-55	III	55	17.6	0.032	1	5	21 10 14.7	-45 48 45

Table D.1 continued from previous page

ACO	RAB1950	DEB1950	Xcen	Ycen	BMtype	Count	m10	z	Rich	Dclass	_RA_icrs	_DE_icrs
3750	21 10.6	-49 48	87	10	II-III:	99	18.5	0.0	2	6	21 14 02.4	-49 35 34
3751	21 11.0	-43 05	106	101	II-III	31	17.0	0.0	0	5	21 14 15.3	-42 52 33
3752	21 11.3	-27 20	69	146	II	32	17.3	0.0	0	5	21 14 14.7	-27 07 33
3753	21 11.6	-27 00	73	164	I-II	30	18.1	0.0	0	6	21 14 32.3	-26 47 32
3754	21 12.1	-45 41	111	-39	II-III	35	18.0	0.0	0	6	21 15 25.0	-45 28 30
3755	21 12.2	-43 35	117	74	II-III	34	16.9	0.0	0	5	21 15 27.8	-43 22 30
3756	21 12.5	-42 49	122	117	II-III	39	16.2	0.0	0	4	21 15 44.6	-42 36 29
3757	21 15.3	-45 27	-121	-25	I-II	63	17.8	0.0	1	5	21 18 35.9	-45 14 21
3758	21 17.7	-26 57	17	-102	II-III	42	18.1	0.0	0	6	21 20 37.6	-26 44 14
3759	21 18.7	-33 17	74	93	II-III	67	19.4	0.0	1	6	21 21 43.8	-33 04 11
3760	21 18.7	-70 45	-97	-41	III	108	19.4	0.0	2	6	21 23 17.4	-70 32 09
3761	21 20.4	-76 48	75	-99	II-III	32	18.0	0.0	0	5	21 25 56.4	-76 35 03
3762	21 21.0	-85 03	-18	-3	III	74	19.1	0.0	1	6	21 31 23.3	-84 49 55
3763	21 21.0	-87 26	-9	-130	II-III	52	18.2	0.0	1	5	21 38 06.4	-87 12 45
3764	21 22.8	-34 56	118	4	II-III	53	16.6	0.0	1	5	21 25 51.0	-34 43 00
3765	21 23.7	-53 18	-31	92	II-III	70	19.6	0.0	1	6	21 27 11.5	-53 04 57
3766	21 23.8	-49 29	-56	26	III:	84	19.1	0.0	2	6	21 27 10.4	-49 15 57
3767	21 24.0	-42 53	-41	115	II-III	44	17.4	0.0	0	5	21 27 12.4	-42 39 57
3768	21 24.1	-73 07	-64	-166	III	93	19.3	0.0	2	6	21 28 55.6	-72 53 54
3769	21 24.9	-33 02	-128	106	III	67	19.0	0.0	1	6	21 27 54.7	-32 48 54
3770	21 25.9	-21 06	57	-59	I-II	40	18.0	0.0	0	6	21 28 43.6	-20 52 52
3771	21 26.1	-51 02	-36	-52	III	42	16.1	0.0796	0	4	21 29 30.5	-50 48 51
3772	21 26.4	-42 58	-17	111	II-III	69	17.0	0.0	1	5	21 29 36.0	-42 44 50
3773	21 26.6	-20 06	67	-5	I	32	19.1	0.0	0	6	21 29 24.7	-19 52 50
3774	21 27.9	-45 17	-3	-13	II	47	17.2	0.0	0	5	21 31 08.8	-45 03 46
3775	21 28.4	-43 32	2	80	II	76	17.5	0.0	1	5	21 31 36.3	-43 18 45
3776	21 28.4	-68 58	-60	56	II-III	54	19.1	0.0	1	6	21 32 42.6	-68 44 43
3777	21 29.4	-52 15	-8	-119	II:	78	19.3	0.0	1	6	21 32 49.8	-52 01 42
3778	21 29.6	-22 52	-104	114	II-III	55	17.4	0.0	1	5	21 32 26.7	-22 38 42
3779	21 29.6	-85 16	-8	-14	III	63	18.8	0.0	1	5	21 39 56.7	-85 02 32
3780	21 29.8	-72 55	-43	-154	II	86	19.5	0.0	2	6	21 34 31.6	-72 41 39
3781	21 30.5	-67 04	-61	159	II-III	79	16.6	0.0	1	5	21 34 38.0	-66 50 38
3782	21 30.7	-62 15	-139	-81	II?	40	16.1	0.0557	0	4	21 34 31.6	-62 01 38
3783	21 30.8	-42 52	26	115	II?	118	18.5	0.1955	2	6	21 33 58.9	-42 38 38
3784	21 31.0	-28 46	30	70	II-III	58	19.0	0.0	1	6	21 33 55.7	-28 32 38
3785	21 31.0	-53 51	27	82	II	45	16.0	0.0775	0	4	21 34 28.4	-53 37 37
3786	21 31.1	-82 17	-106	-135	I	32	18.6	0.0	0	5	21 38 27.6	-82 03 32
3787	21 32.8	-37 28	-36	-131	III	100	19.6	0.0	2	6	21 35 52.1	-37 14 33
3788	21 34.1	-33 03	-25	108	III:	64	17.8	0.0	1	5	21 37 05.3	-32 49 30
3789	21 34.1	-67 29	-34	138	II	51	18.8	0.0	1	6	21 38 13.9	-67 15 28
3790	21 34.7	-42 01	65	160	III	38	18.9	0.0	0	6	21 37 51.0	-41 47 28
3791	21 34.7	-43 05	64	103	II-III	44	18.7	0.0	0	6	21 37 52.3	-42 51 28
3792	21 34.7	-47 37	39	129	III	81	18.6	0.0	2	6	21 37 58.6	-47 23 28
3793	21 36.0	-52 18	69	146	II-III	35	17.2	0.0	0	5	21 39 23.9	-52 04 25
3794	21 36.1	-27 23	-27	-125	II:	88	19.6	0.0	2	6	21 38 59.8	-27 09 25
3795	21 36.1	-32 18	87	-120	II?	51	16.8	0.0	1	5	21 39 04.3	-32 04 25
3796	21 36.1	-51 37	48	-85	I-II	46	16.9	0.0756	0	5	21 39 28.6	-51 23 24
3797	21 36.4	-27 20	-19	-124	III	68	18.9	0.0	1	6	21 39 17.8	-27 06 24
3798	21 36.7	-47 20	77	-125	III	37	19.2	0.0	0	6	21 39 57.6	-47 06 23
3799	21 37.0	-72 57	-17	-157	III	50	15.4	0.0	1	3	21 41 38.4	-72 43 20
3800	21 38.5	-44 35	99	22	III	48	18.0	0.0	0	6	21 41 41.4	-44 21 19
3801	21 41.8	-87 00	4	-107	III	39	19.1	0.0	0	6	21 55 27.6	-86 45 57
3802	21 42.5	-46 15	-128	-68	III	58	18.0	0.0	1	6	21 45 42.6	-46 01 09
3803	21 42.5	-53 35	118	90	II:	54	18.6	0.0	1	6	21 45 54.2	-53 21 08
3804	21 42.7	-26 08	51	-59	II-III:	77	17.9	0.0	1	5	21 45 34.0	-25 54 09
3805	21 42.8	-26 12	56	-63	III	66	18.0	0.0	1	6	21 45 40.0	-25 58 08

Table D.1 continued from previous page

ACO	RAB1950	DEB1950	Xcen	Ycen	BMtype	Count	m10	z	Rich	Dclass	_RA_icrs	_DE_icrs
3806	21 43.1	-57 31	75	134	II	115	16.0	0.0747	2	4	21 46 37.9	-57 17 07
3807	21 43.6	-23 31	68	80	III	50	18.3	0.0	1	5	21 46 25.8	-23 17 06
3808	21 43.6	-26 39	66	-88	III	52	18.9	0.0	1	6	21 46 28.3	-26 25 06
3809	21 43.8	-44 08	-121	46	III	73	15.9	0.0	1	4	21 46 57.6	-43 54 06
3810	21 44.2	-64 42	-92	14	III:	76	19.4	0.0	1	6	21 48 03.3	-64 28 04
3811	21 44.5	-47 20	-107	-126	II?	70	19.6	0.0	1	6	21 47 43.6	-47 06 04
3812	21 45.1	-32 57	100	111	III	30	16.4	0.0	0	5	21 48 03.5	-32 43 03
3813	21 45.7	-31 59	-62	-106	I	32	16.8	0.0	0	5	21 48 38.5	-31 45 01
3814	21 46.2	-30 56	-57	-49	II	112	17.4	0.0	2	5	21 49 07.5	-30 42 00
3815	21 46.7	-33 41	118	71	II-III:	65	19.1	0.0	1	6	21 49 39.9	-33 26 59
3816	21 47.0	-55 33	-98	-32	I-II	39	15.1	0.0352	0	3	21 50 26.3	-55 18 58
3817	21 47.9	-50 15	-105	-15	II:	85	18.3	0.0	2	6	21 51 10.9	-50 00 56
3818	21 48.2	-48 17	-107	92	II-III	118	18.2	0.0	2	6	21 51 25.9	-48 02 55
3819	21 49.0	-53 48	-88	61	III	66	18.6	0.0	1	6	21 52 22.4	-53 33 53
3820	21 49.3	-48 38	-96	72	II-III:	66	18.4	0.0	1	6	21 52 32.1	-48 23 52
3821	21 50.0	-44 14	-60	42	II-III	75	17.8	0.0	1	5	21 53 08.2	-43 59 51
3822	21 50.6	-58 05	129	102	II-III	113	16.2	0.076	2	4	21 54 06.2	-57 50 49
3823	21 50.7	-33 26	162	83	II-III	50	18.5	0.0	1	6	21 53 39.0	-33 11 49
3824	21 54.1	-27 07	-74	-110	II:	60	19.1	0.0	1	6	21 56 57.4	-26 52 42
3825	21 54.8	-60 38	-102	-35	III	77	15.8	0.0744	1	4	21 58 22.4	-60 23 39
3826	21 56.5	-56 24	-34	-76	II	62	14.9	0.0754	1	3	21 59 54.5	-56 09 36
3827	21 58.2	-60 11	-80	-11	I	100	16.4	0.0993	2	5	22 01 43.8	-59 56 32
3828	21 58.8	-20 35	-55	-29	II	40	19.0	0.0	0	6	22 01 34.2	-20 20 31
3829	21 59.7	-41 53	-65	-101	III?	88	19.3	0.0	2	6	22 02 45.3	-41 38 29
3830	22 00.1	-61 50	-64	-99	II	72	19.0	0.0	1	6	22 03 41.0	-61 35 28
3831	22 00.2	-46 04	36	-55	III	81	19.0	0.065	2	6	22 03 19.8	-45 49 28
3832	22 02.4	-30 42	-138	-37	I-II	48	18.0	0.0	0	6	22 05 16.9	-30 27 24
3833	22 02.6	-30 44	129	-36	II-III	40	17.6	0.0	0	5	22 05 28.9	-30 29 23
3834	22 02.6	-47 46	23	122	III	154	18.2	0.0	3	6	22 05 45.3	-47 31 23
3835	22 02.9	-39 18	-34	38	III	74	18.6	0.0	1	6	22 05 54.1	-39 03 22
3836	22 06.2	-52 04	49	-108	I	81	17.2	0.0	2	5	22 09 25.9	-51 49 15
3837	22 06.4	-27 34	-93	131	I-II	60	17.5	0.0	1	5	22 09 14.1	-27 19 15
3838	22 07.2	-28 20	-83	91	II-III	71	19.1	0.0	1	6	22 10 02.5	-28 05 14
3839	22 07.3	-49 10	62	46	II	115	17.7	0.0	2	5	22 10 27.7	-48 55 13
3840	22 07.6	-40 07	13	-5	I-II	43	18.0	0.0	0	6	22 10 35.9	-39 52 13
3841	22 08.3	-48 50	69	64	II-III:	112	18.3	0.0	2	6	22 11 26.9	-48 35 11
3842	22 08.5	-38 59	23	56	II-III:	62	18.2	0.0	1	6	22 11 28.6	-38 44 11
3843	22 08.7	-50 44	71	-38	II-III:	105	18.9	0.0	2	6	22 11 53.3	-50 29 10
3844	22 10.6	-35 00	114	1	II-III	52	16.8	0.0	1	5	22 13 30.9	-34 45 07
3845	22 11.4	-48 04	98	104	II:	72	18.5	0.0	1	6	22 14 31.1	-47 49 05
3846	22 11.5	-27 19	-126	-124	III:	69	19.0	0.0	1	6	22 14 19.2	-27 04 05
3847	22 11.8	-17 16	109	149	II-III	30	19.3	0.0	0	6	22 14 31.0	-17 01 05
3848	22 12.3	-43 31	-117	78	II	49	18.8	0.0	0	6	22 15 20.0	-43 16 03
3849	22 12.7	-51 48	103	-96	II-III	42	15.8	0.0678	0	4	22 15 53.4	-51 33 02
3850	22 13.2	-53 39	104	70	II-III:	47	17.3	0.0	0	5	22 16 25.8	-53 24 01
3851	22 13.5	-52 50	107	114	I-II	33	15.8	0.0529	0	4	22 16 42.6	-52 35 01
3852	22 13.6	-19 34	-132	27	III	65	19.1	0.0	1	6	22 16 20.2	-19 19 01
3853	22 13.6	-39 31	75	26	III	43	18.6	0.0	0	6	22 16 34.0	-39 16 01
3854	22 14.8	-35 58	-102	-52	II	130	17.2	0.1214	3	5	22 17 42.9	-35 42 58
3855	22 15.5	-43 16	-87	93	II-III	35	19.3	0.0	0	6	22 18 31.0	-43 00 57
3856	22 15.8	-39 09	98	45	II-III	125	17.9	0.0	2	5	22 18 45.2	-38 53 57
3857	22 16.3	-38 20	106	89	II-III	43	19.2	0.0	0	6	22 19 14.5	-38 04 56
3858	22 16.6	-34 58	-85	2	III	57	18.0	0.0	1	6	22 19 29.8	-34 42 55
3859	22 16.7	-37 16	111	146	II-III	62	18.9	0.0	1	6	22 19 37.5	-37 00 55
3860	22 16.7	-57 21	45	142	III:	32	18.8	0.0	0	6	22 20 00.3	-57 05 54
3861	22 16.9	-37 24	112	138	III	76	17.8	0.0	1	5	22 19 49.6	-37 08 55

Table D.1 continued from previous page

ACO	RAB1950	DEB1950	Xcen	Ycen	BMtype	Count	m10	z	Rich	Dclass	_RA_icrs	_DE_icrs
3862	22 16.9	-46 12	-69	-64	II	35	18.2	0.0	0	6	22 19 57.5	-45 56 54
3863	22 16.9	-49 20	145	35	II-III	63	18.7	0.0	1	6	22 20 01.0	-49 04 54
3864	22 17.0	-52 44	-132	116	II	60	16.6	0.0	1	5	22 20 11.2	-52 28 54
3865	22 17.0	-72 10	147	-125	II?	87	19.3	0.0	2	6	22 21 01.7	-71 54 53
3866	22 17.6	-35 25	-72	-22	II-III	46	17.7	0.0	0	5	22 20 29.9	-35 09 53
3867	22 18.0	-57 55	53	112	III	36	16.6	0.0	0	5	22 21 18.8	-57 39 52
3868	22 18.1	-50 34	-101	-31	II-III	96	19.2	0.0	2	6	22 21 14.1	-50 18 52
3869	22 18.2	-55 23	-110	-21	II:	49	15.1	0.0396	0	3	22 21 26.6	-55 07 52
3870	22 18.7	-52 50	-118	113	II	51	19.0	0.0	1	6	22 21 52.8	-52 34 51
3871	22 19.5	-58 36	41	75	II-III	60	19.3	0.0	1	6	22 22 49.3	-58 20 49
3872	22 20.1	-52 42	-107	120	II-III	52	19.3	0.0	1	6	22 23 16.1	-52 26 48
3873	22 20.3	-29 34	70	23	I-II	56	18.9	0.0	1	6	22 23 07.5	-29 18 48
3874	22 20.9	-43 01	142	-164	II-III	69	18.5	0.0	1	6	22 23 53.4	-42 45 47
3875	22 22.8	-57 29	90	135	I-II:	86	17.7	0.0	2	5	22 26 04.0	-57 13 43
3876	22 23.2	-48 00	-11	-160	I	36	18.1	0.0	0	6	22 26 15.6	-47 44 43
3877	22 23.2	-49 10	-50	46	I-II	103	17.1	0.0	2	5	22 26 16.9	-48 54 43
3878	22 24.0	-32 12	-5	152	III	44	17.4	0.0	0	5	22 26 50.6	-31 56 42
3879	22 24.1	-69 17	-40	40	I-II	114	16.0	0.0224	2	4	22 27 49.8	-69 01 41
3880	22 25.0	-30 50	124	-45	II	31	15.6	0.0	0	4	22 27 49.5	-30 34 40
3881	22 25.4	-33 48	11	66	III	34	18.7	0.0	0	6	22 28 15.4	-33 32 39
3882	22 26.8	-36 47	28	-93	II-III?	30	19.2	0.0	0	6	22 29 41.2	-36 31 37
3883	22 27.1	-48 26	-25	87	II	40	17.4	0.0	0	5	22 30 08.9	-48 10 36
3884	22 28.2	-63 04	-101	103	II-III	32	18.6	0.0	0	6	22 31 35.9	-62 48 34
3885	22 28.4	-30 27	-99	-24	II-III:	33	19.1	0.0	0	6	22 31 12.8	-30 11 34
3886	22 28.5	-55 00	-35	-3	III	31	16.0	0.075	0	4	22 31 40.1	-54 44 34
3887	22 29.9	-39 18	-24	40	II-III	36	18.5	0.0	0	6	22 32 48.3	-39 02 32
3888	22 31.5	-37 59	-7	110	I-II	107	17.6	0.168	2	5	22 34 23.0	-37 43 29
3889	22 32.0	-30 49	-59	-42	II	95	19.4	0.0	2	6	22 34 48.4	-30 33 28
3890	22 34.1	-58 50	-100	62	II:	63	19.0	0.0	1	6	22 37 19.3	-58 34 25
3891	22 34.5	-60 14	-90	-14	III	32	17.0	0.0	0	5	22 37 45.4	-59 58 24
3892	22 35.1	-30 58	-22	-49	II-III	50	17.9	0.0	1	5	22 37 54.0	-30 42 23
3893	22 35.3	-24 10	-110	46	I	39	18.6	0.0	0	6	22 38 02.4	-23 54 23
3894	22 35.6	-22 20	-121	-123	II-III	47	19.0	0.0	0	6	22 38 19.4	-22 04 23
3895	22 36.0	-36 57	125	-101	II-III	47	15.5	0.0	0	4	22 38 51.4	-36 41 22
3896	22 36.1	-38 05	-129	-166	II-III	78	17.9	0.0	1	5	22 38 58.1	-37 49 22
3897	22 36.6	-17 39	158	129	II	63	16.6	0.0	1	5	22 39 17.2	-17 23 21
3898	22 37.1	-62 40	-45	127	III	46	17.1	0.0	0	5	22 40 24.4	-62 24 20
3899	22 37.4	-38 51	55	63	II-III	37	17.8	0.0	0	5	22 40 16.4	-38 35 20
3900	22 37.5	-24 06	-82	49	II-III	35	19.1	0.0	0	6	22 40 14.1	-23 50 20
3901	22 38.6	-38 03	-101	-161	II-III	74	19.3	0.0	1	6	22 41 27.6	-37 47 18
3902	22 39.0	-42 52	-130	114	II-III	33	18.5	0.0	0	6	22 41 54.8	-42 36 17
3903	22 41.7	-30 19	54	-12	III	95	19.0	0.0	2	6	22 44 28.6	-30 03 13
3904	22 41.8	-43 48	-101	65	III	79	18.8	0.0	1	6	22 44 42.7	-43 32 13
3905	22 41.9	-55 53	63	-50	II-III:	67	19.1	0.0	1	6	22 45 00.0	-55 37 13
3906	22 41.9	-61 02	-42	-53	III	67	18.0	0.0	1	6	22 45 07.1	-60 46 13
3907	22 42.1	-63 04	-15	106	III	46	17.4	0.0	0	5	22 45 22.5	-62 48 12
3908	22 42.6	-45 18	-91	-15	III	41	17.7	0.0	0	5	22 45 31.6	-45 02 12
3909	22 42.8	-44 33	-91	25	II-III	50	19.2	0.0	1	6	22 45 43.0	-44 17 12
3910	22 43.0	-46 15	-93	-69	II-III	47	17.5	0.0	0	5	22 45 56.3	-45 59 11
3911	22 43.1	-52 59	77	106	II-III	58	17.1	0.0381	1	5	22 46 08.3	-52 43 11
3912	22 43.6	-36 21	-52	-69	II:	41	15.6	0.0	0	4	22 46 25.5	-36 05 11
3913	22 44.1	-84 38	-95	5	II-III?	67	18.5	0.0	1	5	22 50 16.7	-84 22 08
3914	22 44.3	-60 37	-28	-30	II-III	57	19.3	0.0	1	6	22 47 29.3	-60 21 09
3915	22 44.6	-52 19	92	141	II-III	55	17.1	0.0	1	5	22 47 37.1	-52 03 09
3916	22 44.7	-72 11	49	-117	I-II	39	17.5	0.0	0	5	22 48 20.8	-71 55 09
3917	22 45.5	-32 00	98	-104	III	56	19.3	0.0	1	6	22 48 16.8	-31 44 08

Table D.1 continued from previous page

ACO	RAB1950	DEB1950	Xcen	Ycen	BMtype	Count	m10	z	Rich	Dclass	_RA_icrs	_DE_icrs
3918	22 46.0	-28 50	-168	63	I-II	39	18.6	0.0	0	6	22 48 45.2	-28 34 07
3919	22 46.1	-59 56	-16	5	III	64	18.9	0.0	1	6	22 49 15.4	-59 40 07
3920	22 46.2	-41 11	-120	-64	I-II	68	18.3	0.0	1	6	22 49 03.8	-40 55 07
3921	22 46.5	-64 39	10	22	II	93	16.7	0.0	2	5	22 49 47.0	-64 23 06
3922	22 46.7	-52 02	-110	-109	II-III	51	17.5	0.0	1	5	22 49 42.0	-51 46 06
3923	22 46.8	-61 11	-11	-62	III	58	18.0	0.0	1	6	22 49 58.9	-60 55 06
3924	22 48.7	-62 37	1	-138	II	38	18.8	0.0	0	6	22 51 54.2	-62 21 03
3925	22 48.9	-46 51	-31	-98	II	38	16.2	0.0516	0	4	22 51 49.0	-46 35 03
3926	22 49.0	-33 39	7	73	III	171	18.8	0.0	3	6	22 51 47.0	-33 23 03
3927	22 49.4	-60 50	4	-42	III	91	18.5	0.0	2	6	22 52 33.1	-60 34 03
3928	22 49.5	-33 51	13	64	III:	63	18.1	0.0	1	6	22 52 17.0	-33 35 03
3929	22 49.6	-32 32	141	-133	III?	65	19.1	0.0	1	6	22 52 22.3	-32 16 03
3930	22 49.8	-31 26	145	-74	II:	76	18.9	0.0	1	6	22 52 33.8	-31 10 02
3931	22 50.1	-71 49	-142	-109	II-III	113	17.5	0.0	2	5	22 53 38.9	-71 33 01
3932	22 50.4	-73 15	-62	94	II-III	32	17.6	0.0	0	5	22 54 02.0	-72 59 01
3933	22 50.6	-34 46	25	15	III	64	19.0	0.0	1	6	22 53 23.3	-34 30 01
3934	22 50.8	-33 59	27	56	II?	113	19.3	0.224	2	6	22 53 34.8	-33 43 01
3935	22 51.1	-62 23	15	-125	II-III	58	17.8	0.0	1	5	22 54 16.5	-62 07 00
3936	22 51.2	-35 11	32	-8	III	95	18.0	0.0	2	5	22 53 59.4	-34 55 01
3937	22 51.4	-46 37	-8	-85	III	129	19.3	0.0	2	6	22 54 18.1	-46 21 00
3938	22 52.0	-55 51	-108	-46	II?	92	18.3	0.0	2	6	22 55 01.8	-55 34 59
3939	22 52.0	-58 28	23	83	III	88	17.5	0.0	2	5	22 55 04.8	-58 11 59
3940	22 52.3	-60 38	25	-32	III	105	18.2	0.0	2	6	22 55 25.4	-60 21 59
3941	22 52.8	-61 13	24	-64	II-III?	43	18.3	0.0	0	6	22 55 55.9	-60 56 58
3942	22 53.4	-74 25	-47	32	I-II	46	18.9	0.0	0	6	22 57 04.0	-74 08 57
3943	22 53.5	-28 40	-81	74	I-II	60	19.3	0.0	1	6	22 56 14.0	-28 23 58
3944	22 53.6	-40 17	-46	-15	I-II:	50	18.3	0.0	1	6	22 56 25.5	-40 00 58
3945	22 54.8	-39 22	-35	36	I?	40	19.4	0.0	0	6	22 57 36.8	-39 05 56
3946	22 54.9	-56 38	157	-95	III	64	18.9	0.0	1	6	22 57 55.4	-56 21 56
3947	22 55.1	-59 01	42	53	II	92	18.0	0.0	2	6	22 58 10.0	-58 44 56
3948	22 55.9	-26 57	-123	-105	I-II	42	19.3	0.0	0	6	22 58 36.9	-26 40 55
3949	22 56.1	-20 15	-127	-12	III	43	18.9	0.0	0	6	22 58 46.4	-19 58 55
3950	22 56.9	-56 30	-70	-79	III	88	18.4	0.0	2	6	22 59 54.4	-56 13 53
3951	22 57.0	-18 54	-118	60	II-III	67	17.8	0.0	1	5	22 59 39.8	-18 37 54
3952	22 57.3	-46 03	47	-55	II-III	49	17.8	0.0	0	5	23 00 10.0	-45 46 53
3953	22 57.4	-45 35	47	-30	III	39	18.9	0.0	0	6	23 00 15.7	-45 18 53
3954	22 57.9	-61 20	60	-70	III	91	18.2	0.0	2	6	23 00 59.5	-61 03 52
3955	22 58.0	-43 35	55	77	III	38	19.0	0.0	0	6	23 00 50.3	-43 18 52
3956	22 58.4	-43 56	59	58	III	30	17.3	0.0	0	5	23 01 14.4	-43 39 52
3957	22 59.1	-60 27	70	-23	I-II	56	19.4	0.0	1	6	23 02 09.8	-60 10 51
3958	22 59.6	-29 28	-8	31	I-II	37	19.1	0.0	0	6	23 02 19.3	-29 11 51
3959	22 59.7	-33 40	-142	69	II-III	69	17.4	0.0	1	5	23 02 27.0	-33 23 50
3960	23 00.1	-35 12	-134	-11	III	73	18.5	0.0	1	6	23 02 51.6	-34 55 50
3961	23 00.3	-38 07	22	103	II	60	19.4	0.0	1	6	23 03 04.9	-37 50 50
3962	23 00.6	-39 26	23	33	III	89	19.3	0.0	2	6	23 03 23.5	-39 09 49
3963	23 01.0	-44 35	82	22	III	40	16.8	0.089	0	5	23 03 50.1	-44 18 49
3964	23 01.7	-20 11	-56	-9	II-III	42	18.1	0.0	0	6	23 04 21.8	-19 54 48
3965	23 02.5	-53 18	-31	93	III	35	19.2	0.0	0	6	23 05 25.4	-53 01 47
3966	23 02.6	-60 23	93	-20	II	43	17.7	0.0	0	5	23 05 38.0	-60 06 47
3967	23 02.6	-60 55	-155	-54	III	65	18.3	0.0	1	6	23 05 38.6	-60 38 47
3968	23 02.8	-39 23	47	36	III	94	18.6	0.0	2	6	23 05 34.9	-39 06 47
3969	23 02.8	-44 25	101	32	III	55	17.0	0.0699	1	5	23 05 37.5	-44 08 47
3970	23 03.0	-45 29	101	-26	III	60	17.3	0.0	1	5	23 05 50.0	-45 12 47
3971	23 03.0	-60 58	101	-55	II-III	136	18.0	0.0	3	6	23 06 02.5	-60 41 47
3972	23 03.1	-44 38	103	19	II-III	64	17.4	0.0	1	5	23 05 55.5	-44 21 47
3973	23 04.8	-56 02	-12	-54	I-II	65	19.1	0.0	1	6	23 07 44.7	-55 45 45

Table D.1 continued from previous page

ACO	RAB1950	DEB1950	Xcen	Ycen	BMtype	Count	m10	z	Rich	Dclass	_RA_icrs	_DE_icrs
3974	23 04.9	-67 45	-100	118	II?	35	19.5	0.0	0	6	23 08 05.3	-67 28 45
3975	23 05.0	-58 57	113	55	II-III?	67	18.5	0.0	1	6	23 07 59.3	-58 40 45
3976	23 05.4	-61 08	-142	-62	II	73	18.7	0.0	1	6	23 08 25.4	-60 51 44
3977	23 07.3	-40 42	93	-35	II	61	19.0	0.0	1	6	23 10 04.5	-40 25 43
3978	23 08.7	-29 04	-172	47	II-III	58	18.3	0.0	1	6	23 11 23.8	-28 47 41
3979	23 10.2	-68 15	-71	92	III	55	19.3	0.0	1	6	23 13 20.5	-67 58 40
3980	23 10.3	-28 38	118	74	I-II	36	19.3	0.0	0	6	23 12 59.4	-28 21 40
3981	23 10.6	-58 42	153	66	II-III	62	19.4	0.0	1	6	23 13 32.5	-58 25 39
3982	23 11.4	-67 52	-68	112	I-II	64	17.8	0.0	1	5	23 14 31.0	-67 35 38
3983	23 11.5	-63 19	-103	89	II	74	18.6	0.0	1	6	23 14 30.7	-63 02 38
3984	23 12.6	-38 04	-122	98	II-III	114	18.3	0.0	2	6	23 15 20.2	-37 47 38
3985	23 13.3	-23 36	88	74	I-II	36	16.8	0.0	0	5	23 15 57.5	-23 19 37
3986	23 13.8	-74 57	25	4	I-II	30	17.8	0.0	0	5	23 17 09.3	-74 40 36
3987	23 14.0	-48 33	120	79	II-III	50	17.3	0.0	1	5	23 16 48.3	-48 16 36
3988	23 14.2	-73 52	29	62	II-III	41	18.0	0.0	0	6	23 17 29.6	-73 35 36
3989	23 15.4	-35 57	33	-45	II?	65	19.3	0.0	1	6	23 18 06.8	-35 40 35
3990	23 15.7	-68 03	-45	104	II-III	98	19.0	0.0286	2	6	23 18 46.3	-67 46 35
3991	23 16.0	-57 42	-75	125	III	49	18.1	0.0	0	6	23 18 53.2	-57 25 35
3992	23 17.2	-73 34	41	78	II	31	16.5	0.0	0	5	23 20 25.9	-73 17 34
3993	23 17.3	-52 24	141	-128	III	30	19.2	0.0	0	6	23 20 07.2	-52 07 34
3994	23 18.1	-66 17	-57	-67	II-III?	66	19.3	0.0	1	6	23 21 06.3	-66 00 33
3995	23 18.5	-69 58	-28	2	II	103	18.8	0.0	2	6	23 21 35.3	-69 41 33
3996	23 18.7	-22 23	155	-126	III	59	18.4	0.0	1	6	23 21 20.5	-22 06 33
3997	23 18.7	-24 27	-115	29	II-III	39	18.1	0.0	0	6	23 21 21.0	-24 10 33
3998	23 18.9	-42 10	-13	153	I	40	17.7	0.0	0	5	23 21 38.2	-41 53 33
3999	23 20.0	-52 04	-86	-109	III	52	18.0	0.0	1	5	23 22 48.1	-51 47 32
4000	23 20.3	-40 55	-39	-48	I-II	46	19.2	0.0	0	6	23 23 01.4	-40 38 32
4001	23 20.5	-61 44	-39	-90	II-III	79	18.8	0.0	1	6	23 23 24.2	-61 27 31
4002	23 21.9	-65 37	-39	-30	III	59	18.9	0.0	1	6	23 24 51.1	-65 20 30
4003	23 22.1	-23 23	-74	87	II	49	19.0	0.0	0	6	23 24 44.3	-23 06 30
4004	23 22.1	-37 14	-22	147	III	39	19.0	0.0	0	6	23 24 47.8	-36 57 30
4005	23 23.5	-53 37	-127	74	III	91	18.7	0.0	2	6	23 26 17.5	-53 20 29
4006	23 24.7	-62 41	-25	126	II-III:	86	19.0	0.0	2	6	23 27 34.7	-62 24 28
4007	23 25.6	-69 12	-35	6	III	100	17.7	0.0	2	5	23 28 34.8	-68 55 28
4008	23 27.6	-39 36	30	22	I	66	16.7	0.0	1	5	23 30 17.2	-39 19 27
4009	23 27.9	-29 33	54	25	I	36	17.6	0.0	0	5	23 30 32.8	-29 16 27
4010	23 28.5	-36 47	-82	-96	I-II	67	16.7	0.0	1	5	23 31 10.3	-36 30 26
4011	23 29.0	-34 43	-78	15	II-III?	95	18.2	0.0	2	6	23 31 39.7	-34 26 26
4012	23 29.1	-34 06	-78	49	II-III	35	19.2	0.0	0	6	23 31 45.6	-33 49 26
4013	23 29.2	-35 33	-75	-29	III	51	18.9	0.0	1	6	23 31 51.9	-35 16 26
4014	23 29.8	-25 46	20	-41	II	35	17.6	0.0	0	5	23 32 25.8	-25 29 26
4015	23 29.8	-37 43	58	124	II-III	36	18.4	0.0	0	6	23 32 28.2	-37 26 25
4016	23 32.0	-69 36	28	24	III	34	16.4	0.0	0	5	23 34 54.4	-69 19 24
4017	23 32.2	-66 39	17	-86	II-III	65	19.6	0.0	1	6	23 35 03.4	-66 22 24
4018	23 32.7	-52 35	17	-137	II-III	42	17.5	0.0	0	5	23 35 25.6	-52 18 24
4019	23 33.6	-58 12	47	99	III	60	18.9	0.0	1	6	23 36 21.5	-57 55 23
4020	23 35.0	-69 34	47	26	II-III	51	18.0	0.0	1	6	23 37 52.1	-69 17 23
4021	23 35.5	-38 23	116	86	II-III	52	17.2	0.0	1	5	23 38 09.1	-38 06 23
4022	23 35.7	-51 08	43	-59	II-III	45	18.6	0.0	0	6	23 38 24.0	-50 51 22
4023	23 36.5	-85 29	-26	-27	III	46	19.2	0.0	0	6	23 40 21.0	-85 12 22
4024	23 37.0	-69 46	56	12	II-III	68	19.3	0.0	1	6	23 39 50.7	-69 29 22
4025	23 37.1	-49 55	57	5	II	33	18.2	0.0	0	6	23 39 47.2	-49 38 22
4026	23 38.3	-37 48	-124	115	II-III	45	16.4	0.0	0	5	23 40 56.3	-37 31 21
4027	23 39.0	-56 15	-3	-65	III	33	19.4	0.0	0	6	23 41 42.3	-55 58 21
4028	23 40.5	-64 04	67	52	III	68	18.1	0.0	1	6	23 43 14.6	-63 47 21
4029	23 41.0	-38 33	-94	76	III	43	17.7	0.0	0	5	23 43 37.9	-38 16 20

Table D.1 continued from previous page

ACO	RAB1950	DEB1950	Xcen	Ycen	BMtype	Count	m10	z	Rich	Dclass	_RA_icrs	_DE_icrs
4030	23 42.5	-50 36	102	-32	II-III	44	19.2	0.0	0	6	23 45 09.5	-50 19 20
4031	23 42.8	-24 46	-90	14	I	55	19.2	0.0	1	6	23 45 23.9	-24 29 20
4032	23 43.6	-20 04	-57	-2	I-II	40	18.1	0.0	0	6	23 46 11.4	-19 47 20
4033	23 43.6	-64 42	-97	14	III	41	19.3	0.0	0	6	23 46 19.0	-64 25 20
4034	23 44.0	-52 35	37	132	I	67	18.7	0.0	1	6	23 46 39.3	-52 18 20
4035	23 44.1	-33 53	89	59	II-III?	83	18.9	0.0	2	6	23 46 42.6	-33 36 20
4036	23 44.5	-63 03	-98	102	III	61	19.0	0.0	1	6	23 47 11.8	-62 46 19
4037	23 44.6	-28 36	-20	79	III	118	18.7	0.0	2	6	23 47 12.0	-28 19 19
4038	23 45.1	-28 25	-16	89	III	117	14.0	0.0283	2	2	23 47 41.9	-28 08 19
4039	23 45.6	-36 33	102	-83	II:	63	19.0	0.0	1	6	23 48 12.6	-36 16 19
4040	23 45.6	-68 04	102	102	II-III	56	19.6	0.0	1	6	23 48 19.1	-67 47 19
4041	23 46.1	-29 04	-167	50	I	72	19.0	0.0	1	6	23 48 41.8	-28 47 19
4042	23 46.2	-32 03	-2	-106	II	35	19.6	0.0	0	6	23 48 48.0	-31 46 19
4043	23 46.3	-31 34	-160	-85	I-II	53	19.1	0.0	1	6	23 48 54.0	-31 17 19
4044	23 46.8	-27 16	-163	147	III	40	17.7	0.0	0	5	23 49 23.5	-26 59 19
4045	23 47.7	-19 28	-5	31	I	53	17.5	0.0	1	5	23 50 16.9	-19 11 19
4046	23 47.8	-41 51	-23	-97	III	50	19.2	0.0	1	6	23 50 24.6	-41 34 19
4047	23 47.9	-68 43	-62	69	III	55	19.2	0.0	1	6	23 50 35.8	-68 26 19
4048	23 48.2	-38 42	-19	70	II?	85	18.5	0.0	2	6	23 50 48.2	-38 25 19
4049	23 49.0	-28 39	31	77	III	39	14.8	0.0283	0	3	23 51 35.3	-28 22 18
4050	23 49.5	-67 57	122	107	II	88	19.5	0.0	2	6	23 52 10.3	-67 40 18
4051	23 50.9	-63 01	-59	106	I-II	36	17.8	0.0	0	5	23 53 32.2	-62 44 18
4052	23 51.4	-79 16	-23	42	II-III	39	18.1	0.0	0	5	23 54 08.8	-78 59 18
4053	23 52.2	-27 57	68	113	III	64	16.6	0.0	1	5	23 54 46.8	-27 40 18
4054	23 52.6	-28 49	74	67	III	73	18.2	0.0	1	5	23 55 10.7	-28 32 18
4055	23 52.8	-21 28	-90	-76	II?	60	18.8	0.0	1	6	23 55 22.4	-21 11 18
4056	23 53.4	-37 34	35	131	II-III:	43	18.5	0.0	0	6	23 55 59.0	-37 17 18
4057	23 53.8	-79 42	-16	19	II-III	38	18.0	0.0	0	5	23 56 29.5	-79 25 18
4058	23 54.0	-36 54	-66	-101	III	55	18.4	0.0	1	6	23 56 34.8	-36 37 18
4059	23 54.1	-34 57	-64	3	I	66	15.3	0.0456	1	3	23 56 40.7	-34 40 18
4060	23 54.5	-69 45	-28	15	III	54	18.6	0.0	1	6	23 57 07.1	-69 28 18
4061	23 54.6	-23 49	-70	64	III	40	19.1	0.0	0	6	23 57 10.3	-23 32 18
4062	23 55.1	-65 30	-31	-26	II-III	38	19.1	0.0	0	6	23 57 42.1	-65 13 18
4063	23 55.7	-28 01	-55	109	III	61	18.9	0.0	1	6	23 58 16.2	-27 44 18
4064	23 56.0	-60 16	-29	-13	I-II	38	18.1	0.0	0	6	23 58 35.1	-59 59 18
4065	23 56.2	-21 32	-50	-80	III	64	18.5	0.0	1	6	23 58 46.1	-21 15 18
4066	23 56.3	-71 47	132	-101	II-III	39	17.6	0.0	0	5	23 58 53.9	-71 30 17
4067	23 56.4	-60 57	-27	-48	III	72	16.9	0.0	1	5	23 58 59.0	-60 40 17
4068	23 57.2	-39 45	74	13	III	45	16.7	0.0	0	5	23 59 46.1	-39 28 18
4069	23 57.5	-21 40	-34	-89	II-III	59	18.7	0.0	1	6	00 00 03.9	-21 23 18
4070	23 57.7	-30 39	-30	-33	II	52	18.0	0.0	1	6	00 00 15.9	-30 22 18
4071	23 57.8	-28 23	-30	89	III	115	19.6	0.0	2	6	00 00 21.9	-28 06 18
4072	23 58.1	-21 23	-26	-74	II-III	45	18.6	0.0	0	6	00 00 39.8	-21 06 18
4073	23 58.1	-46 50	-18	-98	II:	45	19.1	0.0	0	6	00 00 40.0	-46 33 17
4074	23 58.2	-36 41	-21	-87	III	60	17.1	0.0	1	5	00 00 45.9	-36 24 18
4075	23 58.5	-47 01	-16	-107	III	40	19.0	0.0	0	6	00 01 03.8	-46 44 17
4076	23 59.2	-48 31	-7	80	II-III	64	18.7	0.0	1	6	00 01 45.6	-48 14 17